Integrated study on the interaction between upper mantle and mafic melt evidenced by wehrlite xenoliths from the Nógrád-Gömör Volcanic Field (Northern Pannonian Basin, Central Europe)

by

Levente Patkó

Ph.D. dissertation

Faculty of Science
Eötvös Loránd University

Ph.D. school of Earth Sciences
Chair: Prof. Judit Bartholy, D.Sc.
Department of Meteorology
Institute of Geography and Earth Sciences
Eötvös Loránd University

Ph.D. program of Geology and Geophysics
Chair: Prof. Szabolcs Harangi, D.Sc.
Department of Petrology and Geochemistry
Institute of Geography and Earth Sciences
Eötvös Loránd University

Advisor

Prof. Csaba Szabó, Ph.D.
Lithosphere Fluid Research Laboratory
Department of Petrology and Geochemistry
Institute of Geography and Earth Sciences
Eötvös Loránd University

Consultants

Prof. Robert J. Bodnar, Ph.D.
Fluids Research Group
Department of Geosciences
Virginia Polytechnic Institute and State University

István J. Kovács, Ph.D.
Geodetic and Geophysical Institute
Research Centre for Astronomy and Earth Sciences

2020
Budapest

Table of Contents

Table of Figures

Abstract

The Nógrád-Gömör Volcanic Field (NGVF) is located in the northern part of the Pannonian Basin, and is one of the five known Neogene xenolith bearing alkali basalt occurrences.

In addition to the dominant lherzolites, clinopyroxene-enriched upper mantle xenoliths classified as wehrlites are also common (~20% of all xenoliths) in the central part of the NGVF. In this Ph.D. research, a dozen wehrlite xenoliths were thoroughly investigated in order to determine the conditions of their formation. Specific textural features, including clinopyroxene-rich patches in an olivine-rich lithology, orthopyroxene relicts in the cores of newly-formed clinopyroxenes and vermicular spinel forms all suggest that wehrlites were formed as a result of intensive interaction between a metasomatic agent and the peridotite wall rock. Based on the major and trace element geochemistry of the rock-forming minerals, significant enrichment in basaltic (Fe, Mn, Ti) and high field strength elements (Nb, Ta, Hf, Zr) was observed, compared to compositions of common lherzolite xenoliths. The composition of the metasomatic agent is interpreted to be a mafic silicate melt, which was further confirmed by numerical modelling of trace elements using the plate model. The model results also show that the melt/rock ratio played a key role in the degree of petrographic and geochemical transformation.

The wehrlitization process was accompanied by structural hydroxyl enrichment in clinopyroxenes. In the olivines, diffusion-driven syn- and post-entrapment decrease of structural hydroxyl overprinted the likely enrichment, leading to the total loss of original hydrogen content.

The process of wehrlite formation also caused sulfide precipitation resulting in elevated sulfide abundance compared to lherzolites. Wehrlitic sulfides show higher bulk Fe, but lower bulk Ni contents compared to the lherzolitic sulfides. In addition, the sulfides in wehrlites are enriched in Zn, Cd, Sb, Tl and depleted in Ge, Se, Te and Re compared to the sulfides in lherzolites. These chemical characteristics are probably due to sulfide precipitation took place at greater depth than the wehrlite formation. The δ^{56}Fe signatures show isotopic fractionation between lherzolites and wehrlites with heavier isotope compositions in the wehrlitic sulfides. All these results indicate enrichment of sulfide, and consequently, transition metals (siderophile and chalcophile elements) during of the wehrlite-forming metasomatism in the subcontinental lithospheric mantle.

According to model calculations, the wehrlite formation also influenced the electrical resistivity values of the upper mantle. The presence of a body with low electrical resistivity (<10 Ωm) on

the magnetotelluric image suggests a ~30 km long and ~15 km thick mantle volume affected by the wehrlitization.

The lack of equilibrium and the conclusions drawn by using variable lherzolitic precursors in the model both indicate that the wehrlitization was the last event that occurred shortly before xenolith entrainment in the host basalt. It is highly likely that the wehrlitization and the Neogene basaltic volcanism are related to the same magma production event. The petrographic and geochemical transformation of the upper mantle beneath basalt volcanic fields, as presented in this study, can be an accurate representation of similar tectonic regions worldwide.

Magyar nyelvű összefoglaló

A nógrád-gömör vulkáni terület (NGVT) a Pannon-medence északi részén található, és egyike annak az öt neogén alkali bazaltos területnek, amely felsőköpeny xenolitokat szállított a felszínre. A domináns lherzolit mellett nagy számban (~20 %) került elő klinopiroxén gazdag wehrlit xenolit az NGVT központi régiójából. Jelen Ph.D. dolgozatban részletesen megvizsgáltam egy tucat wehrlit xenolitot a keletkezésük körülményeinek meghatározásának céljából. Különleges szöveti sajátságok, mint a klinopiroxén- és olivin-gazdag csomók megjelenése, újonnan keletkezett klinopiroxénekben lévő ortopiroxén maradványok, valamint vermikuláris spinellek jelenléte mind azt mutatják, hogy a wehrlit fluidum és peridotitos falkőzet kölcsönhatása révén keletkezett. A kőzetalkotó ásványok fő- és nyomelemgeokémiai tulajdonságai alapján a lherzlithoz képest a wehrlit gazdagabb bazaltos (Fe, Mn, Ti) és nagy térerejű elemekben (Nb, Ta, Hf, Zr). A kőzettani és geokémiai tulajdonságok alapján a metaszomatózist okozó fluidum egy mafikus összetételű szilikátos olvadék lehetett, amit a nyomelemeken alapuló numerikus modellezés is megerősített. A modellezés eredményei szintén rámutattak arra, hogy az olvadék/kőzet arány meghatározza a metaszomatizált köpeny új kőzettani és geokémiai tulajdonságait.

A wehrlitesedés a klinopiroxének szerkezeti hidroxil tartalmának növekedésével járt együtt. Ez a gazdagodás valószínűleg az olivint is érintette, azonban a xenolit felszínre jutása közben és utána történt diffúziós szerkezeti hidroxil veszteség felülírhatta ezt az állapotot.

A wehrlit képződése szulfidok kiválásával is együtt járt, ami révén nagyobb a szulfid ásványok jelenléte, mint a lherzolitban. A wehrlites szulfidok nagyobb Fe és kisebb Ni tartalommal jellemezhetők, mint a lherzolitban. Emellett a wehrlites szulfidok a lherzolitos szulfidokhoz képest gazdagabbak Zn, Cd, Sb, Tl, míg kimerültebbek Ge, Se, Te és Re elemekben. Ezek a geokémiai tulajdonságok a wehrlit képződésénél mélyebbi szulfid kiválására utalnak. A δ^{56}Fe érték különbségei a két xenolit sorozatban a metaszomatózis során történt izotópfrakcionációra utalnak, amely a nehezebb Fe izotóp dúsulását eredményezte a wehrlites szulfidokban. Összességében elmondható, hogy a szulfidok alapján a metaszomatózis az átmenetifémek (sziderofil es kahlkofil elemek) jelentős gazdagodását eredményezte az átalakult köpenytérfogatban.

A jelen dolgozatban részletezett becslés alapján a wehrlitesedés jelentősen csökkenti az érintett felsőköpeny elektromos ellenállását. Éppen ezért a kis elektromos ellenállással (<10 Ωm)

jellemezhető test megjelenése a magnetotellurikus inverzión egy ~30 km hosszú és ~15 km széles metaszomatizált zónára utal.

A kémiai egyensúly hiánya és a modellezés eredményei egyaránt arra utalnak, hogy a wehrlitesedés az utolsó mélybeli folyamat lehetett, ami közvetlenül a xenolitok felszínre szállítása előtt történt. Mindez és a metaszomatikus fluidum becsült összetétele arra utalnak, hogy a wehrlitesedés a neogén bazaltos vulkanizmushoz kapcsolódik. A jelen Ph.D. tanulmány részletes petrográfiai és geokémiai eredmények által mutatja be, hogy olvadékáramlás révén milyen komplex átalakulás éri a bazaltos területek alatti felsőköpenyt szerte a Földünkön.

1. Introduction and aims

Mankind has limited connection with the Earth's interior, even though it has a huge impact on our lives as the source of numerous surface processes. In particular, mantle plays a key role in plate tectonics resulting in both beneficial (e.g., ore body formation) and hazardous (e.g., volcanism, seismic activity) phenomena. To understand such complex processes, gathering information from the mantle is essential. Most of our knowledge is indirect, based on deep geophysical methods such as magnetotellurics or seismic tomography, which can reveal the electrical conductivity and seismic wave propagation in the mantle, respectively. However, direct information is available from mantle rocks appearing on the surface. Peridotite and ophiolite massifs are extensive volumes (> km^3) of mantle materials, which are exposed on the surface during tectonic processes. These massifs allow to examine the spatial distribution of different deep-seated events. However, due to the long and complex metamorphic history, these mantle materials are often highly altered. In contrast, upper mantle xenoliths hosted by fast ascending alkali basalts, kimberlites or lamprophyres, can preserve their original characteristics, despite their smaller size (~cm scale). Therefore, xenoliths are the best material to study mantle processes and their impact on petrographical, geochemical, deformational and geophysical features.

The Carpathian-Pannonian region (CPR) is an excellent natural laboratory, as it has five Neogene alkali basalt locations with mantle derived xenoliths. From west to east these are the following: Styrian Basin Volcanic Field, Little Hungarian Plain Volcanic Field, Bakony-Balaton Highland Volcanic Field, Nógrád-Gömör Volcanic Field and Perşani Mountains Volcanic Field. Based on the data of great number of mantle xenoliths, lherzolite is the dominant rock type in the CPR with subordinate harzburgite and dunite in the xenolith record (Szabó et al., 2004 and references therein). These modal compositions are frequent in the European mantle lithosphere (Downes, 2001) and indicate different stages of geochemical depletion (e.g., Puziewicz et al., 2011) or enrichment (e.g., Le Roux et al., 2007; Bali et al., 2007). Less attention has been paid to the petrogenesis of clinopyroxene-enriched peridotites, i.e. wehrlite. Wehrlite, although presents in several localities worldwide, was only collected in bigger proportion (> 5 %) in the central part of Nógrád-Gömör Volcanic Field (NGVF) within the CPR (Patkó et al., 2020).

Wehrlite roks are unlikely to represent partial melting residues (e.g., Kelemen, 1990). Two processes are commonly invoked to explain the formation of wehrlite: either it represents high pressure cumulate that crystallized from melt trapped near the crust-mantle transitional zone,

forming lenses or dikes (Frey and Prinz, 1978; Girardeau and Francheteau, 1993; Rocco et al., 2013), or it may result from metasomatism triggered by fluid/melt-peridotite interaction. The metasomatic agent of wehrlite formation can be either carbonate melts/fluids, producing magnesian wehrlites (e.g., Hauri et al., 1993; Rudnick et al., 1993; Yaxley et al., 1998; Coltorti et al., 1999; Kogarko et al., 2001; Scott et al., 2014) or silicate melts, leading to Fe-rich wehrlites (e.g., Zinngrebe and Foley, 1995; Peslier et al., 2002a; Rivalenti et al., 2004; Ackerman et al., 2009a; Shaw et al., 2005; 2018).

This Ph.D. research studies 12 wehrlite xenoliths from the NGVF with the aim to determine the conditions of their formation. The most widely applied approach in such investigations includes the analyses of petrographic and geochemical characteristics, both for the whole-rocks and the constituent phases. Thus, I report detailed petrographic, major and trace element geochemical data for the wehrlites and compare these results to the characteristics of the local clinopyroxene-poor peridotites (Liptai et al., 2017). I also aimed to determine the geochemical composition of the metasomatic agent. Therefore, equilibrium melt estimation was carried out using partition coefficients between silicate melt and clinopyroxene. To improve this estimation, trace element modelling applying the plate model of Vernières et al. (1997) was carried out. Hence, my work contributes to a better understanding of the nature of the metasomatic process that leads to the formation of wehrlitic mantle domains.

In addition to the rock-forming constituents, sulfides are also affected by mantle metasomatism (e.g., Büchl et al., 2002; Lorand et al., 2003; Luguet et al., 2008; Ackerman et al., 2013; Wainwright et al., 2015; Harvey et al., 2015). Sulfides are the main hosts of highly siderophile (Os, Ir, Ru, Rh, Pt, Pd, Re, Au) and chalcophile elements (Zn, As, Sb, Bi, Cu, Ag, Cd, Pb, Tl, Te, Se, In) (e.g., Lorand and Luguet, 2016). Therefore, studying sulfides in peridotites is essential to understand the budget of these elements in the upper mantle. Studies on mantle sulfides are mostly focusing on the characteristics of Platinum Group Elements (PGE) and Re-Os isotope systematics (Luguet and Reisberg, 2016 and references therein). Furthermore, most studies are based on bulk rock analyses. However, it is evident that in situ analyses can reveal more details on the complexity of the sulfide characteristics (e.g., Griffin et al. 2002). Therefore, more and more researches supply in situ data from mantle sulfides (Guo et al., 1999; Alard et al., 2000; 2011; Delpech et al., 2012; González-Jiménez et al., 2014; Saunders et al., 2015; 2016; Ciążela et al., 2018; Wang et al., 2018; D'Errico et al., 2019). To better understand the behavior

of siderophile and chalcophile elements during wehrlitization, detailed *in situ* major and trace element analyses were performed, as well as Fe isotope measurements on wehrlitic sulfides. To quantify the compositional change linked to the metasomatism, comparison to sulfides of non-wehrlitized xenoliths were carried out. As a result, my Ph.D. research contributes significantly to extending the knowledge on subcrustal metal behavior along melt migration channels.

Since the establishment of the unpolarized infrared (IR) method (Kovács et al., 2008; Sambridge et al., 2008), the analyses of nominally anhydrous minerals (NAMs) with respect to their structural hydroxyl content became easier to implement. Indeed, numerous studies applying this method were published in the last decade (e.g., Pintér et al., 2015; Demouchy et al., 2015; Denis et al., 2015; Biró et al., 2016; Patkó et al., 2019; Tollan and Hermann, 2019; Lange et al., 2019). In my Ph.D. study, I analyzed the NAMs in wehrlite, aiming to determine the volatile change linked to wehrlitization. I integrated these new results in the database published from the CPR (Falus et al., 2008; Schmädicke et al., 2013; Aradi et al., 2017; Lange et al., 2019).

In recent years, several case studies showed that far more information can be gathered by combining petrologic data with geophysical models (Khan et al., 2006; Fullea et al., 2011; Jones et al., 2012; Vozár et al., 2014). Thus, I compared electrical resistivities calculated for wehrlite xenoliths with those acquired with deep geophysical survey (Novák et al., 2014). The main goal of this comparison was to estimate the spatial distribution of the metasomatized mantle volume, as it may be more extensive than previously thought, solely based on the areal extent and volume of erupted material.

All these various data collected in my Ph.D. project have important implications for developing a more refined understanding of wehrlitization in all tectonic settings, where mafic melts ascended to the surface in the past or in recent times. The joint interpretation of deep geophysics and xenolith geochemistry provides means to better understand geophysical data in locations where upper mantle rocks are not available. Even though my Ph.D. program focuses on a single volcanic field, the results could be significant and applicable for wehrlite bodies in similar tectonic environments worldwide.

2. Geological background

2.1. Evolution of the Carpathian-Pannonian region

The Pannonian Basin is situated in East-Central Europe and is surrounded by the Alpine, Carpathian and Dinaric orogenic chains (Fig. 2.1). The complex tectonic evolution of this extensional back-arc basin has been discussed by numerous studies (e.g., Royden et al., 1982; Csontos et al., 1992; Horváth, 1993; Csontos, 1995; Fodor et al., 1999; Bada and Horváth, 2001; Horváth et al., 2006; Schmid el al., 2008; Kovács et al., 2012a; Balázs et al. 2016). The Pannonian Basin consists of two different tectonic megaunits: ALCAPA in the northwest with Mediterranean affinity and Tisza-Dacia in the southeast with dominantly European origin (Stegena et al., 1975; Balla, 1984; Kázmér and Kovács, 1985; Csontos et al., 1992; Csontos and Vörös, 2004). The two megaunits are divided by the Mid-Hungarian Shear zone (Kázmér and Kovács, 1985; Csontos and Nagymarosy, 1998; Fodor et al, 1998) (Fig. 2.1).

The Tertiary evolution of the CPR can be dividedd into three stages (Fodor et al., 1999). The initial tectonic phase was dominated by transpressional stress field from the Eocene to the late Oligocene and dextral strike-slip faults, especially along the Periadriatic Line and its eastward continuation, the Balaton Line (Fig. 2.1). This was followed a pure strike-slip type regime from the latest Oligocene to early Miocene era and led to the juxtaposition of ALCAPA and Tisza-Dacia by extrusion (Kázmér and Kovács, 1985; Ratschbacher et al., 1991; Horváth, 1993) (Fig. 2.2). The escaping motion is closely related to the northward movement of the Adriatic microplate, and additionally facilitated by an asthenospheric flow (Kovács and Szabó, 2008). The displacement of ALCAPA eventually reached ~4–500 km (Kovács et al., 2000) and was accompanied by the filling of the Carpathian embayment (Csontos et al., 1992; Csontos, 1995) (Fig. 2.2). Some of the studies argue that the extruded ALCAPA was only a crustal block (Csontos et al., 1992; Fodor et al., 1999; Huismans et al., 2001; Horváth et al., 2006), whereas according to others, the entire lithosphere was involved (Willingshofer et al., 1999; Kovács and Szabó, 2008). Based on mantle xenoliths, the extrusion has affected at least part of the lithospheric mantle (Bali et al., 2008b; Kovács and Szabó, 2008). Subsequently, due to space problems, counter-clockwise rotation of ALCAPA and clockwise rotation of Tisza-Dacia block started in the latest Early Miocene (Márton, 1987; Csontos et al., 1992; Márton and Fodor, 2003) (Fig. 2.2). Simultaneously, two distinct phases of extension were established (Bada and Horváth, 2001; Huismans et al., 2001). The first

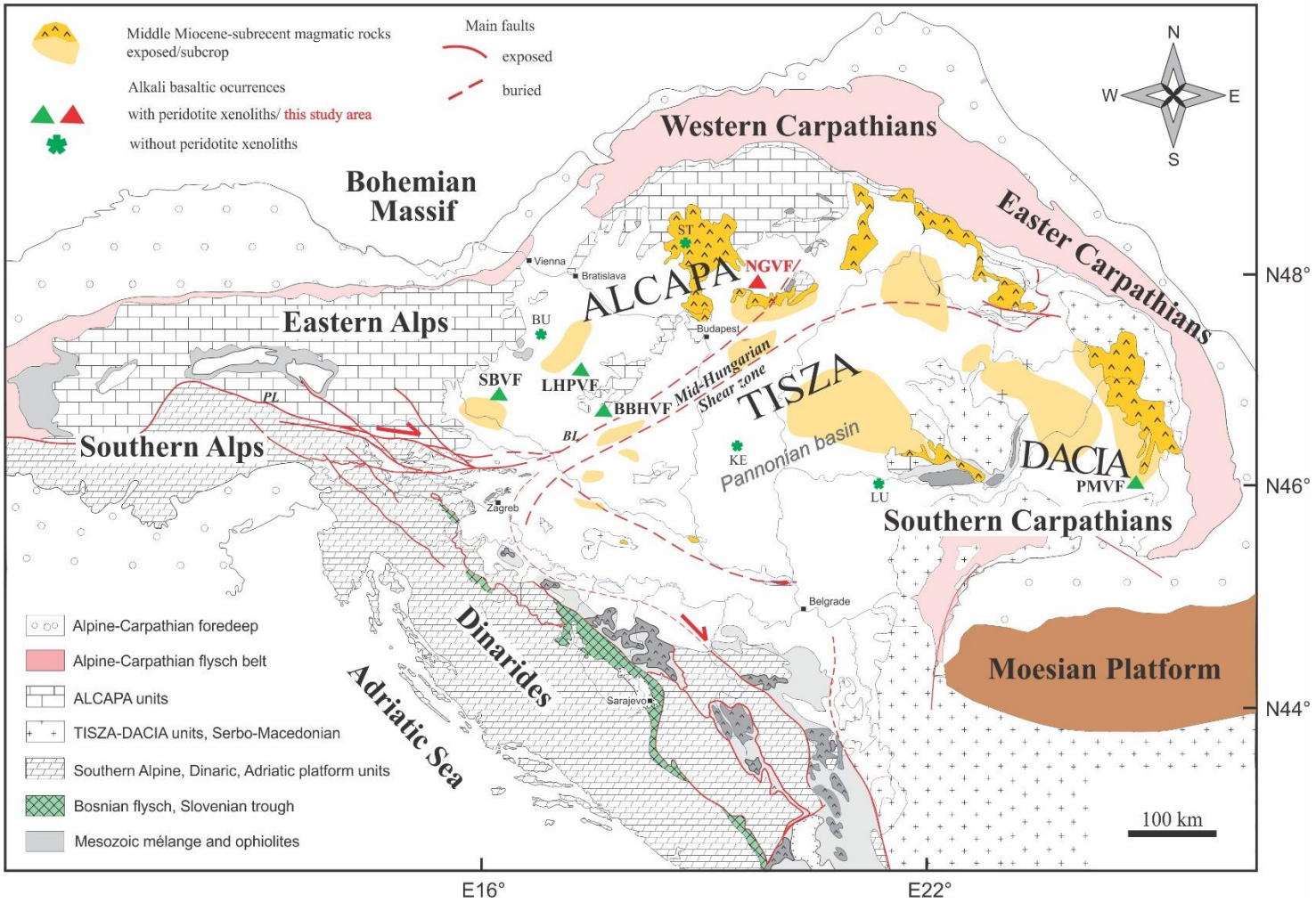

Figure 2.1 Present-day location of major tectonic units in the Carpathian-Pannonian region (modified after Kovács et al., 2007). Tectonic lines abbreviations: PL – Periadriatic Line; BL – Balaton Line. Abbreviations of alkali basaltic localities from west to east: SBVF – Styrian Basin Volcanic Field; BU – Burgenland basalts; LHPVF – Little Hungarian Plain Volcanic Field; BBHVF – Bakony-Balaton Highland Volcanic Field; ST – Štiavnica basalts; KE – Kecel basalts (buried); NGVF – Nógrád-Gömör Volcanic Field; LU – Lucareț basalts; PMVF – Perşani Mountains Volcanic Field.

period of extension happened in the Middle Miocene (17.5–14 Ma) with a consequence of asthenosphere doming. Prior to the second phase of extension in the Late-Miocene (11.5–8 Ma), a short tectonic inversion of compression took place between 14–11.5 Ma (Fodor et al., 1999; Huismans et al., 2001). Several theories were proposed for the reason of the extension: subduction roll-back effect (Royden et al., 1982; Horváth, 1993), thermal erosion related to the asthenospheric doming (Stegena et al., 1975), gravitational instability of the mantle lithosphere (Houseman and Gemmer, 2007), or all of these together. During the extension, the lithospheric mantle was subjected to greater thinning compared to the crust with δ = ~4–8 and β = ~1.5 in the central CPR, respectively, (Huismans et al., 2001), where the thinning factors δ and β indicate the ratio of thicknesses before and after the extension. Therefore, the crust and the lithosphere are very thin in the Pannonian Basin (~25–30 and 60–70 km, respectively) (Horváth, 1993) (Fig. 2.3). Following the extension, large-scale inversion led to a compressional tectonic regime (Fodor et al., 1999; Horváth et al., 2006; Balázs et al., 2016). This deformation event is currently still active, due to the convergence of the Adria microplate to the European platform (Horváth and Cloetingh, 1996; Dombrádi et al., 2010; Bada et al., 2007).

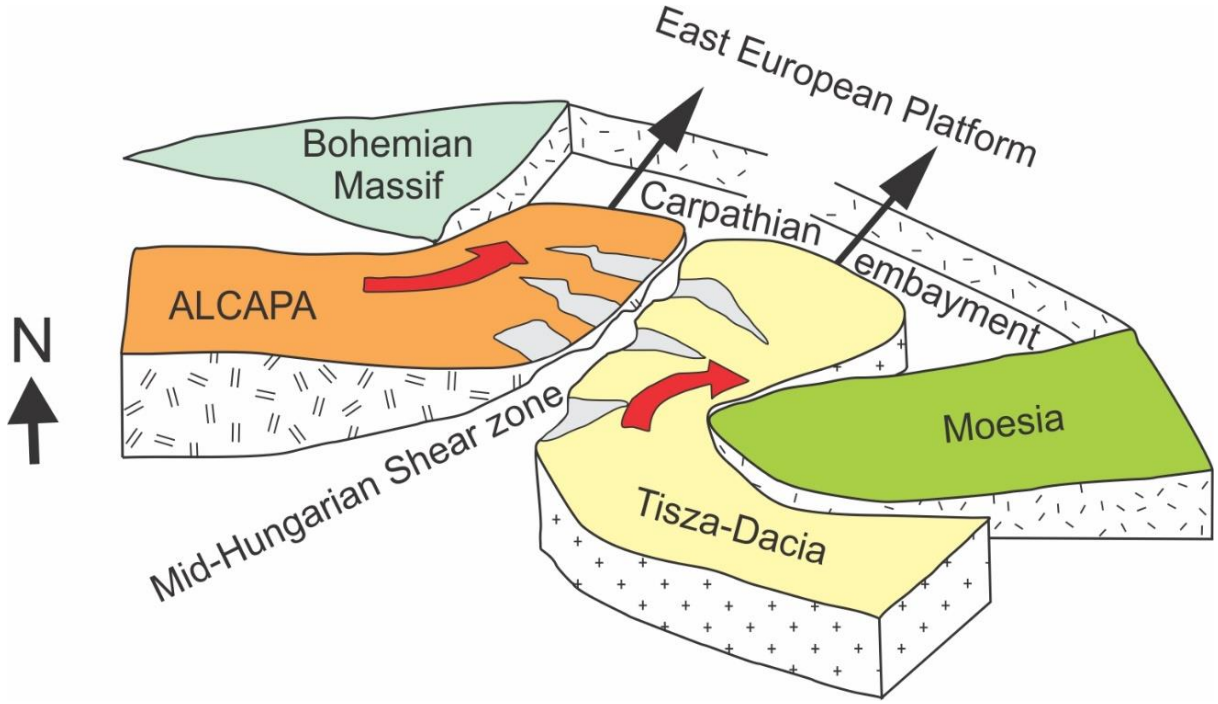

Figure 2.2 Tectonic model of the late Tertiary evolution of the Carpathian-Pannonian region modified after Csontos and Nagymarosy (1998). Black arrows show the movement of the megaunits, whereas red arrows indicate the rotational directions.

2.2. Neogene volcanism in the Carpathian-Pannonian region

During the last 21 Ma, widespread volcanism took place in the CPR closely linked to its tectonic evolution (Fig. 2.1). The volcanic products can be classified into four main groups based on their petrographic and geochemical characteristics, as well as the timing and spatial distribution of the eruption (Szabó et al., 1992; Pécskay et al., 1995; 2006; Harangi, 2001; Seghedi et al., 2004a; Harangi and Lenkey, 2007; Lexa et al., 2010; Seghedi and Downes, 2011). These groups are the following: 1. Miocene (21–11 Ma) felsic volcanites; 2. Miocene to Holocene (18–0.1 Ma) calc-alkaline rocks; 3. Miocene to Holocene (18–1 Ma) potassic and ultrapotassic rocks; 4. Late Miocene to Holocene (10–0.1 Ma) Na-alkaline volcanites.

1. The felsic volcanites are dominantly represented by rhyolitic to dacitic pyroclasts appearing throughout the Pannonian and Transylvanian Basins (Szabó et al., 1992). These thick (up to 750 m) ignimbrite and tuff sequences are mostly covered by young sediments and exposed only in a few areas (Szakács et al., 1998). Their genesis is connected to the anatexis of crustal rocks due to enhanced heat flow (Póka et al., 1998). Alternatively, their origin is linked to the mixing of mantle and crust derived melts (Harangi et al., 2005) with significant fractionational crystallization happening in shallow magma chambers (< 6 km) (Lukács et al., 2005).

2. Calc-alkaline rocks are the most frequent volcanic rocks in the CPR (Fig. 2.3) and vary from basaltic andesite to rhyolite in composition, with gradually decreasing ages towards the southeast (Pécskay et al., 1995; 2006). The related volcanic forms are variable and include composite stratovolcanoes, effusive fields, dome/flow complexes, subvolcanic intrusive complexes and monogenetic volcanic forms (Lexa et al., 2010). The calc-alkaline volcanism shows differences between the northern and eastern segment of the CPR. In case of the northern CPR, it is suggested that extension plays the key role in melt generation, and either an enriched lithospheric mantle or the asthenosphere is suggested as source (Harangi and Lenkey, 2007). The subduction-related signature (e.g., high SiO_2, $^{87}Sr/^{86}Sr$, Th/Y and low Nb/Y; Seghedi and Downes, 2011) of these melts can be inherited from former subduction process (Kovács and Szabó, 2008). In contrast, in the eastern CPR, the volcanism is closely related to subduction (Mason et al., 1998; Seghedi et al., 2004a; Harangi and Lenkey, 2007; Seghedi and Downes, 2011) and

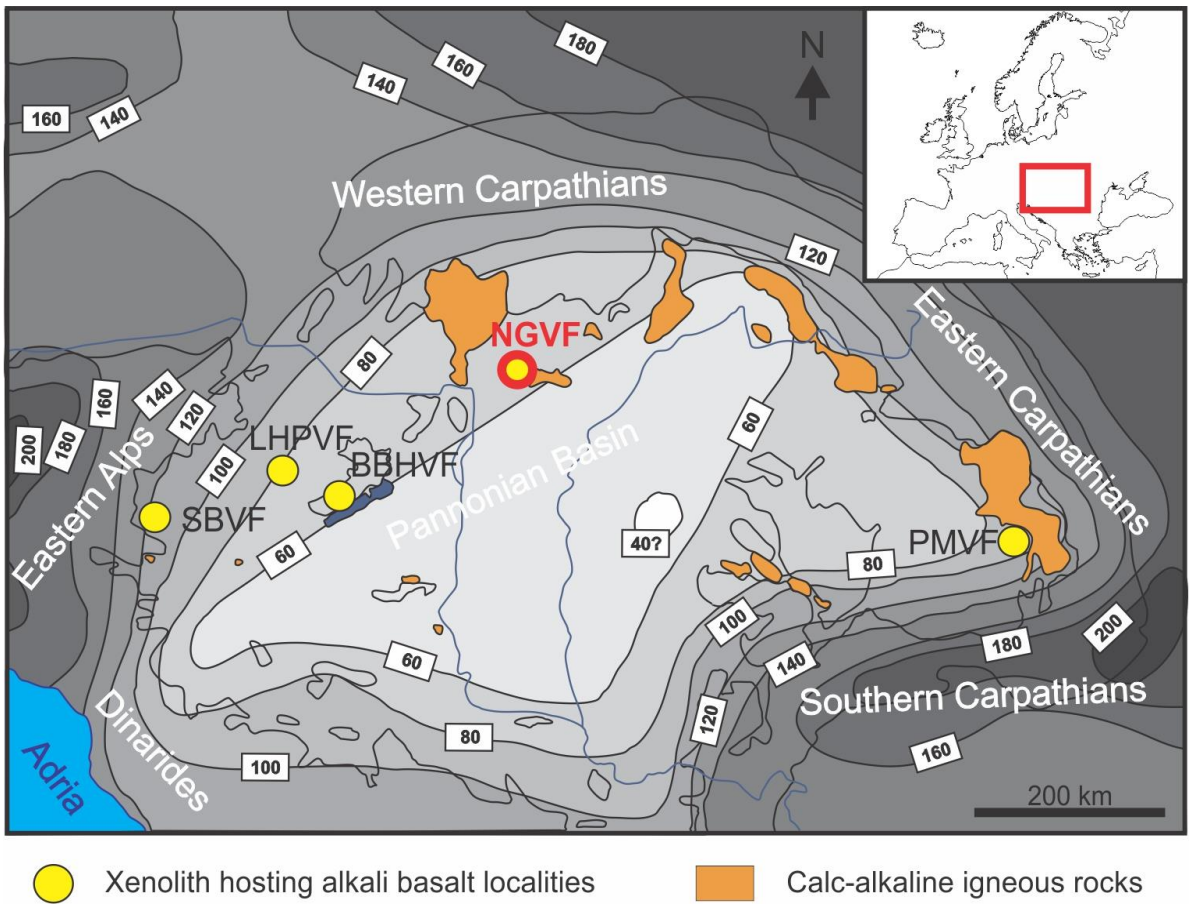

Figure 2.3 Lithospheric thickness in the Carpathian-Pannonian region (modified after Lenkey, 1999) with the spatial distribution of calc-alkaline volcanic rocks and xenolith-bearing alkali basalt localities (after Szabó et al., 2004). Abbreviations are the following: SBVF – Styrian Basin Volcanic Field; LHPVF – Little Hungarian Plain Volcanic Field; BBHVF – Bakony-Balaton Highland Volcanic Field; NGVF – Nógrád-Gömör Volcanic Field; PMVF – Perşani Mountains Volcanic Field.

postdates the major extensional phase (Pécskay et al., 1995; 2006). The melt generation in the mantle wedge is possibly associated with gradual slab break-off (Harangi and Lenkey, 2007). Mason et al. (1996) noted that the significant crustal contamination and fractional crystallization also modified the composition of these melts.

3. The distribution of potassic and ultrapotassic rocks, namely shoshonite, trachyandesite, latite and leucitite, is scattered in limited volumes in the CPR (Harangi et al., 1995). Their sources are believed most likely K-enriched, metasomatized lithospheric mantle segments, which were partially melted because of the heating effect of the upwelling asthenosphere (Harangi, 2001).

4. Monogenetic volcanic fields forming Na-alkaline volcanic rocks (Fig. 2.1) consist of nepheline basanites, alkali basalts and their differentiated variations such as nepheline tephrites, trachybasalts and trachyandesites (Lexa et al., 2010). The generation of these asthenosphere derived melts is still a matter of debate. Some studies proposed adiabatic decompressional melting of the upwelling asthenosphere following the main extension period, as a main reason for the melt generation (Embey-Isztin et al., 1993; Ali and Ntaflos, 2011). Seghedi et al. (2004b) and Wilson and Downes (2006) argued that small scale deep thermal plumes are responsible for the melt generation. However, this scenario was ruled out by more recent studies because of the lack of thermal anomalies (Harangi and Lenkey, 2007; Harangi et al. 2015). Harangi et al. (2015) highlighted the role of asthenospheric flows into the central CPR, as a response to to the suction effect of the extension. This study suggested that the melting took place in areas where the lithosphere-asthenosphere boundary is steep. According to a recent study, compression beginning in the tectonic inversion stage of the CPR evolution may have squeezed partial melt out from the hydrated asthenospheric dome (Kovács et al., 2020).

2.3. Chemical and physical characteristics of the subcontinental lithospheric mantle in the Carpathian-Pannonian region – a review based on Neogene alkali basalt hosted xenoliths

The Na-alkaline lavas and pyroclasts contain numerous upper-mantle derived xenoliths in five locations in the CPR (Szabó et al., 2004) (Fig. 2.3). Among the xenolith-bearing localities, the Styrian Basin Volcanic Field (SBVF) and Perşani Mountains Volcanic Field (PMVF) are situated in the peripheral, whereas the Little Hungarian Plain Volcanic Field (LHPVF) and the Bakony-Balaton Highland Volcanic Field (BBHVF) are situated in the central part of the CPR (Fig. 2.3). The Nógrád-Gömör Volcanic Field (NGVF) has a transitional location between the Pannonian Basin and the Carpathians (Fig. 2.3). All these localities have xenoliths derived only from the spinel stability field, except for a subordinate number of PMVF xenoliths which contain garnet (Tóth et al., 2006; Luffi et al., 2015). However, orthopyroxene±clinopyroxene±spinel clusters and symplectites appearing in SBVF, LHPVF, BBHVF and PMVF xenoliths are believed to represent decompressional breakdown products after former garnets (Embey-Isztin et al., 1989; Falus et al., 2000; Falus et al., 2007). These petrologic observations confirm that mantle uplift has

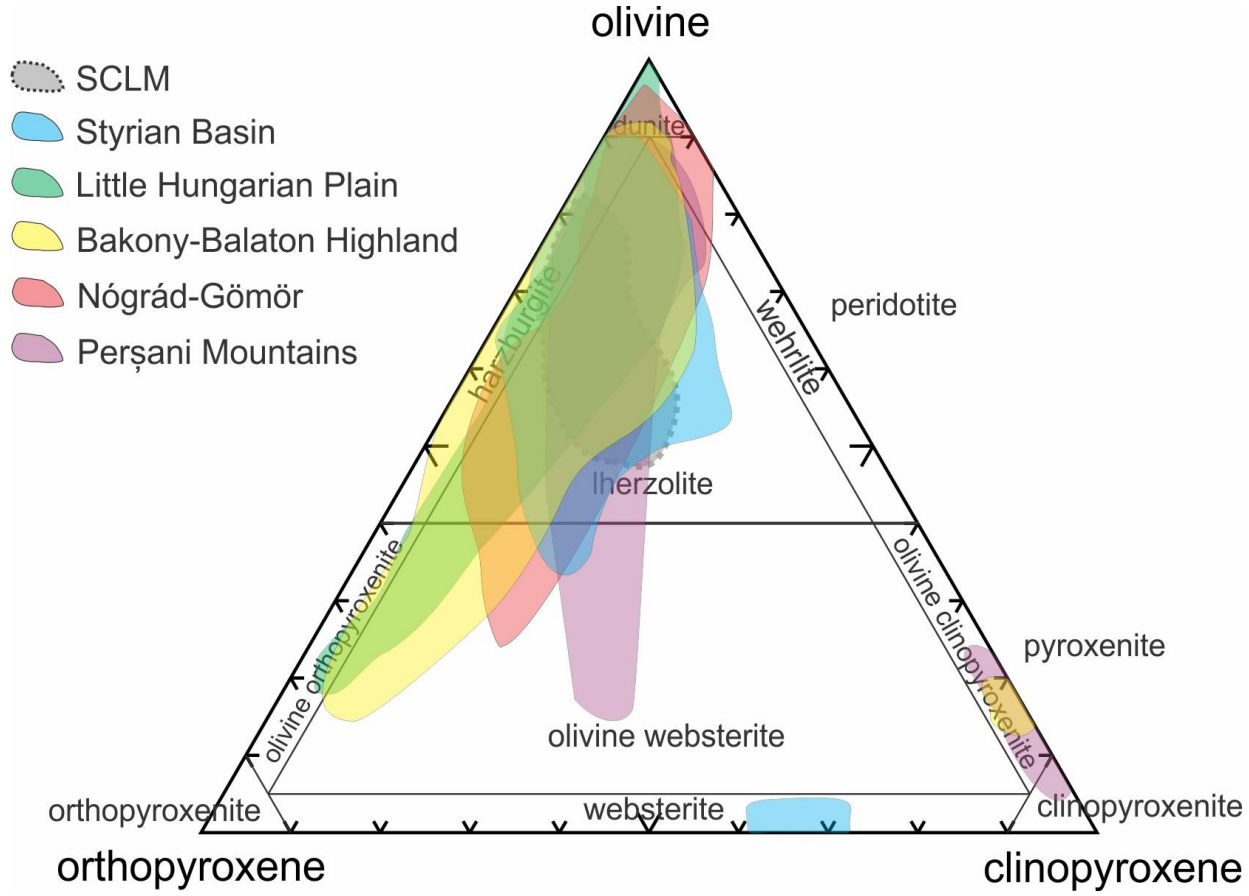

Figure 2.4 Modal compositions and rock types of mantle xenoliths from the different localities in the Carpathian-Pannonian region on the diagram of Streckeisen (1976), along with the average composition of the European subcontinental lithospheric mantle (SCLM; Downes,1997). Sources of the data for the different volcanic fields: Styrian Basin – Kurat et al. (1980), Vaselli et al. (1996), Aradi et al. (2017); Little Hungarian Plain – Embey-Isztin et al. (1989), Downes et al. (1992), Szabó et al. (1995), Nédli et al. (2009); Bakony-Balaton Highland – Embey-Isztin et al. (1989), Downes et al. (1992), Bali et al. (2007), (2008a), Nédli et al. (2009), Berkesi et al. (2012); Nógrád-Gömör – Szabó and Taylor (1994), Liptai et al. (2017); Perșani Mountains – Vaselli et al. (1995), Falus et al. (2008), Kovács et al. (2018), Lange et al. (2019).

occurred beneath the Pannonian Basin. Based on several studies (Kurat et al., 1980; Downes et al., 1992; Szabó and Taylor, 1994; Szabó et al., 1995; Vaselli et al., 1995; 1996; Bali et al., 2007; 2008a; Falus et al., 2008; Nédli et al., 2009; Berkesi et al., 2012; Aradi et al., 2017; Liptai et al., 2017; Kovács et al., 2018; Lange et al., 2019). lherzolite is the dominant rock type in the CPR (Fig. 2.4). Other peridotite types such as harzburgite, wehrlite, dunite and pyroxenite, also occur in the xenolith record indicating complex history with depletion and enrichment episodes (Fig. 2.4).

Xenoliths with depleted character, having low 'basaltic element' (Al, Ca, Na, Ti) and light rare earth element (LREE) concentrations, can be found in all localities (Kurat et al., 1980; Embey-Isztin et al., 1989; Downes et al., 1992; Szabó and Taylor, 1994; Szabó et al., 1995; Vaselli et al., 1995; Embey-Isztin et al., 2001; Liptai et al., 2017). These results suggest that there are mantle domains throughout the CPR, where the melt extraction was not followed by refertilization. Although mantle metasomatism with high melt/rock ratio can also lead to geochemical depletion (Kelemen et al., 1992), this scenario was not proposed in prior studies.

Based on petrographic and geochemical considerations, three different types of enrichment can be distinguished, which all were observed in the CPR. In case of modal metasomatism, first defined by Harte (1983), newly formed minerals appear in the mantle additionally to the common olivine, pyroxenes, spinel/garnet phases. These minerals are dominantly hydrous amphibole and mica, or less frequently, apatite, carbonate, titanite, ilmenite, zircon etc. (Ionov et al., 1997). In the CPR, amphiboles are the most abundant proofs of modal metasomatism (Kurat et al., 1980; Downes et al., 1992; Szabó and Taylor, 1994; Szabó et al., 1995; Vaselli et al., 1996; Bali et al., 2002; Szabó et al., 2009; Hidas et al., 2010; Aradi et al., 2017; Liptai et al., 2017; Kovács et al., 2018). Amphibole, which is dominantly pargasite (Szabó et al., 2004), has the highest abundance in the peripheral localities (SBVF and PMVF), appearing mostly interstitially and sometimes as layers or veins (Vaselli et al., 1995; Zanetti et al., 1995; Coltorti et al., 2007a; Szabó, 2013). In PMVF xenoliths, scattered apatite grains are associated with amphibole veins (Vaselli et al., 1995; Szabó, 2013). Based on their geochemical characteristics, amphibole has can form in different environments, namely intraplate or suprasubduction settings (Coltorti et al., 2007b). The other common hydrous phase is mica, specifically phlogopite, which was found in xenoliths both in the NGVF (Szabó and Taylor, 1994; Szabó et al., 1995) and in the SBVF (Aradi et al., 2017). The presence of metasomatic carbonates was limited to the BBHVF (Bali et al., 2002; Demény et al., 2004) and the PMVF (Chalot-Prat and Arnold, 1999). In an exotic case, extremely unusual quartz appears in a websterite xenolith (Bali et al., 2008b).

The other type of metasomatism is cryptic metasomatism, first mentioned by Dawson (1984). This covers geochemical, especially trace element changes in the existing phases without the introduction of new mineral phases. Such metasomatism was revealed by several studies throughout the CPR (Vaselli et al., 1995; Szabó et al., 1995; Dobosi et al., 1999; 2010; Liptai et al., 2017).

Recently, O'Reilly and Griffin (2013) introduced the term stealth metasomatism. This metasomatic type results in mineralogical change, however, the newly-formed phases are the same as the major rock-forming silicates present in the mantle, namely olivine or pyroxenes. Thus, careful textural and geochemical investigation is needed to identify stealth metasomatism. This kind of refertilization was also discovered in the CPR in the form of orthopyroxene (Szabó et al., 1995; Bali et al., 2007; 2008b) or clinopyroxene enrichment (Patkó et al., 2020) in the BBHVF and the NGVF, respectively.

The variable mantle metasomatic events can be linked to different agents including fluids or melts. Fluids are dominated by CO_2, but H_2O and N_2 volatile phases were also detected based on fluid inclusion studies (Huraiová and Konečný, 1994; Szabó and Bodnar, 1996; 1998; Hidas et al., 2010; Berkesi et al., 2012; Aradi et al., 2019). In the CPR, the presence of both carbonate (Chalot-Prat and Arnold, 1999; Bali et al., 2002; Demény et al., 2004) and silicate melts were revealed. Within the silicate melts, a primitive mafic (Vaselli et al., 1995; Liptai et al., 2017; Patkó et al., 2020) and a silica-rich (Szabó et al., 1995; Bali et al., 2007; 2008b; Créon et al., 2017) types were distinguished with asthenospheric and subduction origin, respectively. Melt compositions were determined with the study of silicate melt pockets (Bali et al., 2002; 2008a) and silicate melt inclusions (Szabó et al., 1996; 2009; Hidas et al., 2010). The presence of sulfide melts was also documented by Szabó and Bodnar (1995). The aforementioned variation of metasomatic agents is mostly linked to the complex Neogene melt generation and volcanism of the CPR.

In mantle environment, H_2O can occur not only as molecular water in fluid inclusions and silicate melt inclusions (e.g., Berkesi et al., 2009; Hidas et al., 2010), but also as structurally bound hydroxyl incorporated in mineral structures (e.g., Bell and Rossman, 1992; Demouchy and Bolfan-Casanova, 2016; Peslier et al., 2017; Xia et al., 2019). The structural hydroxyl content of NAMs in the CPR is higher in peripheral localities (Falus et al., 2008; Aradi et al., 2017; Lange et al., 2019) than in the central part of the basin (Liptai et al., 2019a). NAMs of the NGVF xenoliths also show low structural hydroxyl contents (Patkó et al., 2019). The higher structural hydroxyl contents in the marginal regions are probably due to subducted slab released fluids (Falus et al., 2008; Aradi et al., 2017), whereas the low structural hydroxyl contents in the central part is controlled by extension related decrease of water activity (Patkó et al., 2019).

In addition to the geochemical characteristics, the xenoliths can reveal information on the physical conditions of the lithospheric mantle. The textural features of the upper mantle xenoliths

show differences between the distinct localities in the CPR. In the SBVF, protogranular and porphyroclastic fabrics are dominant (Vaselli et al., 1996; Dobosi et al., 1999; Falus et al., 2000; Coltorti et al., 2007a; Aradi et al., 2017), using the nomenclature of Mercier and Nicolas (1975). These texture types indicate little to moderate deformation (Mercier and Nicolas, 1975). In contrast, the more deformed porphyroclastic and equigranular textures are most frequent in the LHPVF and BBHVF (Downes et al., 1992; Szabó et al., 1995; Nédli et al., 2009; Hidas et al., 2010). In these localities, poikilitic fabric (after the definition of Mercier, 1977) is also abundant (Bali et al., 2007; Berkesi et al., 2012; Embey-Isztin et al., 2014). In the NGVF, there is a gradual change from coarse granular (Lenoir et al., 2000) dominance in the north to porphyroclastic-equigranular dominance in the south (Liptai et al., 2019b). The PMVF xenoliths are mainly characterized by porphyroclastic and equigranular textures (Vaselli et al., 1995), and this is the only locality where extremely deformed mylonitic fabric (Christie, 1960) appears as well (Falus et al., 2008).

Based on the examination of crystal preferred orientation (CPO) patterns of mantle silicates, especially the dominant olivines, the deformation style and degree can be estimated. The two most common CPO types in the CPR xenoliths are the [010]-fiber (or axial-[010]) and the orthorhombic (Hidas et al., 2007; Falus et al., 2008; 2011; Aradi et al., 2017; Liptai et al., 2019b). The former is related to axial shortening or transpression, whereas the latter is explained by simple or pure shear (Tommasi et al., 1999). These deformation styles fit the collisional and extrusional tectonics of the CPR and its neighboring areas. Although postkinematic annealing (coarsening) appears due to the percolation of hydrous fluids/melts, it was shown to barely modify the original CPO (Aradi et al., 2017; Liptai et al., 2019b).

As a conclusion, the lithospheric mantle in the CPR shows a complex evolution. Although metasomatism-related imprints appear in all xenolith localities, they are the most significant in the western and eastern marginal parts of the CPR, where the presence of subducted slabs are proposed as an explanation. The deformation characteristics of the xenoliths in the entire CPR are consistent with recent tectonic evolution of the area.

2.4. Characteristics of volcanism and ultramafic xenoliths in Nógrád-Gömör

In the Nógrád-Gömör area, two distinct stages of Neogene volcanic activity can be recognized. The older, Miocene (~16 Ma; Pécskay et al., 2006) garnet-bearing calc-alkaline

andesite is represented by Karancs Hill (Lantai, 1991; Harangi et al. 2001), situated west of the Medves Plateau (Fig. 2.5). The other is the Na-alkaline volcanic rocks forming the monogenetic volcanic field consisting of maars, diatremes, tuff cones, cinder/spatter cones and lava flows (Konečný et al., 1995a). In the western part of the volcanic field, the lava flows built up two plateaus, Babi Hill and Medves Plateau (Jugovics, 1971) (Fig. 2.5). The variable alkali basaltic rock types of the NGVF include basanite, basaltic trachyandesite and phonotephrite (Dobosi et al., 1995). The NGVF basalts have OIB-like character based on their trace element and isotopic compositions (Dobosi et al., 1995). The basaltic volcanic activity in the NGVF took place between 6.17–1.35 Ma based on K-Ar dating (Balogh et al., 1981). New results of combined U/Pb and (U-Th)/He geochronometry (Hurai et al., 2013) have slightly extended the period of volcanism (7–0.3 Ma).

The NGVF is the northernmost ultramafic xenolith-bearing alkali basalt locality in the CPR (Fig. 2.3). In the NGVF, both Type-I (Embey-Isztin, 1978; Hovorka and Fejdi, 1980; Szabó and Taylor, 1994; Konečný et al., 1995b; 1999; Liptai et al., 2017) and Type-II ultramafic rocks (Kovács et al., 2004; Zajacz et al., 2007) have been reported, based on the classification of Frey and Prinz (1978).

The Type-I NGVF xenoliths are compositionally lherzolite, harzburgite, wehrlite and olivine websterite (Szabó and Taylor, 1994; Konečný et al., 1999; Liptai et al., 2017; Patkó et al., 2020) (Fig. 2.4). Liptai et al. (2017) divided the Type-I NGVF xenoliths into two groups based on their geochemistry: Group I, in which the olivine has mg# $\geq$ 89 and Group II, in which the olivine has mg# < 89. Further division was done based on rare earth element (REE) depletion ('A' subgroups) or enrichment ('B' subgroups) of clinopyroxenes, respectively. The Group IA and IIA xenoliths are partial melting residues, and contain subduction-related Nb-poor amphibole. The formation of Group IB and IIB xenoliths are possibly linked to two different metasomatic events, among which the former is characterized by U-Th-Nb-Ta- and LREE-enrichment in amphibole and clinopyroxene, whereas the latter resulted in Fe-Mn-Ti-LREE enrichment (Liptai et al., 2017).

The type-II ultramafic xenoliths, also called cumulates, are olivine clinopyroxenite, clinopyroxenite, wehrlite and plagioclase-bearing ultramafic rock (Kovács et al., 2004; Zajacz et al., 2007). These rocks are crystallized from mafic melts trapped near the Moho (crust-mantle transitional zone; Kovács et al., 2004; Zajacz et al., 2007).

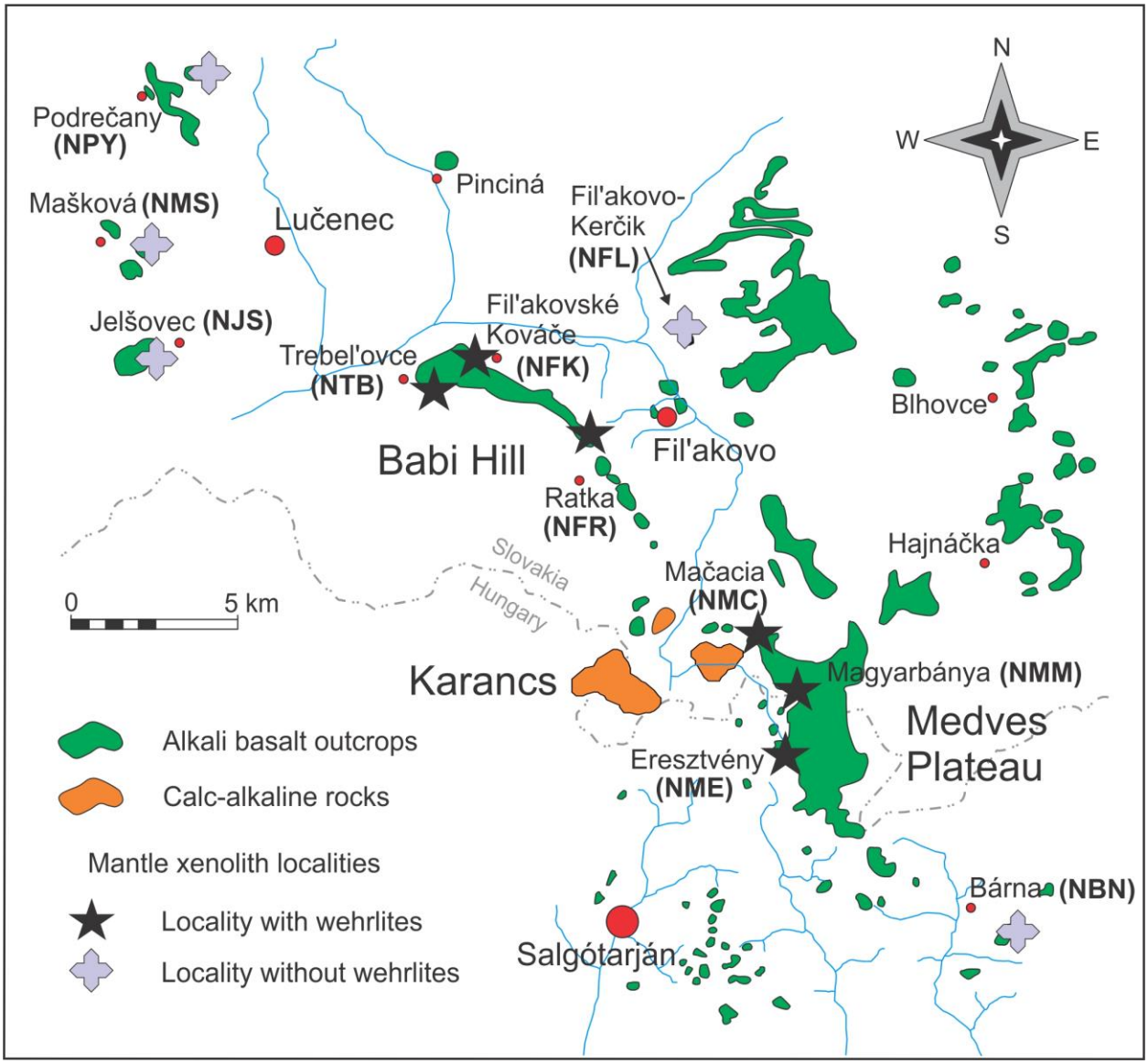

Figure 2.5 Alkali basalt localities and xenolith sampling locations in the Nógrád-Gömör Volcanic Field (modified after Jugovics, 1971). Wehrlite-hosting quarries or outcrops from NW to SE are Trebel'ovce (Terbeléd) (NTB), Fil'akovské Kováče (Fülekkovácsi) (NFK), Ratka (Rátka) (NFR), Mačacia (Macskalyuk) (NMC), Magyarbánya (NMM) and Eresztvény (NME).

Some studies in the NGVF aimed to determine the composition and trapping conditions of fluids (Huraiová and Konečný, 1994; Szabó and Bodnar, 1996; 1998) and melts (Szabó et al., 1996; Zajacz et al., 2007) both in Type-I and Type-II ultramafic xenoliths. These results show that the volcanic activities in the past were accompanied by significant fluid/melt migration, which affected the peridotite wall rock. These metasomatic events possibly resulted in structural hydroxyl enrichment as demonstrated by the wehrlite xenoliths (Patkó et al., 2019), which are

thought to be linked to the latest metasomatism beneath the NGVF (Liptai et al., 2017; Patkó et al., 2020). In contrast, prior metasomatic episodes were possibly overprinted by structural hydroxyl loss due to decreasing water activity during the Miocene extension (Patkó et al., 2019).

The physical properties of NGVF xenoliths are the focus of recent papers (Klébesz et al., 2015; Liptai et al., 2019b). According to the results, olivine CPOs have dominantly [010]-fiber and orthorhombic patterns. Such CPO patterns are linked to dislocation creep in a transpressional regime, which is consistent with recent tectonic evolution of the CPR. The wehrlitization is also proposed to have an effect on the deformational characteristics via postkinematic annealing (Liptai et al., 2019b). The S receiver-function analyses revealed that the Moho and lithosphere-asthenosphere boundary beneath the NGVF have a depth of 25±5 and 65±10 km, respectively (Klébesz et al., 2015). Note, however that Tašárová et al. (2009) (using 3-D gravity modelling) and Bielik et al. (2010) (using integrated 2-D modeling of gravity, geoid, topography, and surface heat flow data) suggested greater lithospheric thickness ~80–100 km and ~100–120 km, respectively, beneath the NGVF.

3. Sampling and analytical techniques

3.1. Sampling

Xenolith locations can be divided into three main regions with different petrographic, geochemical and deformational characteristics: northern (quarries Podrečany, Mašková and Jelšovec), central (Babi Hill and Medves Plateau, as well as a separate basalt volcano, Fil'akovo-Kerčik), and southern (Bárna-Nagykő) (Fig. 2.5; Liptai et al., 2017). In this Ph.D. research I concentrate on six quarries from the two basalt plateaus in the central part of the region, which are Eresztvény [NME], Magyarbánya [NMM], Mačacia [NMC] from Medves Plateau, and Ratka [NFR], Fil'akovské Kováče [NFK], Trebel'ovce [NTB] from Babi Hill (Fig. 2.5; Table 1). The reason of this focus is that wehrlite xenoliths were only found in these localities. More than 150 xenoliths were collected, among which ~20 % of the xenoliths were classified as wehrlites. Based on petrographic features, twelve representative wehrlite xenoliths, two from each locality, were selected for detailed petrographic and geochemical study.

Table 1. List of the sampling localities of the Nógrád-Gömör wehrlite xenoliths.

Locality	Abbreviation	Coordinates
Trebeľovce	NTB	48°17'25.4"N 19°44'02.2"E
Fiľakovské Kováče	NFK	48°17'17.8"N 19°44'32.8"E
Ratka	NFR	48°15'39.8"N 19°47'17.1"E
Mačacia	NMC	48°10'56.4"N 19°51'30.2"E
Magyaránya	NMM	48°10'10.9"N 19°51'53.6"E
Eresztvény	NME	48°09'19.3"N 19°52'00.6"E

The twelve selected alkali basalt lava hosted xenoliths (Table 2) have either angular (NTB1120, NFK1110, NFR1117A, NFR1119B, NME1110, NME1129D) or rounded shapes (NTB1109, NFK1137A, NMC1302B, NMC1343, NMM1114, NMM1129) and range from 3 to 5 cm in diameter. In some cases, there is evidence of interaction between the host basalt and the xenoliths. These are reaction coronas at the margins, consisting of either brown clinopyroxenes (NFR1117A, NFR1119B, NME1110, NME1129D) (Fig. 3.1a-b) or assemblages of rhönite, augite, magnetite, plagioclase and glass after amphibole breakdown (NTB1120, NFK1110, NMM1114) (Fig. 3.1c-d) or minor basalt infiltrations into the xenoliths (NTB1120, NFK1137A, NMC1302B, NMC1343, NME1129D). The studied xenoliths are fresh, with the exception of NMC1302B that has iddingsitic alteration at the rims of olivine.

In case of two xenoliths (NTB1109, NME1110) additional thick sections were prepared (NTB1109/section 2, NME1110/section 2) in order to expose sufficient number of sulfides for analyses.

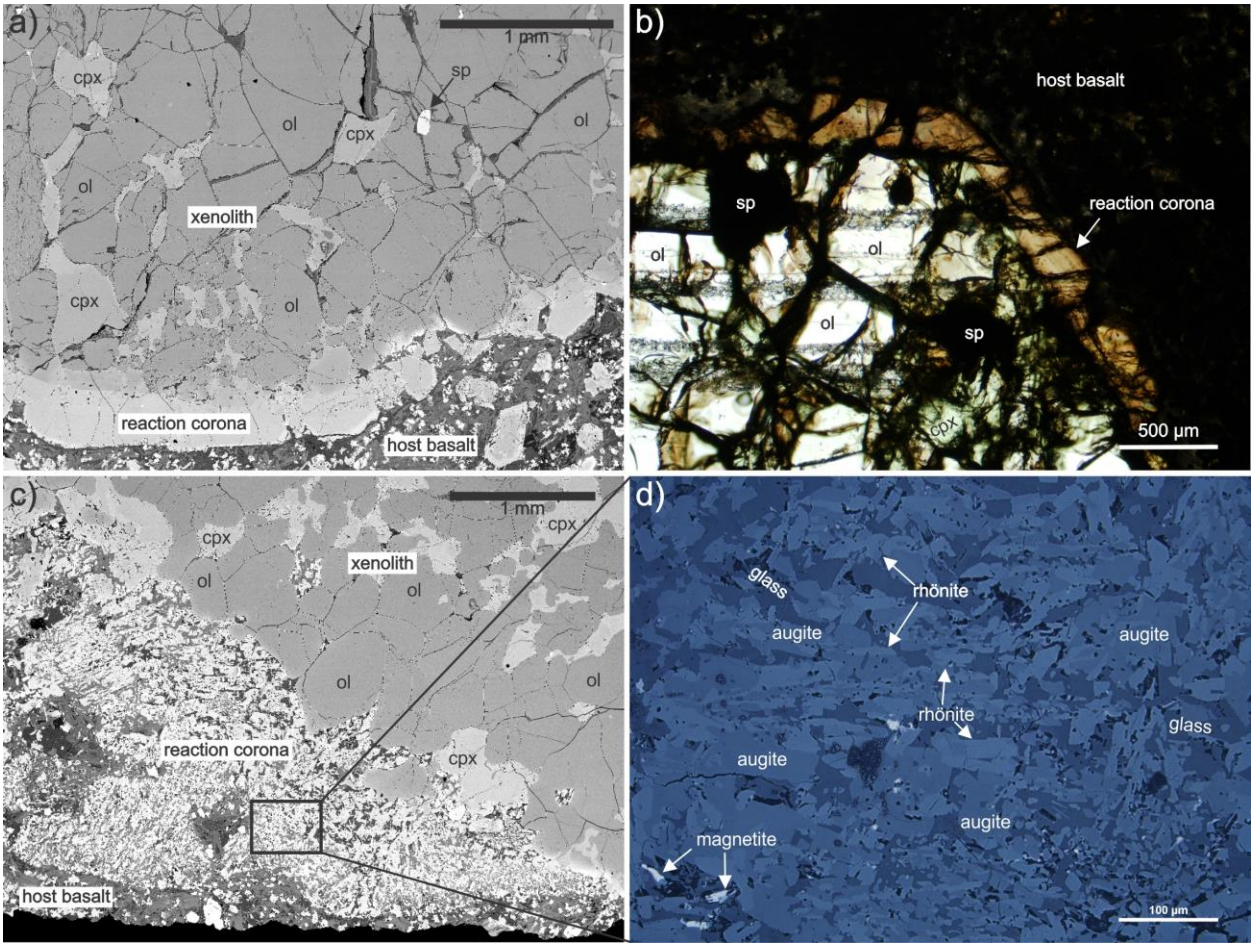

Figure 3.1 Photomicrographs of host basalt and wehrlite xenolith interactions from the Nógrád-Gömör Volcanic Field: **(a)** Back-scattered SEM image and **(b)** 1N transmitted light image of a reaction corona consisting of clinopyroxenes in the xenolith–host basalt contact zone in xenolith NFR1117A. **(c)** Back-scattered SEM image and **(d)** reflected light image of a reaction corona consisting of rhönite, augite, magnetite, plagioclase, glass assemblage after amphibole breakdown in the xenolith–host basalt contact zone in xenolith NTB1120. Abbreviations: ol – olivine; cpx – clinopyroxene; sp – spinel.

3.2. Analytical Techniques

3.2.1. Optical microscopy

Petrographic examination of the xenoliths and their sulfides were conducted with a Nikon Eclipse LV100 POL polarizing microscope at the Lithosphere Fluid Research Laboratory (LRG) at Eötvös Loránd University, Budapest. Photomicrographs were taken with a Nikon DS-Fi1 digital camera attached to the microscope, running NIS Elements AR 2.20 digital imaging software. Thin sections of the wehrlites were digitized with a HP Scanjet 2400 scanner adjusting 2400 dpi resolution. The scanned images were used to determine modal compositions using point counting method with the JMicroVision software developed by Nicolas Roduit (https://www.jmicrovision.com/).

3.2.2. Electron microscopy

Backscattered electron (BSE) images were taken with an AMRAY 1830 I/T6 scanning electron microscope equipped with an EDAX PV 9800 energy dispersive spectrometer in the Department of Petrology and Geochemistry at Eötvös Loránd University (Budapest). The images were taken at routine conditions of 20 keV and 1 nA. The modal composition of the sulfides was determined using Corel PhotoPaint X8 program of the Corel X8 software package based on the area of the different sulfide phases appearing on BSE images.

3.2.3. Electron microprobe (EMPA)

Major element analyses of the rock-forming minerals (olivine, orthopyroxene, clinopyroxene and spinel) were conducted using a CAMECA SX-50 electron microprobe in Padua (Italy) at CNR Institute for Geosciences and Earth Resources (IGG). The instrument operated with routine conditions of 20 kV accelerating voltage and 20 nA beam current. Counting times were 10 s at the peak and 5 s at the background for major elements and 20 s at peak and 10 s at the background for minor elements. Standard deviation is ≤ 1 % for major elements and 3–5 % for minor elements. Calibration was carried out based on the following standards: Amelia albite (Na), periclase (Mg), corundum (Al), diopside (Si, Ca), orthoclase (K), Mn-Ti oxide (Mn, Ti), Cr-oxide (Cr), hematite (Fe), Ni-oxide (Ni).

The major element composition of the sulfide phases (monosulfide solid solution-mss, pentlandite, pyrrhotite, chalcopyrite) were determined using CAMECA SX-50 and CAMECA SX-

100 electron microprobe in Padua (Italy) at CNR Institute for Geosciences and Earth Resources (IGG) and in Hannover (Germany) at the Institute of Mineralogy, Leibniz University of Hannover, respectively. The operating conditions were 20 kV accelerating voltage and 20 nA beam current in Padua, and 15 kV accelerating voltage and 15 nA beam current in Hannover. Counting times were 10 s at the peak and 5 s at the background for major elements. Standard deviation is ≤ 1 % for major elements. Calibration was carried out based on the following standards in both laboratories: native metals (Cu, Co), pyrite (S, Fe), and synthetic Ni-oxide (Ni). Both applied instruments are equipped with four wavelength dispersive spectrometers (WDS) and one energy dispersive spectrometer (EDS). In all cases the weight percentages were obtained from X-ray counts by applying the PAP correction program (Pouchou and Pichoir, 1991).

3.2.4. Laser-Ablation Inductively Coupled Mass Spectrometry (LA-ICP-MS)

Trace element analyses of clinopyroxenes were carried out by laser ablation inductively coupled plasma mass spectrometry (LA-ICP-MS) at the Department of Geosciences at Virginia Tech (Blacksburg, VA, USA). The system includes an ArF Excimer laser attached to an Agilent 7500ce quadrupole-based inductively coupled plasma mass spectrometer. The laser acquisition parameters were: 193 nm wavelength, ~7–10 J/cm^2 energy density, 5 Hz repetition rate and 32–60 μm spot size. The ablation cell was small in volume (~ 1.5 cm^3) and continuously flushed with He gas at ~1.2 L/min. The auxiliary Ar gas flow was 1.03 L/min, and the reaction cell was used in hydrogen mode. A dwell time of 10 ms per isotope was applied. Following a 60 s gas background analyses with the laser shutter closed, the laser shutter was opened and the sample was ablated for 60 s. The NIST612 synthetic glass (Pearce et al., 1997) was used as the calibration standard and was analyzed twice at the beginning and end of each analytical session to correct for drift. The internal standard was the ^{40}Ca isotope. Data reduction was carried out by the AMS software (Mutchler et al., 2008).

Trace element concentrations of the sulfides were obtained at the Institute of Mineralogy, Leibniz University of Hannover, Germany, with the use of an ELEMENT-XR (Thermo Scientific, Germany) fast-scanning sector field ICP-MS coupled to a femtosecond laser ablation (fs-LA) system (Solstice, Spectra-Physics, USA). The wavelength of the laser was 194 nm and yielded energy pulses of 50 mJ in the fourth harmonic. Repetition rates of 10 Hz and 10–28 Hz were applied, and spot sizes of 60 μm and 30–60 μm were used for standards and sulfide grains,

respectively. The advantage of the ultrashort pulses is the prevention of elemental fractionation and minimization of matrix effects (Horn and von Blanckenburg, 2007). The carrier gas was He and the auxiliary gas was Ar. NIST-610 and PGE-A reference materials were used as external standards. For internal standards, we used the average Ni concentrations, which were previously measured with EMPA. We carried out data reduction, including drift correction, with the Matlab-based SILLS (Signal Integration for Laboratory Laser System) software (Guillong et al., 2008). The light PGE (^{99}Ru, ^{101}Ru, ^{103}Rh, ^{105}Pd, and ^{106}Pd) isotopes required interference correction for the argides of ^{63}Cu, ^{65}Cu, ^{61}Ni, and ^{59}Co isotopes. The correction of the interferences was done by measuring the ZnS (Mineralogical Association of Canada (MAC)), native Ni, native Cu, and Co-rich pyrite (MAC) reference materials for comparison of the pure metal signals with the metal argide signals.

3.2.5. Fe isotope analyses

In situ iron isotopes of sulfides were determined using femtosecond laser ablation (fs-LA) system (Solstice, Spectra-Physics, USA) combined with a NeptunePlus (Thermo Scientific, Germany) multi-collector ICP-MS operated in low resolution mode at the Institute of Mineralogy, Leibniz University of Hannover, Germany. We report our results as δ^{56}Fe and δ^{57}Fe (i.e., deviations of ^{56}Fe/^{54}Fe and ^{57}Fe/^{54}Fe from IRMM-014 standard expressed in ‰). In addition, in-house JM puratronic (PURA) Fe-standard (99.995 % Puratronic, Johnson Matthey, lot No. FE495007IF2) was measured (Table 15) at the beginning of every analytical session, in order to make sure that the operating conditions of the laser are appropriate. All samples and PURA standard were analyzed with a repetition rate of 167 Hz, whereas it was 45 Hz for the IRMM-014 standard measurements. We used a laser beam with a diameter of 20–40 μm for sulfides and 60 μm for standards (Table 15). Relative standard errors of <0.1 ‰ and <0.15 ‰ were achieved for δ^{56}Fe and δ^{57}Fe values, respectively.

3.2.6. Fourier transform infrared spectroscopy (FTIR)

FTIR microscopic analysis to analyze structural hydroxyl in NAMs was performed in the Research Centre for Natural Sciences of the Hungarian Academy of Sciences in Budapest using a Varian FTS 7000 FTIR spectrometer coupled to a Varian UMA-600 IR microscope. The analyses were performed using unpolarized infrared light. Infrared spectra of olivine and clinopyroxene

were obtained between 4000 and 400 cm^{-1}, using a maximum of 100×100 μm aperture size. Orthopyroxene grains were inappropriate for analyses due to their small (< 100 μm) size. The samples were measured with a 'Globar' light source, KBr beam-splitter and an MCT detector. At least 128 scans were accumulated from each spot with a 4 cm^{-1} resolution.

The method of Kovács et al. (2008) and Sambridge et al. (2008) for unpolarized infrared light makes it possible to determine the concentration of structural hydroxyl accurately even from few (n > 5) unoriented anisotropic crystals such as olivine and clinopyroxene. Obviously the more unoriented grains are considered, the more accurate is the estimation. However, the accuracy of pyroxene measurements can be still satisfactory if < 5 or even only one unoriented grains are considered (Xia et al., 2013a; Liu et al., 2015). This method may be applied only if the maximum linear unpolarized absorbance is < 0.15, a criterion that was always met in this study. The total polarized absorbance (A_{tot}) is estimated as three times the average unpolarized integrated absorbance. Olivines show no structural hydroxyl-related bands. Therefore, further data reduction was only applied for clinopyroxenes. A_{tot} for clinopyroxenes in each sample was obtained using the OPUS® software, applying the following steps: (1) background correction using the concave rubber-band correction routine with 2 iterations and 64 baseline points; (2) averaging the spectra; (3) integration of spectral ranges of structurally bound hydroxyl with B-type integration applying uniform intervals for all samples (3765–3000 cm^{-1}). Integrated total absorbance values are normalized to 1 cm thickness. The thickness of the sections was measured with a Mitutoyo analogue micrometer, which is accurate to 2–3 μm within the thickness range considered. The A_{tot} is then converted to absolute concentration of structural hydroxyl (expresses as H_2O equivalent in wt. ppm) using the mineral-specific calibration factors of Bell et al. (1995) for clinopyroxene (k_{cpx}=0.14).

The detection limit of the micro-FTIR technique for nominally anhydrous silicate minerals is routinely at or below 1 ppm for structural hydroxyl (e.g., Bell et al., 1995) if the measurement conditions are optimal. This means that the degree of atmospheric interference (e.g., atmospheric moisture and carbon-dioxide) is minimalized, the measurement spot is free of hydrous inclusions, contaminations and alteration products, the thin section is 200–300 μm thick and the aperture size is at least ~50 ∗ 50 μm. This practice ensures the maximum signal to noise ratio during analysis.

The FTIR spectra are available on the PULI (Pannonian Uniform Lithospheric Infrared spectral database) website (http://puli.mfgi.hu/).

4. Results

4.1. Wehrlite petrography

All xenoliths are identified as wehrlite based on the modal classification of Streckeisen (1976). They are composed of 72–82 vol. % olivine, with an average of 76 vol. % (Table 2). Clinopyroxene and spinel abundances range between 10–24 and 1–6.5 vol. %, respectively. Orthopyroxene is entirely absent in two xenoliths (NFK1137A, NMM1129) and is observed only as a minor constituent (~0.5 vol. %) in the others as relict. Similarly, up to 2 vol. % brown glass can be observed around small clinopyroxene or spinel grains, except in xenoliths NFK1137A and NME1129D where it is completely absent.

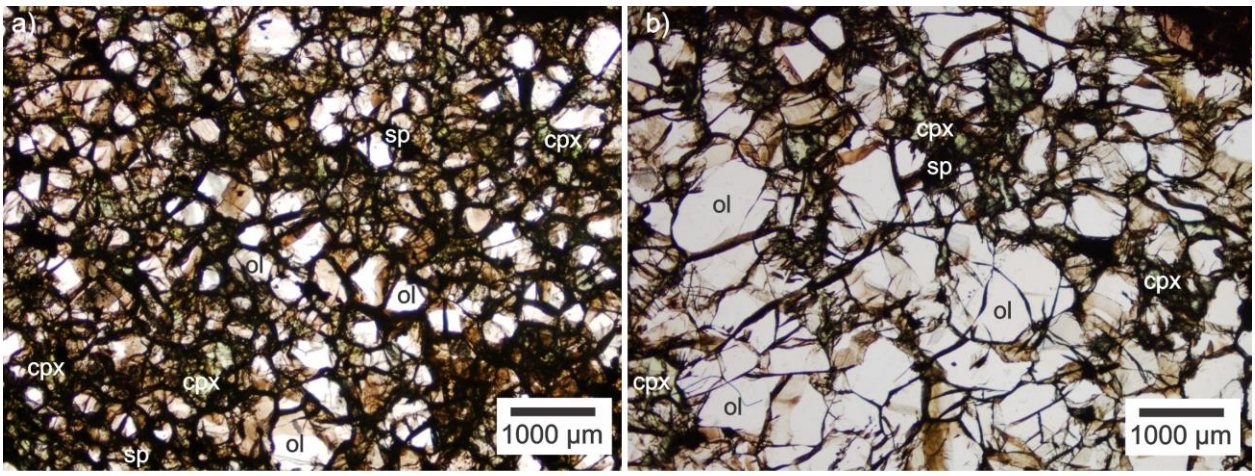

Figure 4.1 Photomicrographs of wehrlite xenoliths showing different textural characteristics from the Nógrád-Gömör Volcanic Field. **(a)** Fine-grained texture of xenolith NTB1109 (transmitted light image). **(b)** Coarse-grained texture of xenolith NFR1119B (transmitted light image).

Clinopyroxene and spinel is disseminated in xenoliths NTB1109 and NFR1119B (Fig. 4.1). However, all other wehrlites consist of two, modally and texturally different, irregularly shaped areas composed of olivine- and clinopyroxene-rich assemblages (Fig. 4.2a) with dimensions of 0.1–1.0 cm.

Olivine in the olivine-rich patches is subhedral, coarse-grained (0.5–1.8 mm) and encloses tiny (50–150 µm) round spinel and sometimes orthopyroxene as inclusions (Fig. 4.2b). Orthopyroxene inclusions hosted in olivines are sometimes partially surrounded by clinopyroxene (Fig. 4.2c). The less common interstitial clinopyroxene and spinel are also subhedral and small

Table 2. Petrography of the studied NGVF wehrlite xenoliths. The equilibrium temperature calculations are based on the Ca in orthopyroxene thermometer of Nimis and Grütter (2010) modified after Brey and Köhler (1990). Pressures values were estimated using the appropriate geotherm (alkaline basalt province geotherm; Jones et al., 1983) and the equilibrium temperatures.

Sample	Rock name	Texture	Modal composition (%)					Equilibrium temperature (°C)	P (Gpa)
			ol	opx	cpx	sp	gl	$T_{ca\text{-}in\text{-}opx\ by\ NG}$	
NTB1109	wehrlite	fine-grained	79.0	0.5	19.0	1.0	0.5	—	—
NTB1120	wehrlite	ol- and cpx-rich patches	73.0	0.5	24.0	2.0	0.5	—	—
NFK1110	wehrlite	ol- and cpx-rich patches	75.0	0.5	20.5	2.0	2.0	—	—
NFK1137A	wehrlite	ol- and cpx-rich patches	74.5	—	23.0	2.5	—	—	—
NFR1117A	wehrlite	ol- and cpx-rich patches	76.5	0.5	21.0	1.5	0.5	985	1.4
NFR1119B	wehrlite	coarse-grained	82.5	0.5	10.0	6.5*	0.5	1000	1.4
NMC1302B	wehrlite	ol- and cpx-rich patches	74.5	0.5	22.0	1.0	1.5	1009	1.4
NMC1343	wehrlite	ol- and cpx-rich patches	77.0	0.5	20.0	1.5	1.0	1021	1.5
NMM1114	wehrlite	ol- and cpx-rich patches	72.0	0.5	23.5	3.0	1.0	1055	1.6
NMM1129	wehrlite	ol- and cpx-rich patches	80.5	—	17.5	1.5	0.5	—	—
NME1110	wehrlite	ol- and cpx-rich patches	76.0	0.5	22.0	1.5	—	—	—
NME1129D	wehrlite	ol- and cpx-rich patches	75.0	0.5	23.0	1.0	—	—	—

* Extremely high spinel content is due to a huge interstitial spinel grain

Abbreviations: ol – olivine, opx – orthopyroxene, cpx – clinopyroxene, sp – spinel, gl – glass

(0.2–0.7 mm). Some clinopyroxenes host 70–200 μm orthopyroxene inclusions. The grain boundaries are linear and often meet in 120º triple junctions. Stress induced undulating extinction is sometimes recognized.

Clinopyroxene-rich patches exhibit a poikilitic texture with a 'finger-like' microfabric, whereby fine grained (0.1–0.4 mm), rounded or elongated olivine crystals are enclosed by coarse grained (0.3–0.7 mm), oriented and elongated clinopyroxene oikocrystals (enclosing crystals in poikilitic fabric) with an aspect ratio of 4:1–8:1 (Fig. 4.2d). Entire clinopyroxene-rich patches show uniform extinction. Clinopyroxenes with tabular habit and larger size (5–10 mm) also occur in clinopyroxene-rich patches. Spinel appears either as interstitial, spherical grains (0.2–0.9 mm), as inclusions in olivine or clinopyroxene (50–150 μm), or as vermicular-shaped grains hosted by clinopyroxene (Fig. 4.2e). The vermicular-shaped spinels consist of numerous small (20–40 μm), irregular crystals. The clusters have diameters of 0.1–0.8 mm, similar in size to interstitial spinels, and have a ~70–30 clinopyroxene/spinel ratio. Although some wehrlites (NTB1109, NTB1120, NFK1137A, NMM1129, NME1129D) contain both interstitial and vermicular spinels, only xenolith NFK1137A contains partly interstitial and partly vermicular single grains displaying a gradual transition between the two forms (Fig. 4.2f). In such grains, the vermicular spinel portion is always clinopyroxene-hosted, whereas the interstitial portion is adjacent to olivines. In a few patches, 200–400 μm angular or rounded orthopyroxene relicts occur in the cores of clinopyroxene crystals (Fig. 4.2g). In xenolith NMC1302B, orthopyroxene also appears in olivine from a clinopyroxene-rich patch. Two wehrlite xenoliths that do not contain olivine- and clinopyroxene-rich patches have fine-grained (NTB1109) and coarse-grained textures (NFR1119B), with average grain sizes of 0.2–0.3 mm and 0.5–0.7 mm, respectively (Fig. 4.1). Mineral constituents in xenolith NTB1109 are mostly rounded, however, in wehrlite NFR1119B they are tabular shaped. In wehrlites, a large number of fluid, silicate melt, and sulfide melt inclusions are present in both olivine and clinopyroxene (Patkó et al., 2018). In this Ph.D. thesis I focus exclusively on the sulfides.

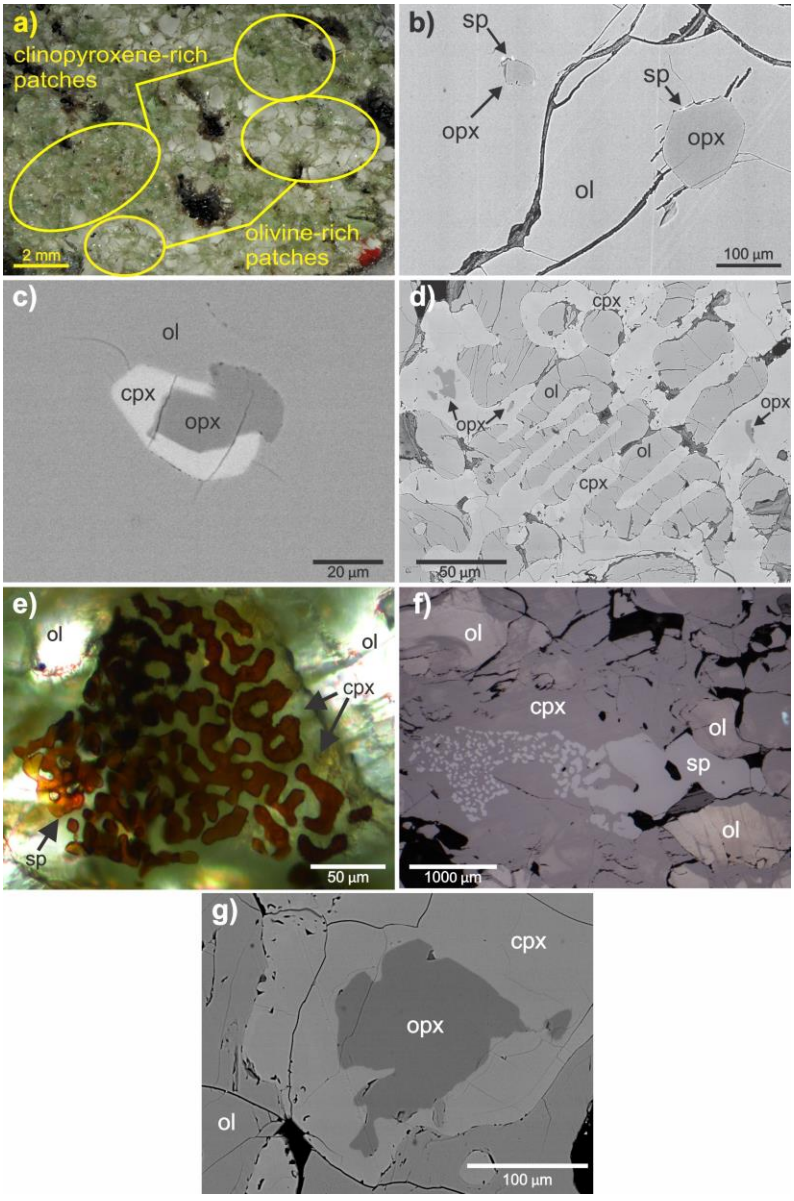

Figure 4.2 Photomicrographs of wehrlite xenoliths from the Nógrád-Gömör Volcanic Field showing different textural characteristics. **(a)** Typical wehrlitic texture composed of olivine- and clinopyroxene-rich assemblage (stereomicroscopic image) (NMM1129). **(b)** Orthopyroxene inclusions hosted by olivine with spinel at the boundary between the orthopyroxene and the olivine (back-scattered SEM image) (NFR1119B). **(c)** Orthopyroxene inclusion enclosed in olivine with newly formed clinopyroxene at the orthopyroxene-olivine interface (back-scattered SEM image) (NMC1343). **(d)** 'Finger-like' microfabric with elongated olivine and clinopyroxene (back-scattered SEM image) (NFR1117A). Note that the clinopyroxenes contain tiny orthopyroxene inclusions. **(e)** Vermicular spinel hosted by clinopyroxene (transmitted light image using 1 nicol and conical light) (NFK1137A). **(f)** Partly vermicular and partly interstitial spinel. Note that the vermicular forms are hosted by clinopyroxene, whereas the interstitial segment is adjacent to olivine (reflected light image) (NFK1137A). **(g)** Relict orthopyroxene in newly formed clinopyroxene, showing clinopyroxene replacement texture (back-scattered SEM image) (NTB1120).

4.2. Major element composition of minerals

Significant variations in olivine compositions are observed among the different wehrlite xenoliths (Table 3; Appendix 1). However, olivines within a single xenolith show almost homogeneous chemistry (Fig 4.3a) with the exception of those in xenoliths NFR1119B and NMC1302B. In these xenoliths, two compositional groups can be distinguished based on their FeO and MnO concentrations (Fig. 4.4a) with no corresponding differences in their petrographic position. The group with lower FeO and MnO content has 10.0–10.6 wt. % FeO and 0.08–0.17 wt. % MnO in NFR1119B, and 11.5–13.1 and 0.13–0.20 wt. % in NMC1302B, respectively. On the other hand, olivines with higher FeO and MnO contents contain 13.0–13.8 and 15.4–15.9 wt. % FeO and 0.19–0.24 and 0.21–0.25 wt. % MnO, respectively (Fig. 4.4a). FeO shows a positive correlation with MnO content in wehrlites, except for xenoliths NFK1110 and NFK1137A (Fig 4.3a). The minimum (0.83 in NFK1110) and maximum (0.88 in NFR1119B) Mg# ($Mg/[Mg+Fe^{2+}]$) are both lower than the average Phanerozoic mantle Mg# of 0.90-0.91 (e.g., Gaul et al., 2000). The Mg# shows positive correlation with NiO and negative correlation with MnO (Fig. 4.5). No correlation was observed between the Mg# and olivine modal content. Furthermore, there is no systematic difference between olivines in olivine-rich patches and those in clinopyroxene-rich patches.

Clinopyroxene, which is dominantly diopside (Morimoto, 1988), have highly variable chemistry represented by patchy inhomogeneities not only between xenoliths (Table 4; Appendix 2), but also within a single xenolith. In the whole series, Al_2O_3, TiO_2 and CaO correlate positively with each other and range between 2.11–8.53, 0.16–1.64 and 18.6–23.3 wt. %, respectively (Fig. 4.3b). Similar ranges are observed only in xenolith NME1129D, with concentration ranges from 3.45–8.53 (Al_2O_3), 0.37–1.64 (TiO_2) and 19.2–21.2 wt. % (CaO) (Fig. 4.4b). In contrast, Al_2O_3, TiO_2 and CaO correlate negatively with MgO and SiO_2. Iron shows no correlation with other basaltic elements (Al, Ti, Ca, Na). The Mg# ($Mg/[Mg+Fe_{tot}]$) varies widely among the xenoliths. The lowest value is observed in xenolith NMM1114 (0.84), whereas the highest value occurs in xenolith NFR1119B (0.90) (Table 4). Neither the textural position (olivine- or clinopyroxene-rich patch) nor the habit ('finger-like' or tabular) of clinopyroxenes show any relationship with their composition.

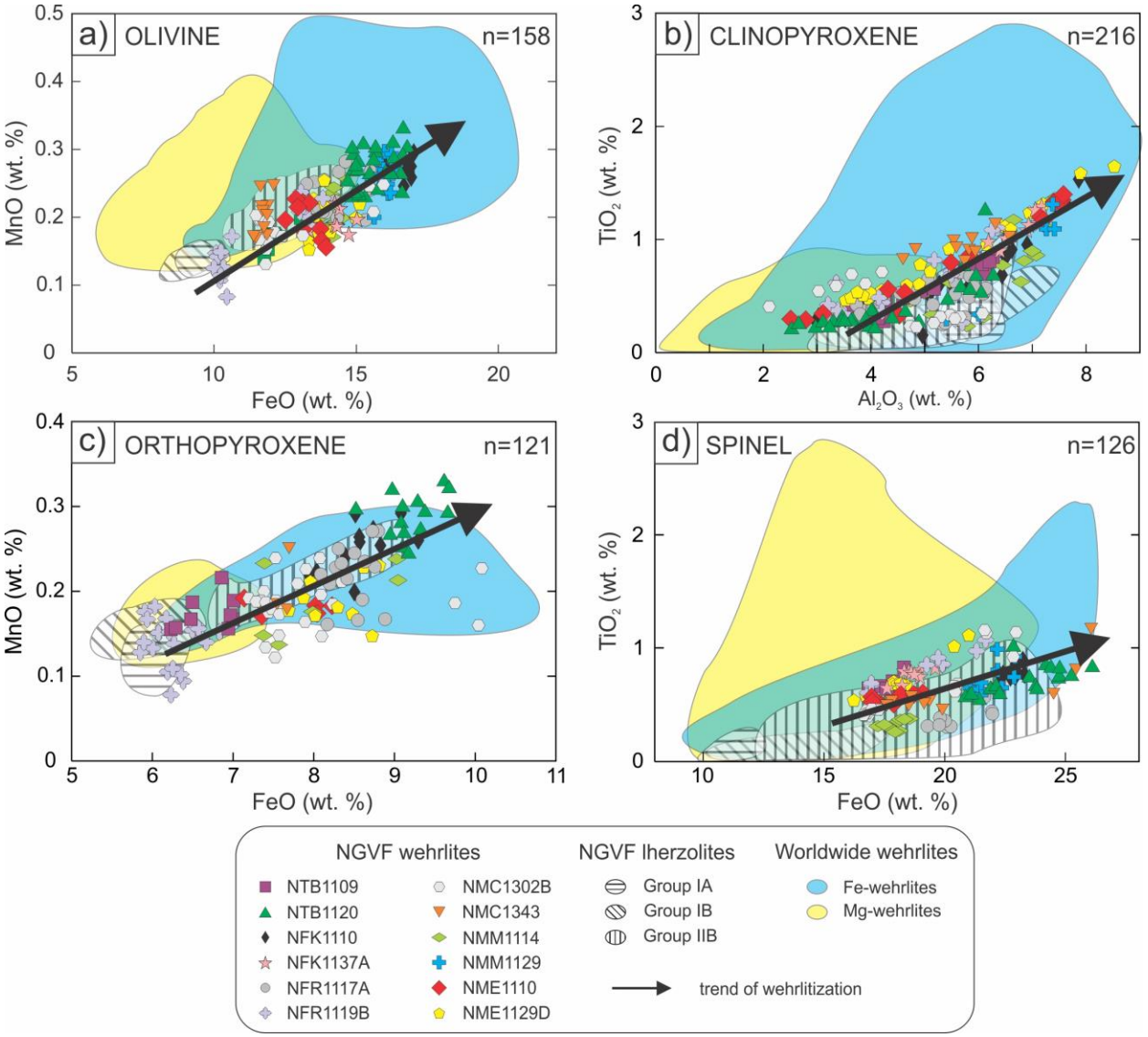

Figure 4.3 Major element composition of the NGVF wehrlite xenoliths. The chemical variation diagrams shown are: **(a)** FeO vs. MnO in olivine **(b)** Al_2O_3 vs. TiO_2 in clinopyroxene **(c)** FeO vs. MnO in orthopyroxene **(d)** FeO vs. TiO_2 in spinel. The different NGVF lherzolite groups are from Liptai et al. (2017). Reference for Fe-wehrlites are based on: Zinngrebe and Foley, 1995; Xu et al., 1996; Peslier et al., 2002a; Rivalenti et al., 2004; Ionov et al., 2005; Shaw et al., 2005; 2018; Raffone et al., 2009; Zhang et al., 2010; Xiao et al., 2010. Reference for Mg-wehrlites are based on: Yaxley et al., 1991; 1998; Hauri et al., 1993; Xu et al., 1996; Coltorti et al., 1999; Neumann et al., 2002; Raffone et al., 2009; Scott et al., 2014.

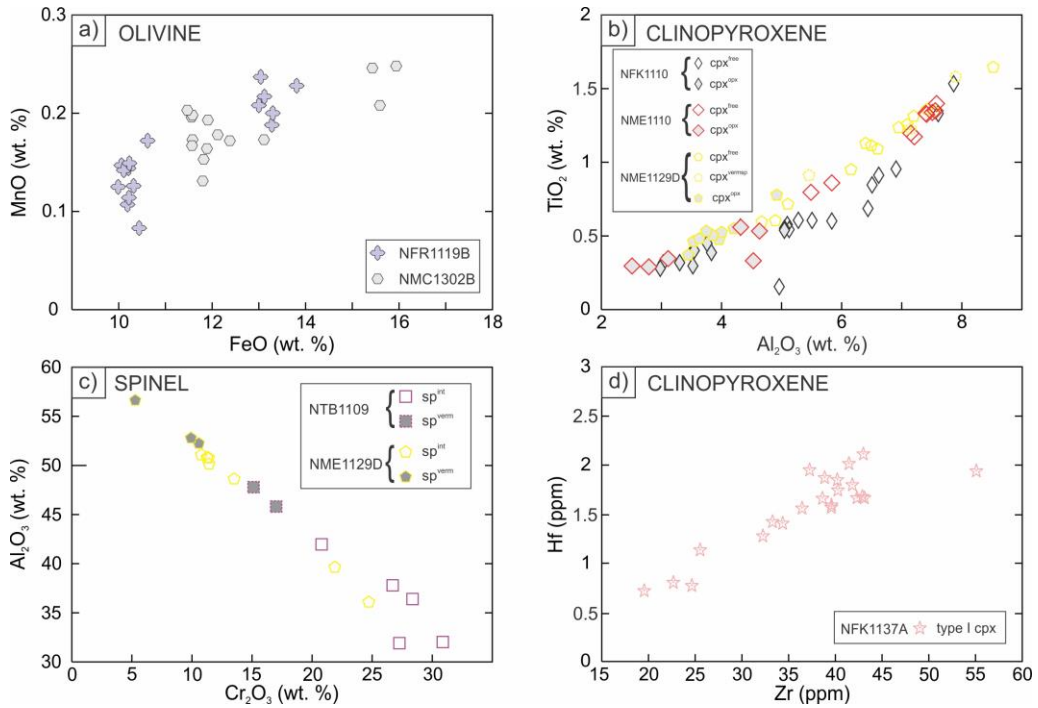

Figure 4.4 Geochemical data for individual xenoliths, including phases that occur in different textural settings. **(a)** FeO vs. MnO in olivine **(b)** Al_2O_3 vs. TiO_2 in clinopyroxene **(c)** Cr_2O_3 vs. Al_2O_3 in spinel and **(d)** Zr vs. Hf in clinopyroxene. Abbreviations: cpx^{free} - vermicular spinel and orthopyroxene free clinopyroxenes; cpx^{vermsp} - clinopyroxenes hosting vermicular spinel; cpx^{opx} - clinopyroxenes hosting orthopyroxene relict; sp^{int} – interstitial spinel; sp^{verm} – vermicular spinel; type I cpx – clinopyroxene with convex upward REY patterns.

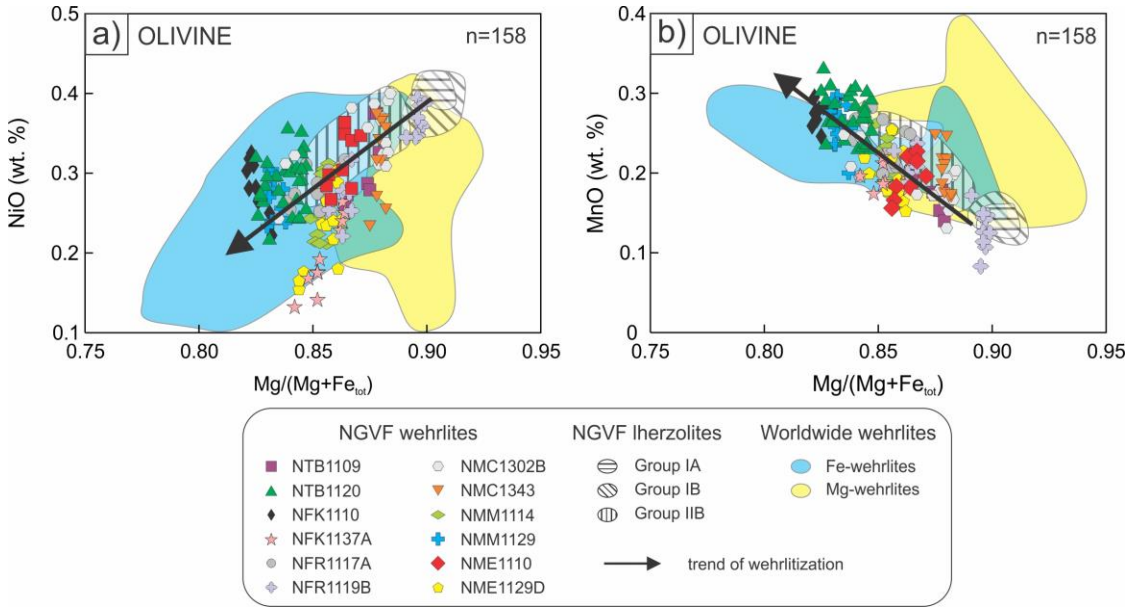

Figure 4.5 Relationship between the mg# and **(a)** NiO and **(b)** MnO in olivine. The different NGVF lherzolite groups are from Liptai et al. (2017). References for Mg- and Fe-wehrlites are the same as in Fig. 4.3.

Table 3. Major element compositions (in wt. %) of olivine in the studied Nógrád-Gömör wehrlite xenoliths. Given error is 2 σ.

Sample	n	SiO_2	FeO*	MnO	MgO	CaO	NiO	Total	$Mg/(Mg+Fe_{tot})$
NTB1109	7	40.6 ± 0.2	12.3 ± 0.6	0.17 ± 0.02	47.4 ± 0.5	0.20 ± 0.03	0.31 ± 0.05	100.98	0.87
NTB1120	29	39.3 ± 0.3	15.6 ± 0.7	0.27 ± 0.03	45.1 ± 0.5	0.17 ± 0.03	0.29 ± 0.03	100.73	0.84
NFK1110	10	39.4 ± 0.2	16.6 ± 0.4	0.28 ± 0.02	44.1 ± 0.4	0.17 ± 0.02	0.28 ± 0.03	100.83	0.83
NFK1137A	10	39.8 ± 0.3	14.0 ± 0.7	0.20 ± 0.02	46.5 ± 0.6	0.19 ± 0.02	0.20 ± 0.05	100.89	0.86
NFR1117A	14	39.8 ± 0.6	14.3 ± 0.7	0.23 ± 0.03	46.3 ± 0.6	0.16 ± 0.07	0.28 ± 0.02	101.07	0.85
NFR1119B	16	40.3 ± 0.4	11.4 ± 1.5	0.16 ± 0.05	48.7 ± 1.3	0.15 ± 0.03	0.33 ± 0.05	101.04	0.88
NMC1302B	15	39.9 ± 0.4	12.7 ± 1.6	0.19 ± 0.03	48.0 ± 1.3	0.10 ± 0.03	0.34 ± 0.04	101.23	0.87
NMC1343	11	40.9 ± 0.4	11.7 ± 0.2	0.20 ± 0.03	47.8 ± 0.3	0.12 ± 0.01	0.32 ± 0.05	101.04	0.88
NMM1114	12	39.8 ± 0.2	14.1 ± 0.2	0.22 ± 0.03	46.2 ± 0.4	0.14 ± 0.02	0.25 ± 0.04	100.71	0.85
NMM1129	13	39.1 ± 0.2	16.0 ± 0.3	0.26 ± 0.03	44.6 ± 0.2	0.15 ± 0.02	0.27 ± 0.02	100.38	0.83
NME1110	9	40.0 ± 0.2	13.3 ± 0.5	0.20 ± 0.03	46.8 ± 0.4	0.16 ± 0.02	0.32 ± 0.04	100.78	0.86
NME1129D	12	40.1 ± 0.2	14.0 ± 0.7	0.20 ± 0.03	46.3 ± 0.3	0.18 ± 0.01	0.22 ± 0.05	101.00	0.86

n – number of analyses

*total iron expressed as FeO

Table 4. Major element compositions (in wt. %) of clinopyroxene in the studied Nógrád-Gömör wehrlite xenoliths. Given error is 2 σ.

Sample	Textural position	n	SiO_2	TiO_2	Al_2O_3	Cr_2O_3	FeO*	MnO	MgO	CaO	Na_2O	Total	$Mg/(Mg+Fe_{tot})$
NTB1109	cpx^{free}	5	51.2 ± 1.5	0.64 ± 0.33	5.44 ± 1.13	1.27 ± 0.34	3.71 ± 0.42	0.12 ± 0.03	16.1 ± 0.9	20.4 ± 0.6	1.01 ± 0.09	99.89	0.88
	cpx^{vermsp}	5	51.3 ± 0.6	0.68 ± 0.12	5.70 ± 0.60	1.37 ± 0.25	3.99 ± 0.14	0.11 ± 0.02	16.0 ± 0.4	20.3 ± 0.4	0.94 ± 0.07	100.39	0.88
	cpx^{opx}	8	52.1 ± 0.3	0.39 ± 0.07	4.11 ± 0.28	1.34 ± 0.17	3.47 ± 0.13	0.10 ± 0.02	17.5 ± 0.3	19.9 ± 0.3	1.03 ± 0.08	99.94	0.90
NTB1120	cpx^{free}	5	49.5 ± 0.6	0.76 ± 0.29	5.91 ± 0.20	0.89 ± 0.12	4.52 ± 0.17	0.11 ± 0.03	15.0 ± 0.4	21.4 ± 1.1	0.90 ± 0.25	98.99	0.85
	cpx^{vermsp}	7	50.8 ± 1.0	0.38 ± 0.18	4.98 ± 0.90	1.18 ± 0.33	4.86 ± 0.53	0.16 ± 0.03	15.5 ± 0.6	20.3 ± 0.3	1.25 ± 0.27	99.41	0.85
	cpx^{opx}	15	52.2 ± 0.4	0.28 ± 0.05	3.48 ± 0.55	1.00 ± 0.12	4.90 ± 0.31	0.20 ± 0.04	16.7 ± 0.4	19.7 ± 0.5	1.14 ± 0.08	99.60	0.86
NFK1110	cpx^{free}	12	50.0 ± 1.0	0.78 ± 0.37	6.15 ± 1.00	0.79 ± 0.22	4.99 ± 0.65	0.13 ± 0.03	15.0 ± 0.7	20.6 ± 0.3	0.98 ± 0.05	99.42	0.84
	cpx^{opx}	11	52.0 ± 0.7	0.41 ± 0.10	3.81 ± 0.72	1.13 ± 0.14	4.72 ± 0.34	0.15 ± 0.03	16.6 ± 0.6	20.0 ± 0.3	1.05 ± 0.05	99.87	0.86
NFK1137A	cpx^{free}	2	49.0 ± 0.1	1.13 ± 0.01	7.11 ± 0.01	0.98 ± 0.09	3.81 ± 0.01	0.11 ± 0.02	15.0 ± 0.1	21.7 ± 0.1	0.71 ± 0.01	99.53	0.87
	cpx^{vermsp}	8	49.3 ± 0.6	1.04 ± 0.19	6.59 ± 0.55	1.02 ± 0.19	3.88 ± 0.27	0.09 ± 0.03	15.2 ± 0.5	21.5 ± 0.3	0.80 ± 0.06	99.42	0.87
NFR1117A	cpx^{free}	17	50.9 ± 0.6	0.50 ± 0.14	5.39 ± 0.57	0.97 ± 0.24	4.25 ± 0.45	0.12 ± 0.02	15.7 ± 0.3	20.7 ± 0.4	1.08 ± 0.09	99.61	0.87
	cpx^{opx}	15	52.4 ± 0.5	0.36 ± 0.05	3.74 ± 0.37	1.18 ± 0.18	4.41 ± 0.38	0.13 ± 0.02	16.7 ± 0.4	19.9 ± 0.4	1.10 ± 0.05	99.92	0.87
NFR1119B	cpx^{free}	9	50.8 ± 0.8	0.67 ± 0.32	5.74 ± 0.39	1.22 ± 0.16	3.41 ± 0.70	0.10 ± 0.01	16.0 ± 0.4	20.6 ± 0.3	1.11 ± 0.18	99.65	0.89
	cpx^{opx}	8	52.4 ± 0.5	0.42 ± 0.10	3.67 ± 0.44	1.32 ± 0.19	3.38 ± 0.38	0.12 ± 0.02	17.5 ± 0.6	20.2 ± 1.0	0.99 ± 0.15	100.00	0.90
NMC1302B	cpx^{free}	9	51.3 ± 0.3	0.29 ± 0.04	5.33 ± 0.42	0.85 ± 0.10	3.40 ± 0.06	0.11 ± 0.03	16.2 ± 0.2	21.5 ± 0.1	0.95 ± 0.04	99.93	0.89
	cpx^{opx}	6	52.2 ± 0.7	0.59 ± 0.11	3.38 ± 0.74	1.08 ± 0.09	4.55 ± 0.14	0.16 ± 0.03	17.5 ± 0.6	19.3 ± 0.3	0.97 ± 0.09	99.73	0.87
NMC1343	cpx^{free}	10	51.3 ± 0.5	0.96 ± 0.10	5.68 ± 0.60	1.16 ± 0.19	3.35 ± 0.34	0.08 ± 0.04	15.2 ± 0.6	21.8 ± 1.1	0.93 ± 0.27	100.46	0.89
NMM1114	cpx^{free}	13	50.3 ± 1.1	0.73 ± 0.36	6.48 ± 0.68	0.86 ± 0.30	3.95 ± 0.39	0.11 ± 0.02	15.4 ± 0.5	20.7 ± 0.8	1.09 ± 0.24	99.62	0.87
	cpx^{opx}	6	51.6 ± 0.8	0.50 ± 0.14	4.76 ± 0.85	0.95 ± 0.15	4.22 ± 0.18	0.13 ± 0.04	16.9 ± 0.6	19.8 ± 0.7	1.02 ± 0.03	99.88	0.87
NMM1129	cpx^{free}	6	49.3 ± 1.1	0.83 ± 0.47	6.69 ± 0.93	0.64 ± 0.08	4.63 ± 0.94	0.12 ± 0.03	14.9 ± 0.8	21.0 ± 0.3	0.97 ± 0.04	99.08	0.85
NME1110	cpx^{free}	9	49.3 ± 0.7	1.20 ± 0.22	7.02 ± 0.79	0.86 ± 0.21	3.94 ± 0.30	0.09 ± 0.03	15.0 ± 0.4	21.4 ± 0.1	0.91 ± 0.04	99.72	0.87
	cpx^{opx}	6	52.3 ± 0.5	0.39 ± 0.12	3.65 ± 0.95	1.00 ± 0.19	4.12 ± 0.39	0.10 ± 0.02	17.2 ± 0.6	20.3 ± 0.7	0.89 ± 0.03	99.95	0.88
NME1129D	cpx^{free}	13	49.8 ± 1.1	1.10 ± 0.31	6.54 ± 1.12	0.84 ± 0.23	4.37 ± 0.29	0.11 ± 0.03	15.1 ± 0.6	20.8 ± 0.2	0.94 ± 0.05	99.60	0.86
	cpx^{vermsp}	3	49.3 ± 1.3	1.24 ± 0.33	6.83 ± 1.25	0.96 ± 0.36	4.35 ± 0.16	0.10 ± 0.01	14.9 ± 0.6	20.8 ± 0.3	0.94 ± 0.04	99.42	0.86
	cpx^{opx}	9	52.2 ± 0.6	0.52 ± 0.11	3.92 ± 0.44	1.12 ± 0.12	4.26 ± 0.40	0.13 ± 0.02	16.9 ± 0.6	20.2 ± 0.6	0.93 ± 0.07	100.18	0.88

n - number of analyses

*total iron expressed as FeO

cpx^{free} - clinopyroxene without orthopyroxene relicts and vermicular spinel; cpx^{opx} - clinopyroxene hosting orthopyroxene relict; cpx^{vermsp} - clinopyroxene hosting vermicular spinel

Orthopyroxenes, which are enstatites (Morimoto, 1988), show no notable compositional variations within individual xenoliths. In contrast, significant compositional differences are observed among the different xenoliths (Table 5; Appendix 3). The FeO and MnO contents show positive correlation and vary between 5.85–10.1 and 0.08–0.33 wt. %, respectively, for the whole series (Fig. 4.3c). The Mg# (Mg/[Mg+Fe_{tot}]) in orthopyroxene ranges between 0.85 (NTB1120) and 0.91 (NFR1119B). The average CaO concentration is higher in clinopyroxene-hosted orthopyroxenes (0.76–2.21 with an average of 1.33 wt. %), whereas the Al_2O_3 content is lower (1.52–4.71 with an average of 2.59 wt. %) compared to those hosted in olivine (0.74–1.15 with an average of 0.87 wt. % and 2.84–3.92 with an average of 3.59 wt. %, respectively) (Fig. 4.6a; Table 5). In contrast, the CaO shows no correlation with Na_2O (Fig. 4.6b) or FeO (Fig. 4.6c).

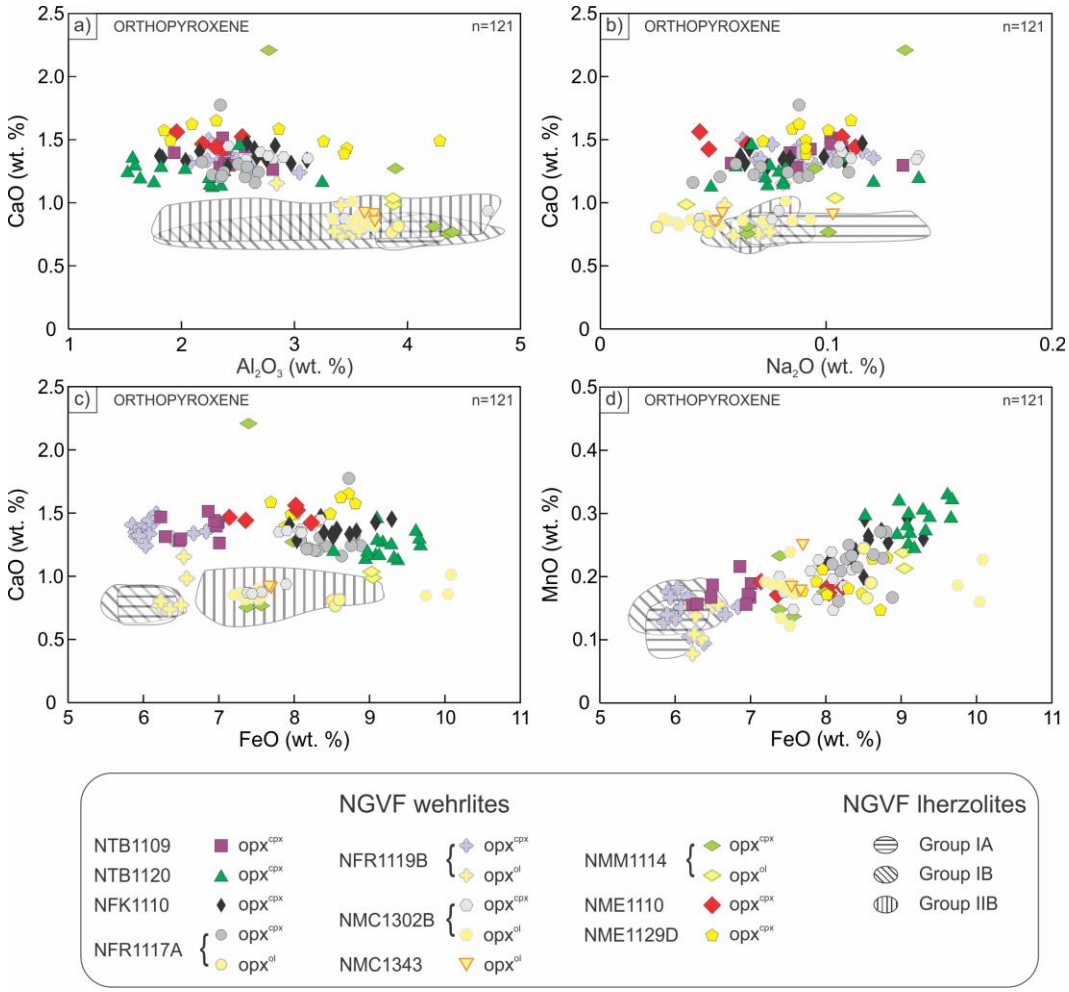

Figure 4.6 Relationship between **(a)** Al_2O_3 vs. CaO **(b)** Na_2O vs. CaO **(c)** FeO vs. CaO and **(d)** FeO vs. MnO in relict orthopyroxene with respect to their textural position (opx^{cpx} - orthopyroxene inclusion hosted by clinopyroxene; opx^{ol} - orthopyroxene inclusion hosted by olivine). The different NGVF lherzolite groups are from Liptai et al. (2017).

Table 5. Major element compositions (in wt. %) of orthopyroxene in the studied Nógrád-Gömör wehrlite xenoliths. Given error is 2 σ.

Sample	Textural position	n	SiO_2	TiO_2	Al_2O_3	Cr_2O_3	FeO*	MnO	MgO	CaO	Total	$Mg/(Mg+Fe_{tot})$
NTB1109	opx^{cpx}	9	55.7 ± 0.2	0.12 ± 0.01	2.42 ± 0.23	0.56 ± 0.04	6.70 ± 0.32	0.17 ± 0.02	33.5 ± 0.4	1.38 ± 0.09	100.55	0.90
NTB1120	opx^{cpx}	14	55.1 ± 0.3	0.11 ± 0.02	2.08 ± 0.48	0.47 ± 0.12	9.21 ± 0.31	0.29 ± 0.03	31.6 ± 0.2	1.23 ± 0.09	100.09	0.86
NFK1110	opx^{cpx}	12	55.2 ± 0.3	0.13 ± 0.03	2.48 ± 0.44	0.42 ± 0.07	8.57 ± 0.39	0.25 ± 0.03	32.0 ± 0.4	1.37 ± 0.06	100.42	0.87
NFR1117A	opx^{cpx}	12	55.5 ± 0.3	0.15 ± 0.03	2.45 ± 0.16	0.50 ± 0.07	8.47 ± 0.28	0.22 ± 0.03	32.5 ± 0.3	1.28 ± 0.16	101.07	0.87
	opx^{ol}	3	54.7 ± 0.1	0.06 ± 0.01	3.89 ± 0.03	0.35 ± 0.05	8.55 ± 0.05	0.20 ± 0.04	32.3 ± 0.1	0.80 ± 0.03	100.85	0.87
NFR1119B	opx^{cpx}	14	55.8 ± 0.2	0.13 ± 0.03	2.44 ± 0.27	0.60 ± 0.05	6.15 ± 0.30	0.15 ± 0.03	33.8 ± 0.3	1.37 ± 0.07	100.44	0.91
	opx^{ol}	8	55.4 ± 0.2	0.07 ± 0.03	3.39 ± 0.23	0.47 ± 0.08	6.37 ± 0.15	0.13 ± 0.03	33.8 ± 0.1	0.84 ± 0.15	100.47	0.90
NMC1302B	opx^{cpx}	11	54.8 ± 0.4	0.16 ± 0.07	3.14 ± 0.65	0.49 ± 0.06	7.89 ± 0.32	0.19 ± 0.03	32.6 ± 0.4	1.20 ± 0.25	100.47	0.88
	opx^{ol}	14	54.6 ± 0.4	0.07 ± 0.02	3.57 ± 0.09	0.41 ± 0.07	7.98 ± 1.08	0.18 ± 0.03	32.7 ± 0.8	0.86 ± 0.05	100.37	0.88
NMC1343	opx^{ol}	3	55.2 ± 0.1	0.10 ± 0.01	3.68 ± 0.05	0.39 ± 0.05	7.64 ± 0.08	0.21 ± 0.04	32.4 ± 0.2	0.91 ± 0.04	100.53	0.88
NMM1114	opx^{cpx}	5	54.9 ± 0.5	0.12 ± 0.06	3.93 ± 0.68	0.32 ± 0.06	7.54 ± 0.26	0.18 ± 0.04	32.2 ± 0.2	1.16 ± 0.62	100.35	0.88
	opx^{ol}	2	54.4 ± 0.1	0.09 ± 0.02	3.87 ± 0.01	0.27 ± 0.04	9.04 ± 0.01	0.23 ± 0.02	31.4 ± 0.1	1.01 ± 0.04	100.31	0.86
NME1110	opx^{cpx}	5	55.3 ± 0.3	0.17 ± 0.03	2.27 ± 0.22	0.46 ± 0.15	7.76 ± 0.48	0.18 ± 0.01	32.8 ± 0.5	1.48 ± 0.06	100.42	0.88
NME1129D	opx^{cpx}	9	55.4 ± 0.5	0.21 ± 0.03	2.83 ± 0.85	0.38 ± 0.08	8.28 ± 0.41	0.19 ± 0.03	32.1 ± 0.6	1.52 ± 0.09	101.91	0.87

n - number of analyses
*total iron expressed as FeO
opx^{cpx} - relict orthopyroxene in clinopyroxene
opx^{ol} - orthopyroxene inclusion in olivine

Table 6. Major element compositions (in wt. %) of spinel in the studied Nógrád-Gömör wehrlite xenoliths. Given error is 2 σ.

Sample	Textural position	n	TiO_2	Al_2O_3	Cr_2O_3	FeO*	MnO	NiO	MgO	Total	$Mg/(Mg+Fe^{2+})$	Cr/(Cr+Al)
NTB1109	sp^{int}	2	0.65 ± 0.02	46.8 ± 1.4	16.1 ± 1.3	17.4 ± 0.2	0.20 ± 0.01	0.28 ± 0.01	18.0 ± 0.4	99.43	0.73	0.19
	sp^{verm}	5	0.69 ± 0.08	36.0 ± 4.2	26.8 ± 3.7	17.8 ± 0.6	0.17 ± 0.02	0.25 ± 0.03	16.4 ± 0.4	98.11	0.70	0.33
NTB1120	sp^{int}	11	0.65 ± 0.10	43.9 ± 1.2	16.5 ± 1.2	22.2 ± 1.3	0.24 ± 0.04	0.28 ± 0.03	15.9 ± 0.8	99.67	0.66	0.20
	sp^{verm}	8	0.77 ± 0.12	40.2 ± 3.3	18.4 ± 3.1	24.4 ± 1.0	0.24 ± 0.04	0.27 ± 0.03	15.2 ± 0.6	99.48	0.64	0.24
NFK1110	sp^{int}	10	0.78 ± 0.05	48.4 ± 1.6	10.9 ± 2.0	22.7 ± 0.3	0.19 ± 0.02	0.32 ± 0.04	16.6 ± 0.2	99.89	0.67	0.13
NFK1137A	sp^{int}	5	0.74 ± 0.08	48.3 ± 1.7	14.0 ± 1.3	18.3 ± 0.5	0.17 ± 0.02	0.23 ± 0.04	18.2 ± 0.4	99.94	0.73	0.16
	sp^{verm}	4	0.78 ± 0.03	47.0 ± 0.6	15.0 ± 0.5	18.9 ± 0.4	0.16 ± 0.04	0.22 ± 0.02	17.9 ± 0.1	99.96	0.72	0.18
NFR1117A	sp^{int}	9	0.38 ± 0.09	44.4 ± 0.7	17.2 ± 0.7	20.5 ± 1.0	0.17 ± 0.02	0.29 ± 0.03	16.8 ± 0.5	99.74	0.69	0.21
NFR1119B	sp^{int}	9	0.83 ± 0.15	37.2 ± 3.0	26.0 ± 4.4	19.1 ± 1.9	0.17 ± 0.03	0.23 ± 0.03	16.3 ± 0.5	99.83	0.69	0.32
NMC1302B	sp^{int}	14	0.66 ± 0.30	44.2 ± 3.1	18.7 ± 1.8	19.1 ± 2.5	0.19 ± 0.04	0.30 ± 0.04	17.0 ± 1.2	100.15	0.69	0.22
NMC1343	sp^{int}	11	0.63 ± 0.21	42.0 ± 4.3	20.7 ± 3.6	20.5 ± 3.2	0.23 ± 0.04	0.26 ± 0.02	15.8 ± 1.7	100.12	0.66	0.25
NMM1114	sp^{int}	9	0.32 ± 0.04	51.0 ± 1.8	12.0 ± 1.9	17.9 ± 0.4	0.16 ± 0.03	0.26 ± 0.03	18.4 ± 0.3	100.04	0.73	0.14
NMM1129	sp^{int}	10	0.73 ± 0.14	48.2 ± 2.3	11.8 ± 2.0	21.9 ± 0.7	0.19 ± 0.03	0.29 ± 0.04	16.5 ± 0.6	99.61	0.67	0.14
NME1110	sp^{int}	9	0.54 ± 0.04	48.7 ± 1.1	14.4 ± 1.2	17.7 ± 0.8	0.15 ± 0.02	0.31 ± 0.03	18.2 ± 0.4	100.00	0.73	0.17
NME1129D	sp^{int}	3	0.56 ± 0.02	54.0 ± 2.6	8.59 ± 2.9	16.5 ± 0.3	0.12 ± 0.03	0.31 ± 0.01	19.5 ± 0.4	99.58	0.76	0.10
	sp^{verm}	4	0.87 ± 0.22	43.8 ± 7.0	17.9 ± 6.4	19.2 ± 1.6	0.17 ± 0.03	0.21 ± 0.05	17.4 ± 1.3	99.55	0.71	0.22
	sp^{incl}	3	0.68 ± 0.01	50.7 ± 0.5	11.2 ± 0.3	18.2 ± 0.2	0.15 ± 0.03	0.28 ± 0.04	18.4 ± 0.1	99.61	0.73	0.13

n - number of analyses
*total iron expressed as FeO
sp^{int} - interstitial spinel
sp^{verm} - vermicular spinel
sp^{incl} - spinel inclusion in cpx

Spinel composition is either homogeneous (in xenoliths NTB1109, NFK1110, NFK1137A, NMM1114) or heterogeneous (in xenoliths NTB1120, NFR1117A, NFR1119B, NMC1302B, NMC1343, NMM1129, NME1110, NME1129D) within a single xenolith. Concentrations of FeO, TiO_2 and MnO show wide ranges (16.2–26.1, 0.26–1.18 and 0.09–0.31 wt. %, respectively) (Table 6; Appendix 4), and correlate positively with one another (Fig. 4.3d). The minimum Mg# ($Mg/[Mg+Fe^{2+}]$) in spinel is 0.65 in xenolith NTB1120, whereas the maximum Mg# is 0.73 in xenolith NMM1114. The Cr# (Cr/[Cr+Al]) ranges between 0.13–0.32. Xenolith NFK1110 shows the minimum Cr# value and this xenolith also shows the minimum olivine Mg# (Table 3). The maximum Cr# of spinel is observed in xenolith NFR1119B, which also has the highest Mg# for all silicates (Table 3; 4; 5). The spinel composition shows no correlation with respect to the olivine- or clinopyroxene-rich textural position.

4.3. Trace element composition of minerals

Clinopyroxene trace element compositions (Table 7; Appendix 5) show uniform multi-element patterns, having low concentrations of highly incompatible (Th, U, Nb, Ta, Pb) and some compatible elements (Co, Ni) (Fig. 4.7). The Hf and Zr compositions show negative anomalies and have slightly higher concentrations compared to the primitive mantle (McDonough and Sun, 1995). The highest average Hf and Zr concentrations are found in xenoliths NFK1137A (1.55 ppm) and NMM1129 (38.7 ppm), respectively, whereas the lowest average values are found in xenolith NTB1109 (0.3 and 9.10 ppm, respectively) (Fig. 4.7). Concentrations of Ti are variable with respect to their neighboring elements (Fig. 4.7). Beside these common features, there are some additional trace element characteristics in the REY patterns (Fig. 4.8) not only between xenoliths, but within xenoliths as well. Three different clinopyroxene groups, type I, type II and type III can be distinguished based on the REY patterns.

All wehrlites, except for xenolith NMC1302B, display convex upward REY patterns with a maximum at Nd, and in case of xenolith NTB1120, at Ce (Fig. 4.8a). Samples displaying this behavior will hereafter be referred to as type I. The normalized LREE and HREE concentrations are 3–8 and 2–3 times higher, respectively, compared to primitive mantle (PM; McDonough and Sun, 1995). The most common REY pattern shows an average Nd_N/Yb_N (normalized to the PM of McDonough and Sun (1995)) that is higher than 1.7 (1.73–3.58), with the exception of

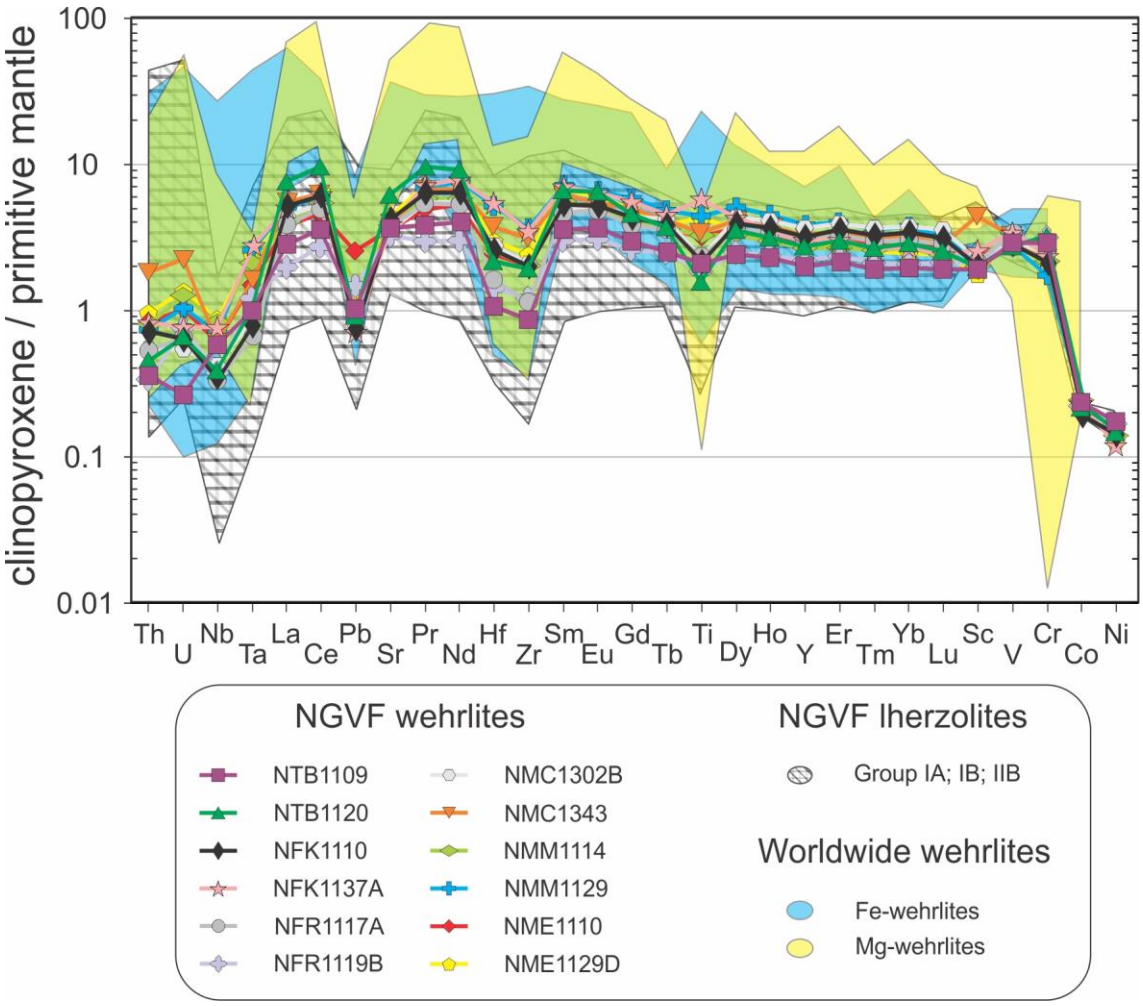

Figure 4.7 Primitive mantle (McDonough and Sun, 1995) normalized multi-element diagram of clinopyroxenes. The NGVF lherzolites are from Liptai et al. (2017). Reference for Fe-wehrlites are based on: Xu et al., 1996; Rivalenti et al., 2004; Shaw et al., 2005; Raffone et al., 2009; Xiao et al., 2010. Reference for Mg-wehrlites are based on: Hauri et al., 1993; Xu et al., 1996; Coltorti et al., 1999; Neumann et al., 2002; Raffone et al., 2009; Scott et al., 2014.

clinopyroxenes hosted in vermicular spinel in xenolith NTB1109 (1.53) and in xenolith NME1110 (1.02) (Table 7). Type I clinopyroxenes appear exclusively in xenoliths NTB1109, NTB1120, NFK1137A, NMM1114 and NME1129D.

Type II clinopyroxenes show a rather flat REY pattern with an average Nd_N/Yb_N ratio lower than 1.7 (0.87–1.54) (Table 7). Both the normalized LREE and HREE data are 2–5 times higher than the PM value (Fig. 4.8b) (McDonough and Sun, 1995). Type II clinopyroxenes are less common compared to type I clinopyroxenes, although this is the only type present in NMC1302B xenolith. This pattern is also characteristic for xenoliths NFR1117A, NMM1129 and NME1110.

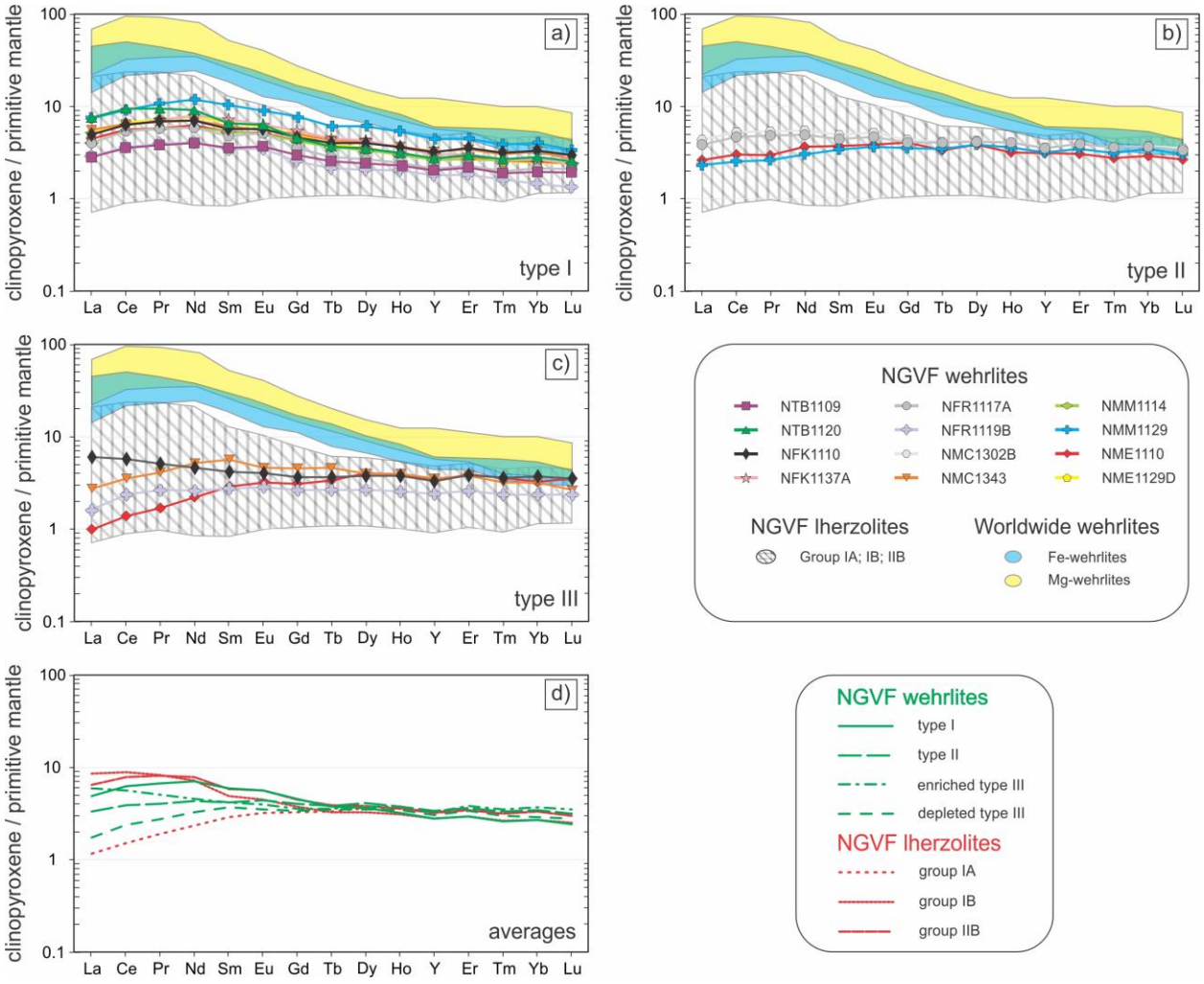

Figure 4.8 Primitive mantle (McDonough and Sun, 1995) normalized REY patterns of **(a)** type I **(b)** type II and **(c)** type III clinopyroxenes of wehrlite xenoliths. **(d)** The average REY distributions for different clinopyroxene types from wehrlite xenoliths along with those from distinct lherzolites based on Liptai et al. (2017). Reference for Fe-wehrlites are based on: Xu et al., 1996; Rivalenti et al., 2004; Shaw et al., 2005; Raffone et al., 2009; Xiao et al., 2010. Reference for Mg-wehrlites are based on: Hauri et al., 1993; Xu et al., 1996; Coltorti et al., 1999; Neumann et al., 2002; Raffone et al., 2009; Scott et al., 2014.

Four xenoliths (NFK1110, NFR1119B, NMC1343, NME1110) display REY patterns of clinopyroxenes that are unlike the type I or type II groups, and hence are referred to as type III. Type III clinopyroxenes have flat HREE pattern, but variable LREE values. Three out of the four xenoliths (NFR1119B, NMC1343, NME1110) show a depletion in LREE. In contrast, in xenolith NFK1110, type III clinopyroxenes show a gradual LREE enrichment (Fig. 4.8c) with 4–6 times

Table 7. Trace element concentrations (in ppm) of clinopyroxenes in the studied Nógrád-Gömör wehrlite xenoliths. Given error is 2 σ.

Sample	Textural position	REE type	n	Th	U	Nb	Ta	La	Ce	Pb	Sr
NTB1109	cpx^{free}	type I	10	0.02 ± 0.01	n.d.	0.34 ± 0.05	0.04 ± 0.01	1.90 ± 0.33	6.39 ± 0.80	0.15 ± 0.03	74.2 ± 6.4
	cpx^{vermsp}		4	0.03 ± 0.01	0.01 ± 0.01	n.d.	n.d.	1.40 ± 0.20	4.82 ± 0.87	n.d.	64.2 ± 5.6
	cpx^{opx}		15	0.03 ± 0.01	0.01 ± 0.01	0.42 ± 0.13	0.04 ± 0.01	1.88 ± 0.24	5.95 ± 0.82	0.16 ± 0.08	74.4 ± 4.2
NTB1120	cpx^{free}	type I	15	0.04 ± 0.02	0.02 ± 0.01	0.26 ± 0.18	0.05 ± 0.03	5.10 ± 0.74	15.5 ± 1.6	0.16 ± 0.08	127 ± 17
	cpx^{vermsp}		4	0.03 ± 0.01	0.02 ± 0.01	0.23 ± 0.05	0.02 ± 0.01	4.81 ± 0.43	15.8 ± 1.5	0.16 ± 0.08	113 ± 19
	cpx^{opx}		13	0.04 ± 0.01	0.01 ± 0.01	0.25 ± 0.11	0.04 ± 0.02	4.67 ± 0.59	16.4 ± 1.0	0.13 ± 0.03	119 ± 12
NFK1110	cpx^{free}	type I	23	0.05 ± 0.02	0.01 ± 0.01	0.26 ± 0.12	0.03 ± 0.02	3.26 ± 0.65	10.7 ± 1.6	0.11 ± 0.03	87.1 ± 4.9
	cpx^{opx}		5	0.04 ± 0.02	0.01 ± 0.01	0.36 ± 0.14	0.05 ± 0.03	3.02 ± 0.62	10.2 ± 1.51	0.11 ± 0.06	84.3 ± 8.8
	cpx^{free}	type III	10	0.08 ± 0.02	0.02 ± 0.01	0.10 ± 0.05	0.01 ± 0.01	3.85 ± 0.30	9.41 ± 0.97	0.12 ± 0.02	74.5 ± 4.5
NFK1137A	cpx^{free}	type I	11	0.06 ± 0.02	0.02 ± 0.01	0.50 ± 0.11	0.09 ± 0.02	3.11 ± 0.32	9.83 ± 0.73	0.12 ± 0.01	75.8 ± 1.4
	cpx^{vermsp}		11	0.07 ± 0.02	0.02 ± 0.01	0.52 ± 0.20	0.11 ± 0.04	3.41 ± 0.58	11.2 ± 1.6	0.09 ± 0.09	78.2 ± 5.3
NFR1117A	cpx^{free}	type I	12	0.03 ± 0.01	0.01 ± 0.01	0.26 ± 0.20	0.04 ± 0.03	2.62 ± 0.68	9.03 ± 2.14	0.11 ± 0.05	84.7 ± 7.7
	cpx^{opx}		9	0.06 ± 0.04	0.01 ± 0.01	0.22 ± 0.19	0.02 ± 0.02	2.76 ± 0.53	8.63 ± 1.57	0.16 ± 0.05	78.3 ± 16.5
	cpx^{free}	type II	8	0.05 ± 0.03	0.02 ± 0.01	0.16 ± 0.07	0.01 ± 0.01	2.27 ± 0.59	7.04 ± 0.83	0.10 ± 0.01	56.8 ± 8.1
NFR1119B	cpx^{free}	type III	18	0.03 ± 0.01	0.02 ± 0.01	0.19 ± 0.02	0.04 ± 0.01	0.97 ± 0.32	3.74 ± 1.10	0.19 ± 0.09	55.1 ± 11.3
	cpx^{opx}	type I	6	0.03 ± 0.01	0.01 ± 0.01	0.26 ± 0.11	0.04 ± 0.01	1.88 ± 0.45	6.11 ± 0.83	0.22 ± 0.11	87.1 ± 15.1
NMC1302B	cpx^{free}	type II	16	0.05 ± 0.01	0.01 ± 0.01	0.22 ± 0.11	0.03 ± 0.02	3.06 ± 0.25	9.06 ± 0.57	0.12 ± 0.03	68.5 ± 5.9
	cpx^{opx}		6	0.03 ± 0.02	0.01 ± 0.01	0.43 ± 0.31	0.05 ± 0.04	2.32 ± 0.86	8.33 ± 2.36	n.d.	74.1 ± 9.5
NMC1343	cpx^{free}	type I	34	0.15 ± 0.09	0.05 ± 0.03	0.39 ± 0.18	0.06 ± 0.03	3.64 ± 0.77	10.8 ± 2.3	0.15 ± 0.07	79.7 ± 15.0
	cpx^{free}	type III	2	0.06 ± 0.03	0.01 ± 0.01	0.42 ± 0.21	0.04 ± 0.01	1.74 ± 0.17	5.80 ± 0.30	0.16 ± 0.08	66.5 ± 1.7
NMM1114	cpx^{free}	type I	17	0.07 ± 0.03	0.03 ± 0.01	0.56 ± 0.25	0.07 ± 0.03	3.00 ± 0.84	10.2 ± 2.4	0.22 ± 0.09	82.9 ± 20.9
	cpx^{opx}		14	0.06 ± 0.02	0.02 ± 0.01	0.53 ± 0.44	0.10 ± 0.05	2.14 ± 0.75	7.65 ± 2.52	0.19 ± 0.04	69.5 ± 11.4
NMM1129	cpx^{free}	type I	9	0.07 ± 0.04	0.03 ± 0.01	0.80 ± 0.31	0.17 ± 0.06	4.79 ± 1.58	15.4 ± 3.6	0.26 ± 0.13	98.5 ± 21.9
	cpx^{free}	type II	8	0.05 ± 0.01	0.02 ± 0.01	0.08 ± 0.04	0.01 ± 0.01	1.51 ± 0.16	4.25 ± 0.47	0.09 ± 0.02	39.2 ± 2.0
NME1110	cpx^{free}	type I	16	0.07 ± 0.03	0.02 ± 0.01	0.42 ± 0.21	0.06 ± 0.04	2.91 ± 0.77	9.33 ± 2.39	0.38 ± 0.32	81.0 ± 12.1
	cpx^{free}	type II	3	0.06 ± 0.01	0.02 ± 0.01	0.40 ± 0.33	0.03 ± 0.01	1.72 ± 0.08	5.09 ± 0.69	n.d.	53.8 ± 4.9
	cpx^{free}	type III	3	0.07 ± 0.01	0.03 ± 0.01	0.11 ± 0.55	n.d.	0.62 ± 0.24	2.23 ± 0.47	n.d.	32.8 ± 2.2
NME1129D	cpx^{free}	type I	16	0.07 ± 0.04	0.03 ± 0.02	0.64 ± 0.19	0.09 ± 0.06	3.59 ± 0.85	12.2 ± 2.1	0.15 ± 0.08	86.9 ± 10.3
	cpx^{vermsp}		6	0.11 ± 0.04	0.03 ± 0.02	0.66 ± 0.19	0.13 ± 0.06	3.96 ± 0.85	13.0 ± 2.1	0.20 ± 0.10	89.7 ± 10.3

Table 7. Continued

Sample	Textural position	Pr	Nd	Hf	Zr	Sm	Eu	Gd	Tb	Ti	Dy
NTB1109	cpx^{free}	1.04 ± 0.13	5.45 ± 0.78	0.33 ± 0.14	9.57 ± 3.37	1.50 ± 0.22	0.55 ± 0.10	1.67 ± 0.25	0.24 ± 0.05	2682 ± 863	1.66 ± 0.34
	cpx^{vermsp}	0.72 ± 0.10	4.11 ± 0.71	0.27 ± 0.07	6.98 ± 2.31	1.32 ± 0.08	0.46 ± 0.07	1.51 ± 0.24	0.24 ± 0.04	1892 ± 207	1.67 ± 0.48
	cpx^{opx}	1.00 ± 0.15	5.07 ± 0.66	0.29 ± 0.14	9.35 ± 3.19	1.47 ± 0.39	0.61 ± 0.12	1.62 ± 0.30	0.26 ± 0.05	2560 ± 698	1.60 ± 0.21
NTB1120	cpx^{free}	2.38 ± 0.19	11.3 ± 1.1	0.58 ± 0.33	19.1 ± 8.7	2.73 ± 0.48	0.96 ± 0.14	2.41 ± 0.27	0.36 ± 0.08	1713 ± 646	2.37 ± 0.42
	cpx^{vermsp}	2.27 ± 0.11	10.9 ± 0.6	0.55 ± 0.19	18.5 ± 3.9	2.42 ± 0.19	0.97 ± 0.02	2.56 ± 0.14	0.39 ± 0.04	1678 ± 554	2.56 ± 0.14
	cpx^{opx}	2.48 ± 0.17	11.9 ± 1.1	0.67 ± 0.35	21.3 ± 7.1	2.71 ± 0.42	1.02 ± 0.09	2.54 ± 0.40	0.36 ± 0.06	2123 ± 688	2.27 ± 0.28
NFK1110	cpx^{free}	1.76 ± 0.19	8.90 ± 0.97	0.67 ± 0.19	19.6 ± 4.3	2.31 ± 0.34	0.87 ± 0.11	2.49 ± 0.32	0.40 ± 0.06	2942 ± 1085	2.75 ± 0.43
	cpx^{opx}	1.71 ± 0.23	8.77 ± 1.64	0.61 ± 0.32	20.0 ± 9.9	2.42 ± 0.48	0.89 ± 0.11	2.58 ± 0.43	0.39 ± 0.08	3235 ± 1095	2.55 ± 0.55
	cpx^{free}	1.29 ± 0.15	5.69 ± 0.59	0.93 ± 0.12	24.7 ± 2.2	1.68 ± 0.32	0.61 ± 0.05	1.95 ± 0.21	0.35 ± 0.04	1428 ± 399	2.53 ± 0.30
NFK1137A	cpx^{free}	1.73 ± 0.18	9.45 ± 1.26	1.45 ± 0.43	35.0 ± 8.8	2.71 ± 0.33	0.93 ± 0.14	2.83 ± 0.61	0.42 ± 0.05	6513 ± 1394	2.85 ± 0.54
	cpx^{vermsp}	1.93 ± 0.24	10.5 ± 1.4	1.66 ± 0.35	38.9 ± 7.3	3.18 ± 0.34	1.02 ± 0.12	3.20 ± 0.46	0.46 ± 0.07	7588 ± 1008	2.93 ± 0.28
NFR1117A	cpx^{free}	1.47 ± 0.33	7.44 ± 1.95	0.44 ± 0.26	12.4 ± 6.3	1.94 ± 0.45	0.79 ± 0.13	1.93 ± 0.37	0.28 ± 0.06	2641 ± 660	1.83 ± 0.31
	cpx^{opx}	1.31 ± 0.18	6.33 ± 0.73	0.39 ± 0.16	11.7 ± 4.5	1.71 ± 0.26	0.68 ± 0.08	1.81 ± 0.28	0.33 ± 0.05	1895 ± 248	2.23 ± 0.33
	cpx^{free}	1.16 ± 0.13	6.09 ± 0.97	0.56 ± 0.10	12.1 ± 3.0	1.95 ± 0.31	0.78 ± 0.11	2.70 ± 0.49	0.49 ± 0.10	3972 ± 1733	3.49 ± 0.71
NFR1119B	cpx^{free}	0.63 ± 0.17	3.08 ± 0.60	0.46 ± 0.10	14.4 ± 3.0	1.11 ± 0.21	0.43 ± 0.07	1.43 ± 0.23	0.26 ± 0.05	2065 ± 286	1.81 ± 0.28
	cpx^{opx}	1.00 ± 0.19	5.08 ± 0.84	0.23 ± 0.07	8.00 ± 3.15	1.40 ± 0.09	0.54 ± 0.09	1.38 ± 0.31	0.21 ± 0.04	2339 ± 466	1.39 ± 0.26
NMC1302B	cpx^{free}	1.36 ± 0.17	6.67 ± 1.35	0.87 ± 0.13	23.9 ± 2.5	1.90 ± 0.45	0.75 ± 0.13	2.28 ± 0.50	0.40 ± 0.06	2303 ± 1377	2.78 ± 0.33
	cpx^{opx}	1.45 ± 0.31	7.49 ± 1.89	0.54 ± 0.33	14.3 ± 8.7	2.37 ± 0.45	0.94 ± 0.14	2.61 ± 0.54	0.46 ± 0.10	4027 ± 751	3.17 ± 0.64
NMC1343	cpx^{free}	1.73 ± 0.41	8.80 ± 1.94	1.09 ± 0.24	33.4 ± 6.5	2.47 ± 0.43	0.86 ± 0.15	2.74 ± 0.52	0.43 ± 0.09	3894 ± 1340	2.75 ± 0.55
	cpx^{free}	1.04 ± 0.05	6.37 ± 0.15	0.72 ± 0.07	16.3 ± 0.3	2.27 ± 0.02	0.70 ± 0.09	2.45 ± 0.13	0.45 ± 0.04	5392 ± 501	2.65 ± 0.20
NMM1114	cpx^{free}	1.63 ± 0.37	8.03 ± 1.57	0.80 ± 0.27	25.1 ± 9.5	2.30 ± 0.38	0.83 ± 0.17	2.45 ± 0.47	0.38 ± 0.05	3658 ± 1620	2.47 ± 0.28
	cpx^{opx}	1.25 ± 0.34	6.59 ± 1.93	0.62 ± 0.48	16.1 ± 10.8	2.19 ± 0.98	0.73 ± 0.17	2.10 ± 0.63	0.33 ± 0.09	4219 ± 1852	2.04 ± 0.51
NMM1129	cpx^{free}	2.71 ± 0.48	14.8 ± 1.1	1.96 ± 0.46	47.9 ± 12.0	4.21 ± 0.55	1.39 ± 0.19	4.25 ± 0.48	0.61 ± 0.09	8283 ± 6011	4.15 ± 0.44
	cpx^{free}	0.67 ± 0.06	3.78 ± 0.26	0.89 ± 0.08	28.3 ± 1.4	1.40 ± 0.19	0.56 ± 0.06	1.94 ± 0.22	0.34 ± 0.02	1944 ± 137	2.64 ± 0.14
NME1110	cpx^{free}	1.49 ± 0.40	7.76 ± 2.13	0.68 ± 0.36	21.5 ± 9.9	2.17 ± 0.51	0.79 ± 0.15	2.36 ± 0.55	0.36 ± 0.08	4406 ± 1505	2.38 ± 0.46
	cpx^{free}	0.76 ± 0.06	4.57 ± 0.24	0.64 ± 0.15	18.1 ± 3.4	1.53 ± 0.33	0.60 ± 0.02	2.22 ± 0.07	0.33 ± 0.02	2756 ± 439	2.60 ± 0.35
	cpx^{free}	0.41 ± 0.06	2.68 ± 0.42	0.75 ± 0.05	20.4 ± 0.5	1.16 ± 0.02	0.49 ± 0.06	1.65 ± 0.32	0.33 ± 0.03	2005 ± 36	2.67 ± 0.16
NME1129D	cpx^{free}	1.99 ± 0.36	10.6 ± 1.9	1.14 ± 0.60	33.1 ± 15.0	3.01 ± 0.57	1.04 ± 0.28	3.20 ± 1.06	0.43 ± 0.12	6820 ± 2814	2.68 ± 0.64
	cpx^{vermsp}	2.17 ± 0.36	10.6 ± 1.9	1.33 ± 0.60	34.4 ± 15.0	3.13 ± 0.57	1.02 ± 0.28	3.07 ± 1.06	0.44 ± 0.12	6933 ± 2814	2.95 ± 0.64
	cpx^{opx}	1.67 ± 0.20	8.63 ± 1.23	0.56 ± 0.34	18.3 ± 8.8	2.40 ± 0.76	0.84 ± 0.13	2.33 ± 0.54	0.34 ± 0.07	3675 ± 1532	2.08 ± 0.43

Table 7. Continued

Sample	Textural position	Ho	Y	Er	Tm	Yb	Lu	Sc	V
NTB1109	cpx^{free}	0.34 ± 0.06	8.46 ± 0.80	0.88 ± 0.20	0.14 ± 0.03	0.88 ± 0.19	0.13 ± 0.03	27.2 ± 9.6	241 ± 20
	cpx^{vermsp}	0.34 ± 0.06	9.05 ± 1.07	1.11 ± 0.22	0.12 ± 0.01	0.95 ± 0.23	0.13 ± 0.01	42.5 ± 2.8	258 ± 21
	cpx^{opx}	0.34 ± 0.08	8.76 ± 1.28	0.97 ± 0.19	0.13 ± 0.03	0.84 ± 0.22	0.13 ± 0.04	30.3 ± 12.1	232 ± 18
NTB1120	cpx^{free}	0.49 ± 0.10	11.9 ± 1.7	1.34 ± 0.19	0.19 ± 0.05	1.29 ± 0.22	0.17 ± 0.03	32.5 ± 3.7	224 ± 40
	cpx^{vermsp}	0.50 ± 0.04	12.6 ± 0.3	1.38 ± 0.05	0.19 ± 0.01	1.31 ± 0.14	0.19 ± 0.02	29.8 ± 1.6	221 ± 25
	cpx^{opx}	0.44 ± 0.07	11.1 ± 1.2	1.23 ± 0.13	0.17 ± 0.02	1.17 ± 0.11	0.16 ± 0.02	30.5 ± 2.5	225 ± 35
NFK1110	cpx^{free}	0.55 ± 0.09	14.0 ± 2.3	1.58 ± 0.30	0.22 ± 0.04	1.49 ± 0.25	0.21 ± 0.04	33.1 ± 3.4	253 ± 61
	cpx^{opx}	0.49 ± 0.09	12.9 ± 2.2	1.41 ± 0.20	0.19 ± 0.04	1.26 ± 0.17	0.19 ± 0.02	33.5 ± 2.6	249 ± 40
	cpx^{free}	0.56 ± 0.06	13.9 ± 1.4	1.67 ± 0.24	0.24 ± 0.02	1.62 ± 0.13	0.23 ± 0.03	29.9 ± 3.1	183 ± 18
NFK1137A	cpx^{free}	0.51 ± 0.07	13.0 ± 1.6	1.40 ± 0.19	0.17 ± 0.07	1.20 ± 0.22	0.16 ± 0.02	44.2 ± 3.0	276 ± 12
	cpx^{vermsp}	0.55 ± 0.08	13.0 ± 1.2	1.28 ± 0.18	0.19 ± 0.07	1.17 ± 0.39	0.17 ± 0.06	39.9 ± 2.4	291 ± 16
NFR1117A	cpx^{free}	0.37 ± 0.08	9.0 ± 1.3	1.00 ± 0.19	0.14 ± 0.02	0.94 ± 0.19	0.14 ± 0.03	30.4 ± 6.6	245 ± 31
	cpx^{opx}	0.48 ± 0.06	11.8 ± 1.4	1.31 ± 0.23	0.19 ± 0.03	1.29 ± 0.17	0.18 ± 0.03	34.6 ± 1.5	238 ± 18
	cpx^{free}	0.76 ± 0.16	19.3 ± 4.2	2.18 ± 0.50	0.32 ± 0.06	2.00 ± 0.42	0.28 ± 0.06	42.2 ± 4.7	369 ± 124
NFR1119B	cpx^{free}	0.38 ± 0.08	10.1 ± 1.2	1.12 ± 0.17	0.16 ± 0.06	0.99 ± 0.38	0.16 ± 0.06	34.9 ± 1.6	242 ± 8
	cpx^{opx}	0.30 ± 0.04	7.76 ± 0.53	0.80 ± 0.17	0.11 ± 0.05	0.65 ± 0.28	0.09 ± 0.05	31.1 ± 1.3	215 ± 9
NMC1302B	cpx^{free}	0.59 ± 0.08	14.9 ± 1.9	1.65 ± 0.15	0.24 ± 0.02	1.62 ± 0.16	0.23 ± 0.03	35.6 ± 3.3	236 ± 35
	cpx^{opx}	0.66 ± 0.12	17.6 ± 3.0	1.90 ± 0.32	0.28 ± 0.03	1.71 ± 0.30	0.27 ± 0.06	37.7 ± 1.4	287 ± 22
NMC1343	cpx^{free}	0.55 ± 0.11	14.1 ± 2.4	1.51 ± 0.30	0.21 ± 0.05	1.43 ± 0.32	0.18 ± 0.05	74.1 ± 39.5	265 ± 49
	cpx^{free}	0.59 ± 0.15	14.8 ± 0.1	1.64 ± 0.21	0.21 ± 0.02	1.39 ± 0.04	0.17 ± 0.01	37.2 ± 0.2	320 ± 26
NMM1114	cpx^{free}	0.46 ± 0.10	12.2 ± 1.8	1.28 ± 0.29	0.11 ± 0.05	1.29 ± 0.32	0.18 ± 0.04	34.0 ± 2.2	254 ± 43
	cpx^{opx}	0.43 ± 0.12	10.1 ± 2.6	1.03 ± 0.27	0.16 ± 0.04	1.01 ± 0.29	0.14 ± 0.03	31.1 ± 2.3	255 ± 40
NMM1129	cpx^{free}	0.80 ± 0.11	19.1 ± 2.4	1.94 ± 0.20	0.27 ± 0.05	1.78 ± 0.32	0.23 ± 0.05	34.1 ± 5.8	240 ± 73
	cpx^{free}	0.54 ± 0.03	13.8 ± 0.7	1.54 ± 0.06	0.22 ± 0.02	1.54 ± 0.05	0.20 ± 0.02	35.7 ± 0.4	206 ± 9
NME1110	cpx^{free}	0.45 ± 0.07	11.8 ± 1.7	1.28 ± 0.18	0.18 ± 0.03	1.12 ± 0.16	0.16 ± 0.03	36.4 ± 3.0	258 ± 28
	cpx^{free}	0.48 ± 0.04	13.5 ± 0.7	1.36 ± 0.26	0.19 ± 0.01	1.30 ± 0.08	0.18 ± 0.05	39.1 ± 0.7	256 ± 29
	cpx^{free}	0.58 ± 0.02	14.3 ± 0.4	1.70 ± 0.06	0.24 ± 0.03	1.42 ± 0.08	0.23 ± 0.07	35.9 ± 1.0	235 ± 4
NME1129D	cpx^{free}	0.53 ± 0.15	13.6 ± 2.6	1.45 ± 0.18	0.19 ± 0.03	1.18 ± 0.32	0.18 ± 0.04	29.9 ± 1.1	295 ± 66
	cpx^{vermsp}	0.53 ± 0.15	13.0 ± 2.6	1.33 ± 0.18	0.17 ± 0.03	1.26 ± 0.36	0.17 ± 0.04	29.1 ± 1.1	298 ± 66
	cpx^{opx}	0.41 ± 0.11	10.6 ± 1.3	1.12 ± 0.19	0.16 ± 0.03	1.00 ± 0.19	0.15 ± 0.03	28.3 ± 2.8	233 ± 21

Table 7. Continued

Sample	Textural position	Cr	Co	Ni	ΣREE	La_N/Lu_N	Nd_N/Yb_N
NTB1109	cpx^{free}	7849 ± 1303	25.0 ± 2.9	338 ± 26	22.74	1.55	2.18
	cpx^{vermsp}	8394 ± 1689	24.1 ± 2.5	359 ± 14	18.88	1.11	1.53
	cpx^{opx}	7281 ± 641	24.7 ± 2.3	344 ± 24	21.87	1.51	2.14
NTB1120	cpx^{free}	8614 ± 2769	22.0 ± 2.3	291 ± 57	46.64	3.10	3.10
	cpx^{vermsp}	9015 ± 1871	24.6 ± 5.8	340 ± 95	46.17	2.62	2.92
	cpx^{opx}	8078 ± 2526	21.0 ± 2.0	252 ± 33	47.48	3.03	3.58
NFK1110	cpx^{free}	6159 ± 1338	20.8 ± 1.5	273 ± 26	37.54	1.65	2.11
	cpx^{opx}	7041 ± 1375	24.6 ± 2.0	323 ± 28	36.12	1.67	2.45
	cpx^{free}	4183 ± 310	18.9 ± 1.6	268 ± 31	31.68	1.71	1.24
NFK1137A	cpx^{free}	6429 ± 1020	23.9 ± 1.0	241 ± 24	37.30	2.09	2.77
	cpx^{vermsp}	5864 ± 933	23.9 ± 1.3	229 ± 22	41.18	2.13	3.16
NFR1117A	cpx^{free}	7548 ± 730	21.8 ± 0.8	278 ± 59	29.92	2.10	2.81
	cpx^{opx}	5624 ± 1127	21.2 ± 0.9	340 ± 19	29.23	2.70	1.73
	cpx^{free}	6843 ± 1931	21.5 ± 0.9	324 ± 19	31.49	4.15	1.07
NFR1119B	cpx^{free}	8103 ± 772	21.5 ± 2.4	325 ± 25	16.26	0.64	1.09
	cpx^{opx}	8067 ± 438	25.1 ± 4.8	318 ± 40	20.94	2.18	2.77
NMC1302B	cpx^{free}	5895 ± 528	21.6 ± 0.7	313 ± 15	32.58	1.40	1.46
	cpx^{opx}	7661 ± 547	22.9 ± 0.9	285 ± 12	33.94	0.89	1.54
NMC1343	cpx^{free}	5900 ± 1690	22.0 ± 1.7	308 ± 29	37.74	2.07	2.15
	cpx^{free}	9279 ± 179	21.9 ± 0.6	290 ± 1	27.45	1.05	1.61
NMM1114	cpx^{free}	5964 ± 1997	24.5 ± 3.2	270 ± 51	46.90	1.75	2.19
	cpx^{opx}	5241 ± 1928	26.5 ± 1.6	262 ± 43	27.79	1.60	2.30
NMM1129	cpx^{free}	4760 ± 2208	27.2 ± 7.6	329 ± 72	76.43	2.21	2.94
	cpx^{free}	4273 ± 307	21.4 ± 0.7	324 ± 16	21.13	0.78	0.87
NME1110	cpx^{free}	6809 ± 1306	24.2 ± 2.2	317 ± 44	32.73	1.50	1.02
	cpx^{free}	6617 ± 1238	22.5 ± 1.2	321 ± 16	22.94	1.04	1.24
	cpx^{free}	4977 ± 28	21.6 ± 1.3	359 ± 8	16.40	0.31	0.67
NME1129D	cpx^{free}	4423 ± 2625	23.6 ± 2.0	241 ± 66	42.30	2.08	3.19
	cpx^{vermsp}	4092 ± 2625	25.7 ± 2.0	191 ± 66	43.81	1.69	2.96
	cpx^{opx}	6126 ± 1088	25.1 ± 1.8	271 ± 52	34.30	2.14	3.04

n - number of analyses; n.d. - not detected

cpx^{free} - clinopyroxene withouth orthopyroxene relicts and vermicular spinel; cpx^{opx} - clinopyroxene hosting relict orthopyroxene; cpx^{vermsp} - clinopyroxene hosting vermicular spinel

higher values compared to the PM (McDonough and Sun, 1995). Similar to type II clinopyroxenes, type III clinopyroxenes also show low Nd_N/Yb_N ratios (0.67–1.61) (Table 7).

Neither the average ΣREE value (16–76 ppm), nor the average La_N/Lu_N ratio (0.3–4.2), shows any relationship with the aforementioned grouping. The minimum values for ΣREE and La_N/Lu_N ratio are derived from type III clinopyroxenes in xenoliths NFR1119B and NME1110, respectively (Table 7). In contrast, the maximum values were found in the type I and type II clinopyroxenes of two different samples, namely xenolith NMM1129 and NFR1117A, respectively (Table 7). In general, the higher the ΣREE content, the higher the La_N/Lu_N ratio.

4.4. Whole rock geochemistry

4.4.1. Major element composition

The whole rock compositions of wehrlite xenoliths (Table 8) were determined based on mass balance calculations using the xenolith modal compositional data and the average mineral compositions. In order to avoid obtaining inappropriate values from a non-representative modal composition, the bulk rock composition of xenolith NFR1119B has been calculated using 1.5 vol. % spinel modality.

FeO, MnO, CaO and Na_2O show negative correlations with SiO_2 and MgO, (Fig. 4.9), which agrees with general upper mantle characteristics. The studied wehrlites have homogeneous CaO, Na_2O and MnO contents (2.22–5.10, 0.11–0.27 and 0.16–0.25 wt. %, respectively). In contrast to basaltic elements, compatible NiO shows a positive correlation with MgO.

4.4.2. Rare earth elements + Yttrium

Wehrlite whole rock REY contents were estimated by mass balance calculations and are shown in Table 8. Olivine, spinel and orthopyroxene compositions were estimated from concentrations in clinopyroxene and mineral/cpx partition relationships using $D^{mineral/melt}$ values of Ionov et al. (2002) and references therein. Yttrium results were calculated from Yb data based on their distribution in primitive mantle (Y concentration is ~9.75 times more than Yb concentration) (McDonough and Sun, 1995). Since we do not know the modal abundance of clinopyroxene grains belonging to different trace element types, we applied the average REE concentrations of the most common type I group clinopyroxenes, with the exception of xenolith NMC1302B, where only type II clinopyroxene is present.

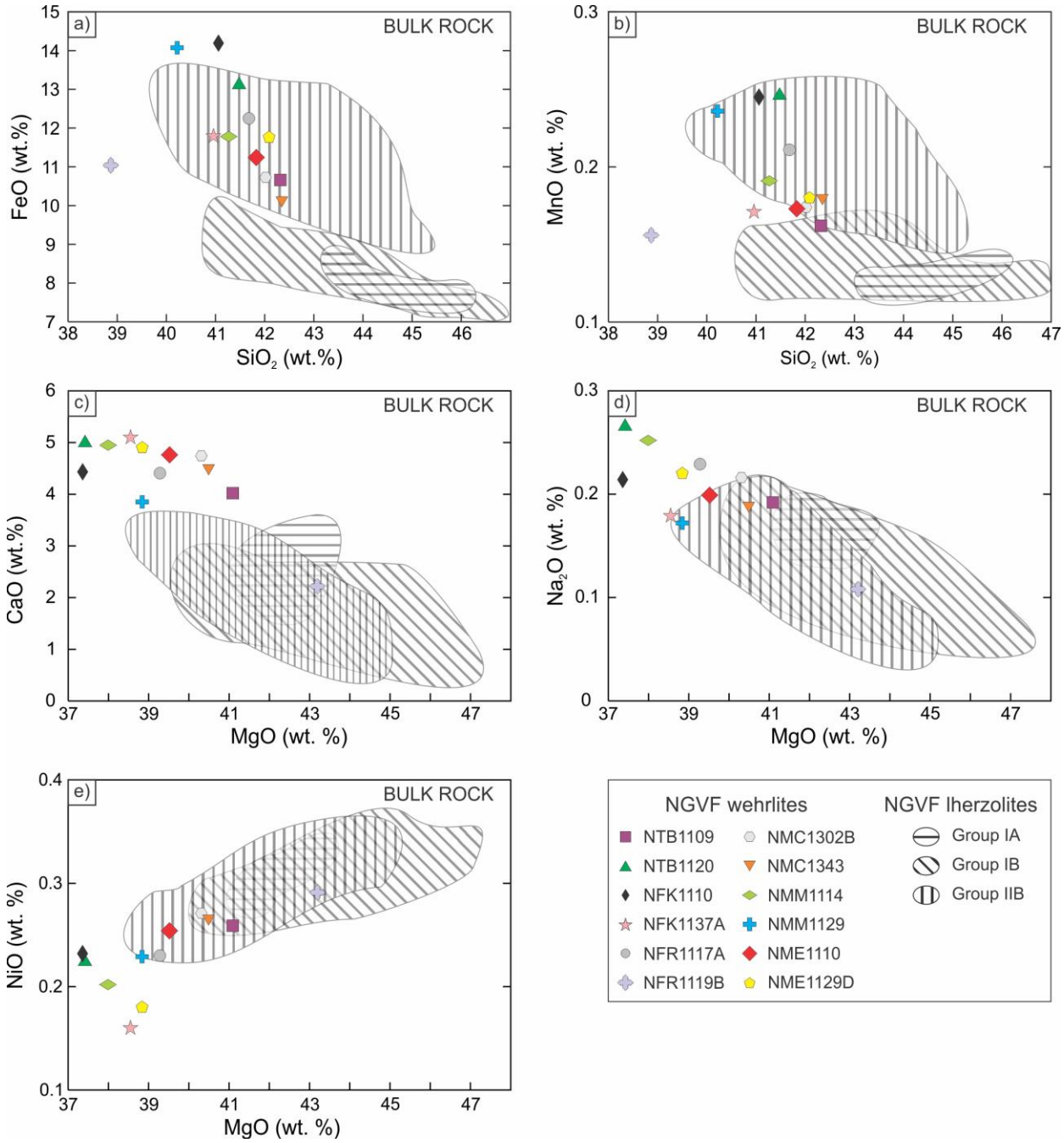

Figure 4.9 Bulk rock relationships of **(a)** SiO_2 vs. FeO **(b)** SiO_2 and MnO **(c)** MgO vs. CaO **(d)** MgO vs. Na_2O **(e)** MgO vs. NiO. Reference lherzolite data are from Liptai et al. (2017).

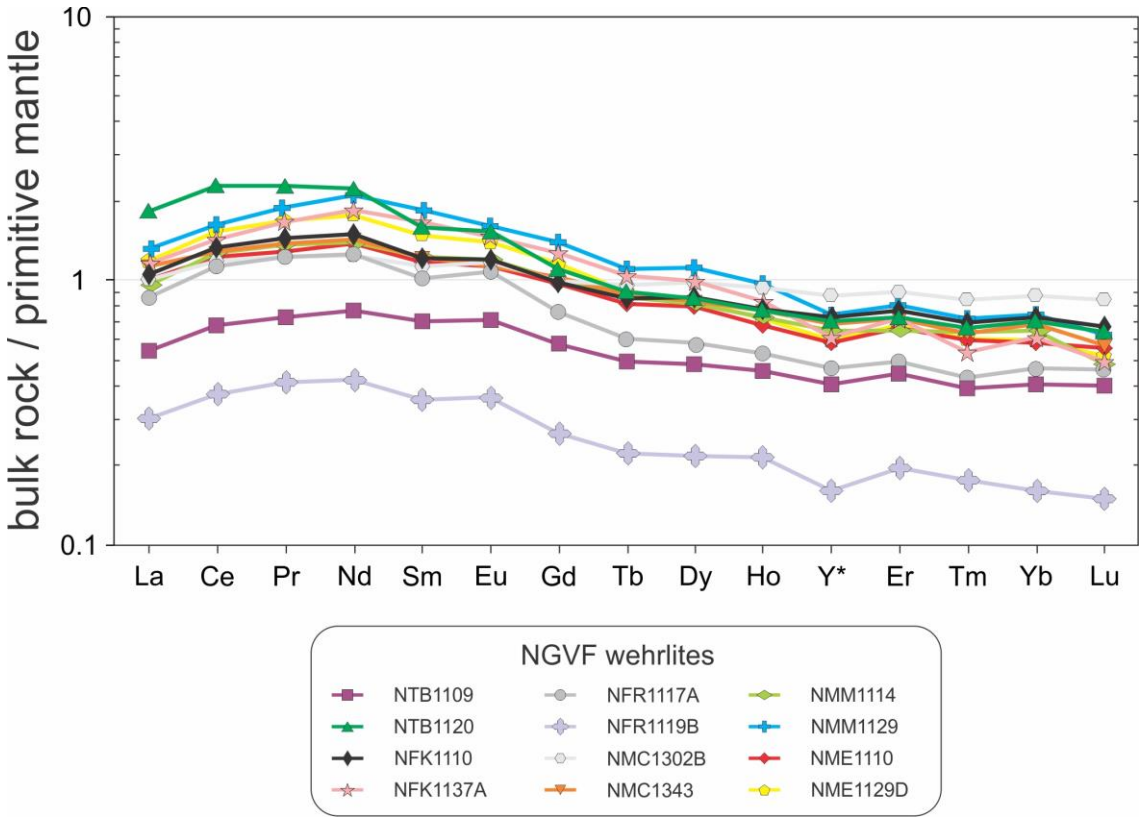

Figure 4.10 Bulk rock trace element distributions of the wehrlite xenoliths. Y* results are calculated from Yb data based on their distrubution in the primitive mantle (Y concentration is ~9.75 times more than Yb concentration) (McDonough and Sun, 1995).

All wehrlites have convex upward REY pattern with a peak dominantly at Nd, or in xenolith NTB1120, at Pr (Fig. 4.10), which is similar to those of clinopyroxene (Fig. 4.8). Most of the wehrlite xenoliths (NTB1120, NFK1110, NFK1137A, NFR1117B, NMC1302B, NMC1343, NMM1114, NMM1129, NME110, NME1129D) have PM normalized LREE contents above 1. In these xenoliths, the ΣREE concentration is between 6.35–11.39 ppm. However, in xenoliths NTB1109 and NFR1119B, all primitive mantle normalized REE values are below 1 and their ΣREE concentrations are the lowest (4.18 and 3.84 ppm, respectively), which coincides with higher MgO, NiO and lower FeO, MnO, CaO, Na_2O whole rock data. The La_N/Lu_N ratio does not differ in the xenoliths and varies within a narrow range of 1.36–2.88.

Table 8. Whole rock major element (wt. %) and trace element (ppm) compositions of the studied xenoliths, calculated with mass balance. Composition of xenolith NFR1119B was estimated assuming 1.5 vol. % spinel modal content.

Sample	NTB1109	NTB1120	NFK1110	NFK1137A	NFR1117A	NFR1119B	NMC1302B	NMC1343	NMM1114	NMM1129	NME1110	NME1129D
SiO_2	42.3	41.5	41.1	41.0	41.7	38.9	42.0	42.4	41.3	40.2	41.8	42.1
TiO_2	0.11	0.12	0.16	0.27	0.11	0.12	0.11	0.21	0.17	0.17	0.21	0.23
Al_2O_3	1.40	1.96	2.26	2.74	1.82	2.98	1.76	1.97	3.08	2.06	1.91	1.91
Cr_2O_3	0.55	0.64	0.48	0.60	0.57	1.88	0.53	0.64	0.61	0.34	0.42	0.39
FeO	10.7	13.1	14.2	11.8	12.2	11.0	10.7	10.1	11.8	14.1	11.2	11.8
MnO	0.16	0.25	0.25	0.17	0.21	0.16	0.17	0.18	0.19	0.24	0.17	0.18
MgO	41.1	37.4	37.4	38.5	39.3	43.2	40.3	40.5	38.0	38.8	39.5	38.8
CaO	4.02	4.99	4.43	5.10	4.41	2.22	4.74	4.50	4.95	3.85	4.76	4.90
Na_2O	0.19	0.27	0.21	0.18	0.23	0.11	0.22	0.19	0.25	0.17	0.20	0.22
NiO	0.26	0.22	0.23	0.16	0.23	0.29	0.27	0.27	0.20	0.23	0.25	0.18
La	0.35	1.19	0.68	0.75	0.56	0.30	0.65	0.74	0.62	0.86	0.65	0.77
Ce	1.12	3.84	2.25	2.41	1.90	0.37	2.00	2.18	2.14	2.74	2.06	2.59
Pr	0.18	0.58	0.37	0.42	0.31	0.41	0.32	0.35	0.35	0.49	0.33	0.43
Nd	0.95	2.79	1.89	2.31	1.58	0.42	1.57	1.79	1.76	2.66	1.73	2.23
Sm	0.28	0.65	0.50	0.68	0.41	0.36	0.46	0.50	0.50	0.75	0.48	0.60
Eu	0.11	0.24	0.19	0.23	0.17	0.36	0.18	0.17	0.19	0.25	0.18	0.22
Gd	0.31	0.60	0.53	0.70	0.41	0.26	0.54	0.56	0.55	0.76	0.52	0.63
Tb	0.05	0.09	0.08	0.10	0.06	0.22	0.09	0.09	0.09	0.11	0.08	0.09
Dy	0.32	0.57	0.58	0.67	0.39	0.22	0.66	0.56	0.55	0.75	0.53	0.56
Ho	0.07	0.11	0.12	0.12	0.08	0.22	0.14	0.11	0.11	0.14	0.10	0.11
Y*	1.73	3.01	3.10	2.62	1.99	0.16	3.74	2.92	2.78	3.20	2.50	2.54
Er	0.19	0.32	0.34	0.31	0.21	0.20	0.40	0.31	0.28	0.35	0.29	0.30
Tm	0.03	0.04	0.05	0.04	0.03	0.18	0.06	0.04	0.04	0.05	0.04	0.04
Yb	0.18	0.31	0.32	0.27	0.20	0.16	0.38	0.30	0.29	0.33	0.26	0.26
Lu	0.03	0.04	0.04	0.03	0.03	0.15	0.06	0.04	0.03	0.04	0.04	0.03
ΣREE	4.18	11.39	7.94	9.06	6.35	3.84	7.50	7.75	7.49	10.28	7.29	8.86

* Y results are calculated from Yb data based on their distrubution in primitive mantle (Y concentration is ~9.75 times more than Yb concentration) (McDonough and Sun, 1995)

4.5. Structural hydroxyl content of the nominally anhydrous minerals (NAMs)

All NAMs were measured with FTIR. However, orthopyroxene grains were inappropriate for analyses due to their small (< 100 μm) size. Moreover, olivines show no structural hydroxyl-related bands. Therefore, only clinopyroxene measurements provide reliable data on their structural hydroxyl contents.

Representative infrared spectra of clinopyroxenes from the wehrlite xenoliths are depicted in Fig. 4.11. The estimated concentrations of structural hydroxyl are listed in Table 9.

Clinopyroxene spectra are classified into three types based on the relative absorption bands of the two most intense bands at ~3630 and ~3525 cm^{-1} (Fig. 4.12; Table 9). Bands at the former position are always present, whereas bands at the latter one are occasionally absent. The three clinopyroxene types (1, 2a and 2b) are defined with quotients of the absorption intensity values of ~3630 and ~3525 cm^{-1} wavenumbers being >1.2 (3630 cm^{-1} dominates), 1.0–1.2 (the two main bands are similar in intensity) and <1.0 (3525 cm^{-1} band dominates), respectively (Fig. 4.12) (Patkó et al., 2019). In most xenoliths, clinopyroxenes belong to type 1 (78 %), whereas type 2a and 2b are present in 9 and 13 %, respectively (Table 9).

In addition to the two main bands, several further bands appear in some of the clinopyroxene spectra (Fig. 4.11; Table 9). In several samples, spectra have shoulders at high wavenumbers (3695–3670 cm^{-1}) (Fig. 4.11). Further weak bands are sometimes present at ~3455–3445 and ~3250–3230 cm^{-1} (Fig. 4.11).

The structural hydroxyl content is mostly inhomogeneous within a single wehrlite with the exception of xenolith NMM1129. This means that there are clinopyroxene grains within individual xenoliths that are poor (21–464 ppm) or rich (202–894 ppm) in structural hydroxyl, with an average of 140 and 481 ppm structural hydroxyl, respectively (Fig. 4.11; Table 9). Based on the aforementioned spectra classification, type 1 clinopyroxenes have higher maximum and average contents of structural hydroxyl (21–894 ppm with an average of 346 ppm) than those with type 2a and type 2b characteristics (53–131 and 60–294 ppm with an average of 92 and 185 ppm, respectively) (Fig. 4.12).

Structural hydroxyl content of olivine and orthopyroxene were estimated in all wehrlites. For this, the analyzed structural hydroxyl content of clinopyroxenes and the partition coefficient of hydrogen between clinopyroxene and other silicates were applied ($D^{cpx/opx}$=2.3; Pintér et al.,

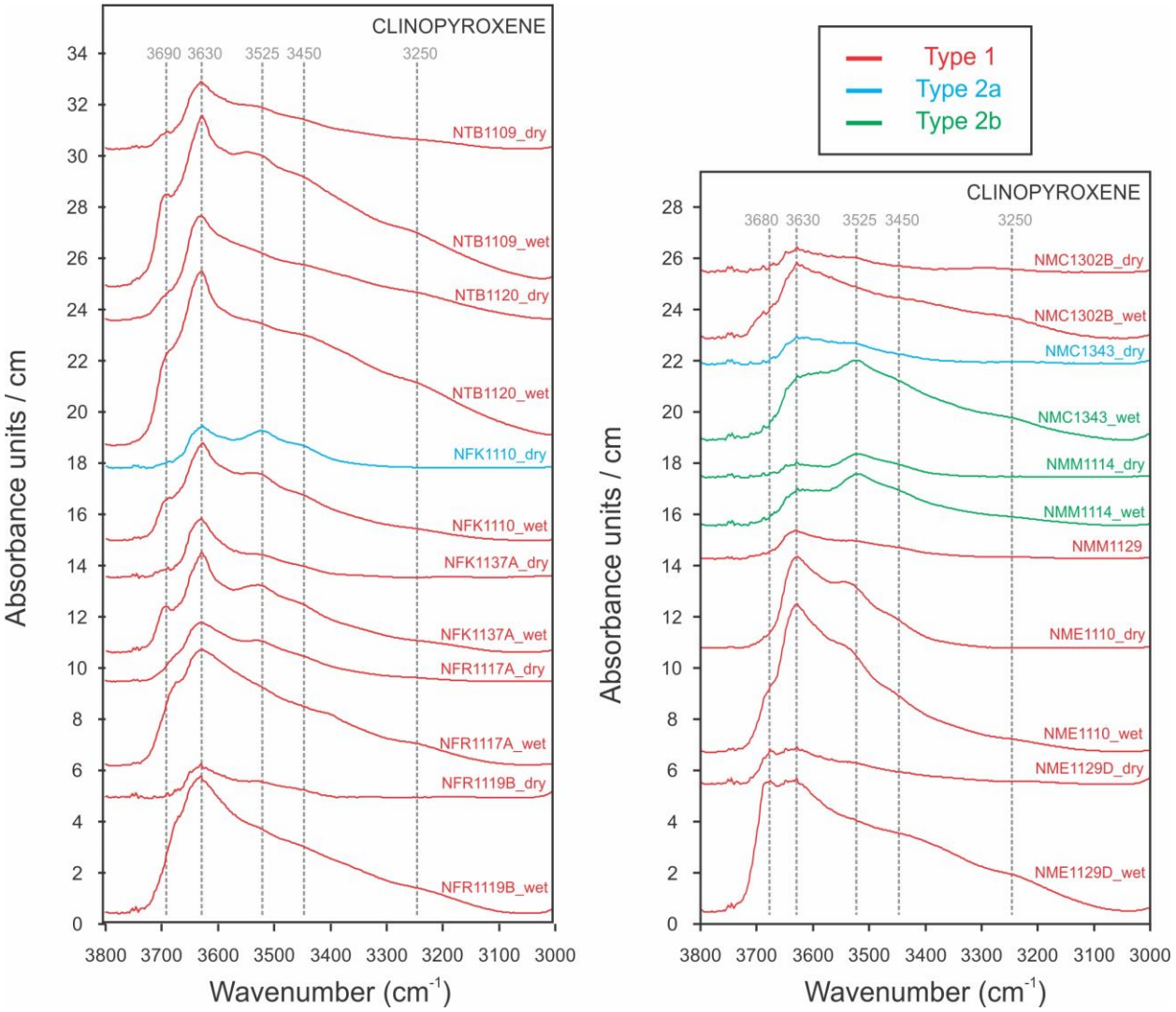

Figure 4.11 Average unpolarized FTIR spectra with classification (Type 1, 2a, 2b) of dry and wet wehrlitic clinopyroxenes.

2015; $D^{cpx/ol}$=10; Xia et al., 2019). The resulting structural hydroxyl contents of orthopyroxenes vary from 9 to 202 ppm (with an average of 65 ppm) and from 88 to 389 ppm (with an average of 214 ppm), whereas those for olivines range from 2 to 46 ppm (with an average of 14 ppm) and from 20 to 89 ppm (with an average of 48 ppm) being in equilibrium with dry and wet clinopyroxene grains, respectively (Table 9).

Two different values were determined for bulk rock structural hydroxyl content. One calculation considers the measured (clinopyroxene) and the estimated (orthopyroxene, olivine) structural hydroxyl content of the mineral constituents weighted by their modal proportion.

Table 9. FTIR characteristics and structural hydroxyl contents (expressed in H_2O equivalent in wt. ppm) of the studied Nógrád-Gömör wehrlite xenoliths.

		Clinopyroxene				Orthopyroxene	Olivine	Bulk rock[0]	Bulk rock[1]
Xenolith	**Inhomogeneity groups**	**Absorption bands**	**Analyzed grains**	**Spectrum type**	**H_2O (ppm)**	**H_2O (ppm)**	**H_2O (ppm)**	**H_2O (ppm)**	**H_2O (ppm)**
NTB1109	dry	3689*, 3629, 3524, 3450'	9	1	227[#]	99[$]	23"	62	43
	wet	3691*, 3628, 3527, 3446', 3251'	3	1	836[#]	363[$]	84"	227	159
NTB1120	dry	3693*, 3631, 3444'	3	1	464[#]	202[$]	46"	146	111
	wet	3687*, 3630, 3526', 3447', 3245'	2	1	894[#]	389[$]	89"	281	215
NFK1110	dry	3687*, 3630, 3524, 3450'	14	2a	131[#]	57[$]	13"	37	27
	wet	3688*, 3628, 3526, 3447'	2	1	363[#]	158[$]	36"	102	75
NFK1137A	dry	3689*, 3633, 3525, 3451'	3	1	109[#]	—	11"	33	25
	wet	3694*, 3631, 3529, 3453'	7	1	360[#]	—	36"	114	83
NFR1117A	dry	3630, 3525	11	1	202	88[$]	20"	58	42
	wet	3675*, 3628, 3401', 3249'	1	1	518[#]	225[$]	52"	150	109
NFR1119B	dry	3631, 3525	4	1	21	9[$]	2"	4	2
	wet	3631	5	1	550	239[$]	55"	102	56
NMC1302B	dry	3629, 3521'	8	1	47	20[$]	5"	14	10
	wet	3693*, 3630	1	1	269[#]	117[$]	27"	80	60
NMC1343	dry	3629, 3526	8	2a	53	23[$]	5"	15	11
	wet	3627, 3523	1	2b	294	128[$]	29"	82	59
NMM1114	dry	3530, 3522	3	2b	59	26[$]	6"	18	14
	wet	3628, 3522	5	2b	202	88[$]	20"	62	47
NMM1129	dry	3630, 3526	4	1	82	—	8"	21	14
NME1110	dry	3629, 3528, 3451'	5	1	206[x]	90[$]	21"	62	46
	wet	3687*, 3629, 3528	7	1	431[#]	187[$]	43"	128	95
NME1129D	dry	3678*, 3631, 3527	3	1	75.0[#]	33[$]	8"	23	17
	wet	3683*, 3633, 3427, 3248	10	1	573[#]	249[$]	57"	176	132

"weak band; *hydrous lamella; [#]slightly overestimated results; [x]similar orientation in most of the grains; [$]the structural hydroxyl content of orthopyroxenes was estimated using the structural hydroxyl content of the clinopyroxenes and the hydrogen partition coefficient between the clinopyroxene and orthopyroxene ($D^{cpx/opx}$=2.3; Pintér et al., 2015); "the structural hydroxyl content of olivines was estimated using the structural hydroxyl content of the clinopyroxenes and the hydrogen partition coefficient between the clinopyroxene and olivine ($D^{cpx/ol}$=10; Xia et al., 2019); [0]based on the measured structural hyroxyl contents of clinopyroxenes and estimated structural hydroxyl contents of orthopyroxenes and olivines; [1]based only on the measured structural hyroxyl contents of clinopyroxenes

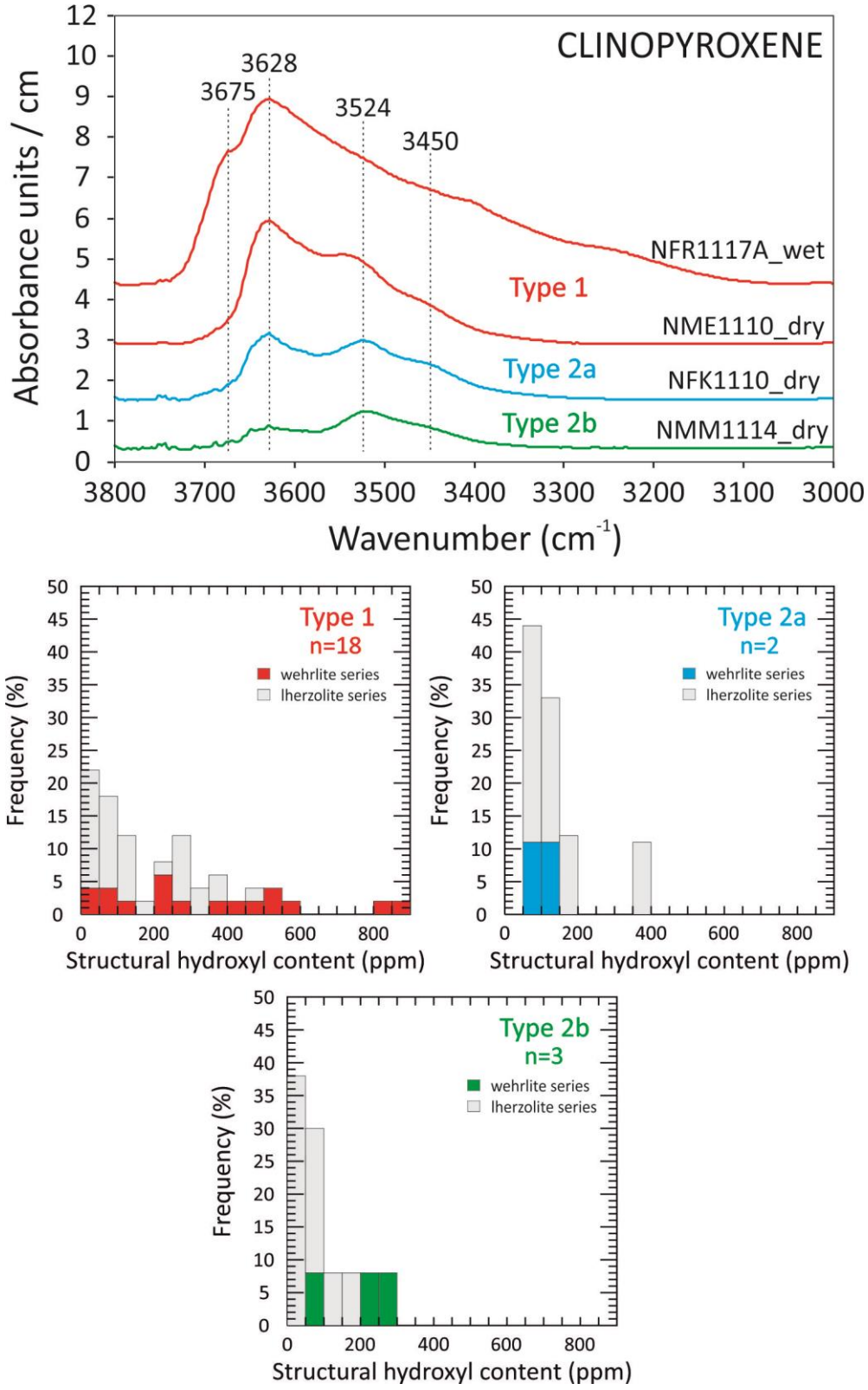

Figure 4.12 Representative average unpolarized FTIR spectrum types of clinopyroxenes from wehrlite xenoliths with accompanying histograms of the structural hydroxyl contents (expressed in H_2O equivalent in wt. ppm). The results of the lherzolitic series are from Patkó et al. (2019).

Accordig to this calculation, the bulk contents of structural hydroxyl range between 4 and 146 ppm (with an average of 41 ppm) for dry and between 62 and 281 ppm (with an average of 137 ppm) for wet grains, respectively (Table 9). The other calculation only takes the measured clinopyroxenes into account, leading to 2–111 ppm (with an average of 30 ppm) and 47–215 ppm (with an average of 99 ppm) ranges for dry and wet grains, respectively (Table 9).

4.6. Estimated electrical resistivity of wehrlites

The electrical resistivity [Ωm] and its reciprocal the conductivity [Sm^{-1}] are important data sources of the structure and composition of the lithosphere. In order to estimate the electrical resistivity of the lithospheric mantle beneath the NGVF including wehrlite, the modified version of the excel worksheet composed by Kovács et al. (2018) was used (Appendix 6). This estimation follows the methodology specified in Fullea (2017). All details including the parameterization follow the steps described in Kovács et al. (2018).

To estimate the resistivity values for NGVF wehrlite xenoliths, the characteristic petrographic and geochemical data of the local mantle are needed in addition to the experimentally derived parameters (e.g., activation enthalpies, pre-exponential terms). Among the required local parameters, the structural hydroxyl content of the nominally anhydrous minerals (NAMs) is probably the most important influencer of the conductivity (Wang et al., 2006; Dai and Karato, 2009; Yoshino et al., 2009; Poe et al., 2010; Yang et al., 2011; Novella et al., 2017). The clinopyroxene, orthopyroxene and olivine can incorporate hydrogen in their structure in decreasing amount, respectively (Bell and Rossman, 1992; Demouchy and Bolfan-Casanova, 2016; Peslier et al., 2017). The analyzed structural hydroxyl contents of wehrlitic clinopyroxenes from Nógrád-Gömör are listed in Table 9, along with the undetectable, hence estimated structural hydroxyl content of orthopyroxenes and olivines.

Further required data are the modal compositions of the xenoliths (Table 2), the X_{Fe} (X_{Fe}=1-Mg#/100) of the silicates (Table 3; 4; 5), equilibrium temperature (Table 2) and pressure. The pressure at the originating depth of the xenoliths is hard to estimate for spinel facies xenoliths. The best approach is to use the alkaline basalt province geotherm (Jones et al., 1983) and the equilibrium temperatures (based on the Ca-in-opx thermometer of Nimis and Grütter (2010) modified after Brey and Köhler (1990)), which allows an estimation for the pressure (Table 2).

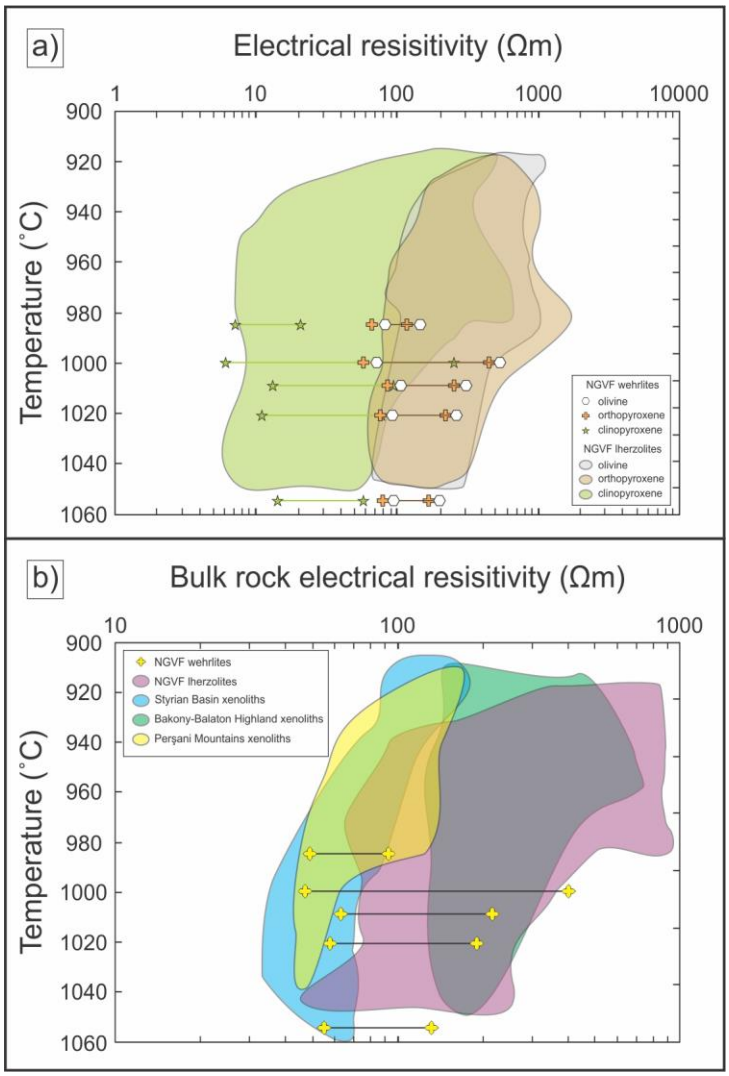

Figure 4.13 (a) Electrical resistivity of the rock-forming minerals (olivine, clinopyroxene, orthopyroxene) of wehrlite xenoliths in the function of equilibrium temperature. The results of dry and wet wehrlitic grains from the same xenoliths are connected with solid lines. The NGVF electrical resisitivity values are from Klébesz et al. (2016). **(b)** Electrical resistivity of of lherzolite and wehrlite bulk rock in the function of equilibrium temperature. The results of dry and wet wehrlitic grains from the same xenoliths are connected with solid lines. Reference data are from Styrian Basin (estimations based on the results of Aradi et al., 2017) Bakony-Balaton Highland (Liptai et al., in prep.) and Perşani Mountains (Kovács et al., 2018; Lange et al., 2019).

The calculated electrical resistivity values are listed in Table 10. The electrical resistivity of the wet and the dry grains of wehrlites were calculated separately (Table 10). In wet grains, resistivity values are the following in decreasing order: olivine (72–106 with an average of 90 Ωm), orthopyroxene (58–86 with an average of 73 Ωm) and clinopyroxene (6–14 with an average of 10 Ωm) (Fig. 4.13a). Dry grains have higher values: 148–538 with an average of 293 Ωm for

olivine, 119–450 with an average of 243 Ωm for orthopyroxene, and 21–253 with an average of 101 Ωm for clinopyroxene (Fig. 4.13a). The bulk rock electrical resistivity calculated using dry grains is 94–406 Ωm (with an average of 208 Ωm), whereas using wet grains it is 47–63 Ωm (with an average of 55 Ωm) (Fig. 4.13b).

Table 10. Electrical resistivity results of the rock forming silicates and bulk rocks of the Nógrád-Gömör wehrlite xenoliths. The values were calculated using the excel worksheet of Kovács et al. (2018) (Supplementary material 3 in the cited publication). Abbreviations: ol - olivine, opx - orthopyroxene, cpx - clinopyroxene, bulk - calculated whole rock.

		Electric resisitivity (Ωm)			
		ol	**opx**	**cpx**	**bulk**
NFR1117A	dry grains	148	119	21	94
	wet grains	83	67	7	49
NFR1119B	dry grains	538	450	253	406
	wet grains	72	58	6	47
NMC1302B	dry grains	310	256	95	217
	wet grains	106	86	13	63
NMC1343	dry grains	267	220	78	192
	wet grains	93	76	11	58
NMM1114	dry grains	202	169	58	133
	wet grains	95	79	14	55

4.7. Sulfide melt inclusions

4.7.1. Sulfide petrography

Sulfides occur as minor modal constituents in the studied wehrlite xenoliths, with ~0.04 vol. % modal presence. Sulfides are consisting of mss (monosulfide solid solution), pentlandite, pyrrhotite and chalcopyrite in various volume fractions (Table 11).

Pyrrhotite is the most common phase in the wehrlites (Fig. 4.14a), whereas mss and pentlandite are less frequent. Chalcopyrite, where it occurs in the thin section, typically forms

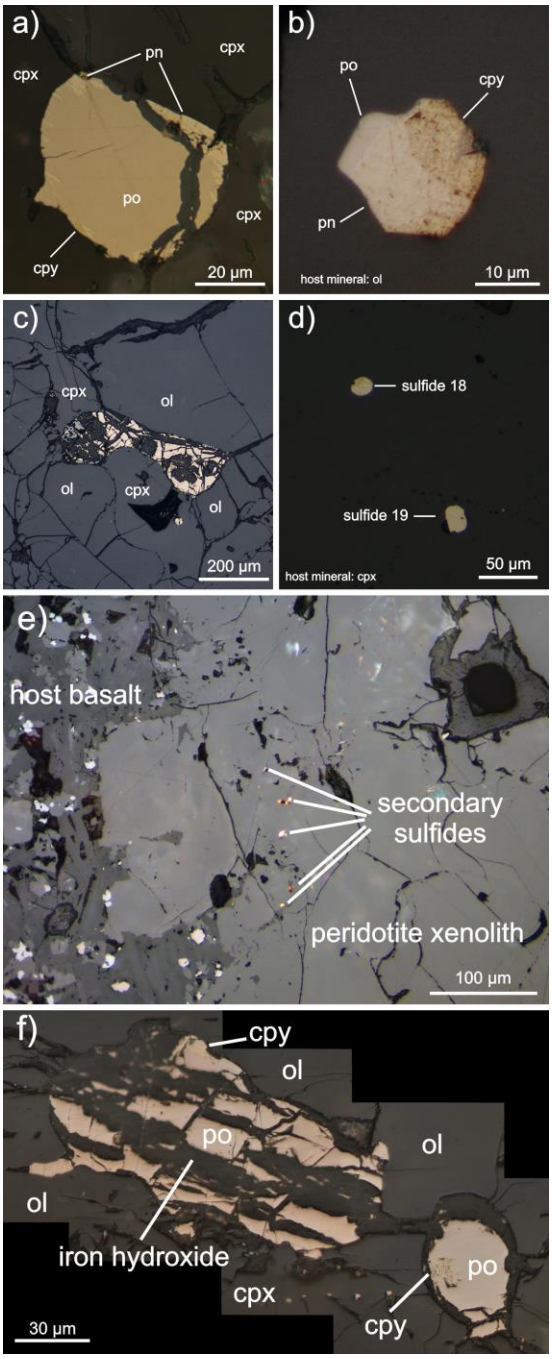

Figure 4.14 Reflected light images of sulfides with different mineral compositions and textural positions from the NGVF wehrlites. **(a)** Typical pyrrhotite-dominated sulfide (sulfide 1f from NTB1120). **(b)** Massive, slightly altered chalcopyrite (cpy) at the edge of the sulfide grain (sulfide 12b from NME1110). **(c)** Interstitial sulfide between silicate grains (sulfide 9 from NME1129D). **(d)** Enclosed sulfides hosted in clinopyroxene (sulfides 18 and 19 from NFK1137A). **(e)** Secondary sulfides situated at the margin of wehrlite xenolith NMM1129. **(f)** Sulfides, partially altered to iron oxyhydroxides, along cracks (sulfide 4 from NME1129D). Abbreviations: mss - monosulfide solid solution; pn - pentlandite; po - pyrrhotite; cpy - chalcopyrite; ol - olivine, cpx - clinopyroxene.

Table 11. Estimated modal compositions of the sulfide grains from the studied Nógrád-Gömör wehrlite xenoliths in vol. %.

			mss	pn	po	cpy
Xenolith	Sulfide grain	Textural position	vol. %			
NTB1109	7	interstitial	—	97	—	3
	12	interstitial	63	37	—	—
	14	interstitial	—	100	—	—
	17	enclosed in ol	—	41	19	40
NTB1109/section 2	3	interstitial	—	—	100	—
	4	interstitial	—	42	58	—
	6	interstitial	—	92	8	—
NTB1120	1e	interstitial	—	52	48	—
	1f	interstitial	—	12	87	1
	1h	interstitial	—	21	79	—
	2	interstitial	—	6	94	—
	6b	interstitial	—	—	100	—
	7a	interstitial	—	—	100	—
	8a	interstitial	—	—	100	—
	8b	interstitial	—	7	92	1
	8d	interstitial	—	42	58	—
	9	interstitial	—	21	79	—
NFK1110	1	enclosed in ol	—	23	77	—
	3	enclosed in cpx	—	35	65	—
NFK1137A	1	enclosed in ol	—	30	49	21
	2	enclosed in ol	20	—	80	—
	3	interstitial	100	—	—	—
NFR1117A	1	interstitial	88	—	—	12
	2	interstitial	100	—	—	—
	3	enclosed in ol	8	—	92	—
	4	interstitial	100	—	—	—
	5	enclosed in cpx	100	—	—	—
	6	interstitial	100	—	—	—
	7	interstitial	100	—	—	—
NFR1119B	1	enclosed in ol	—	30	10	60
	2	enclosed in ol	—	2	85	13
	3	enclosed in ol	—	5	95	—
NMC1302B	1	interstitial	100	—	—	—

Table 11. Continued

Xenolith	Sulfide grain	Textural position	mss	pn	po	cpy
			vol. %			
NMM1114	2	interstitial	100	—	—	—
	3	interstitial	100	—	—	—
	4	interstitial	100	—	—	—
	6	interstitial	82	—	—	18
NMM1129	1	interstitial	—	—	100	—
	2	enclosed in cpx	—	16	78	6
	3	interstitial	100	—	—	—
	4	enclosed in sp	—	8	92	—
	7	enclosed in cpx	—	23	77	—
	8	enclosed in ol	96	—	—	4
NME1110	3a	interstitial	100	—	—	
	4	interstitial	95	—	—	5
	13	enclosed in ol	—	31	69	—
NME1110/section 2	3a	interstitial	100	—	—	—
NME1129D	1	enclosed in cpx	—	—	100	—
	3c	interstitial	—	—	96	4
	4	interstitial	—	—	94	6
	5b	interstitial	—	—	97	3
	5c	enclosed in cpx	—	—	86	14
	5d	interstitial	—	—	99	1
	6a	interstitial	—	—	28	72
	7	enclosed in ol	—	—	78	22
	9	interstitial	—	—	100	—
	10a	interstitial	—	—	91	9
	10b	interstitial	—	—	84	16
	10c	interstitial	—	—	100	—
	15	interstitial	—	—	100	—
	16	interstitial	—	—	95	5
	17	interstitial	—	—	38	62

Abbreviations: mss - monosulfid solid solution, pn - pentlandite, po - pyrrhotite, cpy - chalcopyrite, ol - olivine, cpx - clinopyroxene, sp - spinel.

subordinate crystals (1–40 with an average of 17 vol. % of the sulfide grain) predominating in only three sulfide grains (sulfide 1 in NFR1119B and sulfide 6a and 17 in NME1129D) (Table 11). Chalcopyrite grains often appear on the rim of the sulfide grains and are usually slightly altered (Fig. 4.14b).

Sulfides are present in two textural positions: interstitial (i-type) and enclosed (e-type). I-type sulfides are larger (up to 500 μm) with lobate boundaries and typically occur in triple-junctions between rock-forming minerals (Fig. 4.14c). E-type sulfides are usually isometric, rounded or negative crystal-shaped, with a size of 5–80 μm (Fig. 4.14d). The e-type sulfides are hosted mostly in olivine or clinopyroxene, and rarely in spinel. E-type sulfides represent the 27 % out of all sulfides (Table 11).

Tiny (max. 5 μm in diameter) sulfide inclusions along healed fractures close to host basalts were not considered in this study, since they are usually linked to trails of secondary fluid and silicate melt inclusions (Fig. 4.14e). These sulfides have likely been trapped during the ascent of the host magma (e.g., Roedder, 1984). In addition, some sulfides are altered to iron hydroxides, especially along cracks (Fig. 4.14f), these grains were also omitted from the study.

4.7.2. Sulfide geochemistry

4.7.2.1. Major elements

The major element composition of sulfides in wehrlite xenoliths are summarized in Table 12. The average Fe content of pyrrhotites and Cu content of chalcopyrites are the following: 55.9±3.1 wt. % and 32.5±2.5 wt. %, respectively. The Fe content is uniform in mss and pentlandite from wehrlite (with an average of 48.9±3.2 and 31.9±2.6 wt. %, respectively). Similarly, the Ni content is constant in mss and pentlandites with an average of 11.1±3.4 and 32.3±3.5 wt. %, respectively.

Bulk compositions of the studied sulfides were determined using mass-balance calculations (Table 13; Fig. 4.15; 4.16). The sulfides are Fe-rich (49.4±6.6 wt. %) and Ni-poor (9.6±7.4 wt. %). The Co content, indicating positive correlation with that of Ni, is ranging from 0.01–0.59 with an average of 0.14 wt. %, whereas the Cu concentration varies from 0.01–24.2 with an average of 2.4 wt. % in the sulfides. There are frequently significant variations (10–15 wt. %) in Fe and Ni

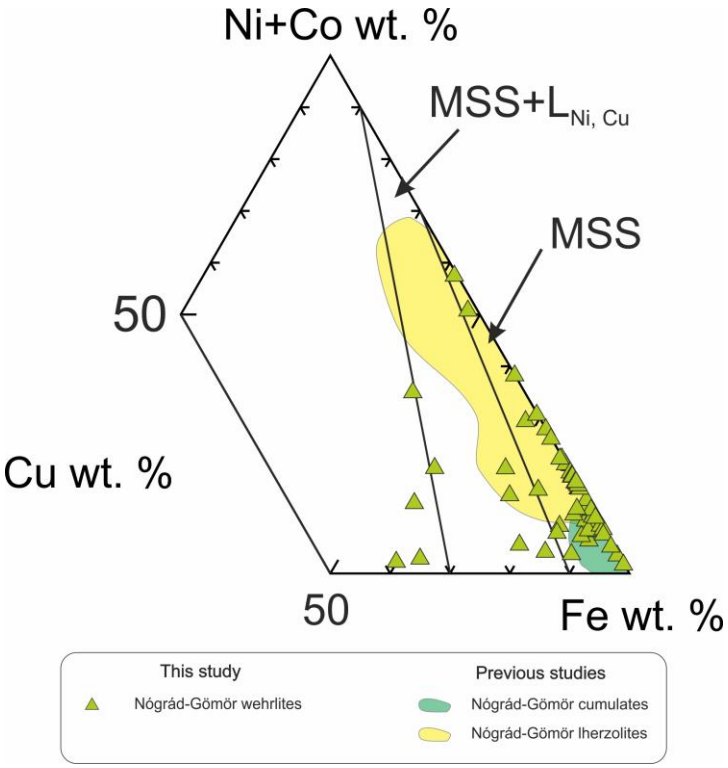

Figure 4.15 Composition of sulfides from wehrlites depicted in the Cu-Ni+Co-Fe system. The stability relations were determined by the experiments of Craig and Kullerrud (1969) carried out at 1000 ˚C. The fields of the Nógrád-Gömör lherzolites and cumulates are from Szabó and Bodnar (1995), Szabó et al. (2019) and Zajacz and Szabó (2003). Mss and L_{Ni+Cu} denote the monosulfide solid solution and Ni- and Cu-rich liquid phase, respectively.

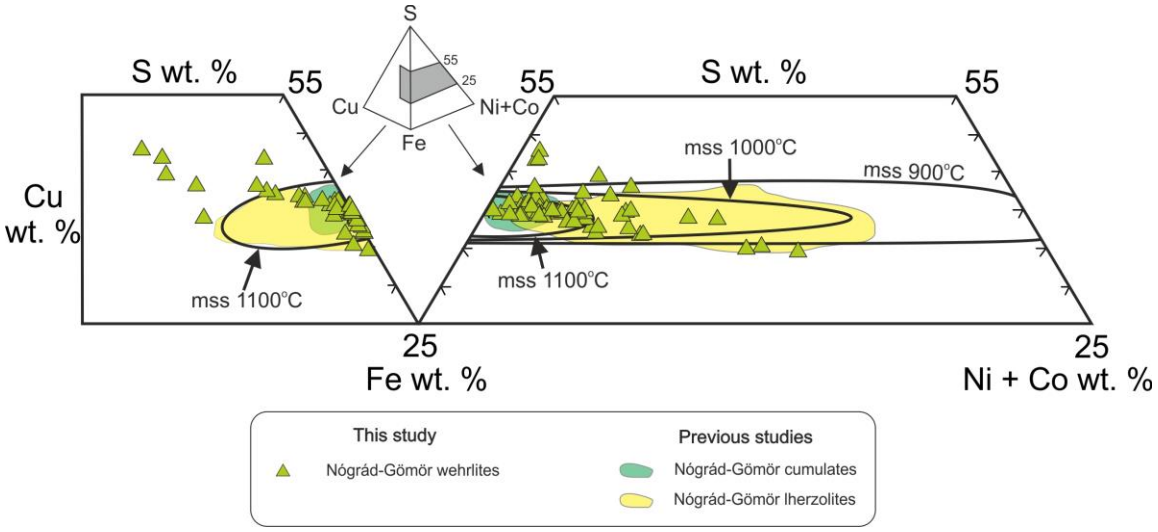

Figure 4.16 Composition of sulfides from wehrlites depicted in the Cu-S-Fe-Ni+Co system. The stability fields are based on the experiments of Kullerud et al. (1969). The fields of Nógrád-Gömör lherzolites and cumulates are from Szabó and Bodnar (1995), Szabó et al. (2019) and Zajacz and Szabó (2003). Mss is monosulfide solid solution.

Table 12. Major element compositions of different phases (in wt. %) appearing in sulfide grains based on electron microprobe analyses in the studied Nógrád-Gömör wehrlite xenoliths.

Xenolith	Sulfide grain	Textural position	Mineral phase	Co	S	Ni	Fe	Cu	Total
NTB1109	7	interstitial	pentlandite	0.24	34.6	34.4	31.6	n.d.	100.84
	7	interstitial	pentlandite	0.25	34.8	33.7	31.6	0.05	100.40
	12	interstitial	pentlandite	0.23	37.3	30.2	33.3	n.d.	101.03
	12	interstitial	mss	0.05	40.0	19.4	41.5	0.05	101.00
	14	interstitial	pentlandite	0.19	34.5	38.0	28.2	0.37	101.26
	17	enclosed in ol	pyrrhotite	n.d.	39.8	2.15	58.1	n.d.	100.05
	17	enclosed in ol	pentlandite	0.34	36.2	29.5	32.5	n.d.	98.54
	17	enclosed in ol	chalcopyrite	n.d.	35.7	0.24	30.4	35.7	102.04
NTB1109/ section 2	3	interstitial	pyrrhotite	n.d.	38.7	2.15	57.4	0.11	98.36
	3	interstitial	pyrrhotite	0.03	38.1	6.55	54.6	0.50	99.78
	4	interstitial	pentlandite	0.69	33.8	34.1	31.6	n.d.	100.19
	4	interstitial	pyrrhotite	0.05	39.2	4.22	54.6	0.04	98.11
	4	interstitial	pyrrhotite	n.d.	39.4	4.49	55.4	n.d.	99.29
	6	interstitial	pentlandite	0.39	34.2	34.0	31.6	n.d.	100.19
	6	interstitial	pyrrhotite	n.d.	39.5	3.77	56.6	n.d.	99.87
NTB1120	1e	interstitial	pyrrhotite	n.d.	39.6	2.94	58.2	0.18	100.92
	1e	interstitial	pentlandite	0.63	33.4	33.7	31.1	n.d.	98.83
	1f	interstitial	pyrrhotite	0.03	40.3	3.78	57.3	0.13	101.54
	1f	interstitial	pentlandite	0.79	34.8	35.0	30.7	n.d.	101.29
	1h	interstitial	pentlandite	0.70	34.8	34.5	30.6	0.04	100.64
	1h	interstitial	pyrrhotite	0.03	39.7	5.10	56.0	0.20	101.03
	2	interstitial	pyrrhotite	n.d.	40.0	3.60	57.3	0.07	100.97
	2	interstitial	pentlandite	1.02	34.5	34.7	31.4	0.03	101.65
	6b	interstitial	pyrrhotite	0.02	40.4	4.95	55.4	0.02	100.79
	7a	interstitial	pyrrhotite	0.01	39.2	1.93	59.1	0.11	100.35
	8a	interstitial	pyrrhotite	0.08	39.5	6.05	54.8	n.d.	100.43
	8b	interstitial	pyrrhotite	n.d.	39.7	4.42	56.7	n.d.	100.82
	8b	interstitial	pentlandite	0.70	34.1	34.8	31.2	n.d.	100.80
	8d	interstitial	pyrrhotite	n.d.	38.3	1.32	59.5	n.d.	99.12
	8d	interstitial	pentlandite	0.40	33.8	30.6	34.8	0.21	99.81
	9	interstitial	pyrrhotite	0.04	39.8	5.54	55.2	0.05	100.63
	9	interstitial	pentlandite	0.89	34.6	34.7	30.7	n.d.	100.89

Table 12. Continued

Xenolith	Sulfide grain	Textural position	Mineral phase	Co	S	Ni	Fe	Cu	Total
NFK1110	1	enclosed in ol	pentlandite	0.55	35.5	22.4	39.8	0.10	98.35
	3	enclosed in cpx	pyrrhotite	0.06	38.4	5.88	55.0	n.d.	99.34
	3	enclosed in cpx	pentlandite	0.54	34.7	27.4	36.2	0.83	99.62
NFK1137A	1	enclosed in ol	pyrrhotite	n.d.	39.4	0.36	59.6	0.01	99.37
	1	enclosed in ol	pentlandite	0.70	39.5	26.2	32.1	0.41	98.91
	1	enclosed in ol	pentlandite	0.81	39.5	31.1	27.5	0.53	99.44
	2	enclosed in ol	mss	0.08	38.9	2.67	57.5	0.03	99.18
	3	interstitial	mss	0.14	39.6	9.83	49.3	n.d.	98.87
	3	interstitial	mss	0.16	39.3	10.2	49.1	n.d..	98.76
	3	interstitial	mss	0.13	39.8	8.91	50.0	n.d.	98.84
	3	interstitial	mss	0.19	39.5	10.3	49.5	0.03	99.52
	3	interstitial	mss	0.18	40.0	9.65	49.7	n.d.	99.53
NFR1117A	1	interstitial	mss	0.19	39.0	10.5	49.1	0.03	98.82
	1	interstitial	mss	0.21	38.7	10.9	48.8	0.05	98.66
	2	interstitial	mss	0.13	38.2	9.8	50.9	n.d.	99.03
	2	interstitial	mss	0.15	38.3	9.72	51.6	0.07	99.84
	3	enclosed in ol	pyrrhotite	0.02	38.4	3.76	56.5	n.d.	98.68
	3	enclosed in ol	mss	0.09	37.7	9.94	50.5	0.04	98.27
	3	enclosed in ol	pyrrhotite	n.d.	38.2	3.58	56.4	n.d.	98.18
	4	interstitial	mss	0.18	39.1	15.6	44.4	n.d.	99.28
	5	enclosed in cpx	mss	0.06	38.5	8.24	51.4	0.03	98.23
	6	interstitial	mss	0.19	38.7	11.0	48.8	0.03	98.72
	7	interstitial	mss	0.31	37.9	17.2	42.8	n.d.	98.21
	7	interstitial	mss	0.12	38.6	13.3	46.4	0.07	98.49
NFR1119B	1	enclosed in ol	pentlandite	0.39	33.9	31.7	29.2	4.15	99.34
	2	enclosed in ol	pyrrhotite	0.13	38.8	1.66	58.7	0.04	99.33
	2	enclosed in ol	pyrrhotite	0.13	39.1	1.41	58.3	0.01	98.95
	3	enclosed in ol	pyrrhotite	0.09	39.2	1.32	59.0	n.d.	99.61
	3	enclosed in ol	pyrrhotite	0.06	39.0	1.41	59.2	0.07	99.74

Table 12. Continued

Xenolith	Sulfide grain	Textural position	Mineral phase	Co	S	Ni	Fe	Cu	Total
NMC1302B	1	interstitial	mss	0.12	38.7	11.0	49.2	n.d.	99.02
	1	interstitial	mss	0.20	38.8	11.1	49.4	n.d.	99.50
	1	interstitial	mss	0.16	38.8	11.4	49.4	0.02	99.78
	1	interstitial	mss	0.17	39.3	10.5	49.5	0.05	99.52
	1	interstitial	mss	0.12	38.9	10.4	49.5	0.01	98.93
	1	interstitial	mss	0.19	39.0	10.7	49.5	n.d.	99.39
	1	interstitial	mss	0.13	40.8	6.85	51.5	n.d.	99.28
NMM1114	2	interstitial	mss	0.25	39.0	8.62	51.7	n.d.	99.57
	2	interstitial	mss	0.17	39.0	8.21	51.1	n.d.	98.48
	3	interstitial	mss	0.31	39.0	9.90	49.3	0.01	98.52
	3	interstitial	mss	0.28	39.3	9.76	49.1	0.01	98.45
	4	interstitial	mss	0.29	39.3	15.6	43.8	n.d.	98.99
	4	interstitial	mss	0.38	39.0	16.1	43.5	n.d.	98.98
	6	interstitial	mss	0.14	39.4	14.1	45.1	n.d.	98.74
	6	interstitial	mss	0.18	39.3	15.1	44.7	0.02	99.30
NMM1129	1	interstitial	pyrrhotite	0.14	39.4	6.97	52.8	0.13	99.44
	1	interstitial	pyrrhotite	0.23	39.0	7.07	52.7	0.06	99.06
	2	enclosed in cpx	pyrrhotite	n.d.	38.4	1.69	58.2	0.04	98.33
	2	enclosed in cpx	pentlandite	1.05	33.1	32.9	32.2	0.03	99.28
	3	interstitial	mss	0.24	39.5	11.0	48.6	0.07	99.41
	3	interstitial	mss	0.17	39.1	10.6	48.8	0.06	98.73
	4	enclosed in sp	pyrrhotite	0.05	38.8	3.89	56.0	0.08	98.82
	4	enclosed in sp	pyrrhotite	0.13	38.7	3.96	55.5	0.12	98.41
	7	enclosed in cpx	pentlandite	0.81	33.6	31.7	32.8	0.12	99.03
	8	enclosed in ol	mss	0.15	38.7	7.55	52.7	0.06	99.16
	8	enclosed in ol	mss	0.17	38.9	7.45	52.3	0.07	98.89

Table 12. Continued

Xenolith	Sulfide grain	Textural position	Mineral phase	Co	S	Ni	Fe	Cu	Total
NME1110	3a	interstitial	mss	0.14	39.7	8.19	52.3	n.d.	100.33
	4	interstitial	mss	0.03	36.0	19.6	44.5	0.15	100.28
	13	enclosed in ol	pentlandite	0.36	34.0	34.3	31.2	n.d.	99.86
	13	enclosed in ol	pyrrhotite	n.d.	39.0	3.28	58.0	0.07	100.35
NME1110/ section 2	3a	interstitial	mss	0.07	40.0	9.76	51.0	0.17	101.00
NME1129D	1	enclosed in cpx	pyrrhotite	0.15	41.7	2.56	56.3	n.d.	100.71
	3c	interstitial	pyrrhotite	n.d.	40.5	6.19	53.9	n.d.	100.59
	3c	interstitial	chalcopyrite	n.d.	35.9	0.43	32.5	32.6	101.43
	4	interstitial	pyrrhotite	0.19	39.7	3.71	56.8	0.01	100.41
	4	interstitial	chalcopyrite	0.02	34.2	0.44	30.2	35.4	100.26
	5b	interstitial	pyrrhotite	0.01	40.1	4.82	54.9	n.d.	99.83
	5c	enclosed in cpx	pyrrhotite	0.12	40.4	6.05	54.0	n.d.	100.57
	5c	enclosed in cpx	chalcopyrite	0.10	35.6	0.67	34.6	30.7	101.67
	5d	interstitial	pyrrhotite	0.02	41.4	2.47	56.9	0.36	101.15
	5d	interstitial	pyrrhotite	1.18	45.2	0.82	39.7	12.8	99.70
	9	interstitial	pyrrhotite	n.d.	40.4	4.14	55.7	n.d.	100.24
	10a	interstitial	chalcopyrite	n.d.	36.2	0.57	34.5	29.6	100.87
	10a	interstitial	pyrrhotite	0.12	40.5	4.46	56.1	n.d.	101.18
	10b	interstitial	chalcopyrite	n.d.	35.5	0.11	33.4	31.0	100.01
	10b	interstitial	pyrrhotite	0.18	40.2	5.27	55.1	n.d.	100.75
	10c	interstitial	pyrrhotite	0.04	40.4	5.92	54.7	0.18	101.24
	15	interstitial	pyrrhotite	0.05	40.1	6.79	53.9	0.03	100.87
	16	interstitial	pyrrhotite	0.02	40.1	5.13	55.8	n.d.	101.05

Abbreviations: mss - monosulfid solid solution, ol - olivine, cpx - clinopyroxene, sp – spinel, n.d. - not detected.

Table 13. Bulk sulfide compositions in wt. % obtained by mass balance calculations in the studied Nógrád-Gömör wehrlite xenoliths.

Xenolith	Sulfide grain	Textural position	Co	S	Ni	Fe	Cu	Total
NTB1109	7	interstitial	0.24	34.7	33.0	31.6	1.10	100.64
	12	interstitial	0.12	39.0	23.4	38.5	0.03	101.05
	14	interstitial	0.19	34.5	38.1	28.2	0.37	101.36
	17	enclosed in ol	0.14	36.7	12.6	36.5	14.3	100.24
NTB1109/ section 2	3	interstitial	0.01	38.4	4.35	56.0	0.30	99.06
	4	interstitial	0.31	37.0	16.9	45.2	0.01	99.42
	6	interstitial	0.36	34.6	31.5	33.6	b.d.	100.06
NTB1120	1e	interstitial	0.33	36.3	18.9	44.1	0.09	99.72
	1f	interstitial	0.12	39.6	7.48	53.8	0.47	101.47
	1h	interstitial	0.17	38.7	11.3	50.7	0.16	101.03
	2	interstitial	0.06	39.7	5.42	55.8	0.07	101.05
	6b	interstitial	0.02	40.4	4.95	55.4	0.02	100.79
	7a	interstitial	0.01	39.2	1.93	59.1	0.11	100.35
	8a	interstitial	0.08	39.5	6.05	54.8	b.d.	100.43
	8b	interstitial	0.05	39.3	6.51	54.7	0.36	100.92
	8d	interstitial	0.17	36.4	13.6	49.1	0.09	99.36
	9	interstitial	0.21	38.7	11.7	50.0	0.04	100.65
NFK1110	1	enclosed in ol	0.17	37.7	9.67	51.5	0.02	99.06
	3	enclosed in cpx	0.23	37.1	13.4	48.4	0.29	99.42
NFK1137A	1	enclosed in ol	0.23	38.7	8.83	44.5	7.64	99.90
	2	enclosed in ol	0.02	39.3	0.82	59.2	0.01	99.35
	3	interstitial	0.16	39.7	9.78	49.5	0.01	99.15
NFR1117A	1	interstitial	0.17	38.4	9.45	46.7	4.32	99.04
	2	interstitial	0.14	38.3	9.78	51.2	0.03	99.45
	3	enclosed in ol	0.01	38.3	4.17	56.0	b.d.	98.48
	4	interstitial	0.18	39.1	15.6	44.4	b.d.	99.28
	5	enclosed in cpx	0.06	38.5	8.24	51.4	0.03	98.23
	6	interstitial	0.19	38.7	11.0	48.8	0.03	98.72
	7	interstitial	0.21	38.2	15.2	44.6	0.03	98.24

Table 13. Continued

Xenolith	Sulfide grain	Textural position	Co	S	Ni	Fe	Cu	Total
NFR1119B	1	enclosed in ol	0.16	43.3	10.1	44.6	22.7	120.86
	2	enclosed in ol	0.12	38.4	1.97	54.3	4.74	99.53
	3	enclosed in ol	0.09	38.8	2.88	57.6	0.24	99.61
NMC1302B	1	interstitial	0.15	39.2	10.3	49.7	0.01	99.36
NMM1114	2	interstitial	0.21	39.0	8.41	51.4	b.d.	98.02
	3	interstitial	0.29	39.1	9.83	49.2	0.01	98.43
	4	interstitial	0.33	39.2	15.9	43.6	b.d.	99.03
	6	interstitial	0.13	38.7	12.1	42.3	6.43	99.66
NMM1129	1	interstitial	0.18	39.2	7.02	52.8	0.09	99.29
	2	enclosed in cpx	0.17	37.4	6.60	52.4	2.18	98.75
	3	interstitial	0.21	39.3	10.8	48.7	0.06	99.07
	4	enclosed in sp	0.15	38.3	6.15	53.9	0.13	98.63
	7	enclosed in cpx	0.26	37.6	10.3	50.5	0.13	98.79
	8	enclosed in ol	0.15	38.7	7.21	51.6	1.49	99.15
NME1110	3a	interstitial	0.14	39.7	8.19	52.3	b.d.	100.33
	4	interstitial	0.03	36.0	18.7	43.8	1.93	100.46
	13	enclosed in ol	0.11	37.5	12.9	49.7	0.05	100.26
NME1110/ section 2	3a	interstitial	0.07	40.0	9.76	51.0	0.17	101.00
NME1129D	1	enclosed in cpx	0.15	41.6	2.56	56.3	b.d.	100.61
	3c	interstitial	b.d.	40.4	5.96	53.0	1.30	100.66
	4	interstitial	0.18	39.4	3.52	55.2	2.13	100.43
	5b	interstitial	0.01	40.3	4.69	54.2	0.96	100.16
	5c	enclosed in cpx	0.12	39.7	5.29	51.3	4.30	100.71
	5d	interstitial	0.59	43.2	1.63	48.2	6.82	100.44
	6a	interstitial	0.06	36.8	1.47	38.3	24.2	100.83
	7	enclosed in ol	0.12	39.4	3.37	48.3	9.53	100.72
	9	interstitial	b.d.	40.4	4.14	55.7	b.d.	100.24
	10a	interstitial	0.11	40.2	4.11	54.2	2.66	101.28
	10b	interstitial	0.15	39.5	4.45	51.6	4.97	100.67
	10c	interstitial	0.04	40.4	5.92	54.7	0.18	101.24
	15	interstitial	0.05	40.1	6.79	53.9	0.03	100.87
	16	interstitial	0.02	39.9	4.89	54.7	1.59	101.10
	17	interstitial	0.07	37.3	1.85	40.3	21.3	100.82

Abbreviations: ol - olivine, cpx - clinopyroxene, sp – spinel, b.d. - below detection

content of sulfides appearing within a single xenolith. Generally, the enclosed sulfides have higher Fe (51.0±5.4 wt. %) and lower Ni (7.1±3.9 wt. %) content compared to their interstitial counterparts (48.7±6.9 and 10.6±7.8 wt. %, respectively). Enclosed sulfides show the same composition independently on the type of the hosting mineral.

4.7.2.2. Trace elements

Trace element compositions of sulfides from NTB1109, NTB1120, NME 1110 and NME1129D wehrlite xenoliths are summarized in Table 14. Chalcophile element patterns including the siderophile Ni and Co are presented in Fig. 4.17. All major elements – Ni, Co and Cu - show dominantly higher concentrations compared to the CI chondrite (McDonough and Sun, 1995) (Fig. 4.17), as well as some trace elements, namely Ag (0.6–53 with an average of 10 ppm), Se (20–263 with an average of 65 ppm), As (2–104 with an average of 33 ppm) and Sb (0.5–10 with an average of 3 ppm) (Table 14; Fig. 4.17). In contrast, Zn (3–413 with an average of 61 ppm) and Ge (1–6 with an average of 3 ppm) are characterized by negative anomalies because of their low concentrations (Table 14; Fig. 4.17). Several elements, such as Cd (0.3–5 with an average of 2 ppm), Te (0.6–61 with an average of 9 ppm) and Tl (0.05–3 with an average of 0.8 ppm) show values varying around the CI chondrite (Table 14; Fig. 4.17).

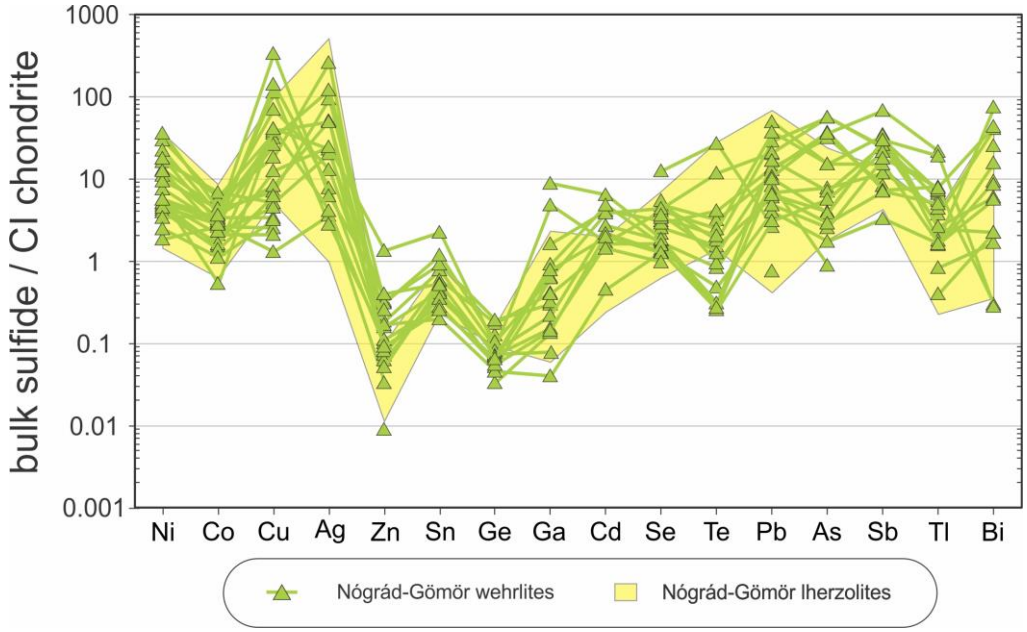

Figure 4.17 Bulk sulfide trace element patterns normalized to Cl chondrite (McDonough and Sun, 1995) for the Nógrád-Gömör wehrlites. The reference lherzolite data are from Szabó et al. (2019).

Table 14. In situ trace element compositions of sulfide grains in the studied Nógrád-Gömör wehrlite xenoliths in ppm determined by fs-LA-ICP-MS. The columns of 1σ show the within-run error linked to the certain measured element.

Sample	NTB1109		NTB1109/section 2			NTB1120						
Sulfide grain	12	14	3	4	6	1e	1f	2	6b	7a	8d	9
Textural position	interstitial	interstitial	interstitial	interstitial	interstitial	interstitial	interstitial	interstitial	interstitial	interstitial	interstitial	interstitial
Repetition rate (Hz)	28	28	25	25	22	23	25	23	23	23	25	23
Beam size (μm)	45	45	50	45	45	40	40	45	40	45	40	45
Cu	991	3745	1506	612	2204	4329	153	247	4951	301	853	406
1σ	142	642	97.8	41.0	218	637	11.5	27.7	834	41.1	50.6	41.9
Zn	47.9	93.6	413	102	22.6	98.6	10.1	2.75	30.8	19.3	56.1	22.1
1σ	5.22	4.88	12.3	7.61	2.62	18.0	1.0	0.972	8.53	3.64	2.66	2.37
Ga	5.60	5.91	44.3	2.70	3.77	<4.03	0.704	1.22	14.8	2.94	<0.696	<0.897
1σ	1.23	0.835	1.32	0.549	0.540	<4.03	0.124	0.207	2.91	0.576	<0.696	<0.897
Ge	1.60	3.21	2.76	5.85	5.25	<17.7	2.23	1.03	<10.6	<4.15	2.64	3.83
1σ	0.491	1.12	0.484	1.51	3.00	<17.7	0.510	0.347	<10.6	<4.15	0.908	1.24
As	58.2	103	28.0	14.1	104	<24.6	<1.77	1.63	28.0	<5.47	<445	<5.00
1σ	11.9	18.3	2.64	3.14	12.1	<24.6	<1.77	0.513	7.89	<5.47	<24.2	<5.00
Se	59.3	91.9	85.6	114	98.9	263	52.2	35.2	63.6	29.1	44.6	99.7
1σ	12.7	13.2	7.36	15.9	12.3	51.2	4.42	5.22	19.6	8.12	6.09	13.9
Ag	10.2	24.2	4.84	4.08	52.8	<4.74	0.715	<0.428	4.62	<1.13	18.8	<1.09
1σ	1.52	3.74	0.383	0.630	5.61	<4.74	0.159	<0.428	1.54	<1.13	1.03	<1.09
Cd	<0.871	2.70	1.16	<1.29	<0.781	<5.33	<0.372	<0.575	2.86	<1.21	<0.794	<1.13
1σ	<0.871	0.630	0.176	<1.29	<0.781	<5.33	<0.372	<0.575	1.20	<1.21	<0.794	<1.13
Sn	0.716	1.95	3.70	1.50	0.946	<5.91	<0.473	<0.560	<4.09	<1.63	1.26	<1.44
1σ	0.234	0.359	1.02	0.482	0.313	<5.91	<0.473	<0.560	<4.09	<1.63	0.397	<1.44
Sb	1.17	3.34	2.08	1.63	3.41	<5.95	<0.431	<0.487	4.66	<1.34	4.91	<1.28
1σ	0.513	0.679	0.295	0.794	0.601	<5.95	<0.431	<0.487	1.46	<1.34	0.454	<1.28

Table 14. Continued

Sample	NTB1109		NTB1109/section 2			NTB1120						
Sulfide grain	12	14	3	4	6	1e	1f	2	6b	7a	8d	9
Te	9.46	26.9	5.77	2.21	4.20	61.6	3.53	1.92	<6.44	<2.38	<1.82	7.26
1σ	2.09	4.25	0.520	1.15	0.724	13.7	0.502	0.502	<6.44	<2.38	<1.82	1.31
Tl	<0.080	<0.074	0.227	0.606	0.366	0.919	0.221	0.055	0.248	0.116	0.339	0.515
1σ	<0.080	<0.074	0.032	0.149	0.061	0.224	0.025	0.025	0.108	0.057	0.045	0.093
Pb	34.0	51.6	90.1	16.6	70.5	6.40	14.7	20.3	121	1.86	50.5	26.9
1σ	5.99	9.76	6.72	1.96	7.65	1.09	0.735	2.58	16.5	0.278	2.50	3.71
Bi	2.79	0.940	1.69	<0.174	0.659	<0.861	1.02	0.242	8.34	0.183	0.243	4.47
1σ	0.594	0.175	0.117	<0.174	0.100	<0.861	0.059	0.054	1.35	0.064	0.048	0.533
Os	4.55	16.2	3.75	9.41	22.4	9.68	7.04	3.32	<0.678	<0.123	9.71	<574
1σ	0.677	2.85	0.344	1.04	1.51	2.52	0.417	0.379	<0.678	<0.123	0.713	<574
Ir	5.96	17.1	3.76	<0.233	23.5	7.66	6.04	2.72	<0.274	<0.137	6.79	<658
1σ	0.892	2.68	0.250	<0.233	1.55	1.08	0.321	0.324	<0.274	<0.137	0.473	<658
Ru	8.54	15.2	6.46	<2.15	34.1	12.8	9.22	5.52	<3.31	<1.28	16.9	<446
1σ	1.45	2.81	0.593	<2.15	2.46	3.89	0.565	0.676	<3.31	<1.28	1.55	<446
Rh	1.36	1.66	0.960	<0.257	3.54	2.32	1.35	0.927	0.430	<0.159	1.63	<55.2
1σ	0.226	0.306	0.060	<0.257	0.250	0.595	0.081	0.126	0.339	<0.159	0.114	<55.2
Pt	2.95	9.65	5.93	<0.405	2.21	<1.05	<0.106	<0.098	<0.470	<0.274	<0.239	<0.221
1σ	0.396	1.56	2.93	<0.405	0.289	<1.05	<0.106	<0.098	<0.470	<0.274	<0.239	<0.221
Pd	5.82	15.7	3.41	<1.34	23.0	8.74	6.09	1.61	<2.25	<0.860	3.42	<3.24
1σ	1.15	2.71	0.284	<1.34	1.53	2.59	0.595	0.179	<2.25	<0.860	0.442	<3.24
Au	0.193	8.54	0.157	<0.355	0.188	2.92	<0.097	<0.104	<0.545	<0.228	<0.223	<0.290
1σ	0.087	1.97	0.068	<0.355	0.075	1.07	<0.097	<0.104	<0.545	<0.228	<0.223	<0.290
Re	0.362	<0.095	0.340	0.959	0.591	0.977	0.319	0.210	0.273	0.118	0.405	<0.565
1σ	0.100	<0.095	0.042	0.131	0.094	0.414	0.035	0.042	0.089	0.046	0.077	<0.565

Table 14. Continued

Sample	NME1110		NME1110/ section 2	NME1129D							
Sulfide grain	4	13	3a	1	3c	4	5b	5c	5d	9	10c
Textural position	interstitial	enclosed in ol	interstitial	enclosed in cpx	interstitial	interstitial	interstitial	enclosed in cpx	interstitial	interstitial	interstitial
Repetition rate (Hz)	25	28	25	25	25	28	25	28	25	23	25
Beam size (μm)	30	45	60	40	40	60	40	40	45	40	45
Cu	4534	530	8530	383	4949	40421	16771	13424	173	746	3141
1σ	434	124	1284	43.6	1201	5649	2317	1819	<9.9	64.8	203
Zn	24.7	18.9	52.1	15.8	28.0	121	33.6	34.4	<3.02	78.4	25.1
1σ	2.72	3.39	6.08	2.38	5.12	16.3	5.92	4.38	<0.346	4.71	1.39
Ga	2.89	<0.793	0.366	3.60	7.20	8.34	81.9	1.32	<0.164	1.39	2.00
1σ	0.325	<0.793	0.070	0.357	0.524	0.674	4.37	0.137	<0.027	0.203	0.143
Ge	<2.87	2.30	1.40	<1.57	2.00	2.09	<4.17	1.68	<0.692	2.16	2.51
1σ	<2.867	0.658	0.280	<1.57	0.529	0.319	<4.17	0.294	<0.128	0.905	0.534
As	68.4	<3.47	3.21	5.32	4.63	6.99	65.6	10.3	<6.11	7.23	12.8
1σ	4.24	<3.47	0.585	0.975	0.733	0.670	10.3	1.46	<0.38	0.926	0.808
Se	74.9	70.6	27.3	20.3	26.2	32.9	38.5	27.0	<10.7	34.1	37.0
1σ	8.17	14.6	4.68	2.55	3.98	4.26	8.74	4.11	<1.12	4.72	4.24
Ag	9.81	<1.18	2.56	<0.674	0.813	1.23	1.55	0.556	<0.117	<0.849	<0.507
1σ	0.859	<1.18	0.366	<0.674	0.232	0.188	0.500	0.118	<0.117	<0.849	<0.507
Cd	<1.01	<1.08	0.321	1.02	1.39	3.42	4.56	1.51	<0.133	1.16	1.94
1σ	<1.01	<1.08	0.091	0.294	0.360	0.398	0.923	0.224	<0.036	0.253	0.203
Sn	<1.00	0.677	0.318	0.832	0.414	0.871	<1.42	0.460	<0.093	<0.671	0.572
1σ	<1.00	0.286	0.093	0.230	0.141	0.103	<1.42	0.088	<0.028	<0.671	0.132
Sb	1.01	<0.960	0.458	0.978	2.48	4.19	9.62	2.99	<0.988	4.07	3.61
1σ	0.315	<0.960	0.126	0.264	0.489	0.418	2.01	0.463	<0.094	0.850	0.508

Table 14. Continued

Sample	NME1110		NME1110/ section 2	NME1129D							
Sulfide grain	4	13	3a	1	3c	4	5b	5c	5d	9	10c
Te	2.95	4.68	1.10	<0.666	<0.704	0.634	<2.01	0.587	<0.148	<1.01	0.721
1σ	0.629	1.27	0.220	<0.666	<0.704	0.130	<2.01	0.140	<0.148	<1.01	0.277
Tl	1.11	<0.122	0.224	0.681	1.07	2.67	3.05	1.01	<0.623	0.978	0.764
1σ	0.182	<0.122	0.037	0.075	0.112	0.310	0.470	0.142	<0.037	0.097	0.093
Pb	31.8	<0.262	9.84	15.9	11.9	25.0	26.0	7.50	<0.290	15.7	40.6
1σ	1.88	<0.124	1.25	2.06	1.21	2.28	3.02	0.889	<0.035	1.37	1.66
Bi	4.80	<0.139	0.617	<0.087	<0.076	0.030	<0.174	0.032	<0.013	<0.088	<0.046
1σ	0.377	<0.139	0.102	<0.087	<0.076	0.012	<0.174	0.009	<0.013	<0.088	<0.046
Os	5.91	13.1	26.8	<0.167	2.35	<0.049	<0.154	<0.033	2.58	<0.292	<0.166
1σ	0.551	2.89	3.64	<0.167	0.179	<0.049	<0.154	<0.033	0.173	<0.292	<0.166
Ir	4.10	12.9	23.3	<0.080	1.65	<0.0189	<0.100	<0.026	2.43	<0.102	<0.093
1σ	0.260	2.10	3.11	<0.080	0.098	<0.0189	<0.100	<0.026	0.135	<0.102	<0.093
Ru	8.54	23.6	40.6	<0.546	2.49	<1.16	<1.21	<1.15	3.50	<0.849	<0.957
1σ	0.756	5.63	4.90	<0.546	0.253	<1.16	<1.21	<1.15	0.245	<0.849	<0.957
Rh	1.69	3.15	7.92	<0.096	1.06	<5.63	<2.04	<2.01	0.548	<0.118	<0.414
1σ	0.191	0.858	0.931	<0.096	0.188	<5.63	<2.04	<2.01	0.035	<0.118	<0.414
Pt	<0.238	14.0	0.715	<0.158	0.063	<0.033	<0.856	<0.099	0.125	<0.127	<0.156
1σ	<0.238	3.94	0.124	<0.158	0.035	<0.033	<0.856	<0.099	0.014	<0.127	<0.156
Pd	1.32	28.1	11.4	<0.566	1.49	<12.3	<5.61	<4.49	0.340	<0.807	<0.947
1σ	0.480	7.38	1.39	<0.566	0.395	<12.3	<5.61	<4.49	0.059	<0.807	<0.947
Au	<0.190	0.382	<0.081	<0.115	<0.043	<0.024	<0.233	<0.031	<0.015	<0.136	<0.140
1σ	<0.190	0.206	<0.081	<0.115	<0.043	<0.024	<0.233	<0.031	<0.015	<0.136	<0.140
Re	0.278	0.289	0.054	0.077	0.153	<0.140	<0.279	<0.145	0.065	0.211	<0.266
1σ	0.065	0.102	0.017	0.024	0.034	<0.140	<0.279	<0.145	0.009	0.054	<0.266

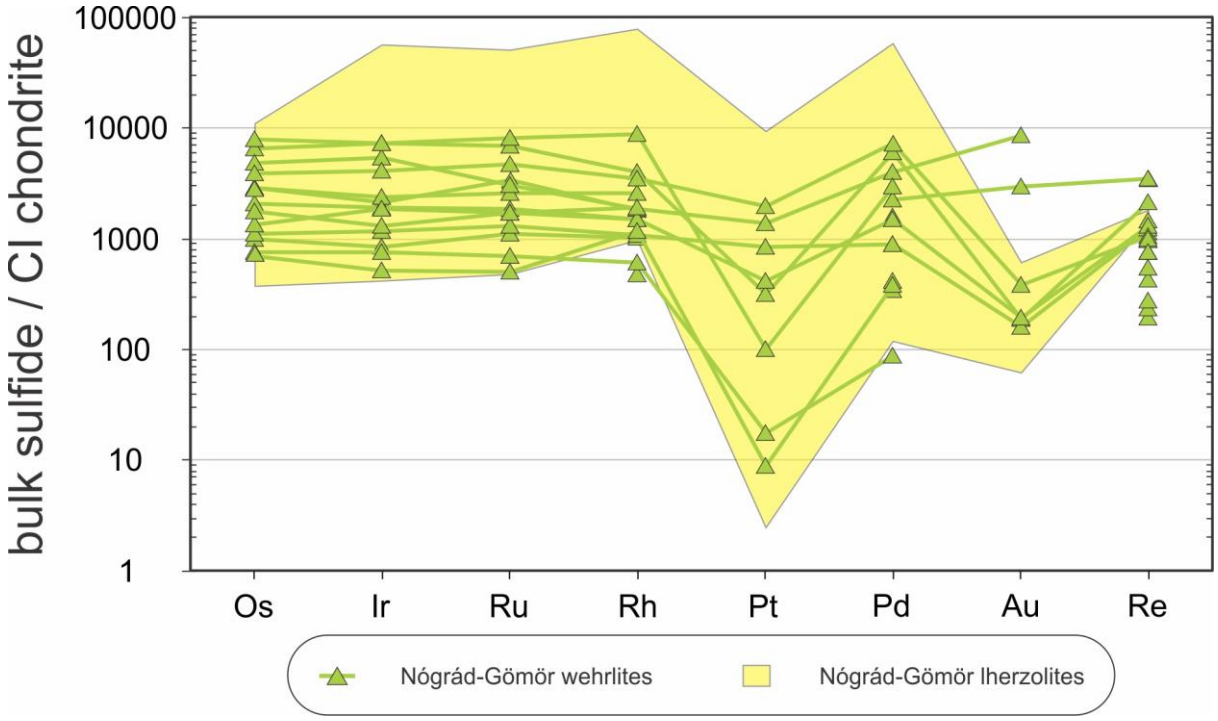

Figure 4.18 Highly-siderophile element contents of bulk sulfides normalized to the Cl chondrite (McDonough and Sun, 1995) in the Nógrád-Gömör lherzolites and wehrlites. The reference lherzolite data are from Szabó et al. (2019).

Siderophile elements show significant enrichment compared to the CI chondrite and exhibit mostly flat distribution from Os to Rh and a depression at Pt (Fig. 4.18). In NME1129D and NTB1120 wehrlite xenoliths, Pt values also show depression, as well as Au in sulfides from NME1129D and NME1110 wehrlite xenoliths (Table 14; Fig. 4.18). All of these less highly siderophile elements have wide concentration ranges in the wehrlites (Pt: 0.06–14 with an average of 4 ppm, Pd: 0.3–28 with an average of 8 ppm, and Au: 0.2–9 with an average of 2 ppm), whereas the most incompatible Re shows a narrower concentration range (0.05–1 with an average of 0.3 ppm) (Table 14; Fig. 4.18).

4.7.2.3. Fe stable isotopes in sulfides

In situ Fe stable isotope (^{54}Fe, ^{56}Fe, ^{57}Fe) measurements have been carried out in sulfides from NTB1109, NTB1120 and NME1110 wehrlite xenoliths and results are listed in Table 15. The δ^{56}Fe and δ^{57}Fe values (deviations of ^{56}Fe/^{54}Fe and ^{57}Fe/^{54}Fe, respectively, expressed in ‰) were calculated based on the following equations (Oeser et al., 2014):

$$\delta^{56}Fe = \left[\left(\frac{\left({}^{56}Fe/{}^{54}Fe\right)_{sample}}{\left({}^{56}Fe/{}^{54}Fe\right)_{reference}}\right) - 1\right] x1000 \qquad \delta^{57}Fe = \left[\left(\frac{\left({}^{57}Fe/{}^{54}Fe\right)_{sample}}{\left({}^{57}Fe/{}^{54}Fe\right)_{reference}}\right) - 1\right] x1000$$

The δ^{56}Fe values range from -0.20 to +0.84 ‰ (average: +0.33), whereas δ^{57}Fe values are between -0.26 and +1.22 ‰ (average: +0.47) for wehrlite xenoliths (Fig. 4.19). The δ^{57}Fe is expected to be ~1.5 times higher than the δ^{56}Fe, which is fulfilled by our results. The Fe stable isotope signatures show no correlation with the bulk sulfide Fe compositions (Fig. 4.20). Based on δ^{56}Fe data, sulfides in NTB1109 and NTB1120 wehrlite xenoliths have lower (-0.20–+0.06 with an average of -0.11 ‰), whereas those in NME1110 and NME1129D wehrlite xenoliths show higher values (0.66–0.84 with an average of 0.76 ‰) (Table 15; Fig. 4.20).

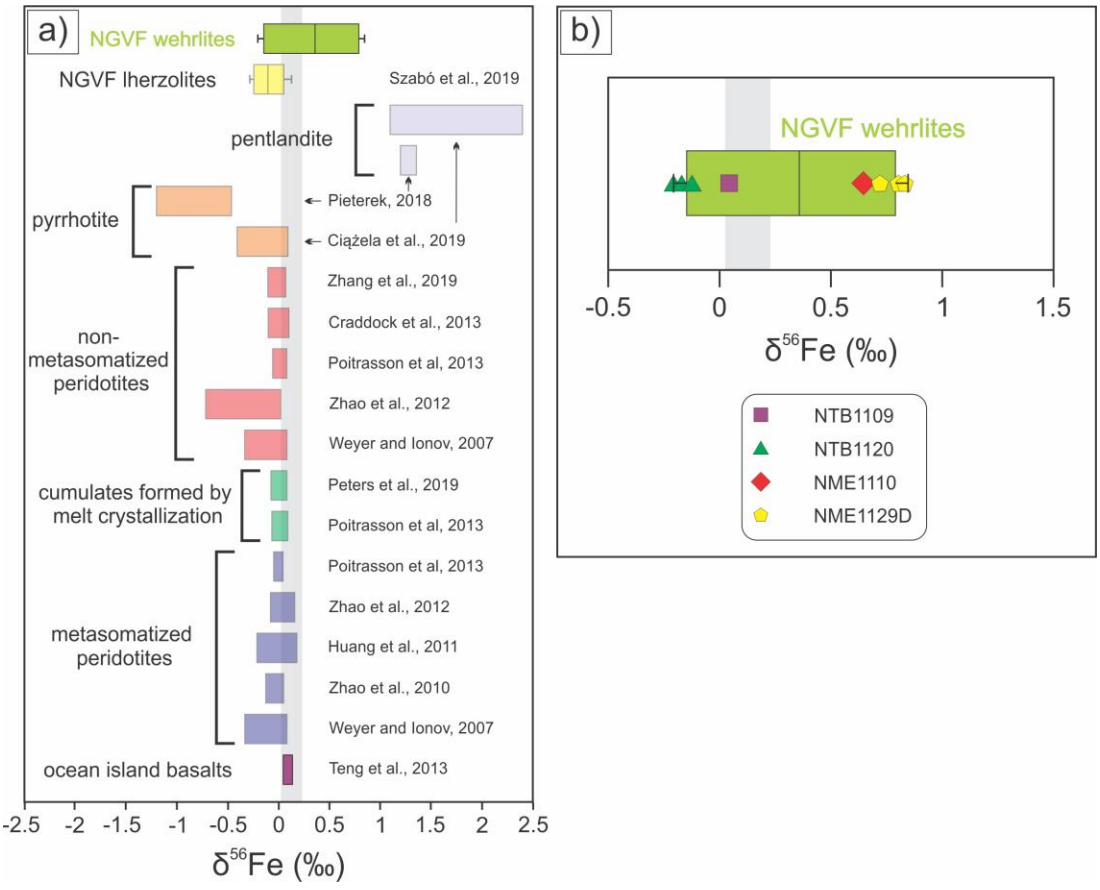

Figure 4.19 (a) δ^{56}Fe signatures of sulfides from the Nógrád-Gömör wehrlites with respect to reference data including NGVF wehrlites (Szabó et al., 2019). **(b)** All data points from wehrlitic sulfides are shown in details. Solid black lines within the wehrlitic boxes denote the median. Grey field represents the range for terrestrial mantle (Craddock et al., 2013). Data from Pieterek (2018) and Ciążela et al. (2019) refer to in situ analyses of pentlandites and pyrrhotites from gabbro of the lower oceanic crust. The rest of the results refer to whole-rock measurements.

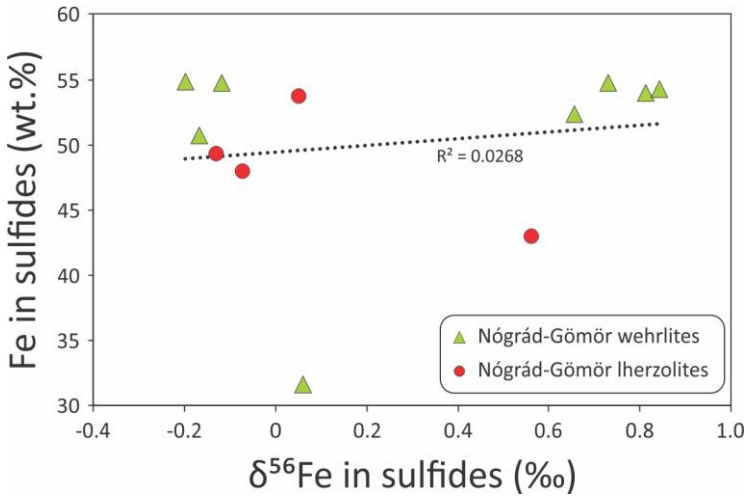

Figure 4.20 Correlations between Fe content and δ^{56}Fe of sulfides in selected Nógrád-Gömör wehrlite and lherzolite xenoliths. The lherzolite data are from Szabó et al. (2019).

Table 15. In situ stable iron isotope signatures of sulfides from Nógrád-Gömör wehrlite xenoliths. The values of 2σ columns are calculated from the propagation of the within-run relative standard error of the sample and the within-run relative standard errors of the two bracketing standards (IRMM-014).

Sample	Sulfide grain	Textural position	Repetition rate (Hz)	Beam size (μm)	δ^{56}Fe (‰)	±2σ (‰)	δ^{57}Fe (‰)	±2σ (‰)
NTB1109	7	interstitial	167	20	0.06	0.13	0.07	0.38
NTB1120	1h	interstitial	167	30	-0.17	0.08	-0.24	0.20
	8a	interstitial	167	30	-0.20	0.08	-0.26	0.15
	8b	interstitial	167	20	-0.12	0.08	-0.17	0.13
NME1110	3a	interstitial	167	20	0.66	0.09	0.85	0.15
NME1129D	10a	interstitial	167	20	0.84	0.07	1.12	0.14
	15	interstitial	167	30	0.81	0.08	1.22	0.16
	16	interstitial	167	30	0.73	0.09	1.17	0.18
PURA standard			167	60	0.07	0.06	0.12	0.09
PURA standard			167	60	0.14	0.05	0.24	0.09
PURA standard			167	60	0.15	0.05	0.20	0.08
PURA standard			167	60	0.09	0.06	0.18	0.10
PURA standard			167	60	0.05	0.06	0.08	0.12
PURA standard			167	60	0.15	0.07	0.22	0.12
PURA standard			167	60	0.10	0.06	0.10	0.10
PURA standard			167	60	-0.01	0.06	0.01	0.11
PURA standard			167	60	0.05	0.06	0.04	0.10
PURA standard			167	60	0.09	0.06	0.16	0.12
PURA standard			167	60	0.06	0.05	0.05	0.09
PURA average					0.09		0.13	

5. Discussion

5.1. Wehrlite formation

Petrographic observations, such as reaction coronas and breakdown of amphiboles at the contact between host basalt and xenolith (Fig. 3.1) and the lack of any relationship between the size and position of orthopyroxene relicts and their distance from the host basalt, besides geochemical features (e.g., rock-forming minerals showing compositional zoning only at the margins of xenoliths; Fig. 3.1), indicate that the host basaltic melt only interacted with the rind of the xenoliths. Therefore, the host basalt could not have been responsible for the wehrlitization process observed in the interiors of xenoliths. Accordingly, the clinopyroxene-rich lithology must have formed before the xenolith was entrained in the basalt melt.

Orthopyroxenes occurring within clinopyroxenes show irregular shapes, characteristic of relict crystals (Fig. 4.2g). These crystals are considered to have been involved in wehrlite formation and were partially replaced by newly formed clinopyroxenes (Fig. 4.2g). This petrographic observation clearly demonstrates that wehrlite is a product of a reaction between a metasomatic agent and the peridotite wall rock. The presence of orthopyroxene indicates that the wehrlite precursor lithology was highly likely lherzolite, the characteristic rock type of the upper mantle in the study area (Liptai et al., 2017).

The appearance of orthopyroxenes in clinopyroxene cores (Fig. 4.2g) also reveals that the metasomatic agent migrated along grain boundaries. The moderate LREE/HREE fractionation (La_N/Lu_N: 0.7–3.6; Fig. 4.8) and the dominant convex upward trace element patterns of type I clinopyroxene (Fig. 4.8a) in wehrlite xenoliths indicate that the metasomatic process was controlled by diffusion process (Navon and Stolper, 1987; Bodinier et al., 1990). According to Bodinier et al. (1990), diffusion-controlled metasomatism takes place in close proximity to migration pathways of the metasomatic agent, which is supported by our petrographic observations including the entirely new mineral assemblage (Fig. 4.2a) and metasomatic reactions related to both pyroxenes (Fig. 4.2g) and spinel (Fig. 4.2f).

Based on their elevated basaltic element (Fe, Mn, Ti, Ca, Al) contents compared to those of Group IA, IB and IIB lherzolites of Liptai et al. (2017) (Fig. 4.3), olivines, clinopyroxenes and spinels were all affected by the metasomatism, regardless to their textural position. This is strong geochemical evidence for a common and extensive metasomatic event in the upper mantle beneath the NGVF. The proposed lherzolite precursor is also confirmed by the geochemistry of the

wehrlitization trends, which always indicate Group IA and Group IB lherzolite fields (Liptai et al., 2017) as the starting major element compositions for olivine, pyroxenes and spinel (Fig. 4.3; 4.5). The wehrlitization trends partially overlap with Group IIB lherzolites of Liptai et al. (2017), however some wehrlite xenoliths have higher basaltic element (Fe, Mn, Ti, Ca, Al) compositions than those of Liptai et al. (2017) (Fig. 4.3; 4.5). This observation supports the interpretation of Liptai et al. (2017) that Group IIB lherzolites were formed during the same event as the wehrlites, as explained below. The convex upward REY pattern shown by type I clinopyroxenes in wehrlites (Fig. 4.8a) agrees well with that of Group IIB NGVF lherzolites (Fig. 4.8d), confirming their common origin. The flat REY distribution in type II clinopyroxenes of wehrlite xenoliths (Fig. 4.8b), as well as the LREE-enriched and LREE-depleted patterns of type III clinopyroxenes of wehrlite xenoliths (Fig. 4.8c), are also similar to the Group IIB, Group IB and Group IA lherzolites (Fig. 4.8d). Interestingly, a restricted number of clinopyroxene grains in wehrlites that show trace element patterns similar to Group IA xenoliths of Liptai et al. (2017) (Fig. 4.8d) may represent preserved portions of ther upper mantle remaining unaffected by metasomatism. This suggests that the last wehrlitization event has not entirely overprinted the precursor lherzolite. Lower basaltic major element concentrations, e.g., in NTB1109 and NFR1119D wehrlites, compared to other wehrlites represent further evidence that some areas remained unaffected by the metasomatic event (Fig. 4.3).

5.2. Composition and chemical evolution of the metasomatic agent

5.2.1. Nature of the metasomatic agent

According to previous studies on wehrlites worldwide (e.g., Rudnick et al., 1993; Zinngrebe and Foley, 1995; Yaxley et al., 1998; Coltorti et al., 1999; Peslier et al., 2002a), the metasomatic agent responsible for orthopyroxene consumption and clinopyroxene formation could be either a silicate melt or a carbonate melt, forming Fe- or Mg-wehrlites, respectively. Consequently, supercritical CO_2–H_2O-rich fluids, generated by decarbonation of carbonate melts, can also cause Mg-wehrlite formation (Yaxley et al., 1991). Moreover, the metasomatic melt need not be pure silicic or carbonatic endmember. Lee and Wyllie (1997) conducted experiments in the nephelinite-dolomite-Na_2CO_3 and nephelinite-calcite systems and proposed silicate-carbonate liquid mixing during magmatic processes at upper mantle conditions as a possible mechanism leading to the

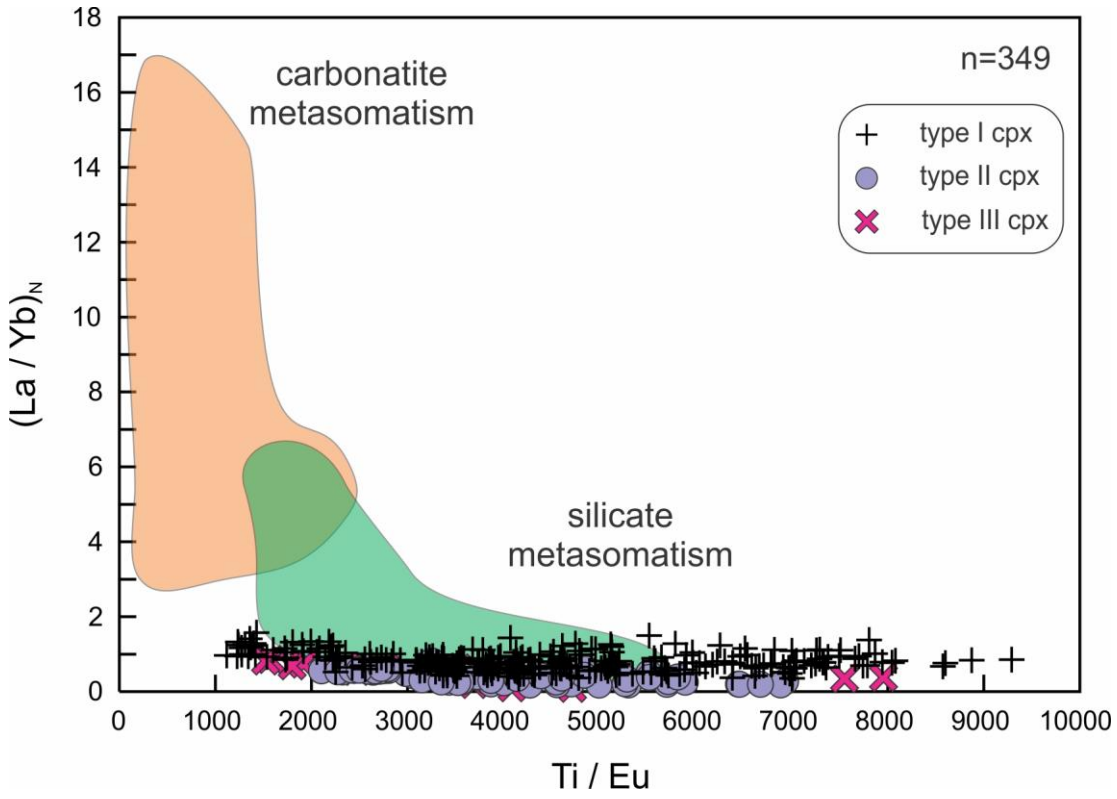

Figure 5.1 Plot of $(La/Yb)_N$ vs. Ti/Eu for the different clinopyroxene groups of Nógrád-Gömör wehrlite xenoliths. Areas of silicate and carbonate metasomatism are from Coltorti et al. (1999).

formation of 'carbonatic silicate' (e.g., Xiao et al., 2010) or 'silicic carbonate' melts (e.g., Neumann et al., 2002) depending on the dominant component.

The NGVF wehrlites contain neither carbonate phases nor apatite, which normally occur in Mg-wehrlites as a result of decarbonation processes (Yaxley et al., 1991, 1998; Hauri et al., 1993; Rudnick et al., 1993; Scott et al., 2014). This suggests that NGVF wehrlite formation is not related to carbonate melts. Furthermore, the observed 10–24 vol. % clinopyroxene mode (Table 2) is lower than the clinopyroxene content in products of carbonate-dominated metasomatism (20–40 vol%; Gervasoni et al., 2017). The calculated low CaO/Al_2O_3 ratio (3–5.7) in clinopyroxenes (Table 4) (>5 in carbonate-dominated metasomatism; Yaxley et al., 1991) is inconsistent with carbonate-dominated metasomatism, but is characteristic of mafic melt-driven metasomatism (e.g., Peslier et al., 2002a; Ionov et al., 2005; Raffone et al., 2009; Xiao et al., 2010). Similarly, the low Mg# in rock-forming silicates (0.86, 0.88, 0.87 for olivine, orthopyroxene and clinopyroxene, respectively; Tables 3–5) in the NGVF wehrlites is characteristic of mafic melt-driven metasomatism (e.g., Zinngrebe and Foley, 1995; Peslier et al., 2002a; Raffone et al., 2009).

In contrast, the high Mg# in silicates (≥0.9; Yaxley et al., 1991) is typical of carbonate-dominated metasomatism. All clinopyroxenes in NGVF wehrlites show high Ti/Eu and low La_N/Yb_N ratios (~1100–12,000 and 0.2–3.8, respectively), which is characteristic of silicate metasomatism (Coltorti et al., 1999) (Fig. 5.1). Furthermore, the major element trends of NGVF wehrlites overlap with worldwide Fe-wehrlite trends, but not with Mg-wehrlite fields (Fig. 4.3; 4.5).

The presence of silicate melt inclusion hosted by clinopyroxene and olivine in the wehrlite suggests that the metasomatic agent is a silicate melt, without a carbonate melt component. The silicate melt inclusion always contains low-to-moderate density (0.17–0.57 g/cm^3) CO_2-dominated bubbles (Patkó et al., 2018). All of the observed geochemical features are consistent with a mafic silicate melt metasomatic agent (Patkó et al., 2018).

5.2.2. Metasomatic melt composition

To constrain the main geochemical features of the silicate melt agent, we compared the mineral compositions of the product wehrlite and the potential precursor lherzolite xenoliths (Group IA, IB and IIB xenoliths of Liptai et al., 2017) collected from the same locations of the central NGVF (Fig. 2.5). The wehrlites show enrichment of Fe, Mn, Ca in olivines, Fe, Mn, and Ca enrichment in orthopyroxenes, Fe, Ti, Al, and Mn enrichment in clinopyroxenes, and Fe and Ti enrichment in spinels, compared to compositions of these phases in all lherzolite groups (Fig. 4.3; 4.5; 4.6). In contrast, the trace element characteristics of clinopyroxenes in the wehrlite and lherzolite series are similar (Fig. 4.7; 4.8). Among the HFS elements, Ti shows a positive correlation with Nb and Ta (Fig. 5.2a) and with Zr and Hf (Fig. 5.2b) in clinopyroxenes of all wehrlites and Group IIB lherzolites. This positive correlation is significant even within single xenoliths, particularly for Zr and Hf in xenolith NFK1137A (r^2 = 0.89 and 0.85, respectively) (Fig. 4.4d). These observations suggest that the wehrlitization accompanied with a moderate HFSE enrichment.

In order to constrain the composition of the metasomatic agent, we performed simple calculations based on the average trace element composition of wehrlitic clinopyroxenes (Table 7) and widely used alkaline silicate melt-clinopyroxene partition coefficients of Hart and Dunn (1993) and Ionov et al. (2002) for the trace elements listed in Table 16. The trace element composition of the inferred melt (Table 16) has a pattern of gradually decreasing abundance

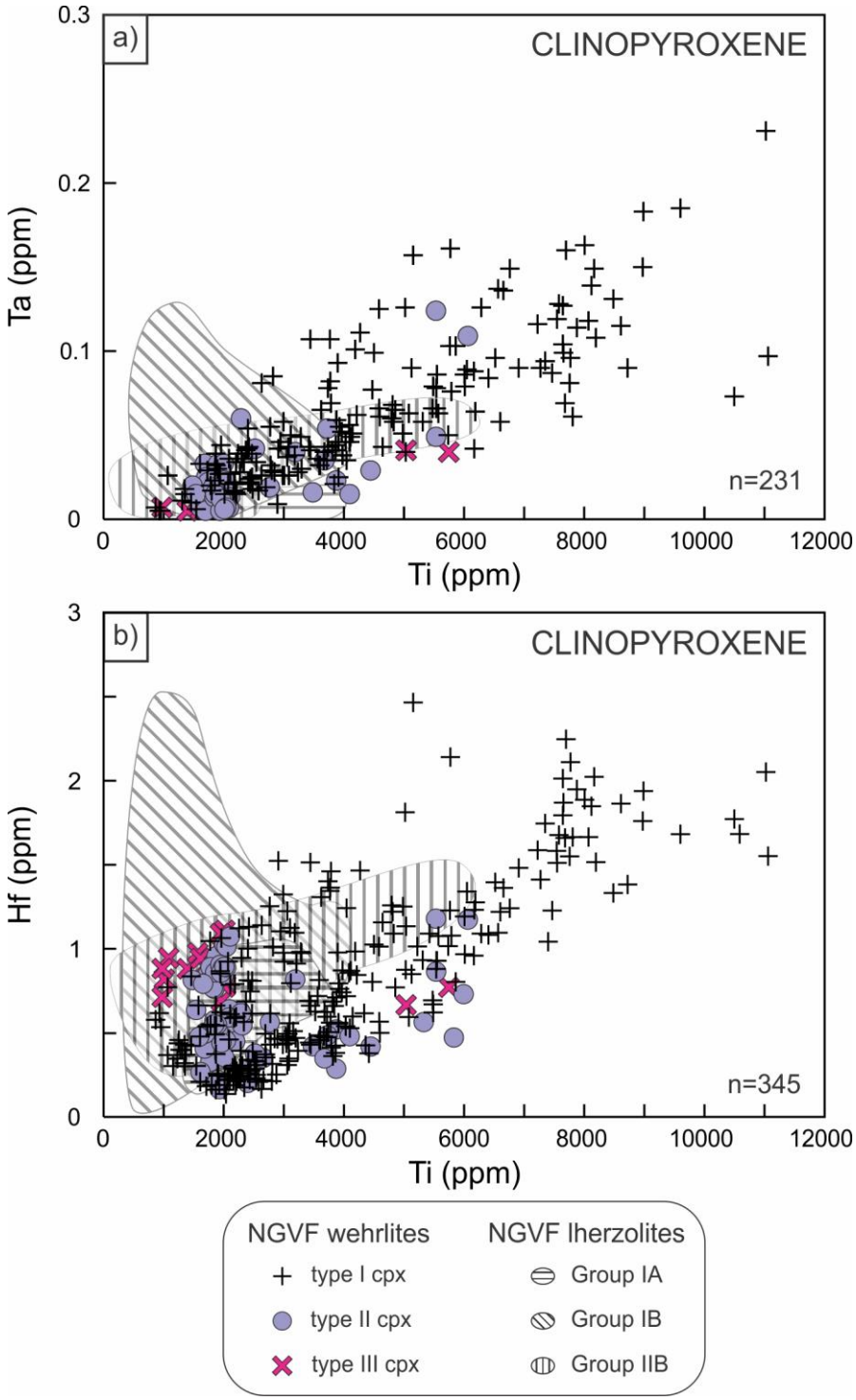

Figure 5.2 Relationships between **(a)** Ti vs. Ta and **(b)** Ti vs. Hf for the different clinopyroxene groups in Nógrád-Gömör wehrlite xenoliths compared to groups of lherzolite xenolits. Reference lherzolite data are from Liptai et al. (2017).

towards less incompatible elements with depletion of Pb, and Hf (Fig. 5.3). The trace element concentrations of the inferred equilibrium melt are all above the primitive mantle values, except for Cr and V (McDonough and Sun, 1995). The multi-element pattern of the calculated equilibrium melt shows a good correspondence with both the analyzed (Dobosi et al., 1995) and the modelled primitive (non-fractionated and non-contaminated) composition of the NGVF host alkali basalt (Zajacz et al., 2007) (Fig. 5.3; Table 16). A connection is also observed between the calculated equilibrium melt concentrations and the average OIB melt composition of Sun and McDonough (1989) (Fig. 5.3). These overlaps indicate that the inferred metasomatic agent and the NGVF host basalt are similar in composition and could be related to a comparable mantle source and melting event resulting in an OIB-like melt character.

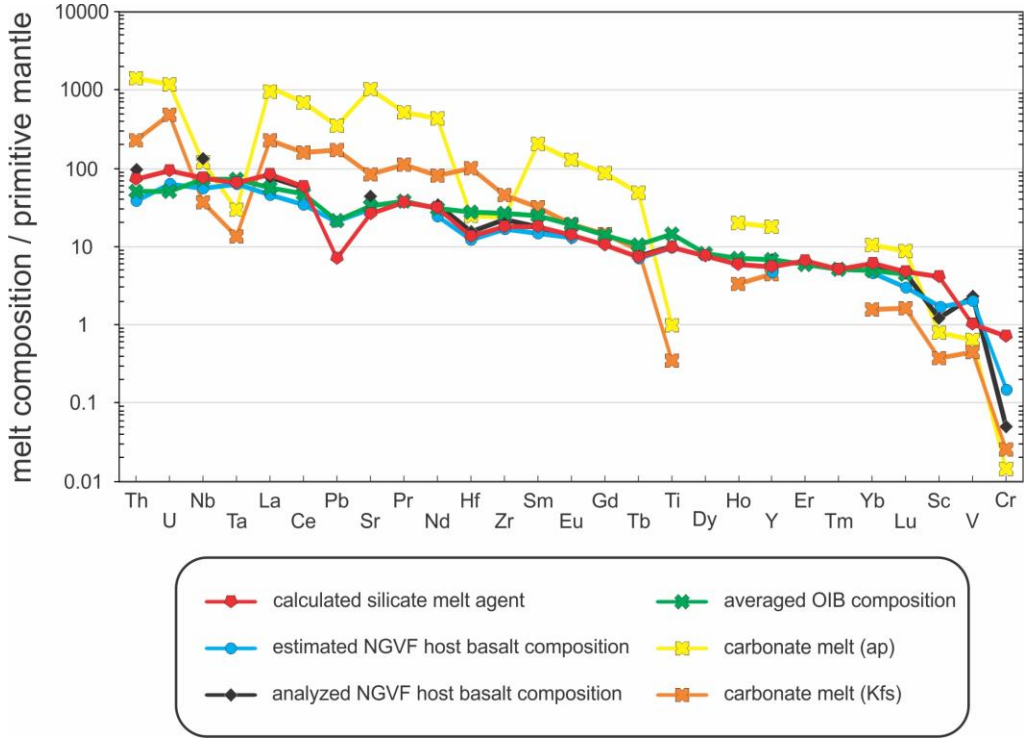

Figure 5.3 Estimated trace element composition of the metasomatic agent using the averaged trace element composition of Nógrád-Gömör wehrlitic clinopyroxenes and silicate melt-clinopyroxene partition coefficients of Ionov et al. (2002) for Th, U, Nb, Ta, La, Ce, Pb, Sr, Pr, Nd, Hf, Zr, Sm, Eu, Gd, Tb, Ti, Dy, Ho, Er, Tm, Yb and Lu; and Hart and Dunn (1993) for Y, Sc, V and Cr. The obtained primitive mantle (McDonough and Sun, 1995) normalized trace element distribution is compared to the trace element composition of the estimated local non-fractionated, non-contaminated host alkali mafic melt from cumulate xenoliths (Zajacz et al., 2007); the average trace element composition of the analyzed host alkali basalts (Dobosi et al., 1995); the average trace element composition of the ocean island basalts (Sun and McDonough, 1989) and the trace element composition of carbonate melt based on melt inclusions hosted by apatites (carbonatite ap) and potassium feldspars (carbonatite Kfs) (Guzmics et al., 2008).

Table 16. Equilibrium melt composition results of the Nógrád-Gömör wehrlite xenoliths. The input solid phase compositions are the average values of the trace element measuremants (Table 7). The partition coefficients used here for Th, U, Nb, Ta, La, Ce, Pb, Sr, Pr, Nd, Hf, Zr, Sm, Eu, Gd, Tb, Ti, Dy, Ho, Er, Tm, Tb, Lu are from Ionov et al. (2002), and for Y, Sc, V, Cr are from Hart and Dunn (1993). The estimated primitive (non-fractionated, non-contaminated) host basalt composition is obtained from cumulates (Zajacz et al., 2007). The whole rock composition of the host basalt is based on X-ray fluorescence spectrometry (Dobosi et al., 1995).

Element	**Calculated wehrlitizing melt agent composition (ppm)**	**Estimated host basalt composition (ppm) (Zajacz et al., 2007)**	**Whole rock compositions of the host basalt (ppm) (Dobosi et al., 1995)**
Th	5.3	3.0	7.6
U	1.9	1.3	–
Nb	49	36	86
Ta	2.8	2.3	–
La	54	30	50
Ce	109	58	92
Pb	2.1	3.0	–
Sr	621	592	846
Pr	11	–	–
Nd	41	30	42
Hf	3.8	3.4	4.4
Zr	167	174	229
Sm	7.5	5.9	7.1
Eu	2.3	2.0	2.0
Gd	5.8	–	–
Tb	0.85	0.70	0.74
Ti	11630	11750	11995
Dy	5.5	–	–
Ho	1.1	–	–
Y	27	20	29
Er	3.1	–	–
Tm	0.4	–	–
Yb	2.9	2.0	2.5
Lu	0.42	0.20	0.31
Sc	26	27	20
V	81	164	184
Cr	1713	381	132

5.2.3. Evolution of the composition of the metasomatic agent during metasomatism

The pristine (un-reacted) metasomatic mafic melt composition must have evolved as a result of geochemical interaction with the lherzolitic wall rock. The main driver of the compositional change could be the dissolution of orthopyroxene to produce a Si-rich melt (e.g., Kelemen, 1990), which subsequently mixes with the pristine metasomatic melt. The resulting modified melt with intermediate SiO_2 content is consistent with the compositions of silicate melt inclusions hosted by wehrlitic olivines and clinopyroxenes (51.1–56.4 wt. % with an average of 54.0 wt. %; Patkó et al., 2018). Chemical evolution of the metasomatizing agent continues until the mixture of the pristine and the modified melts quasi-equilibrates with the wall rock peridotite assemblage and becomes orthopyroxene-saturated (Shaw et al., 2018). This inferred evolution of the metasomatic melt is reflected in the composition of the newly-formed clinopyroxenes that retained orthopyroxene relicts in their cores (Fig. 4.2g). Clinopyroxene grains with such textures have the lowest TiO_2, Al_2O_3 and CaO, but the highest SiO_2 and MgO content among all clinopyroxenes in wehrlites (Fig. 4.4b; 5.4; Table 4). This change in geochemistry occurs because the dissolving orthopyroxenes locally have a large chemical effect on the pristine melt composition. The result is the enrichment (SiO_2, MgO) or depletion of elements (TiO_2, Al_2O_3, CaO) in the clinopyroxenes, in agreement with elemental partitioning preferences between orthopyroxene and clinopyroxene. However, trace element patterns among clinopyroxenes in the various textural occurrences show no differences (Fig. 5.5), probably because of the slow diffusion rate of the trivalent REEs compared to the divalent major cations (e.g., Ca, Fe, Mn) in orthopyroxenes (Cherniak and Liang, 2007). Accordingly, the orthopyroxene transformation into clinopyroxene probably happened at a rate that was faster than the trace element equilibration time. Alternatively, the nearly two orders of magnitude lower LREE concentration in lherzolitic orthopyroxenes, compared to those in coexisting clinopyroxenes (Liptai et al., 2017), was too low to significantly dilute the composition of the metasomatic agent. It is also possible that the higher trace element content of the pristine melt could compensate for the dilution effect.

During the wehrlitization in the NGVF mantle, incongruent orthopyroxene breakdown had not gone to completion (Table 5; Fig. 4.2b, 4.2g) because the metasomatic agent continued to migrate before becoming orthopyroxene saturated. Another possibility is that the metasomatic melt was no longer reactive because it became orthopyroxene saturated. Temperature influences

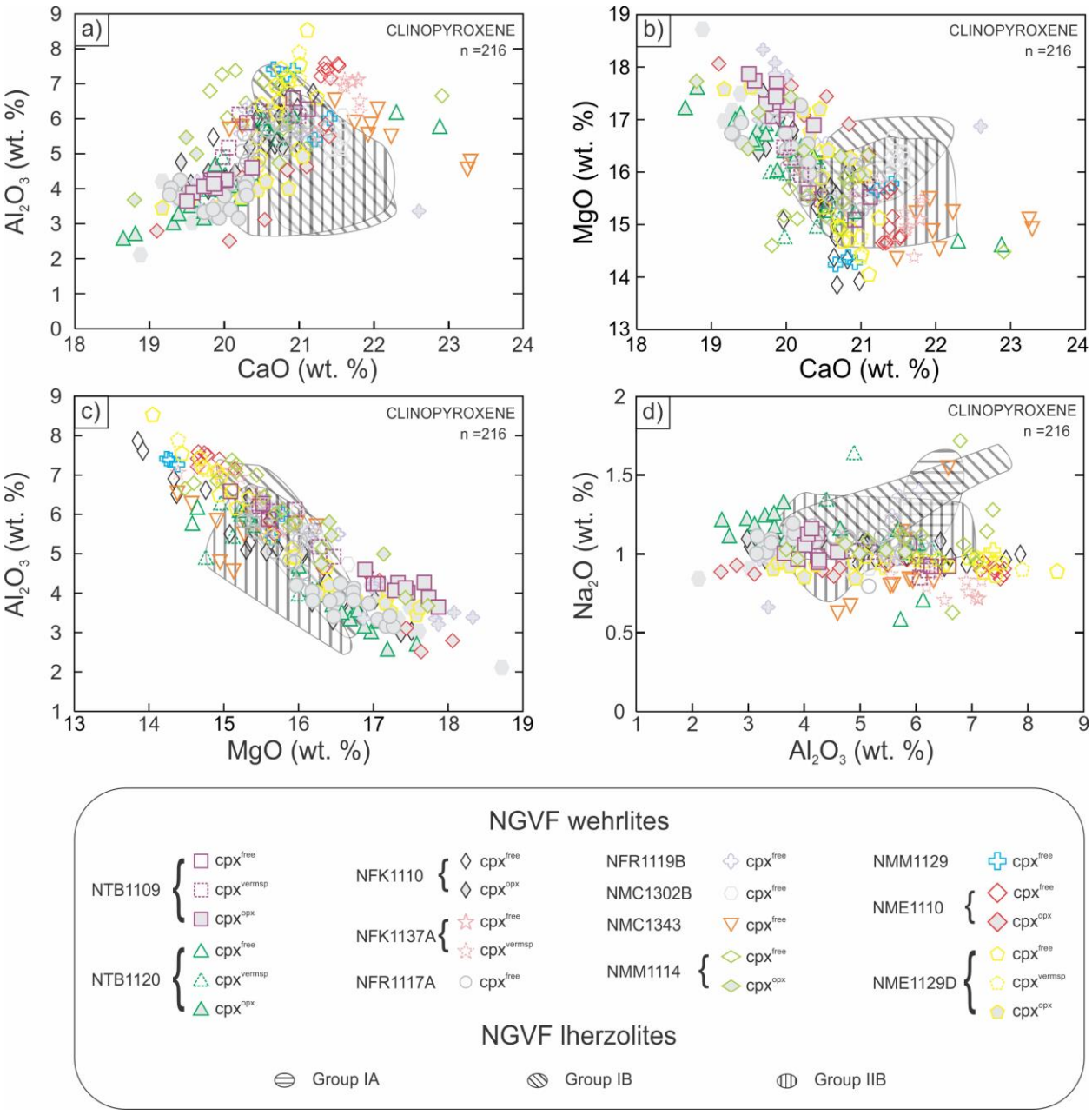

Figure 5.4 Major element compositions of Nógrád-Gömör wehrlitic clinopyroxenes appearing in different textural positions: **(a)** CaO vs. Al_2O_3 **(b)** CaO vs. MgO **(c)** MgO vs. Al_2O_3 **(d)** Al_2O_3 vs. Na_2O (cpx^{free}–clinopyroxenes free of vermicular spinel and orthopyroxene; cpx^{vermsp}–clinopyroxenes hosting vermicular spinel; cpx^{opx}–clinopyroxenes hosting relict orthopyroxene) compared to the NGVF lherzolite xenolith groups of Liptai et al. (2017).

the rate of orthopyroxene dissolution and cooling of the metasomatic agent can lead to slower consumption of orthopyroxenes (Tursack and Liang, 2012). According to Saper and Liang (2014), the slower the melt-rock interaction and the higher the melt/rock ratio, the more intensive the

orthopyroxene dissolution. Other experimental results of Mitchell and Grove (2016) argue that at least 20 % melt fraction is needed for wehrlite formation. Based on thermodynamic modelling of Shaw et al. (2018), the amount of melt required to produce wehrlite depends on the temperature (melt/rock ratio decreases from 0.67 at 1000 ˚C to 0.11 at 1200–1300 ˚C). Therefore, for the plate model calculation (discussed below in section 5.5) the melt/rock ratio for the NGVF wehrlites was assumed to be ~0.3, which indicates that the orthopyroxene preservation is likely not because of the low melt/rock ratio during metasomatism, but rather was due to orthopyroxene oversaturation of the melt.

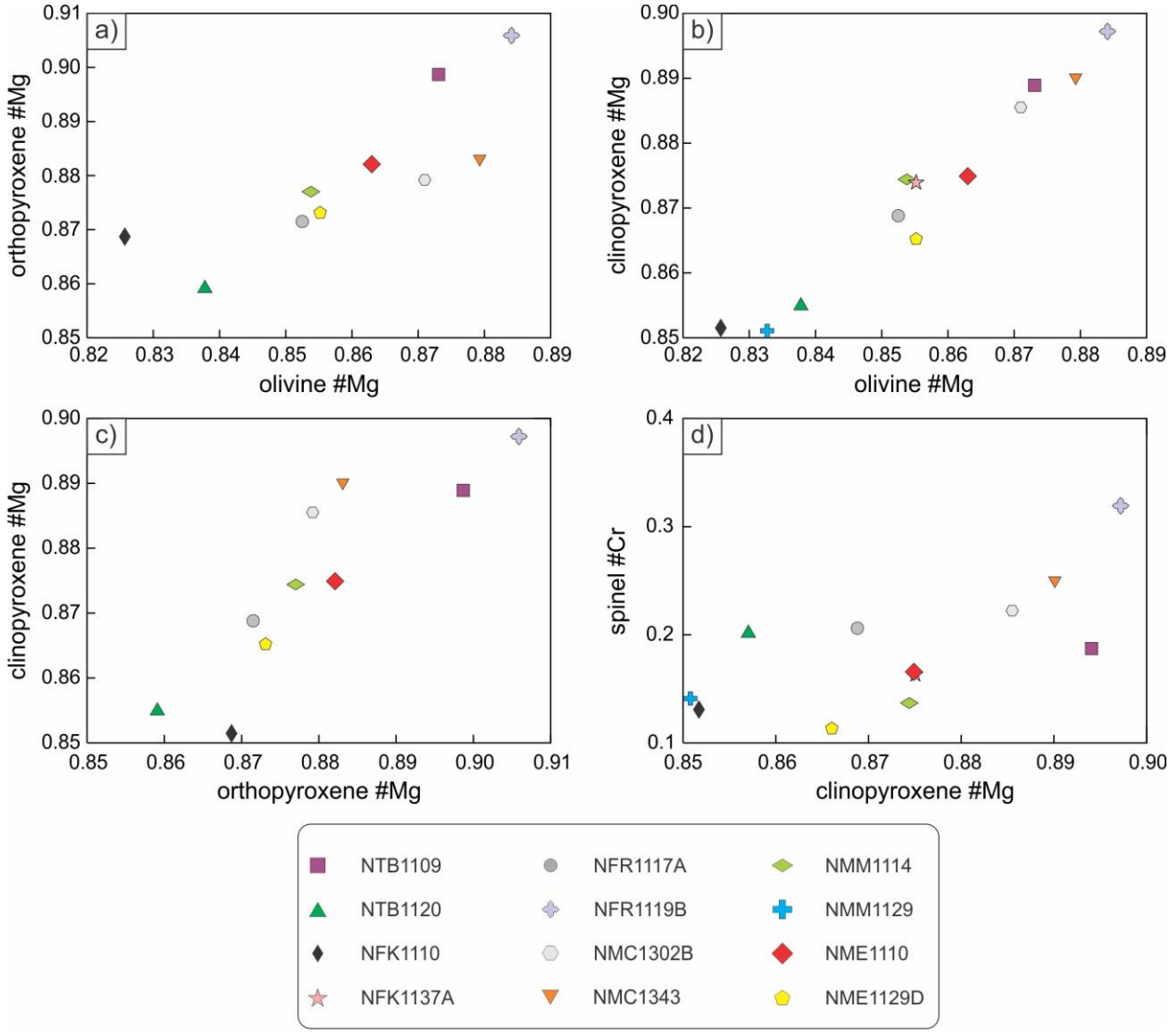

Figure 5.5 Relationships between **(a)** olivine Mg# vs. orthopyroxene Mg#, **(b)** olivine Mg# vs. clinopyroxene Mg#, **(c)** orthopyroxene Mg# vs. clinopyroxene Mg#, **(d)** clinopyroxene Mg# vs. spinel Cr# in Nógrád-Gömör wehrlite xenoliths. Note that the Cr# of the vermicular spinels was excluded in evaluating the averages.

It is known that the volatile content influences the orthopyroxene dissolution rate, i.e., the dissolution rate under hydrous conditions (using synthetic basanite glass with 4 wt.% H_2O as a starting material) is ~ three-times faster due to enhanced diffusion (Shaw, 1999). Fourier-transform infrared (FTIR) spectroscopic analysis of NAMs in the NGVF wehrlites show higher bulk structural hydroxyl content (average 30 ppm for dry and 99 ppm for wet grains; Table 9) compared to the NGVF lherzolites (average 17 ppm) (Patkó et al., 2019). This suggests structural hydroxyl enrichment in wehrlite clinopyroxenes compared to lherzolites due to interaction with the metasomatic melt (see details in chapter 5.6.4.). In contrast, CO_2 has the opposite effect on the rate of orthopyroxene dissolution, compared to H_2O (Shaw et al., 1999). Carbon-dioxide is present in the bubbles in silicate melt inclusions (Patkó et al., 2018) and in fluid inclusions (Szabó and Bodnar, 1996; 1998) in the metasomatized Nógrád-Gömör peridotite xenoliths. The calculated CO_2 contents (1.27–1.94 wt. %) are significantly higher than the measured H_2O concentrations (0.14–0.67 wt. %) in silicate melt inclusions that probably trapped the metasomatic agent (Szabó et al., 1996). Consequently, CO_2 might have played a role in orthopyroxene preservation.

The presence of vermicular spinels (Fig. 4.2e) could also be associated with changes in the composition of the metasomatic agent. Vermicular spinels were also observed to become Cr-rich as a result of complex mixing of pristine and evolved melts in the chromitite zone of Tari-Misaka ultramafic complex from Japan (Arai and Yurimoto, 1994), and in experimental runs (Ballhaus, 1998). The vermicular spinels, also reported in Fe-wehrlites (Ionov et al., 2005; Raffone et al., 2009) and in melt-rock reaction experiments (Van Den Bleeken et al., 2010), occur in four of the studied wehrlites (NTB1109, NTB1120, NFK1137A, NME1129D). The vermicular spinels are Cr-enriched and Al-depleted compared to interstitial spinels in the same xenoliths (Table 6; Fig. 4.4c). Chromium, being highly compatible during dissolution, remains fixed providing relative enrichment, whereas Al, which is incompatible, is partitioned into the metasomatic melt, leaving behind a depleted signature (e.g., Dick et al., 1984). Therefore, spinel nuggets probably represent breakdown relicts of former interstitial spinels, after metasomatism-induced dissolution.

According to Suhr et al. (2008), orthopyroxene dissolution can lead to Cr saturation in the silicate melt and subsequent spinel precipitation. During this process, the metasomatic melt could become oversaturated in Si and dissolve olivine locally. The relicts that remain after olivine dissolution are clinopyroxene-spinel assemblages with a clinopyroxene–spinel ratio (70-30 vol. %), which agrees with our estimations (Fig. 4.2f). Such an origin via dissolution is further

supported by the observation that the vermicular spinels are present exclusively in newly-formed clinopyroxenes (Fig. 4.2e). However, compositional recombination of the vermicular spinel and their host clinopyroxene resulted in extremely high Cr_2O_3 (4.63–7.45 wt. %) and Al_2O_3 (11.8–21.0 wt. %) concentrations, which is inconsistent with these elements having been incorporated in former olivines or being transported in metasomatic melts. Therefore, olivine dissolution is unlikely to have caused the vermicular spinel formation in the NGVF mantle.

5.3. The extent of metasomatism

Based on petrographic observations and geochemical features, wehrlites are considered to be the result of mantle metasomatism according to the following reaction:

$$ol_1 + opx_1 + cpx_1 + \text{mafic silicate melt} = ol_2 + cpx_2 (\pm opx_1) + \text{modified silicate melt}$$

where ol_1, opx_1 and cpx_1 denote the minerals of the precursor lherzolite, whereas the ol_2 and cpx_2 represent the geochemically modified or newly formed minerals of the wehrlites. The orthopyroxene relicts appear as opx_1 on the right side of the equation. The mafic silicate melt is the pristine metasomatic agent, which is modified by orthopyroxene dissolution, and spinel dissolution to a lesser extent, leading to a more evolved modified silicate melt (discussed above in section 5.2.3). The process associated with the increase in clinopyroxene proportion at the expense of orthopyroxene is referred to as stealth mantle metasomatism (O'Reilly and Griffin, 2013). Comparing the Mg# of the wehrlitic silicates with each other and with the Cr# of spinels, positive correlations can be observed (Fig. 5.5), in which the lower Mg# and Cr# values (vermicular spinels were excluded) correspond to higher degrees of metasomatism (Tables 3–5). Therefore, xenoliths NTB1109, NFR1119B, NMC1302B and NMC1343 are the least metasomatized (olivine Mg# > 0.87; clinopyroxene Mg# > 0.88 and spinel Cr# > 0.19), whereas xenoliths NTB1120, NFK1110 and NMM1129 are metasomatized to the greatest extent (olivine Mg# < 0.86; clinopyroxene Mg# < 0.86 and spinel Cr# < 0.20) during the wehrlitization (Fig. 5.5). Indeed, xenoliths NTB1109, NFR1119B, NMC1302B and NMC1343 have low clinopyroxene contents (<22 vol. %; Table 2), and the prior two contain no clinopyroxene- and olivine-rich areas, in contrast to the other wehrlite xenoliths (Fig. 4.1). Furthermore, xenoliths NTB1109, NFR1119B and NMC1343 have the lowest basaltic major element (Fe, Mn, Ti) and LREE concentrations, both in rock-forming mineral (Fig.

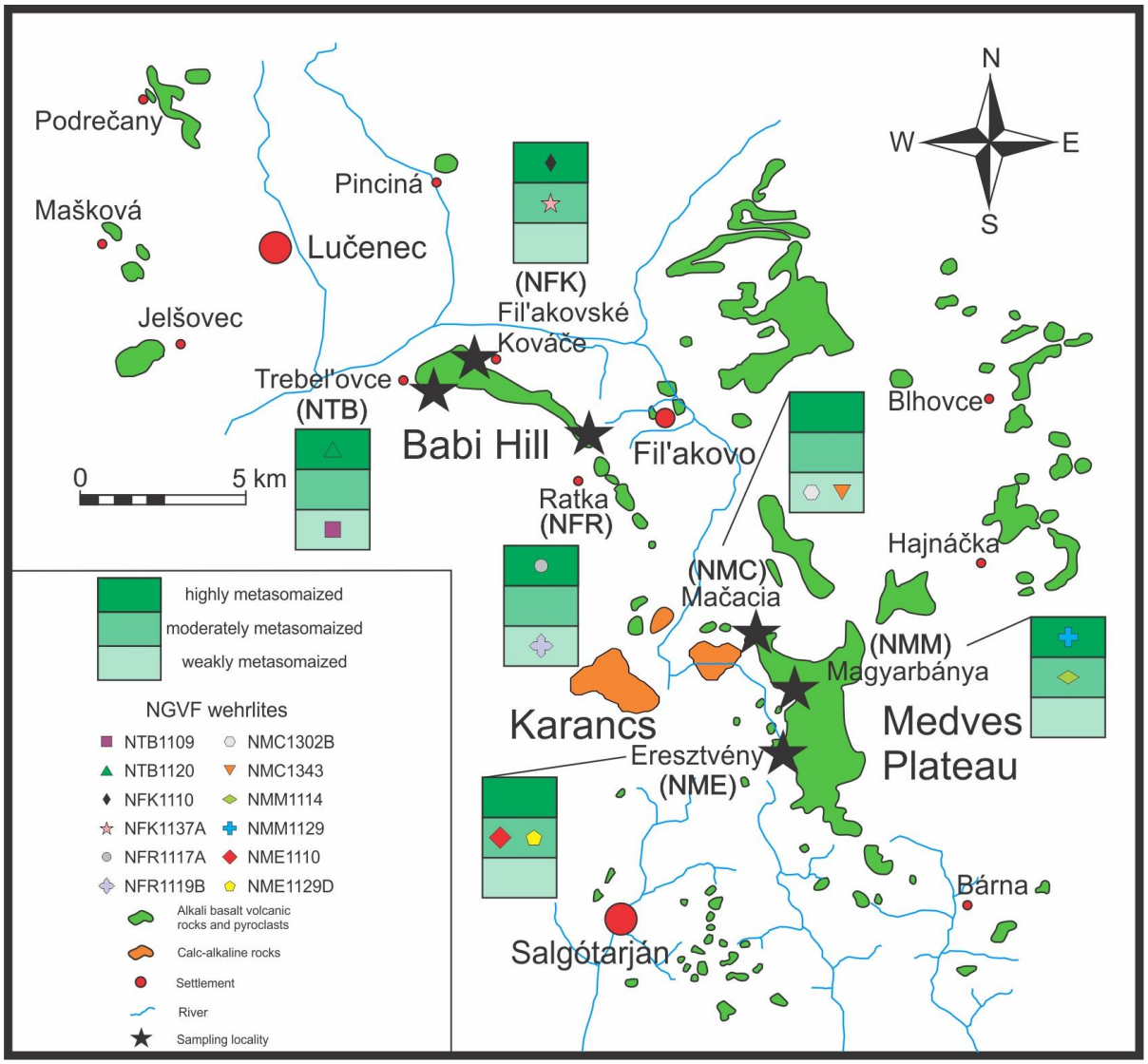

Figure 5.6 Alkali basalt occurrences and wehrlite xenolith sampling locations in the Nógrád-Gömör Volcanic Field. The figure shows the degree of metasomatism of the studied xenoliths for all six locations. The geochemical characteristics of the highly metasomatized xenoliths are the following: olivine mg# < 0.86, clinopyroxene mg# < 0.86 and spinel cr# < 0.20, whereas the weakly metasomatized xenoliths are: olivine mg# > 0.87, clinopyroxene mg# > 0.88 and spinel cr# > 0.19.

4.3; 4.8) and bulk rock compositions (Fig. 4.9; 4.10). In contrast, xenoliths NTB1120, NFK1110 and NMM1129 show high basaltic element content, both in rock-forming minerals and in the bulk rocks (Fig. 4.3; 4.9), as well as high concentrations for LREE (Fig. 4.8) and HFSE (Fig. 4.7). The positive correlation of Mg# of olivines and pyroxenes (Fig. 5.5a and b) indicates a single event causing differential enrichment, which affected the entire mineral assemblage.

It is also important to note that the differences in the degree of metasomatism were found not only between but within xenoliths as well. For example, clinopyroxene compositions in xenoliths NFK1110, NME1110 and NME1129D vary over nearly the whole Al_2O_3 vs. TiO_2 range (Fig. 4.4b) that is defined by all 12 wehrlites studied (Fig. 4.3b). This variability suggests that some areas of single xenoliths are affected more by the metasomatism than other areas in the same xenolith. Similarly, olivines and spinels also show intra-xenolith heterogeneities (Fig. 4.4a, 4.4c). The strongest intra-xenolith heterogeneities are mostly linked to weakly or moderately metasomatized xenoliths. One possible reason to explain why the wide ranges in geochemistry (Fig. 4.4) are not detected in all xenoliths is related to the areal (actually volumetric) extent of the heterogeneities. In some xenoliths (NFK1110, NME1110, NME1129D), the area in which heterogeneities are observed is smaller (μm–mm range) than the size of the xenolith (3–5 cm), whereas in other xenoliths (NMC1343, NM1114) the areal extent of heterogeneities is probably larger (>5 cm) than the dimension of the xenolith. This likely reflects the local characteristics of the melt (e.g., amount, reactivity) or physical features (e.g., more effective migration pathways). The degree or extent of metasomatism of the various xenoliths show no spatial correlation (Fig. 5.6), suggesting that metasomatized mantle portion is present under the entirety of the central NGVF.

5.4. Temperature-pressure conditions of wehrlite formation

In order to calculate an equilibrium temperature, coexisting minerals in the xenoliths should show evidence of textural and chemical equilibrium. However, the studied wehrlites are characterized by a lack of equigranular texture, increase in the proportion of clinopyroxene at the expense of orthopyroxene (Fig. 4.2g), together with the compositional heterogeneity of the rock-forming minerals (Fig. 4.3; Tables 3–6), not only among xenoliths, but even within grains (e.g., in xenoliths NFK1110, NME1110, NME1129D) (Fig.4.4). All of these features suggest that rock-forming minerals did not achieve chemical equilibrium with each other, and thus equilibrium temperature estimations based on these phases are unreliable. However, rounded orthopyroxene relicts enclosed by olivines are present in some wehrlite xenoliths (NFR1117A, NFR1119B, NMC1302B, NMC1343, NMM1114; Table 5) (Fig. 4.2b). These orthopyroxene relicts in olivines have compositional similarity on an Al_2O_3–CaO variation plot with Group IA, IB and IIB NGVF lherzolites as classified by Liptai et al. (2017) (Fig. 4.6a). Also, the orthopyroxene inclusions in

olivine are different from those hosted by newly formed clinopyroxenes, which have systematically elevated CaO contents (Fig. 4.6a). However, other elements (e.g., Na_2O, FeO, MnO) in orthopyroxenes show no systematic differences as a function of their textural occurrence (Fig. 4.6b-d). These observations indicate that orthopyroxene inclusions in olivine were not affected by Ca enrichment, probably due to the mechanical and chemical isolation provided by their host mineral. Therefore, in some cases, olivine hosts might have hindered direct contact between the metasomatic agent and the orthopyroxene by acting as a physical barrier. This interpretation is further supported by the slower diffusion rate for Ca compared to other cations, such as Fe and Mn, in the olivine structure (Coogan et al., 2005 and references therein). Both alternatives assume that such orthopyroxene inclusions (Fig. 4.2b) already existed before the wehrlitization process started.

It is worth investigating whether the olivine could have formed directly from orthopyroxene (e.g., Shaw et al., 2018). Newly formed clinopyroxene at the edge of orthopyroxene inclusions hosted by olivines (Fig. 4.2c) indicates that clinopyroxene is more likely to form than olivine at the expense of orthopyroxene during metasomatism beneath the NGVF. Consequently, the Ca-in-opx thermometer ($T_{Ca\text{-}in\text{-}opx\ by\ NG10}$, Nimis and Grütter, 2010 modified after Brey and Köhler, 1990) was applied to orthopyroxene inclusions in olivine to estimate the pre-wehrlitization thermal conditions of the later transformed mantle. The calculated equilibrium temperatures are of 985–1055 ˚C ($T_{Ca\text{-}in\text{-}opx}$) (Table 2), which is similar to those of the central NGVF lherzolite xenoliths showing a range of 940–1040 ˚C ($T_{Ca\text{-}in\text{-}opx}$) (Liptai et al., 2017 and on data of Szabó and Taylor, 1994; Konečný et al., 1999). This difference is within the error of the geothermometers (±36 ˚C for $T_{Ca\text{-}in\text{-}opx}$) and, therefore, cannot distinguish between equilibrium in a hot mantle volume or an origin of greater depths. Note, however, that equilibrium temperatures of lherzolite xenoliths are usually higher in the central NGVF compared to those from the northern and southern localities (Liptai et al., 2017), which is probably due to the extensive thermal effect of the wehrlitization process. According to Liptai et al. (2019b), this extra heat may have led to post-kinematic annealing that is observed in the microstructures of the xenoliths.

The wehrlites are all derived from the spinel facies zone of the mantle (Fig. 5.7), which suggests a maximum pressure not exceeding 2 GPa (O'Neill, 1981). To better constrain the wehrlite formation pressure conditions, their modal compositions were examined. There is

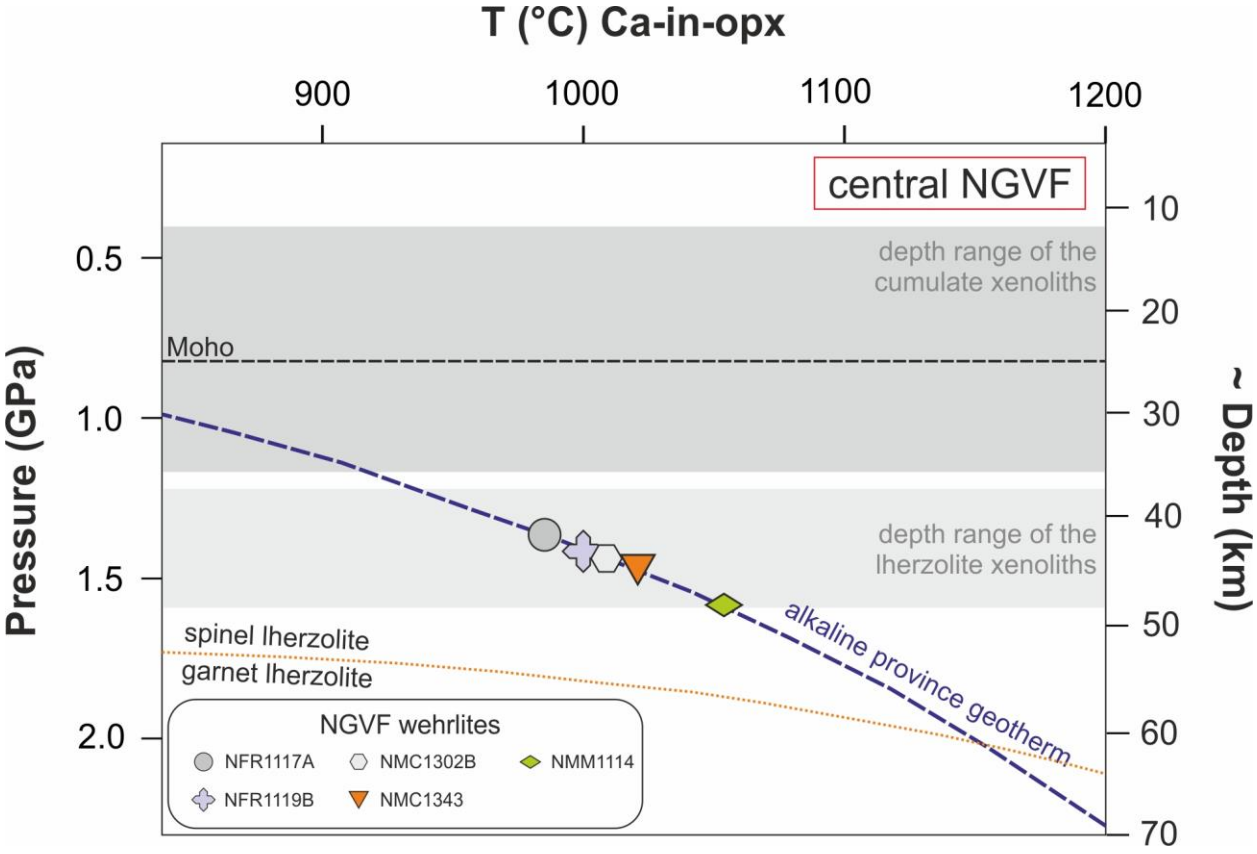

Figure 5.7 Estimation of depth of origin for the studied wehrlite xenoliths with available equilibrium temperature data (Table 2) using the alkaline-province geotherm of Jones et al. (1983). The equilibrium temperatures were obtained with the corrected Ca-in-opx thermometer of Nimis and Grütter (2010). The local Moho depth was estimated by Klébesz et al. (2015). The depth range for the local lherzolites was defined by Liptai (2018). The spinel lherzolite to garnet lherzolite transformation curve (Fo_{90} composition) is taken from O'Reilly et al. (1997).

evidence for the simultaneous crystallization of olivine and clinopyroxene, which show 'finger-like' microtexture in the NGVF wehrlite xenoliths (Fig. 4.2d). This texture suggests reaction of the basaltic liquid and the peridotite (Kelemen, 1990) to produce not only clinopyroxene, but olivine as well. Such microtextures have also been observed in experimental runs (Shaw, 1999) and natural occurrences (e.g., Zinngrebe and Foley, 1995). The 72–82 vol. % (av.: 76 vol. %) olivine modes in NGVF wehrlite xenoliths are better constrained and somewhat higher than those of previously published lherzolite xenoliths representing all lherzolite groups in the central NGVF (65–81 vol. %, av.: 71 vol. % in Szabó and Taylor, 1994; 52–89 vol. %, av.: 75 vol. % in Liptai et al., 2017). The narrow range for olivine modes in wehrlites suggests that the metasomatism led to a uniform olivine volume, independent of the precursor modal composition. The NGVF wehrlites

probably do not have higher olivine content because of the temperature-pressure conditions of the metasomatism ($T_{Ca\text{-}in\text{-}opx}$ = 985–1055 ˚C; ~1–2 GPa). Shaw (1999) demonstrated that orthopyroxene dissolution creates increasing portions of clinopyroxene with decreasing amounts of olivine in experiments as pressure increases from 0.4 GPa to 2 GPa, with only minor olivine at 2 GPa. The olivine/clinopyroxene ratio, which is ~4 in the NGVF wehrlites (Table 2) and ~6, ~13, ~10 in Group IA, IB and IIB lherzolites (Liptai et al., 2017), respectively, clearly show clinopyroxene enrichment with respect to olivine in the wehrlite xenoliths. The formation of more clinopyroxene than olivine indicates a minimum pressure of 1 GPa during wehrlitization (Shaw, 1999). This also suggests that the physical conditions of clinopyroxene formation may play a more significant role than the composition of the precursor rock or the metasomatic agent. A better estimation could be obtained using the appropriate geotherm based on the alkaline basalt province geotherm (Jones et al., 1983). The similar equilibrium temperatures calculated for relicts and lherzolites suggests similar pressure ranges also. Based on these similarities, it is proposed that the wehrlites were derived from a depth of 40–50 km (1.3–1.6 GPa; Table 2) which is in good agreement with that of lherzolite xenoliths of Liptai et al. (2017) (Fig. 5.7). This estimated depth is greater than the wide range of 12–37 km (0.4–0.9 GPa and 0.9–1.2 GPa) assumed for NGVF cumulates that occasionally contain plagioclase (Kovács et al., 2004; Zajacz et al., 2007, respectively) and the 25 ± 5 km for local Moho (Klébesz et al., 2015) (Fig. 5.7).

5.5. Numerical modelling of rare earth element behavior during wehrlitization

In order to test my hypothesis for wehrlite formation that involves interaction between a mafic metasomatic agent and the precursor lherzolite (Fig. 5.3; Table 16), REE numerical modelling was carried out using the plate model of Vernières et al. (1997). This model simulates the chromatographic effects of porous fluid flow, taking complex mantle processes into account, such as melt extraction related to molten peridotite compaction, polybaric melt segregation or fluid-matrix reactions accompanied by melt infiltration (Vernières et al., 1997). Therefore, the plate model is often applied for understanding REE behavior during metasomatism.

It is necessary to constrain the compositions of both reactants for the plate models. The most plausible mafic melt agent is represented by the NGVF alkali basalt. However, the only available chemical compositions for the non-fractionated and non-contaminated mafic melt, i. e., the silicate melt inclusions from the NGVF (Zajacz et al., 2007), is lacking data for several REE, which

hinders the modelling. Therefore, I applied the trace element dataset of Sun and McDonough (1989) for a reactant melt with OIB composition, which is in good agreement with the assumed averaged NGVF basalt composition and closest to the presumed metasomatic melt character (Fig. 5.3; Table 16). Among the four lherzolite xenolith groups of Liptai et al. (2017), Group IA and IB were selected as available lherzolite sources in the modelling, both of which are present in the central NGVF. The Group IA xenoliths have uniformly depleted REE patterns (Fig. 6a in Liptai et al., 2017), whereas the group IB xenoliths have variable REE concentrations (Fig. 6b in Liptai et al., 2017). Therefore, a IB/1 subgroup having convex upward ($La_N/Lu_N > 2$) and a IB/2 subgroup displaying a mostly flat REE distribution ($La_N/Lu_N < 2$) can be distingushed. Thus, I applied the average modal and REE compositions of these three lherzolite groups (IA, IB/1, IB/2), respectively, and simulated interactions with the reactant OIB melt (Appendix 7).

In the model of Vernières et al. (1997), simplified melt-rock interaction zones are created, based on both natural samples and theoretical considerations. In my modelling, I used these well-constrained melt-rock reaction zone boundaries, which structurally consist of: (1) extensive orthopyroxene, clinopyroxene and moderate olivine dissolution, (2) orthopyroxene and clinopyroxene dissolution accompanied by olivine precipitation, (3) dissolution of orthopyroxene and precipitation of olivine, and (4) dissolution of orthopyroxene and precipitation of clinopyroxene. The petrography of the wehrlite xenoliths also confirms that olivine (Fig. 4.2e, discussed above in section 5.2.3.) and orthopyroxene (Fig. 4.2g) dissolution are likely to occur. The possibility that precursor clinopyroxenes melted as well cannot be excluded because of the elevated temperatures during melt infiltration. In addition to the dissolution reactions, the crystallization of new phases is also observable in the wehrlite xenoliths, such as the elongated olivines in clinopyroxene-rich patches (Fig. 4.2d) or clinopyroxene at the expense of orthopyroxene (Fig. 4.2g). The partition coefficients used in the modelling are from Ionov et al. (2002) because they report data for all REE.

The modelling results predict similar modal proportion changes (Appendix 8; 9; 10) regardless of the precursor (Appendix 7). Cells located close to the reaction front are dunites, followed by wehrlites with no orthopyroxenes, wehrlites with orthopyroxenes, clinopyroxene-rich lherzolites (cpx > opx) and orthopyroxene-rich lherzolites (cpx < opx), respectively (Appendix 8; 9; 10).

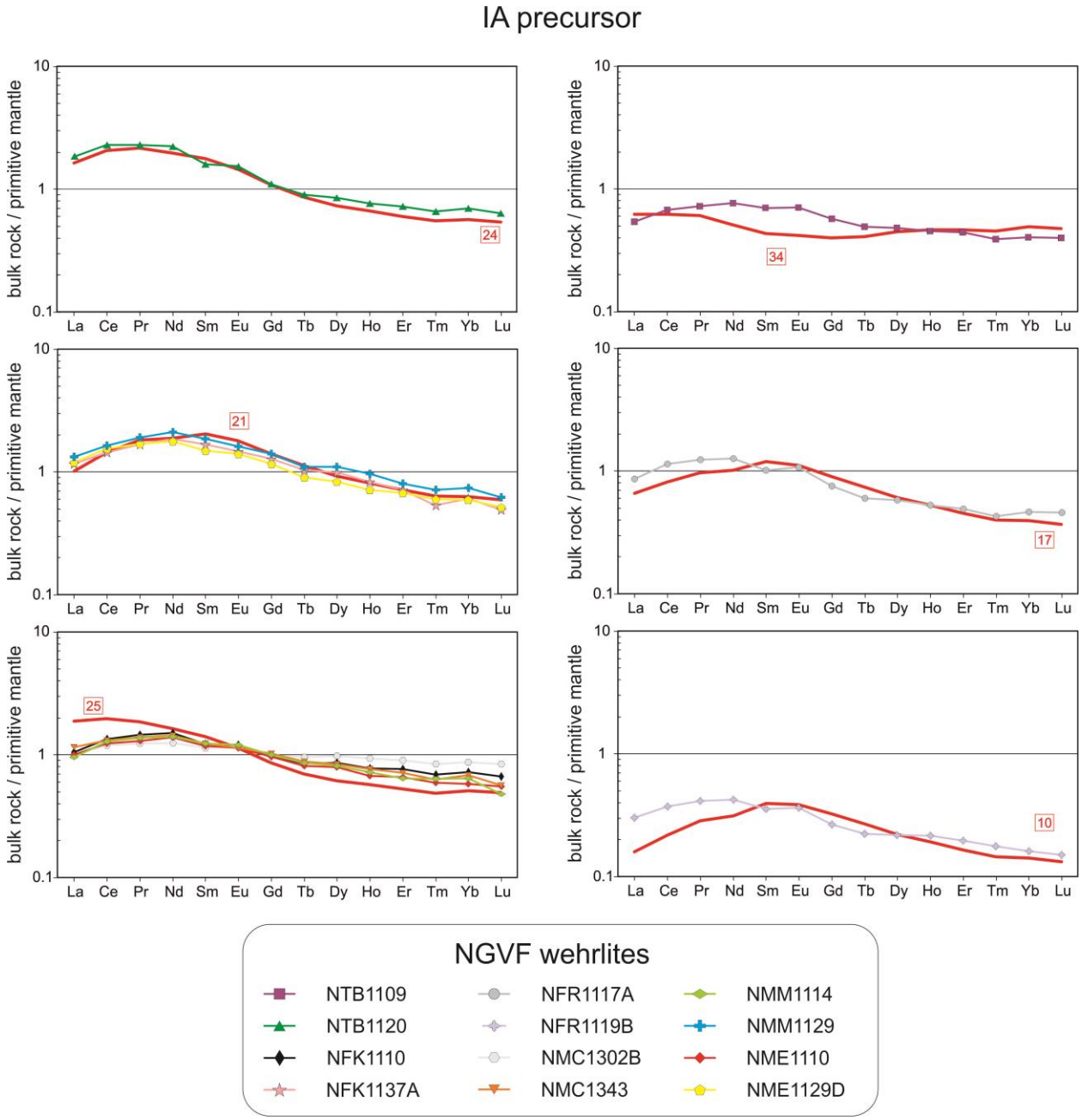

Figure 5.8 Comparison between bulk rock REE distributions of the NGVF wehrlite xenoliths and the best fitting cells (with cell numbers and solid red line) of the plate model (Vernières et al., 1997). The best fitting was determined by applying the least squares method. The wall rock precursors of the best fitting cells are indicated and either belong to Group IA or Group IB/2 lherzolite xenoliths with depleted or flat bulk rock REE patterns, respectively (based on Liptai et al., 2017).

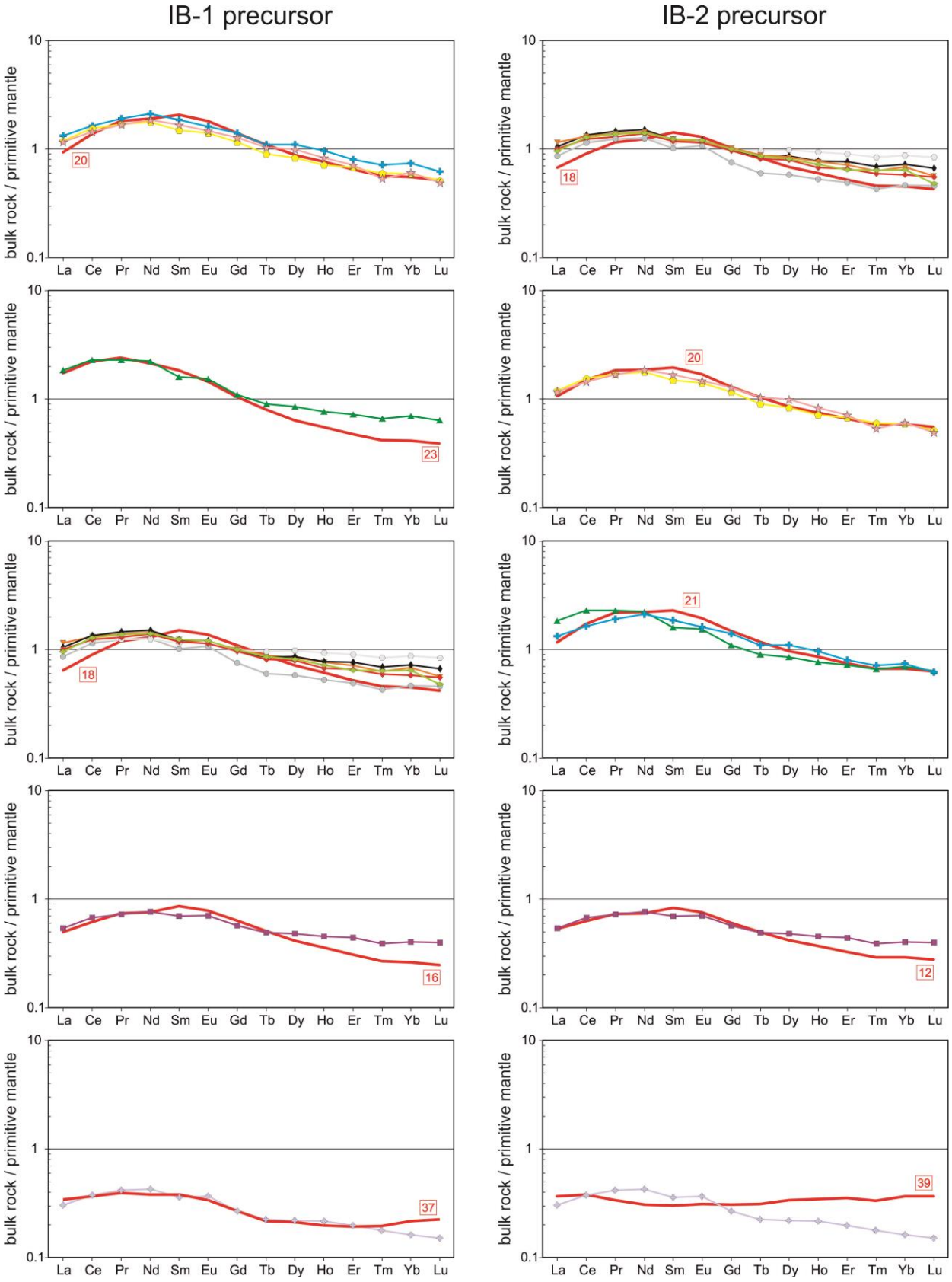

Fig. 5.8. Continued

In order to determine the most realistic model output, (i.e., that which best describes the precursor, namely best fitting cell), the measured (in the thin section) and computed (modelled) REE concentrations were compared to each other by calculating the sum of the squared differences. The model (Appendix 11) that shows the best fit to the data is characterized by the lowest sum of the square values calculated from the measured and modelled values. This method is similar to the calculation of the mean squared error (MSE) applied generally in regression analysis (Montgomery et al., 2012).

Comparison of the bulk REE patterns between the best fitting cells and the NGVF wehrlites resulted in mostly good agreement (Fig. 5.8). In four xenoliths (NTB1120, NFR1117A, NMC1302B, NMM1129) the best fitting cells were obtained using a depleted Group IA lherzolite precursor (Fig. 5.8). In the rest of the xenoliths (NTB1109, NFK1110, NFK1137A, NMC1343, NMM1114, NME1110, NME1129D) the assumed precursor is Group IB/2 lherzolite with a flat REE pattern and in one case (NFR1119B) the precursor is Group IB/1 lherzolite with convex upward REE pattern. This obviously suggests that all Group IA and IB lherzolites are potential precursors, demonstrating that the wehrlitization occurred after the formation of mantle domains with these geochemical characteristics. Another important observation is that wehrlitization results in the affected mantle domain having uniform petrographic and geochemical characteristics (as indicated by the similar bulk REE patterns of the NGVF wehrlites), regardless of variations in the precursor lherzolites (Fig. 4.10).

In addition to the bulk REE patterns, the modal compositions of the chosen modelled cells (Appendix 8; 9; 10) were compared to the NGVF wehrlites (Table 2). Accordingly, the best fitting cells are dominantly wehrlites (Table 17), but with lower clinopyroxene contents and a narrower modal range (11–14 vol. %) compared to the NGVF wehrlites (10–24 vol. %; Table 2). The only exception is xenolith NFR1119B, where the best fitting cell is a clinopyroxene-rich lherzolite Table 17). The modelled melt/rock ratios are mostly between 0.30 and 0.33 (Table 17), with the exception of xenoliths NTB1109, NFR1119B and xenoliths NFR1117A, NMC1302B and NMM1129, in which the lowest (0.22 and 0.18) and the highest (0.39, 0.39 and 0.37) melt/rock ratios were observed, respectively. These values are in good agreement with experimental results simulating the wehrlitization process (discussed above in section 5.2.3.). Xenoliths NTB1109 and NFR119B are weakly metasomatized, whereas NFR1117A and NMM1129 are significantly

Table 17. Best fitting modelled cell results of the plate model (Vernières et al., 1997) calculations linked to the studied Nógrád-Gömör wehrlites. The best fitting cells were chosen using the least squares method. Clinopyroxene-rich lherzolite is a peridotite, where the modal composition of clinopyroxene > orthopyroxene.

Sample	NTB1109	NTB1120	NFK1110	NFK1137A	NFR1117A	NFR1119B	NMC1302B	NMC1343	NMM1114	NMM1129	NME1110	NME1129D
Precursor	IB-2	IA	IB-2	IB-2	IA	IB-1	IA	IB-2	IB-2	IA	IB-2	IB-2
Cell	12	24	18	20	17	37	18	18	18	21	18	20
La	0.346	1.065	0.436	0.692	0.426	0.221	0.447	0.436	0.436	0.658	0.436	0.692
Ce	1.060	3.454	1.509	2.490	1.355	0.610	1.471	1.509	1.509	2.407	1.509	2.490
Pr	0.185	0.553	0.294	0.469	0.247	0.099	0.280	0.294	0.294	0.462	0.294	0.469
Nd	0.927	2.468	1.539	2.333	1.272	0.474	1.471	1.539	1.539	2.340	1.539	2.333
Sm	0.337	0.721	0.577	0.792	0.487	0.153	0.569	0.577	0.577	0.825	0.577	0.792
Eu	0.116	0.223	0.199	0.260	0.172	0.051	0.200	0.199	0.199	0.276	0.199	0.260
Gd	0.331	0.589	0.559	0.707	0.493	0.144	0.573	0.559	0.559	0.761	0.559	0.707
Tb	0.049	0.086	0.082	0.102	0.073	0.021	0.085	0.082	0.082	0.111	0.082	0.102
Dy	0.283	0.496	0.461	0.575	0.409	0.141	0.474	0.461	0.461	0.624	0.461	0.575
Ho	0.055	0.100	0.089	0.112	0.079	0.029	0.091	0.089	0.089	0.122	0.089	0.112
Er	0.143	0.264	0.228	0.289	0.199	0.084	0.232	0.228	0.228	0.312	0.228	0.289
Tm	0.020	0.037	0.031	0.040	0.027	0.013	0.032	0.031	0.031	0.043	0.031	0.040
Yb	0.129	0.249	0.201	0.258	0.174	0.095	0.203	0.201	0.201	0.278	0.201	0.258
Lu	0.019	0.036	0.029	0.037	0.025	0.015	0.029	0.029	0.029	0.040	0.029	0.037
Melt/Rock	0.220	0.330	0.311	0.307	0.391	0.178	0.388	0.311	0.311	0.368	0.311	0.307
Rock name	wehrlite	wehrlite	wehrlite	wehrlite	wehrlite	cpx-rich lhz	wehrlite	wehrlite	wehrlite	wehrlite	wehrlite	wehrlite
ol	87	82	87	86	86	79	85	87	87	84	87	86
opx	0	2	0	0	0	8	0	0	0	0	0	0
cpx	11	14	11	12	13	10	13	11	11	14	11	12
sp	2	2	2	2	2	2	2	2	2	2	2	2
amph	0	0	0	0	0	0	0	0	0	0	0	0

Abbreviations: ol - olivine, opx - orthopyroxene, cpx - clinopyroxene, sp - spinell, amph - amphibole, cpx-rich lhz - clinopyroxene-rich lherzolite

affected by the metasomatic agent (Fig. 5.5), indicating that the degree of the metasomatism and the melt/rock ratio correlates. The high modelled melt/rock ratio (0.39) in xenolith NMC1302B is accompanied by high Mg# (0.87 in olivine and 0.89 in clinopyroxene) and flat REY pattern for clinopyroxene (type II; Fig. 4.8b), and the reason for this behavior is unclear. However, the model fit for this xenolith was poor (Fig. 5.8). Probably this xenolith was affected by another, undefined process as well.

In conclusion, the bulk REE patterns of wehrlites were reproduced with the plate model using depleted IA, flat and convex upward IB precursor lherzolite REE patterns and reactant melt with OIB composition (Fig. 5.8). This modelling comfirms the assumption of Liptai et al. (2017) that wehrlitization represents the last event in the geochemical evolution of the upper mantle beneath the NGVF. The results of the modelling also suggest that melt/rock ratio plays a key role in the degree of petrographic and geochemical transformation of the wall rock. In contrast, the characteristics of the precursors have little effect on the features of the metasomatic product, namely the wehrlite.

5.6. Hydration state of the upper mantle during the wehrlitization

5.6.1. Interpretation of the infrared spectra

Metasomatism can modify the hydration state and hence the infrared spectra characteristics of the upper mantle (e.g., Demouchy and Bolfan-Casanova, 2016 and references therein). Due to the lack of measurable orthopyroxene grains and missing structural hydroxyl-related bands in olivines, only the clinopyroxene spectra can be discussed here. The main hydroxyl bands in NGVF clinopyroxenes, located at ~3630 and ~3525 cm^{-1} (Fig. 4.11), agree well with those reported in natural samples all over the world (Peslier et al., 2002b; Bonadiman et al., 2009; Xia et al., 2010; 2013a; 2013b; Yu et al., 2011; Demouchy et al., 2015; Denis et al., 2015; Li et al., 2015; Pintér et al., 2015; Hao et al., 2016a; Aradi et al., 2017). The most common (78 %) spectrum type of the NGVF wehrlitic clinopyroxenes is characterized by more intense peak at ~3630 cm^{-1} than at other positions (type 1; Fig. 4.12). Similarly, the NGVF lherzolites are dominantly (67 %) belong to the type 1 group (Patkó et al., 2019). This observation in the NGVF is consistent with clinopyroxene spectra reported by other studies, irrespective of their tectonic setting (Bonadiman et al., 2009; Xia et al., 2013a; Pintér et al., 2015). Spectra with equal (type 2a in my nomenclature) or higher intensity (type 2b in my nomenclature) of the peak at 3525 relative to the one at ~3630 cm^{-1} are

present among the wehrlitic (9 and 13 %, respectively) as well as the lherzolitic clinopyroxenes (14 and 19 %, respectively; Patkó et al., 2019). Moreover, such spectra have also been described from the North China Craton, albeit in significantly lower abundance (Xia et al., 2010; 2013b; Li et al., 2015).

It is widely accepted that different stretching bands of structural hydroxyl on the FTIR spectra represent different modes of structural hydroxyl incorporation into NAMs (e.g., Beran and Putnis, 1983). However, the incorporation mechanisms of structural hydroxyl in clinopyroxene are not yet fully understood. Nevertheless, the different bands are possibly linked to incorporation of coupled hydroxyl and trivalent cations or structural hydroxyls in vacant M- and Si-sites (Stalder and Ludwig, 2007). Bands at high wavenumbers (~3675–3695 cm^{-1}) (Fig. 4.12) can be ascribed to hydrous mineral lamellae, most probably amphibole (Ingrin et al., 1989; Della Ventura et al., 2007). Such bands are more common in clinopyroxenes from the wehrlites than in lherzolites in the NGVF (Patkó et al., 2019).

5.6.2. Implications of the structural hydroxyl contents

All wehrlitic olivines are completely 'dry' (i.e. structural hydroxyl is below the limit of detection (≪1 ppm)). This is also the case in most of the NGVF lherzolites with the exception of the Jelšovec (NJS) xenoliths (Fig. 2.5), which show weak structural hydroxyl related bands and have only very low structural hydroxyl contents (~2–4 ppm; Patkó et al., 2019). This observation is inconsistent with the generally higher structural hydroxyl contents reported from other localities in the Carpathian-Pannonian region (CPR) so far. Olivines in the Styrian Basin (SBVF) and Perşani Mountains (PMVF), located at the western and eastern edges of the CPR, respectively (Fig. 2.1), have 3–16 ppm (with an average of ~8 ppm) (Schmädicke et al., 2013; Aradi et al., 2017) and 2–15 ppm (with an average of ~7 ppm) (Falus et al., 2008; Lange et al., 2019) structural hydroxyl (Fig. 5.9a). This agrees well with olivine data from off-craton settings (Peslier, 2010; Demouchy and Bolfan-Casanova, 2016; Peslier et al., 2017; Fig. 5.9a). However, these low values are not unprecedented as similarly 'dry' xenoliths have been reported from several locations in China (Yang et al., 2008; Bonadiman et al., 2009; Xia et al., 2010; 2013b; Hao et al., 2016a; Zhang et al., 2018), France (Gu et al., 2018) and USA (Denis et al., 2018).

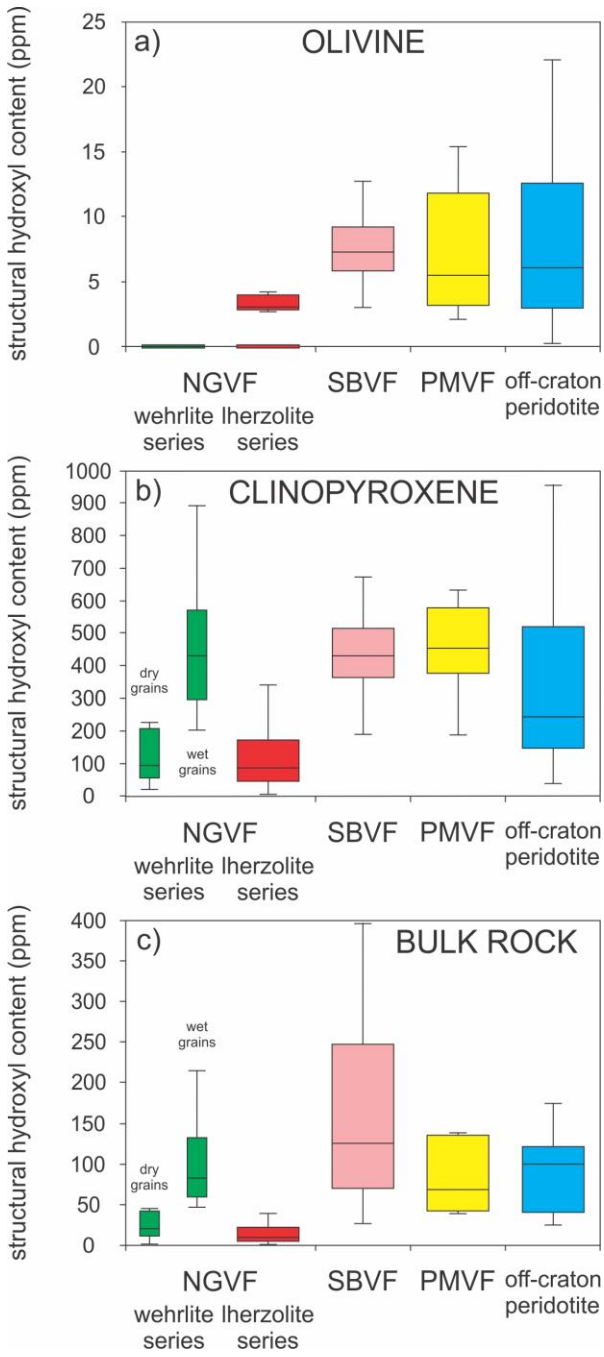

Figure 5.9 Box and whisker diagram of the structural hydroxyl content of **(a)** olivine **(b)** clinopyroxene and **(c)** bulk rock from CPR wehrlite (Nógrád-Gömör) and lherzolite xenoliths (Nógrád-Gömör, Styrian Basin, Perșani Mountains) and worldwide off-craton peridotites. The box and whisker diagram is a visualized version of five-parameters including minimum and maximum values, first and third quartile and the median. Note that the wehrlite and lherzolite xenolith series, as well as the dry and wet grains of wehrlitic clinopyroxenes are distinguished for NGVF. Data sources are the following: Schmädicke et al., 2013 and Aradi et al., 2017 for SBVF xenoliths, Falus et al., 2008; Kovács et al., 2016 and Lange et al., 2019 for PMVF and Peslier, 2010 and references therein for the off-craton peridotites. Abbreviations: NGVF - Nógrád-Gömör Volcanic Field; SBVF - Styrian Basin Volcanic Field; PMVF - Perșani Mountains Volcanic Field.

In order to have implication on the structural hydroxyl concentration of olivines being in equilibrium with pyroxenes, an estimation was carried out based on the structural hydroxyl content of clinopyroxenes and the partition coefficient of hydrogen between clinopyroxene and olivine. The estimated structural hydroxyl concentrations of olivines (2–89 ppm; Table 9) are higher than the aforementioned references and are often around the structural hydroxyl saturation (32–190 ppm) based on experimental runs (Kovács et al., 2012b).

Clinopyroxenes have detectable structural hydroxyl concentrations in all NGVF wehrlites (Table 9) and in almost all lherzolites (Patkó et al., 2019). The wehrlitic clinopyroxene values are variable (Fig. 5.9) due to the concomitant dry (21–464 with an average of 140 ppm) and wet grains (202–894 with an average of 481 ppm) within a single xenolith (Fig. 4.11). The dry grains have equal, whereas the wet grains have higher structural hydroxyl content compared to the clinopyroxenes from NGVF lherzolites (1–481 with an average of 133 ppm; Patkó et al., 2019). Even though some clinopyroxenes include bands related to hydrous minerals at high wavenumbers (~3675–3695 cm^{-1}; Fig. 4.11), the structural hydroxyl contents may be considered as robust, since these lamellae may have formed at the expense of structural hydroxyl in their host pyroxene (e.g., Kang et al., 2017; Schmädicke and Gose, 2017). Even if the source of excess hydroxyl for the formation of hydrous lamellae had been external, their spectral contribution would only cause a subtle overestimation (up to 5 ppm based on the integrated area of amphibole shoulder at 3695 cm^{-1} and the wavenumber specific calibration of Libowitzky and Rossman, 1997).

All in all, the dry clinopyroxenes have lower, whereas the wet clinopyroxenes have similar structural hydroxyl contents compared to those in other xenolith bearing localities in the CPR, which show an average of 433 ppm (values between 190–674 ppm) and 458 ppm (for a range of 186–632 ppm) in the SBVF (Aradi et al., 2017) and PMVF (Falus et al., 2008; Kovács et al., 2016; Lange et al., 2019), respectively (Fig. 5.9b). The SBVF and PMVF values overlap with structural hydroxyl contents from off-cratonic xenoliths worldwide (Peslier, 2010; Demouchy and Bolfan-Casanova, 2016; Peslier et al., 2017; Fig. 5.9b). This suggests that the structural hydroxyl content of the Nógrád-Gömör lherzolites and the dry clinopyroxenes in wehrlites are low not only on a regional, but also on a global scale. In contrast, the clinopyroxenes in wehrlites referred to be wet are just locally enriched in hydrogen, in fact those values agree well with the regional and global values.

The estimated bulk rock structural hydroxyl contents applying dry and wet clinopyroxenes show higher values for wehrlites than for the lherzolites in the NGVF (Patkó et al., 2019; Fig. 5.9c). The dry clinopyroxene-based bulk rock data are lower, whereas the wet clinopyroxene-based bulk rock data are similar to those in the SBVF (average of 452 ppm; Aradi et al., 2017) and the PMVF (average of 103 ppm; Falus et al., 2008; Lange et al., 2019). The wet clinopyroxene-based bulk rock data are also akin to the off-cratonic xenoliths worldwide (Peslier, 2010; Demouchy and Bolfan-Casanova, 2016; Peslier et al., 2017; Fig. 5.9c). It should be noted that most of the SBVF xenoliths contain amphibole (up to 32 vol. %), which significantly increases the bulk structural hydroxyl contents (Aradi et al., 2017). However, even considering this, the bulk structural hydroxyl content of NGVF xenoliths is still relatively low compared to the SBVF data (Fig. 5.9c).

5.6.3. Relationship between geochemical variables and the hydroxyl content

Hydrogen is a highly incompatible element ($D^{peridotite/melt}$ (H_2O) is ~0.001–0.01; Hirschmann et al., 2009) with even lower partition coefficients than La and Ce ($D^{cpx/melt}$ (La) is ~0.05 and $D^{cpx/melt}$ (Ce) is ~0.086, respectively, Hart and Dunn, 1993). Although Hao et al. (2014) suggested a higher partition coefficient for hydrogen ($D^{peridotite/melt}$ (H_2O) is ~0.1), this value is still around that of Ce, which suggests that hydrogen reacts rapidly to depletion or enrichment. Therefore, the relationship between the structural hydroxyl contents and different geochemical variables of NAMs has been widely studied. However, in some cases either no correlation (Falus et al., 2008; Bonadiman et al., 2009; Hao et al., 2016a) or only a weak one has been found (Peslier et al., 2002b; Soustelle et al., 2010; Yu et al., 2011; Hao et al., 2012; 2016b; Doucet et al., 2014; Li et al., 2015; Demouchy et al., 2015; Peslier and Bizimis, 2015; Baptiste et al., 2015; Kilgore et al., 2018; Marshall et al., 2018).

The relationship between the structural hydroxyl contents of wet wehrlitic clinopyroxenes and the major element composition of clinopyroxenes is weak (e.g., r^2=0.003 with FeO; r^2=0.171 with TiO_2; r^2=0.392 with Al_2O_3 and r^2=0.128 with MnO). In this correlation, clinopyroxenes with orthopyroxenes in their core (cpx^{opx}) were not considered because their compositions were highly modified by the dissoluted orthopyroxenes (see details in chapter 5.2.3.). This weak correlation is positive for basaltic elements such as FeO, MnO and TiO_2 (Fig. 5.10a-c). Since the enrichment of these elements is suggested to be linked to the wehrlite formation (see details in chapter 5.2.2.) it

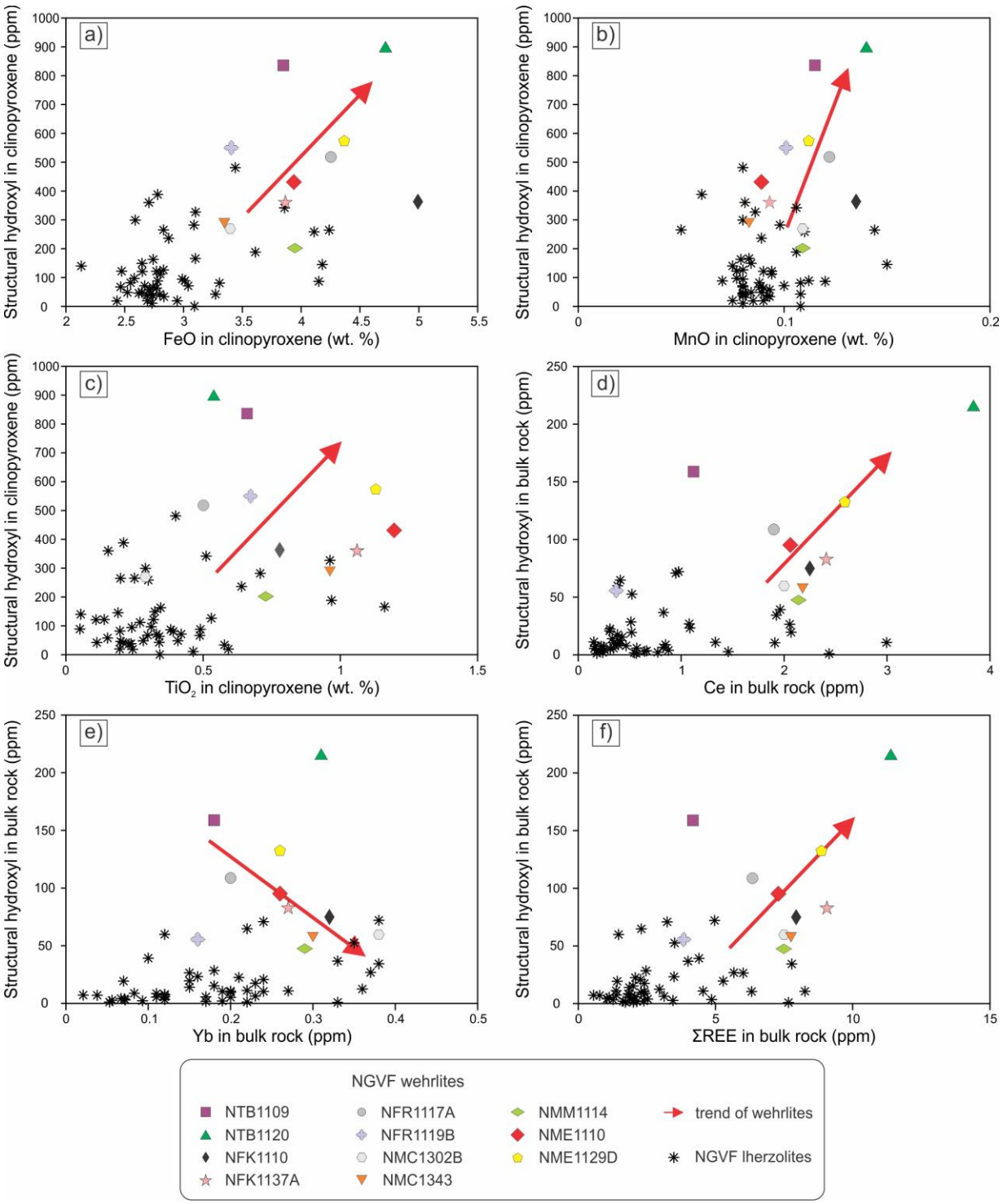

Figure 5.10 Structural hydroxyl content of clinopyroxene in the Nógrád-Gömör wehrlite xenoliths compared with different major elements: **(a)** FeO **(b)** MnO and **(c)** TiO_2. In these plots, clinopyroxenes with relict orthopyroxenes (cpx^{opx}) were not considered. Bulk rock structural hydroxyl contents are also compared with selected trace elements: **(d)** Ce **(e)** Yb and **(f)** ΣREE. Geochemical data of the NGVF lherzolite xenoliths are taken from Liptai et al. (2017), whereas their structural hydroxyl content is from Patkó et al. (2019).

seems reasonable to connect the behavior of the structural hydroxyl to the same metasomatic event. In case of the bulk rock data the structural hydroxyl content shows positive correlation with LREE (Fig. 5.10d), in contrast, its relationship is negative with HREE (Fig. 5.10e). The ΣREE shows positive relationship with structural hydroxyl content (Fig. 5.10f). In summary, the geochemical proxies of the wehrlitization, including basaltic major elements and LRE trace elements, have a weak correlation with the structural hydroxyl content, indicating that the wehrlite formation slightly enriched the affected mantle volume in hydrogen.

The question ariased why do hydrogen and basaltic major elements and LREE transported by the same metasomatic agent have disproportional enrichments? There are several different reasons that can explain this decoupling. Marshall et al. (2018) suggested that the large diffusivity of hydrogen in peridotites resulted in re-equilibrium, which could erase the metasomatism-induced differences in structural hydroxyl contents. Consequently, the structural hydroxyl content decreases in the metasomatized veins or channels but increases in the surrounding wall rocks over geological times (Marshall et al., 2018). Such a re-equilibration is much slower for divalent cations or trivalent REE due to their slower diffusion (10^{-18}–10^{-22} m^2/s at ~1000 ˚C, Cherniak and Dimanov, 2010 and 10^{-19}–10^{-22} m^2/s at ~1000 ˚C, Cherniak and Liang, 2007, respectively) compared to hydrogen (10^{-9}–10^{-14} m^2/s at ~1000 ˚C, Tian et al., 2017), which may explain the decoupling between these elements. The wehrlitization in Nógrád-Gömör possibly happened just before the xenolith entrapment as implied by the presence of orthopyroxene relicts in clinopyroxenes (Fig. 4.2g), intragranular compositional inhomogeneities in the rock-forming minerals (Fig. 4.4), and partially glassy silicate melt inclusions in clinopyroxenes and olivines (Patkó et al., 2018). Furthermore, the presence of dry and wet grains within a single xenolith (Fig. 4.11) suggests structural hydroxyl disequilibrium. Therefore, it is unlikely that re-equilibrium is responsible for the element decoupling.

There are processes (e.g., temperature-driven annealing, oxidation, pressure loss), which can lead to significant hydrogen loss with smaller effect on other elements in xenoliths, hence causing decoupling between them. Peslier and Luhr (2006) pointed out that xenoliths may lose notable proportions of their structural hydroxyl content mainly because of oxidation while being carried by the host magma during ascent, especially in case of an alkali basalt host, which moves more slowly than lamprophyre or kimberlite magmas (Kelley and Wartho, 2000). The calculated ascent rate for the alkali basalt magma in the NGVF is only 0.1 ms^{-1} beneath the Moho, and 5 ms^{-1} in the

crust (Szabó and Bodnar, 1996). Since there are evidences for syn- and post-eruptive structural hydroxyl loss in Nógrád-Gömör xenoliths discussed in chapter 5.6.4. This phenomenon can be a possible reason for moderate relationship between the structural hydroxyl content and variable geochemical parameters (Fig. 5.10). Theoretically, oxidation caused by the host magma can also lead to low structural hydroxyl contents in xenoliths (Peslier et al., 2002b). However, the oxygen fugacity (fO_2) values show no relationship with the structural hydroxyl contents in NGVF (Patkó et al., 2019). This implies that oxidation-related modification of structural hydroxyl contents probably did not occur in the upper mantle nor during entrainment in the host magma.

Additionally, the migration of melts can either modify (Doucet et al., 2014; Gu et al., 2018) or leave unchanged (Denis et al., 2015; Hao et al., 2016b) the structural hydroxyl content of the upper mantle, depending on the water activity in the melt agent. Note that dissolved volatiles, especially CO_2, can significantly influence the water activity in melts. Based on experiments, the higher the CO_2 content of a melt, the lower its water activity (e.g., Sokol et al., 2013). The presence of abundant primary CO_2 fluid inclusions in metasomatized Nógrád-Gömör xenoliths (Szabó and Bodnar, 1996; 1998) suggests that high amounts of CO_2 were previously dissolved in the melt, and therefore its water activity was probably low. In contrast, the structural hydroxyl enrichment in wet clinopyroxene grains in wehrlites (Fig. 5.9b) rather calls for a melt agent having elevated water activity. Since the water activity during metasomatism is changing independently from major and trace elements and is influenced mostly by phase relations (Shaw et al., 2018), a link between hydrogen and other elements carried by the metasomatic agent is not necessary.

5.6.4. Possible explanations for the structural hydroxyl contents in wehrlites

Olivines have no structural hydroxyl related bands neither in NGVF wehrlites nor in lherzolites, with the exception of those collected from Jelšovec locality (Patkó et al., 2019). The diffusional structural hydroxyl loss at very shallow depths or on the surface can be a plausible reason for this feature. The alkali basalts in the SBVF or PMVF probably have similar ascent rates to that was determined for the NGVF (Szabó and Bodnar, 1996). However, unlikely to the NGVF, these two localities have detectable amount of structural hydroxyl content in olivines (Fig. 5.9a). Therefore, it is rather unlikely that a decrease in structural hydroxyl content during ascent is the only explanation for the dry olivines in the NGVF. In the NGVF, the alkali basalt volcanism produced several volcanic edifices including maars, diatremes, tuff cones, cinder/spatter cones and

lava flows (e.g., Konečný et al., 1995a). The numerous slowly cooling lava flows built several 'massive' basalt plateaus (e.g., Medves Plateau, Babi Hill; Fig. 2.5). The majority of the xenoliths are hosted in such lava flows, with the exception of Jelšovec, where the host rock is pyroclastic, forming a maar. Mnatle xenoliths from Jelšovec are the only samples in the NGVF that contain detectable amounts of structural hydroxyl in olivines and higher concentrations in pyroxenes (Patkó et al., 2019). Accordingly, it is suggested that the type of the host rock (i.e. pyroclast vs. 'massive' lava flow) plays a significant role in modifying the structural hydroxyl content. This assumption is supported by the fact that olivines carrying structural hydroxyl in upper mantle xenoliths from other volcanic fields of the CPR (i.e., Styrian Basin and Perşani Mts.) are also hosted predominantly in pyroclastic successions (Falus et al., 2008; Aradi et al., 2017).

In conclusion, xenoliths in pyroclastic rocks appear to preserve their 'original' structural hydroxyl content better than those in lavas. This is due to the faster cooling rate of pyroclastics compared to 'massive' lava flows where the temperature could remain high enough for a longer period of time. Similar conclusions also have been drawn by Lloyd et al. (2016) and Biró et al. (2016). They found that clinopyroxene and quartz phenocrysts show higher structural hydroxyl contents and are closer to equilibrium with their host rocks in volcanic successions, which went through rapid cooling after deposition (i.e. volcanic ash, pyroclastic deposits and basal layers of ignimbrites). The time-span for post-deposition cooling (weeks, maybe months) in most cases is only enough to change the structural hydroxyl content in olivines, in which the diffusion is fast (10^{-11}–10^{-9} m^2/s at 1100 °C; Tian et al., 2017). However, it is not enough to trigger significant modification in the pyroxenes, in which diffusion is slower (10^{-14}–10^{-11} m^2/s at 1100 °C; Tian et al., 2017). Thus olivines are highly sensitive indicators of syn- and post-eruptive loss of structural hydroxyl. Consequently, the presence of 'dry' olivines in the investigated upper mantle xenoliths indicate that considerable loss of hydrogen may have taken place during the post-depositional slow cooling of the lava flows in the NGVF.

Clinopyroxenes in wehrlites have dominantly type 1 spectra (Fig. 4.12). The proportion of anomalous spectra (type 2a, 2b) is lower in wehrlites (22 %) than in lherzolites (33 %; Patkó et al., 2019). This implies that the anomalous spectra characteristics formed by different responses of substitution mechanisms to the structural hydroxyl loss (Patkó et al., 2019) were often overprinted during the wehrlitization. The wet grains are likely equilibrated with the metasomatic melt agent which had high water activity. The similarity of structural hydroxyl content of wet clinopyroxene

grains to the SBVF (Aradi et al., 2017) and PMVF clinopyroxenes (Falus et al., 2008; Lange et al., 2019) (Fig. 5.9b) implies that the metasomatic melt was not extremely rich in hydrogen, which is true for OIBs (0.2–1.6 wt. % H_2O content; Herzberg and Asimow, 2008). The reason why the intra-xenolith structural hydroxyl heterogeneities do not disappear via diffusive equilibration can be that the metasomatism happened just before entrapment of the xenoliths in the uprising basaltic melt.

5.7. The effect of wehrlitization on the electrical resistivity of the upper mantle

Several studies in the past two decades revealed that the structural hydroxyl content of nominally anhydrous minerals (NAMs) plays an important role on electrical resistivity (Wang et al., 2006; Dai and Karato, 2009; Yoshino et al., 2009; Poe et al., 2010; Yang et al., 2011; Jones et al., 2012; Novella et al., 2017). According to these researches, the greater the structural hydroxyl content in the mantle, the lower the electrical resistivity. The presence of wet clinopyroxenes with high structural hydroxyl contents (>202 ppm; Table 9) in the NGVF wehrlites causes high structural hydroxyl concentrations in the bulk rock (>62 ppm; Table 9) suggesting that wehrlites have lower electrical resistivity than 'dryer' lherzolites (Patkó et al., 2019: Fig. 5.9c). Other factors like modal composition, geochemical characteristics and pressure-temperature conditions all have influence on the electrical resistivity, but their effect is less significant (Selway, 2014; Fullea, 2017). According to Karato and Wang (2013), the electrical resistivity of mantle silicates is the following in decreasing order: olivine, orthopyroxene, clinopyroxene. Indeed, clinopyroxene has the lowest electrical resistivity among the mantle silicates beneath the NGVF (Fig. 4.13a). It follows that the elevated clinopyroxene content in wehrlites (~21 vol. %; Table 2) compared to the lherzolites (~9 vol. %; Liptai et al., 2017) results in lower electrical resistivity. The greater iron concentration in the mineral phases (Fig. 4.3), and consequently in bulk rocks (Fig. 4.9), supports lower electrical resistivity (Hinze et al., 1981; Seifert et al., 1982; Omura et al., 1989; Yoshino et al., 2012). Based on experiments conducted with multi-anvil apparatus, increasing pressure and temperature considerably lowers the electrical resistivity in olivines (Xu et al., 2000; Yoshino et al., 2012), whereas in pyroxenes this effect is minimal (Dai et al., 2006). There is a small difference in the pressure-temperature conditions of the NGVF wehrlites (985–1055 with an average of 1014 ˚C using $T_{Ca\text{-}in\text{-}opx\ by\ NG10}$ and 1.3–1.6 PGa; Table 2) and lherzolites (921–1044 with an average of 973 ˚C using $T_{Ca\text{-}in\text{-}opx\ by\ NG10}$ and 1.2–1.5 PGa; Liptai et al., 2017), which may

have a weak additional role in the decreased electrical resistivity of the former. As a conclusion, parameters that influence the electrical resistivity of the mantle rocks are consequently higher in the wehrlites than in the lherzolites. This suggests that the wehrlitization has an effect on the electrical resistivity of the affected mantle volume. Interestingly, the electrical resisitivity of wehrlites with wet characteristics agree well with that in perisdotites from Styrian Basin and Perșani Mountains (Fig. 4.13b), which have high bulk structural hydroxyl contents due to former subduction events (Falus et al., 2008; Aradi et al., 2017; Lange et al., 2019).

Novák et al. (2014) investigated the electrical resistivity of the lithosphere beneath the NGVF applying long period magnetotellurics (MT) in 14 stations along a NW-SE profile. According to the results, a low resistivity anomaly (~5–10 Ωm) was observed at 30–45 km depth below the central part of the NGVF (Novák et al., 2014). This is the region where the wehrlite xenoliths with low electrical resistivity occur (Fig. 2.5). Thus, it is reasonable to assume that the MT measurements reveal the distribution of wehrlitization. Based on this presumption, the metasomatism affected a large volume of the mantle (~30 km long and ~15 km thick), also suggesting that migration of the metasomatic melt along grain boundaries was probably extensive. Note however, that there is a discrepancy between the calculated and the measured resistivity values. Although the proportion of dry and wet grains is unknown in the wehrlites, their bulk electrical resistivity is likely no lower than 40–60 Ωm, which is considerably higher than the measured values. Graphite films on grain boundaries (Mareschal et al., 1995; Glover, 1996; Santos et al., 2002; Jones et al., 2003) or the presence of interconnected fluids/melt (Desissa et al., 2013; Johnson et al., 2016; Ebinger et al., 2017; Magee et al., 2018; Selway et al., 2019) can explain this difference. The appearance of graphite was not confirmed, hence its effect on lowering the electrical resistivity is unlikely. In contrast, the presence of fluids and melts are proved by fluid (Szabó and Bodnar, 1996; 1998) and melt inclusion (Szabó et al., 1996; Patkó et al., 2018) studies. Furthermore, the wehrlite and cumulate formation (Kovács et al., 2004; Zajacz et al., 2007; Patkó et al. 2020) suggest intensive fluid and melt migration especially beneath the central NGVF. The last phase of NGVF volcanism ceased about 0.3 Ma ago in the central part of the volcanic field (Hurai et al., 2013). Since the longevity of such systems may span on the magnitude of 100 ka (Bourdon et al., 1994), some fluids or melts may still exist in the upper mantle beneath the central NGVF, which can lead to a decrease in the electrical resistivity.

5.8. Implications from sulfides hosted by wehrlites

5.8.1. Physical and chemical characteristics of sulfide formation

The sulfide distribution in wehrlite xenoliths shows no spatial relationship with the host basalt or its infiltrations. This observation indicates that all of the wehrlitic sulfides were formed in the upper mantle before xenolith entrapment. Upper mantle sulfides are variable in origin and may represent trapped sulfide melt drops after partial melting events (Szabó and Bodnar, 1995; Pearson et al., 2004; Luguet et al., 2007) or may have been formed during melt metasomatic events (Lorand et al., 2004; Ackerman et al., 2009b; Wainwright et al., 2015; Harvey et al., 2015).

Several lines of evidence support that the sulfides in wehrlites were formed by the same metasomatic melt that modified the rock-forming mineral compositions. The most significant argument is the higher sulfide content of wehrlites (~0.04 vol. %) compared to the precursor lherzolite xenoliths (~0.01 vol. %). This is further supported by the observation that e-type sulfides in wehrlites appear dominantly in olivine and clinopyroxene (Table 11), which are the newly formed minerals during wehrlitization (Fig. 4.2g). Additionally, the pyrrhotite-dominated (Table 11) wehrlitic sulfides have higher bulk Fe and lower Ni contents compared to the lherzolitic sulfides (Fig. 4.15; 4.15), which is consistent with the Fe-enrichment of the rock-forming minerals (Fig. 4.3). If we compare the Fe- and Ni contents of wehrlitic sulfides and silicates, a positive and a negative correlation can be observed, respectively (Fig. 5.11). This indicates a common metasomatic event affecting the geochemistry of both sulfides and silicates in wehrlite xenoliths.

As depicted on Fig. 5.11, major element contents of the wehrlitic sufides correlate with the degree of metasomatism defined by the petrographic and geochemical characteristics of the rock-forming minerals (Fig. 5.6). Indeed, sufides of the weakly-metasomatized NTB1109, NFR1119B and NMC1302B wehrlite xenoliths have the highest Ni content, whereas the sulfides in the highly-metasomatized NTB1120, NFK1110 and NMM129 wehrlite xenoliths have the highest Fe content (Fig. 5.11).

Sulfides must have been precipitated during wehrlitization due to the formation of minerals enriched in Fe (olivine, clinopyroxene) (Fig. 4.3) which led to Fe loss and Si enrichment in the residual melt, resulting in lowering the sulfur concentration for sulfide saturation level (Haughton et al., 1974; O'Neill and Mavrogenes, 2002). Additionally, the higher the pressure, the lower amount of sulfur is needed for sulfide saturation (Mavrogenes and O'Neill, 1999). The wehrlite

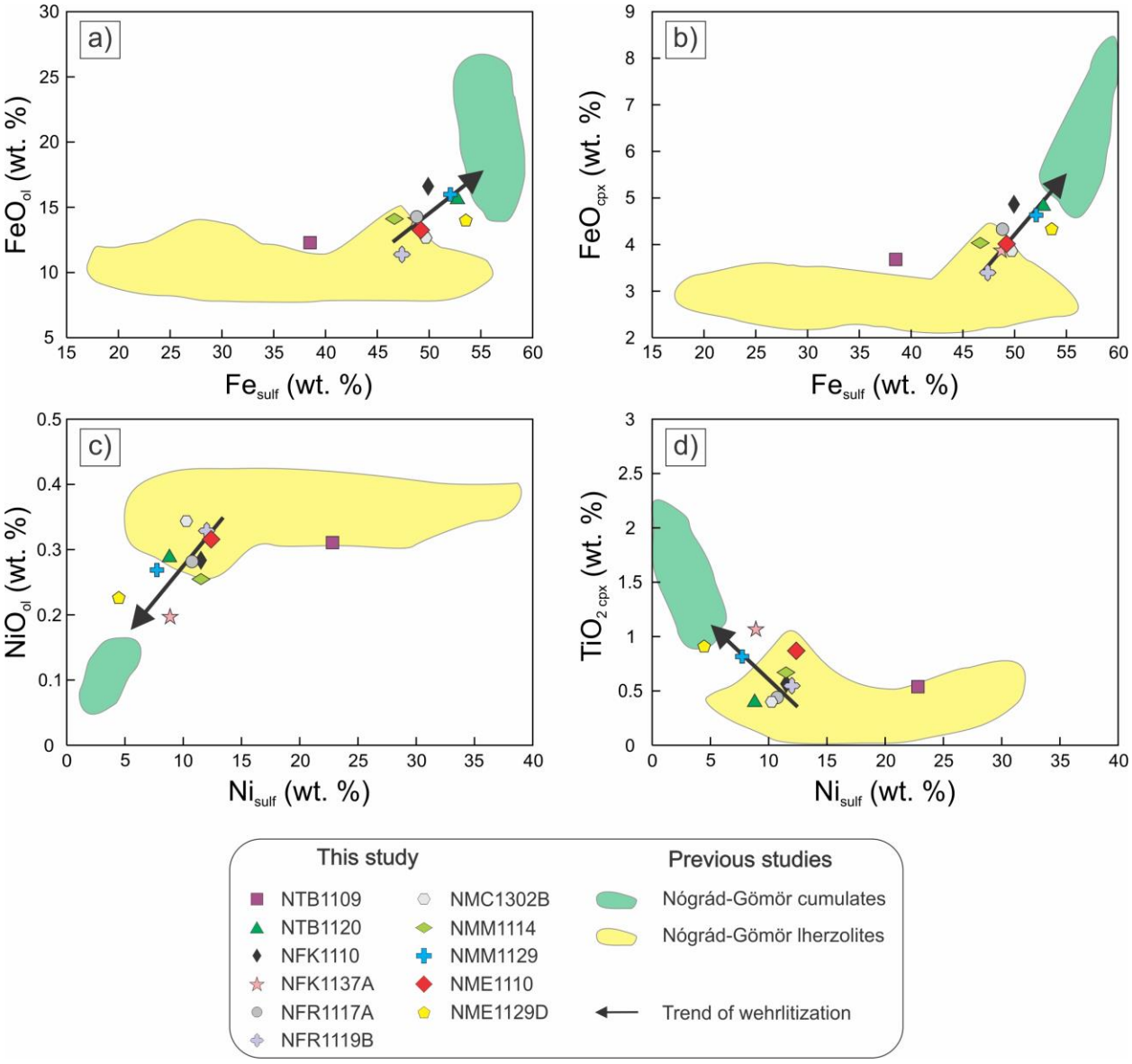

Figure 5.11 Relationship between **(a)** Fe in sulfides vs. FeO in olivines **(b)** Fe in sulfides vs. FeO in clinopyroxenes **(c)** Ni in sulfides vs. NiO in olivines **(d)** Ni in sulfides vs. TiO_2 in olivines from wehrlite, lherzolite and cumulate xenoliths from Nógrád-Gömör. Arrows indicate the wehrlitization trend. The fields of lherzolite and cumulate xenoliths are from Szabó and Bodnar (1995), Szabó et al. (2019) and Zajacz and Szabó (2003).

formation happened at an estimated pressure of 1.3–1.6 GPa (Table 2) where ~1200 ppm S is required for sulfide saturation (Mavrogenes and O'Neill, 1999). Such amount of S is commonly present in basaltic melts under upper mantle conditions (e.g., Jugo et al., 2005). Hence, sulfide precipitation can easily occur even at a modest drop of the sulfide saturation level after Fe loss.

The equilibrium temperature of wehrlitic sulfide was estimated using the experimentally determined monosulfide solid solution (mss) phase relations (Kullerud et al., 1969). The calculated bulk composition as potential initial composition of individual sulfides in each studied wehrlite xenolith indicate higher temperatures (~1050–1100 ˚C; Fig. 4.16) than what was determined with pyroxene-based thermometers (~985–1055 ˚C; Table 2). The appearance of different mineral phases (mms, pentlandite, pyrrhotite, chalcopyrite; Fig. 4.14) in sulfides is a result of crystallization linked to syn- and post-entrapment processes (Kullerud et al., 1969).

To further constrain the formation conditions of wehrlitic sulfides, we compared their geochemical data with sulfides from Nógrád-Gömör cumulates (Zajacz and Szabó, 2003). The cumulates (clinopyroxenites, plagioclase-bearing ultramafic rocks) crystallized from basaltic melts accumulated immediately under the Moho during the Neogene alkali basaltic volcanic event (Kovács et al., 2004; Zajacz et al., 2007). Note that the sampling localities of the cumulates are all situated in the central part of the NGVF, which is the area of wehrlite formation (Fig. 2.5). However, not all cumulate sampling localities contain wehrlite xenoliths, which restricts the comparison.

The studied sulfides entirely overlap with sulfides from Nógrád-Gömör cumulates (Zajacz and Szabó, 2003) in Cu-Ni+Co-Fe, Cu-S-Fe and Fe-S-Ni+Co systems (Fig. 4.15; 4.16). Furthermore, the geochemical evolution of wehrlitic sulfides using coexisting sulfide and silicate minerals points towards the field of Nógrád-Gömör cumulates (Fig. 5.11). The similar geochemical compositions of the sulfides in wehrlites and in cumulates suggest cognate formation. Both wehrlite and cumulate sulfides are related to migrating and crystallizing mafic melts leading to higher Fe and lower Ni, Co contents in them.

5.8.2. The effect of wehrlitization on siderophile and chalcophile element budget

As mentioned above, wehrlitization resulted in Fe enrichment and relative Ni-Co depletion both in sulfides and rock-forming silicates (Fig. 5.11). This correlation is commonly observed in silicates of mafic melt-metasomatized peridotites (Zinngrebe and Foley, 1995; Peslier et al., 2002a; Rivalenti et al., 2004; Ackerman et al., 2009a; Shaw et al., 2005; 2018). However, the knowledge on how highly siderophile and chalcophile trace elements behave during such mafic melt metasomatism is limited, and mostly restricted to PGEs (Büchl et al., 2002; Luguet et al., 2008) or to the oceanic lithosphere (Ciążela et al., 2017; 2018).

The pattern of higly siderophile PGE obtained on Nógrád-Gömör wehrlitic sulfides (Table 14) are highly similar to Nógrád-Gömör lherzolitic sulfides studied by Szabó et al. (2019) Fig. 4.18). Similar PGE contents of sulfides in Nógrád-Gömör wehrlite and lherzolite (Fig. 4.18) may indicate that the metasomatic melt reached equilibrium with the precursor peridotite with respect to these elements. Alternatively, the metasomatic melt could not mobilize the highly siderophile elements. The less compatible PGE, namely Pd and Pt, are controlled by the Cu (chalcopyrite) content (Holwell and McDonald, 2010), and Cu is only minimally enriched in wehrlites. The only element with siderophile affinity, which shows lower concentrations in wehrlitic than in lherzolitic sulfides, is Re (Fig. 5.12). The decreased Re concentration linked to basaltic melt percolation was also observed in xenoliths from east central China (Reisberg et al., 2005), which further suggests that Re is highly involved in such metasomatic events and possibly leaves the system with the melt agent.

Besides the obvious Fe enrichment (Fig. 5.11; 5.13h), some chalcophile trace elements (Zn, Cd, Sb, Tl) also show enrichment in wehrlitc sulfides compared to lherzolitic ones (Fig. 5.12; 5.13a-b). The variation in the concentrations of these elements is also demonstrated with S/Se (Fig. 5.13g-h). This ratio is a widely applied indicator of metasomatism as S is preferentially transported in melts, whereas Se is more compatible, leading to increased S/Se in metasomatized rocks (Lorand and Alard, 2010; Alard et al., 2011). In contrast, some calchophile elements such as Ge, Se and Te show depletion in sulfides in wehrlite xenoliths (Fig. 5.12). The highest concentration of these elements occurs in the weakly-metasomatized NTB1109 wehrlite, whereas the moderately- and highly-metasomatized NTB1120, NME1110, NME1129D wehrlite xenoliths show a stronger depletion of these elements (Fig 5.13). This suggests that the depletion in these elements is related to the degree of metasomatism.

In order to explain these variations, we need to invoke knowledge on how these elements are transported in mafic melts and what partition coefficients are characteristic between mss and coexisting mafic melt or sulfide liquid. It is noteworthy that the way of sulfide transportation in silicate melts is still a matter of debate. Sulfur and associated chalcophile trace elements can be dissolved also in silicate melt (Keays, 1995; Mungall and Su, 2005; Barnes et al., 2008) or can be transported as isolated spherical droplets in silicate melt (de Bremond d'Ars et al., 2001; Bockrath et al., 2004; Ballhaus et al., 2006) in basaltic systems in mantle conditions. It is also questionable

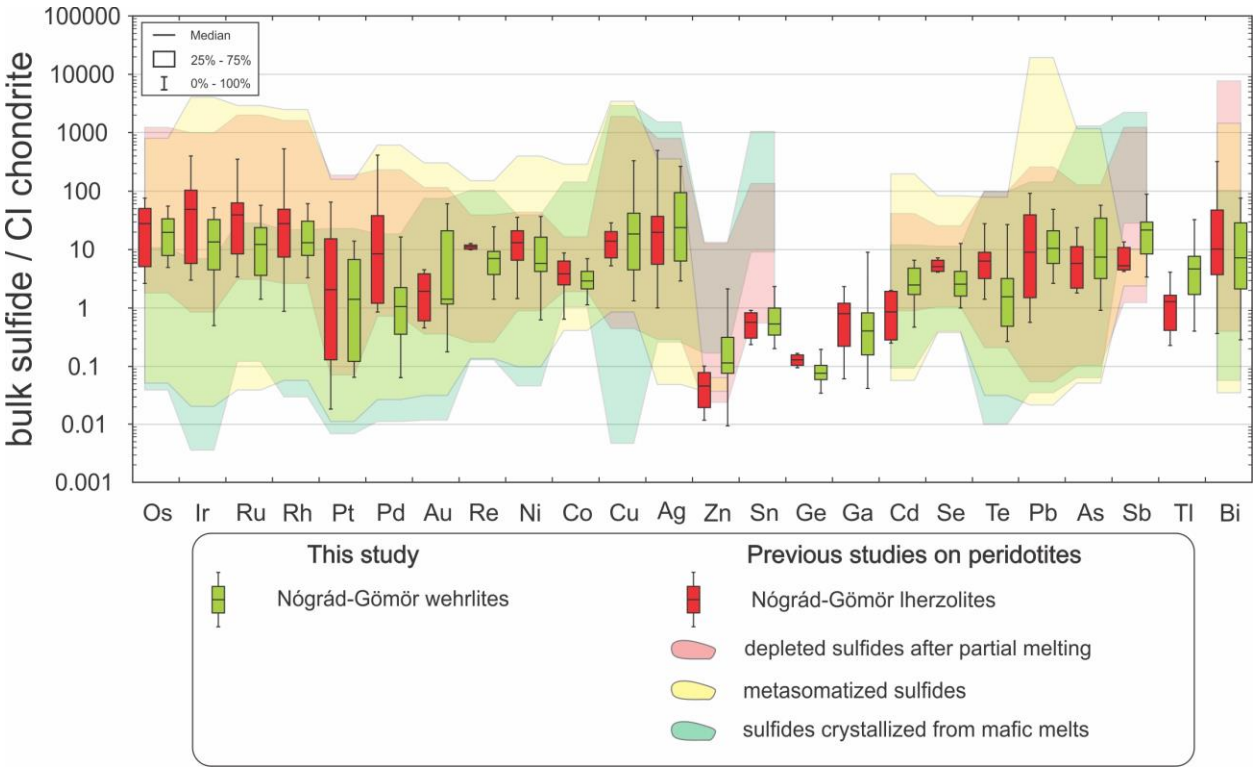

Figure 5.12 Box and whisker diagrams of the CI chondrite-normalized (McDonough and Sun, 1995) trace elements of sulfides in the Nógrád-Gömör wehrlite xenoliths. The reference sulfides from Nógrád-Gömör lherzolite xenoliths are taken from Szabó et al. (2019). Reference fields are based on in situ analyses of genetically diverse sulfide populations from ultramafic xenoliths and massifs: depleted sulfides (Guo et al., 1999; González-Jiménez et al., 2014; Saunders et al., 2015; 2016; Westner et al., 2019), metasomatized sulfides (Alard et al., 2011; Delpech et al., 2012; González-Jiménez et al., 2014; Saunders et al., 2015; Westner et al., 2019) and sulfides precipitated after melt crystallization (Guo et al., 1999; Saunders et al., 2016; D'Errico et al., 2019).

how this transportation mode changes upon reaching sulfur saturation. Therefore, both mss/silicate melt and mss/sulfide melt partition coefficients were applied to estimate the possible geochemical features of the crystallizing sulfides and the residual melts. These are only available for a part of the studied elements (Li and Audétat, 2012; Brenan, 2015; Liu and Brenan, 2015); and the experimental conditions, in which partition coefficients were determined do not always represent mantle conditions (e.g., 0.1 MPa and 926 ˚C in Liu and Brenan, 2015). Among the chalcophile trace elements, which show different concentration in the lherzolites and in the wehrlites (Zn, Cd, Sb, Tl, Ge, Se and Te; Fig. 5.12), Zn and Sb are affined to the silicate melt ($D^{mss/silicate\ melt}$ is 0.55 and 0.06, respectively; Li and Audétat, 2012), whereas the Se and Te are

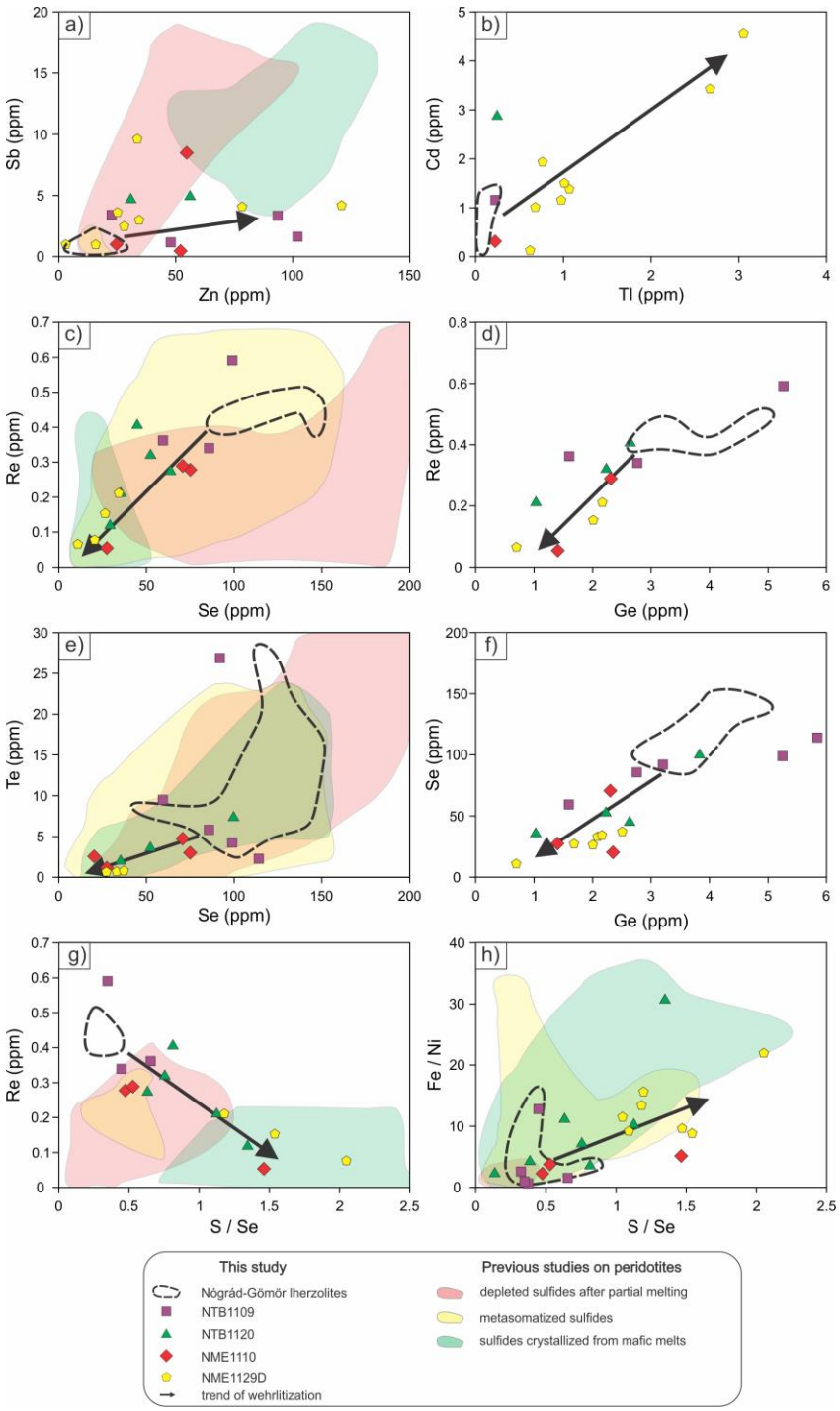

Figure 5.13 Scatterplots comparing various trace element contents in sulfides of the Nógrád-Gömör wehrlite xenoliths. The discrete red circles are sulfides from the Nógrád-Gömör lherzolite xenoliths (Szabó et al., 2019). Red, pale yellow, and green reference fields are based on in situ analyses of genetically diverse sulfide populations from ultramafic xenoliths and massifs: depleted sulfides (Guo et al., 1999; González-Jiménez et al., 2014; Saunders et al., 2015; 2016; Westner et al., 2019), metasomatized sulfides (Alard et al., 2011; Delpech et al., 2012; González-Jiménez et al., 2014; Saunders et al., 2015; Westner et al., 2019), sulfides precipitated after melt crystallization (Guo et al., 1999; Saunders et al., 2016; D'Errico et al., 2019).

compatible with mss ($D^{mss/silicate\ melt}$ is 864 and 618, respectively; Brenan, 2015). These results imply that prior to the wehrlite formation, some sulfide grains may have segregated at greater depth than the wehrlite formation (30 – 50 km), which led to Zn and Sb enrichment and Se and Te depletion in the residual silicate melt.

Using the mss/sulfide melt partition coefficients, among which some were determined at low pressures (< 1 MPa; Barnes et al., 1994; Helmy et al., 2010; Liu and Brenan, 2015), the interpretation is less obvious. Selenium, Te and Sb uniformly prefer sulfide liquid over mss ($D^{mss/sulfide\ melt}$ is 0.75, 0.061 and 0.017, respectively; Brenan, 2015) although these elements behave differently, showing enrichment (Sb) as well as depletion (Se, Te) in the wehrlitic sulfides with respect to the lherzolites (Fig. 5.12). The lack of systematics between the experimental partition coefficients and my results suggest that no segregated sulfide melt was present during the wehrlite formation.

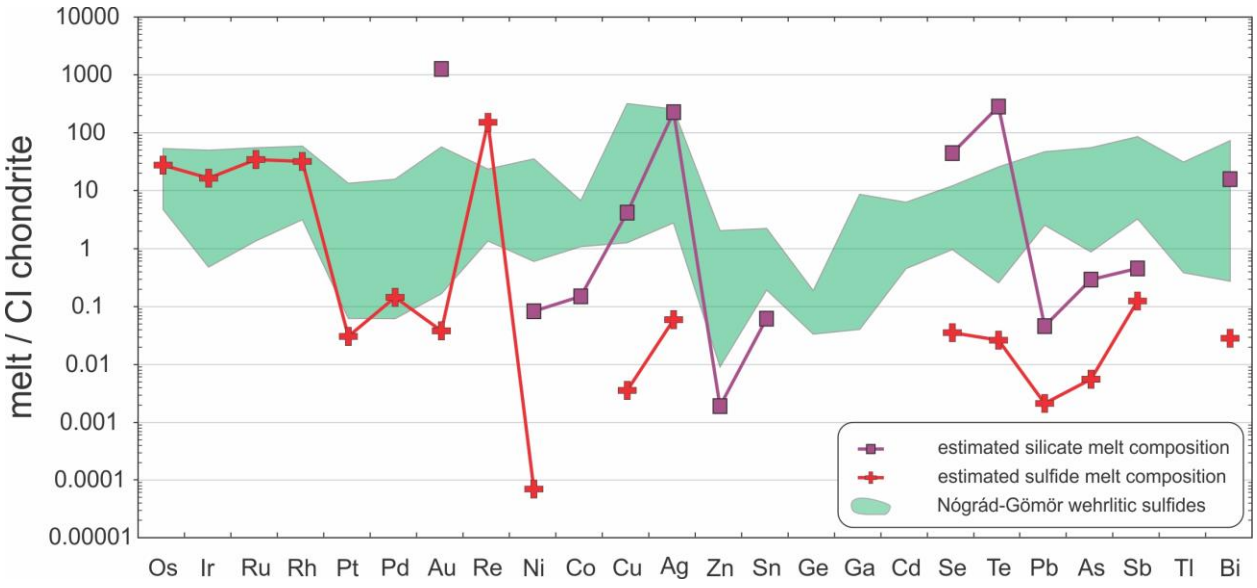

Figure 5.14 Estimated trace element compositions of metasomatic silicate and sulfide melt, using the averaged trace element composition of sulfides from Nógrád-Gömör wehrlite xenoliths and partition coefficients of mss–silicate melt and mss–sulfide melt, respectively. The mss–silicate melt partition coefficients are from Li and Audétat (2012) and Brenan (2015), whereas mss–sulfide melt partition coefficients are from Barnes et al. (1994), Helmy et al. (2010), Brenan (2015) and Liu and Brenan (2015). The obtained CI chondrite-normalized (McDonough and Sun, 1995) trace element distributions are compared to the trace element composition of sulfides from Nógrád-Gömör wehrlite xenoliths.

Table 18. Equilibrium melt composition results (in ppm) for silicate and sulfide melts in Nógrád-Gömör. The input solid phase composition is the averaged trace element content of the sulfides in Nógrád-Gömör wehrlite xenoliths. The mss–silicate melt partition coefficients used here are taken from Li and Audétat (2012) and Brenan (2015), whereas mss–sulfide melt partition coefficients are taken from Barnes et al. (1994); Helmy et al. (2010); Brenan (2015); and Liu and Brenan (2015).

Element	Estimated silicate melt composition	Estimated sulfide melt composition
Os	–	0.708
Ir	–	1.26
Ru	–	0.601
Rh	–	0.480
Pt	–	143
Pd	–	112
Au	0.013	387
Re	–	0.054
Ni	135	144565
Co	29.5	–
Cu	13.9	15277
Ag	0.256	897
Zn	107	–
Sn	11.3	–
Ga	–	–
Ge	–	–
Cd	–	–
Se	0.070	80.9
Te	0.014	139
Pb	553	10627
As	109	5469
Sb	55.6	196
Tl	–	–
Bi	1.12	599

The trace element concentrations of the equilibrium silicate and sulfide melts were estimated using the partition coefficients and the averaged wehrlitic sulfide composition (Table 18). The resulting trace element distributions barely overlap with the pattern defined by the wehrlitic sulfides (Fig. 5.14). Only the Ir-group platinum group elements (IPGE; including Os, Ir, Ru) + Rh suggest equilibrium between sulfide melt and solid sulfide (Fig. 5.14). The lack of agreement

suggests that equilibrium was not reached between sulfides and their possible parent melts (silicate or sulfide), although it is normally reached quickly (<24 h at 1000 ˚C; Zajacz et al., 2013). Similar disequilibrium was observed for wehrlitic silicates (Fig. 4.4). The disequilibrium along with major (Fig. 5.11) and trace element (Fig. 5.13) trends suggest that the metasomatic reaction forming the wehrlitic sulfides (and silicates) happened slightly before xenolith entrapment. This is a significant genetic difference compared to sulfides hosted in pyroxenites, formed by the crystallization of cumulated mafic melts (Guo et al., 1999; Saunders et al., 2016; D'Errico et al., 2019). The composition of the wehrlitic sulfides overlap well with the sulfides crystallized from a mafic melt (Fig. 5.13), suggesting the melt composition is the main control on siderophile and chalcophile element budget.

To have a better constraint on element behavior, it is useful to examine trace element characteristics for different sulfide minerals. Thallium, incorporated dominantly in pyrrhotite phase (cf. Ciążela et al., 2018), is enriched in the wehrlitic sulfides (Fig. 5.12; 5.13b). This suggests that Tl is accompanied with Fe-rich melts, such as the wehrlitizing melt agent beneath Nógrád-Gömör. Indeed, only the weakly-metasomatized NTB1109 wehrlite xenolith shows Tl content plotting in the lherzolitic sulfide field, whereas the moderately- to highly-metasomatized wehrlite xenoliths (NTB1120, NME1110, NME1129D) show at least slightly higher Tl concentrations (Fig. 5.13b). In contrast, Ge and Te dominantly reside in pentlandite (Ciążela et al., 2018), which suggests a refractory mantle segment (Garuti et al., 1984). Accordingly, the wehrlitic sulfides have lower Ge and Te contents compared to the lherzolitic sulfides (Fig. 5.12). The weakly-metasomatized NTB1109 wehrlite xenolith has Ge and Te compositions closest to the lherzolitic sufide fields (Fig. 5.13d-e).

The studied Nógrád-Gömör wehrlitic mantle portions were formed under high melt/rock ratio (~0.3) as indicated from whole rock trace element modelling (Table 17). Prior studies indicated that melt/rock ratio has a key role in melt-rock interaction for the siderophile and chalcophile element budget (Lorand et al., 2004; Ackermann et al., 2009b; Liu et al., 2010; Delpech et al., 2012). The high melt/rock ratio, associated with additional heat, can lead to the removal of sulfides from the wall rock due to their relatively lower melting temperature (Zhang and Hirschmann, 2016), and leaving no or only limited sulfides, always with depleted signatures (Büchl et al., 2002; Lorand et al., 2003). Hence, the lower (~ 0.04 vol. %) sulfide presence in

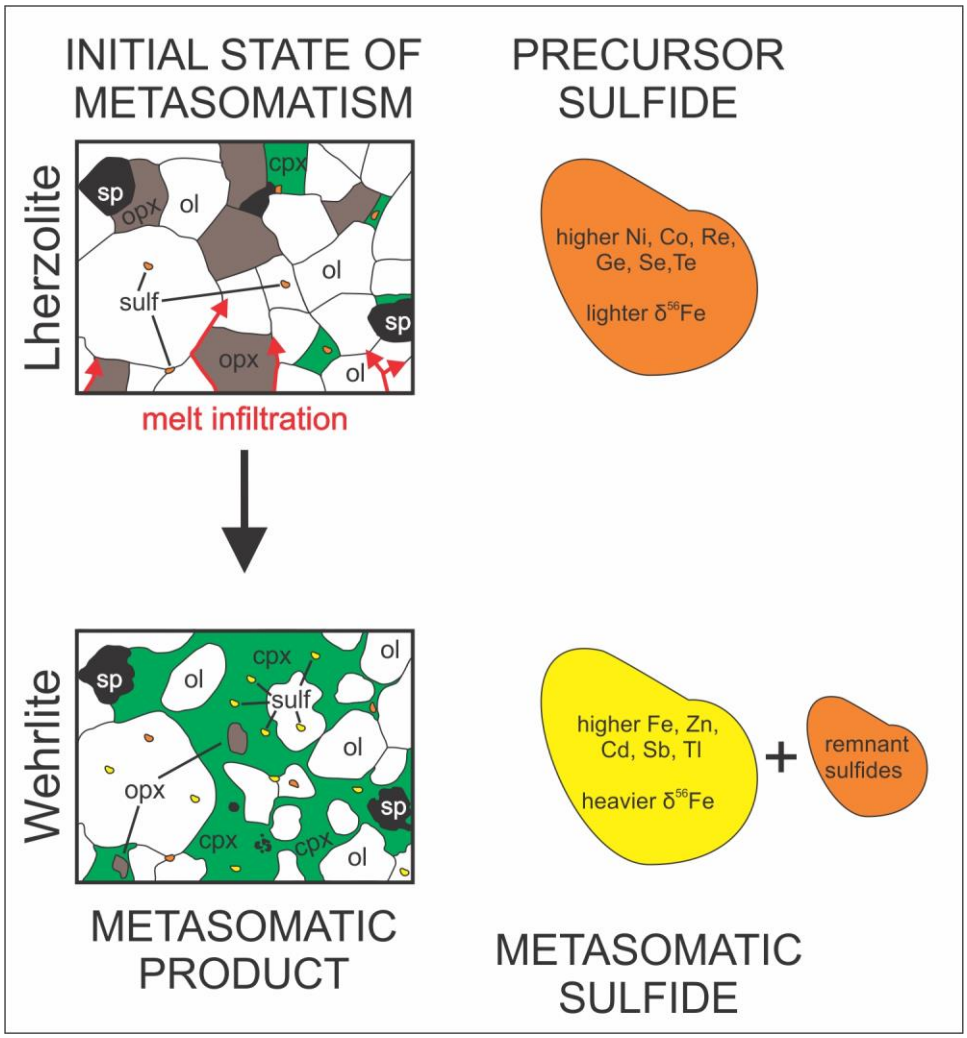

Figure 5.15 Simplistic model of the wehrlitization process with emphasis on sulfide minerals in Nógrád-Gömör lherzolite and wehrlite xenoliths. Geochemical characteristics of the precursor (orange) and metasomatic (yellow) sulfides are highlighted on the right side. Abbreviations: ol–olivine, opx–orthopyroxene, cpx–clinopyroxene, sp–spinel, sulf–sulfide.

wehrlites compared to an averaged or a metasomatized mantle (0.07 vol. %; Fellows and Canil, 2012 and 0.6–1 vol.%; Wang et al., 2009, respectively) may be interpreted with high melt/rock ratio.

Even though the wehrlitization resulted in sulfide enrichment, some sulfides originally present in the precursor lherzolite also appear alongside the newly formed metasomatic ones (Fig. 5.15), as suggested by their overlapping geochemistry with the lherzolitic sulfide fields (Fig. 5.13). Such sulfides are the most abundant in the weakly metasomatized NTB1109 wehrlite xenolith

(Fig. 5.13). The coexistence of non-metasomatized, precursor and metasomatized, newly-formed sufides explains the geochemical heterogeneities within a single xenolith (Fig. 5.13).

5.8.3. Iron isotope systematics during wehrlitization

Iron isotopes have been studied in bulk upper mantle peridotites and in situ in their rock-forming minerals (Zhu et al., 2002; Beard and Johnson, 2004; Weyer et al., 2005; Schoenberg and von Blanckenburg, 2006; Weyer and Ionov, 2007; Zhao et al., 2010; 2012; Huang et al., 2011; Poitrasson et al., 2013; Craddock et al., 2013; Zhang et al., 2019; Peters et al., 2019). In contrast, in situ analyses of upper mantle sulfides are barely available (Ciążela et al., 2019; Pieterek et al., 2018).

The δ^{56}Fe of wehrlitic sulfides can be classified into two groups with values of -0.20–+0.06 (NTB1109 and NTB1120 wehrlite) and +0.66–+0.84 ‰ (NME1110 and NME1129D wehrlite), respectively (Table 15; Fig. 4.19). The group with lower δ^{56}Fe overlaps with, whereas the other with higher δ^{56}Fe exceeds the values determined for precursor lherzolites (-0.28–+0.13 ‰; Szabó et al., 2019; Fig. 4.19). The higher δ^{56}Fe group suggests isotope fractionation during the wehrlitization. In contrast, the lower δ^{56}Fe group rather implies that some wehrlitic sulfides might have preserved their pre-metasomatic Fe isotope characteristics, which is a similar conclusion to what was drawn from the Ca content of olivine-hosted orthopyroxenes (Fig. 4.6) and the coexistence of dry and wet clinopyroxene grains (Fig. 4.11). The NTB1109 xenolith represents weakly-, whereas the NTB1120 xenolith represents highly-metasomatized wehrlite based on petrographic and geochemical characteristics of the rock-forming minerals (Fig. 5.6). However, these wehrlite xenoliths show similar Fe isotope signatures, suggesting that the degree of metasomatism is not the only factor in isotope fractionation. The similar δ^{56}Fe values for sulfides from xenoliths collected in the same locality suggests homogenous Fe isotope characteristics on a sample locality scale (Fig. 4.19).

The higher δ^{56}Fe values of sulfides in NME1110 and NME1129D wehrlites are in good agreement with ^{56}Fe enrichment in bulk rocks affected by silica-undersaturated melts forming metasomatized lherzolites (0.15–0.19 ‰ δ^{56}Fe; Huang et al., 2011) or wehrlites (0.012–0.173 ‰ δ^{56}Fe; Weyer and Ionov, 2007; Zhao et al., 2010; 2012). In contrast, Fe isotope fractionation was not revealed in dunites formed during metasomatism by silica-undersaturated melts (Poitrasson et al., 2013). This suggests that changes in modal proportion of clinopyroxene play a key role in Fe

isotope fractionation. Zhao et al. (2010) showed that the higher the clinopyroxene content of the metasomatic product, the heavier the bulk Fe isotope composition. In contrast, the clinopyroxene content of the wehrlites (Table 2) does not correlate with the δ^{56}Fe value of their sulfides (Table 15). This suggests that the modal composition of the rock-forming constituents cannot buffer the Fe isotope composition of sulfides.

Weyer and Ionov (2007) concluded that the heavy Fe isotope signature of wehrlites is the result of the heavy Fe isotope enriched character of the metasomatic melt. The NGVF wehrlites, however, were likely formed by an OIB-like melt (Fig. 5.3), which typically shows limited and lower δ^{56}Fe values (Teng et al., 2013) compared to the wehrlitic sulfides (Fig. 4.19). Therefore, it is unlikely that the wehrlites inherited their heavier Fe isotope signature from the metasomatic melt.

Kinetic fractionation is also excluded as it would lead to lighter and not heavier isotope signatures in wehrlites (Teng et al., 2011). Moreover, kinetic fractionation is significant only at low melt/rock ratio (Poitrasson et al., 2013), which is not the case for the NGVF wehrlite formation. Alternatively, Fe isotopic fractionation could be induced by changes in the oxygen fugacity (fO_2) (Williams et al. 2004; 2005). Patkó et al. (2019) applied the oxygen barometer of Ballhaus et al. (1991) to reveal that wehrlites have higher fO_2 (0.49–0.74 with an average of 0.62 related to FMQ [fayalite-magnetite-quartz] buffer) compared to the lherzolites (-0.83 to +0.61 with an average of -0.22). However, Williams et al. (2004; 2005) reported that oxidized environment should imply light Fe isotopes, whereas the NGVF wehrlites show higher δ^{56}Fe value (Fig. 4.19) despite their high fO_2. This implies that fO_2 cannot play the key role in Fe isotope fractionation either.

Magma differentiation typically does not affect δ^{56}Fe in basaltic systems (Schuessler et al., 2009; Schoenberg et al., 2009). However, constant bulk δ^{56}Fe during melt differentiation may result from contrasting effect of various crystallizing minerals. For example, the simultaneous fractionation of olivine (preferring lighter Fe isotopes) and spinel (preferring heavier Fe isotopes) can neutralize each other (McCoy-West et al., 2018). In the NGVF wehrlites, clinopyroxene, and to a lesser extent, olivine, crystallized at the expense of orthopyroxene (Fig. 4.2g), which would lead to increasingly heavier δ^{56}Fe in the metasomatic melt. Sulfide crystallization may also increase the δ^{56}Fe value of the melt (Williams et al., 2018; Peters et al., 2019). Hence the evolving metasomatic melt can precipitate sulfide grains with gradually increasing δ^{56}Fe values on its way

to the surface. The wehrlitization is estimated to having taken place in the depth range of 40–50 km below the surface (Fig. 5.7), which is likely enough to produce Fe isotope fractionation during melt migration. Therefore, xenoliths (NME1110 and NME1129D xenolith) with higher δ^{56}Fe may represent fragments of the upper part of the wehrlitized mantle volume.

5.9. Possible links between wehrlitization and Neogene volcanic events

In the Nógrád-Gömör area, two types of Neogene volcanic products with mantle origin can be found on the surface (Fig. 2.5). Besides late Miocene – Pleistocene alkali basalts hosting upper mantle xenoliths, a middle Miocene (~16 Ma; Pécskay et al., 2006) calc-alcaline garnet-bearing andesite laccolith is also known (Lantai, 1991; Harangi et al., 2001) (Fig. 2.5). It is also acknowledged that the Nógrád-Gömör upper mantle xenoliths contain amphibole and phlogopite, whose formation is probably linked to fluids related to a prior subduction event based on their geochemistry (Szabó and Taylor, 1994; Szabó et al., 1996; Liptai et al., 2017). However, the geophysical data show no evidence of subducted oceanic lithosphere remnants beneath the Western Carpathians (Grad et al., 2006; Tašárová et al., 2009 and references therein), making the Miocene subduction highly uncertain. Hence, Liptai et al. (2017) favored an inherited origin for these subduction related phases in the lherzolite xenoliths, relaying on the interpretation of Kovács and Szabó (2008), who suggested that the last subduction that affected the ALCAPA microplate occurred prior to its extrusion from the Alpine collision zone. Hence, it is unlikely that subduction-related melts had any chemical and/or physical influence on the wehrlitization process.

Melts associated with the 7–0.3 Ma (Balogh et al., 1981; Hurai et al., 2013) alkali basalts of the NGVF are interpreted to originate from the asthenosphere (e.g., Embey-Isztin et al., 1993). Their trace element composition is similar to the calculated composition of the metasomatic melt (Fig. 5.3; Table 16), and thus the question arises whether the alkali basalts are in any way associated with the wehrlitization process. Furthermore, the presence of orthopyroxene relicts in clinopyroxenes (Fig. 4.2g), intragranular compositional inhomogeneities in the rock-forming minerals (Fig. 4.4) and partially glassy silicate melt inclusions in clinopyroxenes and olivines (Patkó et al., 2018) all imply that the metasomatism was either ongoing or occurred shortly before the entrainment of xenoliths in the host basalt. Therefore, it is suggested that the melt agent associated with wehrlitization was produced in a major melt generation event that also led to the

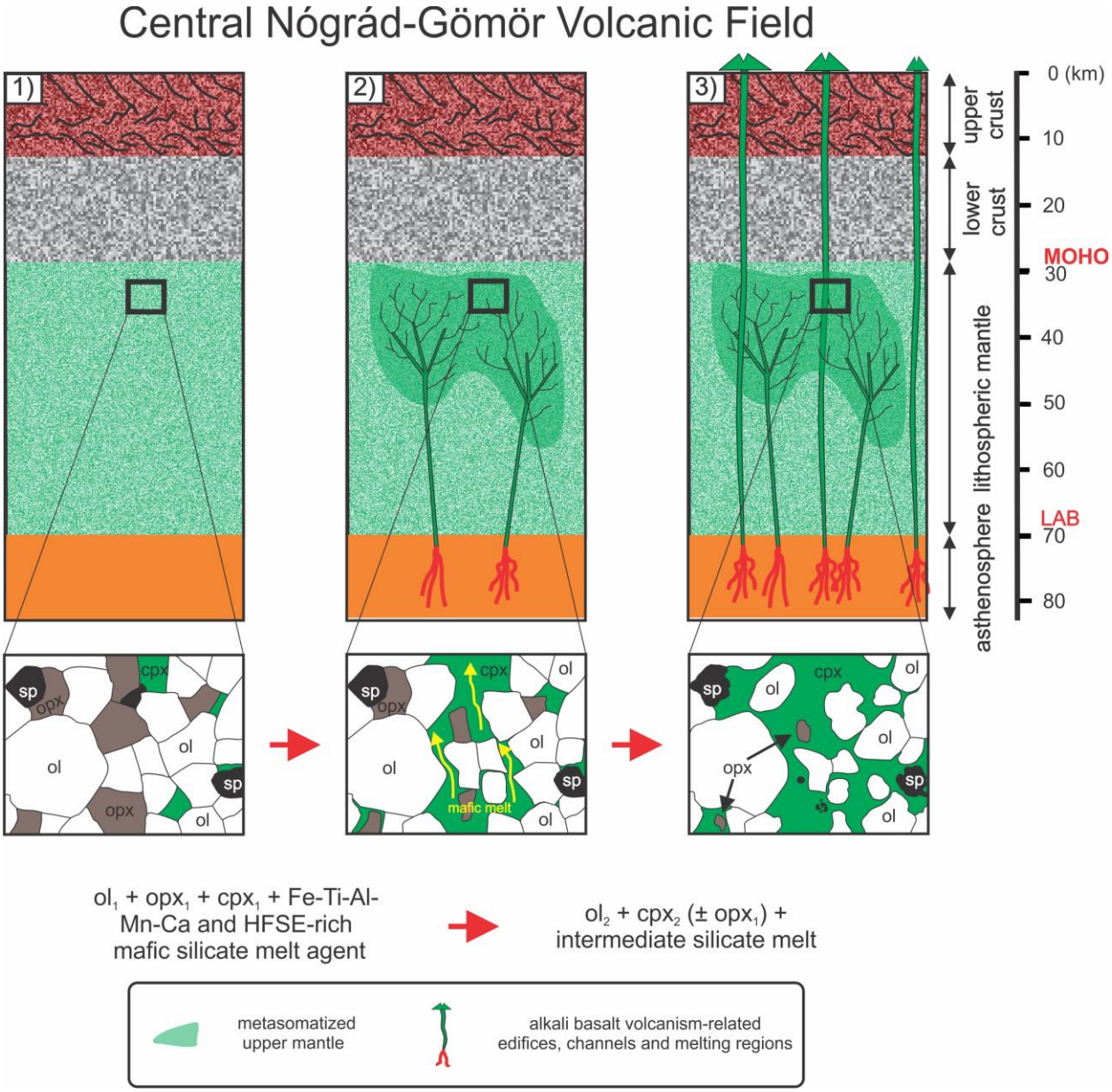

Figure 5.16 Simplified cartoon showing the evolution model for the wehrlitization process in Nógrád-Gömör. The local Moho and LAB (lithosphere-asthenosphere boundary) depths are from Klébesz et al. (2015). 1. The mantle status before the volcanic event. 2. Upward migration of asthenosphere-derived mafic melts leading to metasomatized mantle. 3. The ascending of a new magma batch, which transported the metasomatized mantle fragments as xenoliths to the surface.

host basalt volcanism. According to this scenario, at least two, chemically rather homogeneous batches of magma ascended beneath the central NGVF. One modified the peridotitic mantle and resulted in the formation of wehrlites (Fig. 5.16) and the other brought fragments of both the metasomatically altered and the pristine (lherzolitic) mantle to the surface. During the basaltic

melt-peridotite interaction and fractionation in the upper mantle, orthopyroxene dissolution occurred and silica-rich melts were produced (discussed above in section 5.2.3). Therefore, the presence of silica-rich melts in the mantle environment is not necessarily linked to subduction. Determination of the extent of the metasomatized mantle domain and its relationship to other lithologies is difficult because of the small size of the xenoliths. However, long period MT data beneath the NGVF show a low resistivity (<10 Ωm) body under the Moho (30–50 km) beneath the central part of the NGVF (Novák et al., 2014), the same area where wehrlite xenoliths originate from (Fig. 2.5). The overlap between the electrical resistivity anomaly and the wehrlite sampling localities is consistent with a genetic relationship. The upward melt migration beneath the NGVF was possibly aided by the vertical foliation of the local lithospheric mantle (Liptai et al., 2019b).

6. Remarks

During my Ph.D. program, I carried out a detailed research on the petrographic and geochemical features of the rock-forming minerals, as well as the sensitive sulfides, of a metasomatized upper mantle xenolith series from Nógrád-Gömör Volcanic Field. The geochemistry includes information on major and trace elements, the structural hydroxyl content of silicates, as well as the Fe stable isotopes of sulfides, which all contributed to the understanding of the metasomatic process. The application of rare earth element modelling helped define both the precursor and the metasomatic agent compositions, which proved to be lherzolite and an OIB-like melt, respectively. This numerical modelling also revealed the importance of the melt/rock ratio during metasomatism.

Although my Ph.D. program focuses on xenoliths collected from only a single volcanic field, however, the knowledge gathered from these wehrlites is far beyond the local interest. Since the appearance and migration of mafic silicate melts are not restricted to certain tectonic settings, this knowledge is widely applicable in a geological sense.

Acknowledgements

Above all, I owe thanks to my supervisor, Csaba Szabó, who provided enormous and valuable help ever since I have become a member of the Lithosphere Fluid Reseach Lab (LRG). This long lasting guidance covered part of my bachelor and the entire period of my master degree and continued in my Ph.D. eventually culminating in this thesis. His never-ending interest and extreme endurance showed an example that I will always remember. I am also grateful to my consultants, whose help was essential in my scientific activity during the whole span of my Ph.D. program. Robert J. Bodnar supported my research from the beginning. He allowed me to visit and work two times in his lab at the Virginia Tech for weeks, which was decisive in my subsequent academic life both because of scientific and personal reasons. His personal attitude and approach to science also gave me a lot. I am very grateful to have the opportunity to work with István Kovács, who provided great help in scientific questions. He did not only introduce me to different technics, but also showed me how these can be incorporated in a complex study. This experience helped me a lot in improving the quality of the research I carried out.

Several present and former students of the LRG contributed to my Ph.D. research. These colleagues, are Nóra Liptai, László Aradi, Károly Hidas, Rita Klébesz, Eszter Sendula, Márta Berkesi and Zsanett Pintér, who helped me in interpreting the variable data sets. I am grateful to Silvana Beltrán from whom I got huge help in editing this thesis. Moreover, I am grateful to a number of colleagues from all over the world for their help in different aspects of my research. I owe thanks to Jakub Ciążela, Bartosz Pieterek and François Holtz in their huge help regarding the sulfides from the studied rocks, Attila Novák for having fruitful discussions on magnetotellurics (MT) method and results, Balázs Trásy for his help with data analyses, to Qun-Ke Xia, Jannick Ingrin, Suzanne Y. O'Reilly, William L. Griffin and Viktor Wesztergom for their contribution in interpreting the FTIR data.

Furthermore, I acknowledge the assistance in analytical work from Zsolt Bendő, Ábel Szabó and Zoltán Kovács (SEM) at Eötvös University, Hungary; Anna Maria Fioretti, Raúl Carampin, Orlando Vaselli and Bernardo Cesare (EMPA) at Padua, Italy; Marina Lazarov (fs-LA-ICP-MS) at Hannover, Germany; Luca Fedele and Pilar Lecumberri Sanchez (LA-ICP-MS) at Virginia Tech, USA; Judith Mihály and Csaba Németh (FTIR) at the Hungarian Academy of Science.

My research received financial support from the GINOP-2.3.2-15-2016-00009 research program and the ELTE Institutional Excellence Program (1783-3/2018/FEKUTSRAT) managed by the

Hungarian Ministry of Human Capacities. Further support was provided by the National scholarship for the young outstandings (NTP-NFTÖ-16-0637), the Hungarian Science Foundation (OTKA, 78425 to Csaba Szabó) and the U.S. National Science Foundation (EAR-1624589 to Robert J. Bodnar). I also received support from the research grants of my consultant, István Kovács: the National Research, Development and Innovation Fund of Hungary, financed under the K128122 funding scheme, the Bolyai Postodoctoral Fellowship program of the Hungarian Academy of Sciences, a postdoctoral grant (Grant No. PD101683) of the Hungarian Scientific Research Found (OTKA), the Marie Curie International Reintegration Grant (NAMS-230937) and the Lendület Research Grant to the MTA CSFK Lendület Pannon LitH_2Oscope Research Group. This work has been completed with the support of the National Science Centre Poland (PRELUDIUM 12 no. 2016/23/N/ST10/00288) to Jakub Ciążela.

I received special help from Nóri and László, and last but not least, my family, especially Eszter, who all supported me continuously.

References

Ackerman, L., Jelínek, E., Medaris Jr, G., Ježek, J., Siebel, W., & Strnad, L. (2009a). Geochemistry of Fe-rich peridotites and associated pyroxenites from Horní Bory, Bohemian Massif: Insights into subduction-related melt–rock reactions. Chemical Geology, 259(3-4), 152-167.

Ackerman, L., Pitcher, L., Strnad, L., Puchtel, I. S., Jelínek, E., Walker, R. J., & Rohovec, J. (2013). Highly siderophile element geochemistry of peridotites and pyroxenites from Horní Bory, Bohemian Massif: Implications for HSE behaviour in subduction-related upper mantle. Geochimica et Cosmochimica Acta, 100, 158-175.

Ackerman, L., Walker, R. J., Puchtel, I. S., Pitcher, L., Jelínek, E., & Strnad, L. (2009b). Effects of melt percolation on highly siderophile elements and Os isotopes in subcontinental lithospheric mantle: a study of the upper mantle profile beneath Central Europe. Geochimica et Cosmochimica Acta, 73(8), 2400-2414.

Alard, O., Griffin, W. L., Lorand, J. P., Jackson, S. E., & O'Reilly, S. Y. (2000). Non-chondritic distribution of the highly siderophile elements in mantle sulphides. Nature, 407(6806), 891.

Alard, O., Lorand, J. P., Reisberg, L., Bodinier, J. L., Dautria, J. M., & O'reilly, S. Y. (2011). Volatile-rich metasomatism in Montferrier xenoliths (Southern France): Implications for the abundances of chalcophile and highly siderophile elements in the subcontinental mantle. Journal of Petrology, 52(10), 2009-2045.

Ali, S., & Ntaflos, T. (2011). Alkali basalts from Burgenland, Austria: petrological constraints on the origin of the westernmost magmatism in the Carpathian–Pannonian Region. Lithos, 121(1-4), 176-188.

Aradi, L. E., Berkesi, M., & Szabó, C. (2019). Composition and origin of upper-mantle fluids, based on fluid inclusions in amphibole-rich harzburgite xenoliths from the Styrian Basin *(in Hungarian)*. Földtani Közlöny, 149(1), 35-49.

Aradi, L. E., Hidas, K., Kovács, I. J., Tommasi, A., Klébesz, R., Garrido, C. J., & Szabó, C. (2017). Fluid-Enhanced Annealing in the Subcontinental Lithospheric Mantle Beneath the Westernmost Margin of the Carpathian-Pannonian Extensional Basin System. Tectonics, 36(12), 2987-3011.

Arai, S., & Yurimoto, H. (1994). Podiform chromitites of the Tari-Misaka ultramafic complex, southwestern Japan, as mantle-melt interaction products. Economic Geology, 89(6), 1279-1288.

Bada, G., & Horváth, F. (2001). On the structure and tectonic evolution of the Pannonian basin and surrounding orogens. Acta Geologica Hungarica, 44(2-3), 301-327.

Bada, G., Horváth, F., Dövényi, P., Szafián, P., Windhoffer, G., & Cloetingh, S. (2007). Present-day stress field and tectonic inversion in the Pannonian basin. Global and Planetary Change, 58(1-4), 165-180.

Balázs, A., Matenco, L., Magyar, I., Horváth, F., & Cloetingh, S. A. P. L. (2016). The link between tectonics and sedimentation in back-arc basins: New genetic constraints from the analysis of the Pannonian Basin. Tectonics, 35(6), 1526-1559.

Bali, E., Falus, G., Szabó, C., Peate, D. W., Hidas, K., Török, K., & Ntaflos, T. (2007). Remnants of boninitic melts in the upper mantle beneath the central Pannonian Basin? Mineralogy and Petrology, 90(1-2), 51-72.

Bali, E., Szabó, C., Vaselli, O., & Török, K. (2002). Significance of silicate melt pockets in upper mantle xenoliths from the Bakony–Balaton Highland Volcanic Field, Western Hungary. Lithos, 61(1-2), 79-102.

Bali, E., Zajacz, Z., Kovács, I., Szabó, C. S., Halter, W., Vaselli, O., Török, K., & Bodnar, R. J. (2008b). A quartz-bearing orthopyroxene-rich websterite xenolith from the Pannonian Basin, Western Hungary: evidence for release of quartz-saturated melts from a subducted slab. Journal of Petrology, 49(3), 421-439.

Bali, E., Zanetti, A., Szabó, C., Peate, D. W., & Waight, T. E. (2008a). A micro-scale investigation of melt production and extraction in the upper mantle based on silicate melt pockets in ultramafic xenoliths from

the Bakony–Balaton Highland Volcanic Field (Western Hungary). Contributions to Mineralogy and Petrology, 155(2), 165-179.

Balla, Z. (1984). The Carpathian loop and the Pannonian basin: a kinematic analysis. Geophys. Trans., 30, 313-353.

Ballhaus, C. (1998). Origin of podiform chromite deposits by magma mingling. Earth and Planetary Science Letters, 156(3-4), 185-193.

Ballhaus, C., Berry, R. F., & Green, D. H. (1991). High pressure experimental calibration of the olivine-orthopyroxene-spinel oxygen geobarometer: implications for the oxidation state of the upper mantle. Contributions to Mineralogy and Petrology, 107(1), 27-40.

Ballhaus, C., Bockrath, C., Wohlgemuth-Ueberwasser, C., Laurenz, V., & Berndt, J. (2006). Fractionation of the noble metals by physical processes. Contributions to Mineralogy and Petrology, 152(6), 667-684.

Balogh, K., Mihaliková, A., & Vass, D. (1981). Radiometric dating of basalts in southern and central Slovakia. Západné Karpaty: Séria Geológia, 7, 113-126.

Baptiste, V., Tommasi, A., Vauchez, A., Demouchy, S., & Rudnick, R. L. (2015). Deformation, hydration, and anisotropy of the lithospheric mantle in an active rift: Constraints from mantle xenoliths from the North Tanzanian Divergence of the East African Rift. Tectonophysics, 639, 34-55.

Barnes, S. J., Fiorentini, M. L., Austin, P., Gessner, K., Hough, R. M., & Squelch, A. P. (2008). Three-dimensional morphology of magmatic sulfides sheds light on ore formation and sulfide melt migration. Geology, 36(8), 655-658.

Barnes, S. J., Makovicky, E., Karup-Moller, S., Makovicky, M., & Rose-Hansen, J. (1994). Partition coefficients for Ni, Cu, Pd, Pt, Rh, and Ir between monosulphide solid solution and sulphide liquid and the implications for the formation of compositionally zoned Ni-Cu sulphide bodies by fractional crystallization of sulphide liquid. Mineralogical Magazine, 58, 51-52.

Beard, B. L., & Johnson, C. M. (2004). Inter-mineral Fe isotope variations in mantle-derived rocks and implications for the Fe geochemical cycle. Geochimica et Cosmochimica Acta, 68(22), 4727-4743.

Bell, D. R., & Rossman, G. R. (1992). Water in Earth's mantle: the role of nominally anhydrous minerals. Science, 255(5050), 1391-1397.

Bell, D. R., Ihinger, P. D., & Rossman, G. R. (1995). Quantitative analysis of trace OH in garnet and pyroxenes. American Mineralogist, 80(5-6), 465-474.

Beran, A., & Putnis, A. (1983). A model of the OH positions in olivine, derived from infrared-spectroscopic investigations. Physics and Chemistry of Minerals, 9(2), 57-60.

Berkesi, M., Guzmics, T., Szabó, C., Dubessy, J., Bodnar, R. J., Hidas, K., & Ratter, K. (2012). The role of CO_2-rich fluids in trace element transport and metasomatism in the lithospheric mantle beneath the Central Pannonian Basin, Hungary, based on fluid inclusions in mantle xenoliths. Earth and Planetary Science Letters, 331, 8-20.

Berkesi, M., Hidas, K., Guzmics, T., Dubessy, J., Bodnar, R. J., Szabó, C., Vajna, B., & Tsunogae, T. (2009). Detection of small amounts of H_2O in CO_2-rich fluid inclusions using Raman spectroscopy. Journal of Raman Spectroscopy, 40(11), 1461-1463.

Bielik, M., Alasonati-Tašárová, Z., Zeyen, H., Dérerová, J., Afonso, J., & Csicsay, K. (2010). Improved geophysical image of the Carpathian-Pannonian basin region. Acta Geodaetica et Geophysica Hungarica, 45(3), 284-298.

Biró, T., Kovács, I. J., Király, E., Falus, G., Karátson, D., Bendő, Z., Fancsik, T., & Sándorné, J. K. (2016). Concentration of hydroxyl defects in quartz from various rhyolitic ignimbrite horizons: results from

unpolarized micro-FTIR analyses on unoriented phenocryst fragments. European Journal of Mineralogy, 28(2), 313-327.

Bockrath, C., Ballhaus, C., & Holzheid, A. (2004). Fractionation of the platinum-group elements during mantle melting. Science, 305(5692), 1951-1953.

Bodinier, J. L., Vasseur, G., Vernieres, J., Dupuy, C., & Fabries, J. (1990). Mechanisms of mantle metasomatism: geochemical evidence from the Lherz orogenic peridotite. Journal of Petrology, 31(3), 597-628.

Bonadiman, C., Hao, Y., Coltorti, M., Dallai, L., Faccini, B., Huang, Y., & Xia, Q. (2009). Water contents of pyroxenes in intraplate lithospheric mantle. European Journal of Mineralogy, 21(3), 637-647.

Bourdon, B., Zindler, A., & Wörner, G. (1994). Evolution of the Laacher See magma chamber: Evidence from SIMS and TIMS measurements of U-Th disequilibria in minerals and glasses. Earth and Planetary Science Letters, 126(1-3), 75-90.

Brenan, J. M. (2015). Se–Te fractionation by sulfide–silicate melt partitioning: implications for the composition of mantle-derived magmas and their melting residues. Earth and Planetary Science Letters, 422, 45-57.

Brey, G. P., & Köhler, T. (1990). Geothermobarometry in four-phase lherzolites II. New thermobarometers, and practical assessment of existing thermobarometers. Journal of Petrology, 31(6), 1353-1378.

Büchl, A., Brügmann, G., Batanova, V. G., Münker, C., & Hofmann, A. W. (2002). Melt percolation monitored by Os isotopes and HSE abundances: a case study from the mantle section of the Troodos Ophiolite. Earth and Planetary Science Letters, 204(3-4), 385-402.

Chalot-Prat, F., & Arnold, M. (1999). Immiscibility between calciocarbonatitic and silicate melts and related wall rock reactions in the upper mantle: a natural case study from Romanian mantle xenoliths. Lithos, 46(4), 627-659.

Cherniak, D. J., & Dimanov, A. (2010). Diffusion in pyroxene, mica and amphibole. Reviews in Mineralogy and Geochemistry, 72(1), 641-690.

Cherniak, D. J., & Liang, Y. (2007). Rare earth element diffusion in natural enstatite. Geochimica et Cosmochimica Acta, 71(5), 1324-1340.

Christie, J. M. (1960). Mylonitic rocks of the Moine thrust-zone in the Assynt region, north-west Scotland. Transactions of the Edinburgh Geological Society, 18(1), 79-93.

Ciążela, J., Dick, H. J., Koepke, J., Pieterek, B., Muszynski, A., Botcharnikov, R., & Kuhn, T. (2017). Thin crust and exposed mantle control sulfide differentiation in slow-spreading ridge magmas. Geology, 45(10), 935-938.

Ciążela, J., Koepke, J., Dick, H. J., Botcharnikov, R., Muszynski, A., Lazarov, M., Schuth, S., Pieterek, B., & Kuhn, T. (2018). Sulfide enrichment at an oceanic crust-mantle transition zone: Kane Megamullion (23° N, MAR). Geochimica et Cosmochimica Acta, 230, 155-189.

Ciążela, J., Weyer, S., Weyrauch, M., Horn, I., Dick, H. J. B. & Pieterek, B. (2019). Ni-Fe isotope fractionation during cooling of sulfide liquid. 29th Goldschmidt Conference, Barcelona, Goldschmidt2019 Abstracts.

Coltorti, M., Bonadiman, C., Faccini, B., Grégoire, M., O'Reilly, S. Y., & Powell, W. (2007b). Amphiboles from suprasubduction and intraplate lithospheric mantle. Lithos, 99(1-2), 68-84.

Coltorti, M., Bonadiman, C., Faccini, B., Ntaflos, T., & Siena, F. (2007a). Slab melt and intraplate metasomatism in Kapfenstein mantle xenoliths (Styrian Basin, Austria). Lithos, 94(1-4), 66-89.

Coltorti, M., Bonadiman, C., Hinton, R. W., Siena, F., & Upton, B. G. J. (1999). Carbonatite metasomatism of the oceanic upper mantle: evidence from clinopyroxenes and glasses in ultramafic xenoliths of Grande Comore, Indian Ocean. Journal of Petrology, 40(1), 133-165.

Coogan, L. A., Hain, A., Stahl, S., & Chakraborty, S. (2005). Experimental determination of the diffusion coefficient for calcium in olivine between 900 C and 1500 C. Geochimica et Cosmochimica Acta, 69(14), 3683-3694.

Craddock, P. R., Warren, J. M., & Dauphas, N. (2013). Abyssal peridotites reveal the near-chondritic Fe isotopic composition of the Earth. Earth and Planetary Science Letters, 365, 63-76.

Craig J. R. and Kullerud G. (1969). Phase relations in the Cu-Fe-Ni-S system and their application to magmatic ore deposits. Economic Geology Monographs, 4, 344-358.

Créon, L., Delpech, G., Rouchon, V., & Guyot, F. (2017). Slab-derived metasomatism in the Carpathian-Pannonian mantle revealed by investigations of mantle xenoliths from the Bakony-Balaton Highland Volcanic Field. Lithos, 286, 534-552.

Csontos, L. (1995). Tertiary tectonic evolution of the Intra-Carpathian area: a review. Acta Vulcanologica, 7(2), 1-13.

Csontos, L., & Nagymarosy, A. (1998). The Mid-Hungarian line: a zone of repeated tectonic inversions. Tectonophysics, 297(1-4), 51-71.

Csontos, L., & Vörös, A. (2004). Mesozoic plate tectonic reconstruction of the Carpathian region. Palaeogeography, Palaeoclimatology, Palaeoecology, 210(1), 1-56.

Csontos, L., Nagymarosy, A., Horváth, F., & Kovac, M. (1992). Tertiary evolution of the Intra-Carpathian area: a model. Tectonophysics, 208(1-3), 221-241.

Dai, L., & Karato, S. I. (2009). Electrical conductivity of orthopyroxene: Implications for the water content of the asthenosphere. Proceedings of the Japan Academy, Series B, 85(10), 466-475.

Dai, L., Li, H., Liu, C., Su, G., & Shan, S. (2006). Experimental measurement of the electrical conductivity of pyroxenite at high temperature and high pressure under different oxygen fugacities. High Pressure Research, 26(3), 193-202.

Dawson, J. B. (1984). Contrasting types of upper mantle metasomatism. In: Kornprobst, J. (ed.) Kimberlites II: The mantle and crust/mantle relationships. Elsevier, Amsterdam, pp. 290-294.

de Bremond d'Ars, J., Arndt, N. T., & Hallot, E. (2001). Analog experimental insights into the formation of magmatic sulfide deposits. Earth and Planetary Science Letters, 186(3-4), 371-381.

Della Ventura, G., Oberti, R., Hawthorne, F. C., & Bellatreccia, F. (2007). FTIR spectroscopy of Ti-rich pargasites from Lherz and the detection of O^{2-} at the anionic O3 site in amphiboles. American Mineralogist, 92(10), 1645-1651.

Delpech, G., Lorand, J. P., Grégoire, M., Cottin, J. Y., & O'Reilly, S. Y. (2012). In-situ geochemistry of sulfides in highly metasomatized mantle xenoliths from Kerguelen, southern Indian Ocean. Lithos, 154, 296-314.

Demény, A., Vennemann, T. W., Hegner, E., Nagy, G., Milton, J. A., Embey-Isztin, A., Homonnay, Z., & Dobosi, G. (2004). Trace element and C–O–Sr–Nd isotope evidence for subduction-related carbonate–silicate melts in mantle xenoliths (Pannonian Basin, Hungary). Lithos, 75(1-2), 89-113.

Demouchy, S., & Bolfan-Casanova, N. (2016). Distribution and transport of hydrogen in the lithospheric mantle: A review. Lithos, 240, 402-425.

Demouchy, S., Ishikawa, A., Tommasi, A., Alard, O., & Keshav, S. (2015). Characterization of hydration in the mantle lithosphere: Peridotite xenoliths from the Ontong Java Plateau as an example. Lithos, 212, 189-201.

Denis, C. M., Alard, O., & Demouchy, S. (2015). Water content and hydrogen behaviour during metasomatism in the uppermost mantle beneath Ray Pic volcano (Massif Central, France). Lithos, 236, 256-274.

Denis, C. M., Demouchy, S., & Alard, O. (2018). Heterogeneous hydrogen distribution in orthopyroxene from veined mantle peridotite (San Carlos, Arizona): Impact of melt-rock interactions. Lithos, 302, 298-311.

D'Errico, M. E., Coble, M. A., & Warren, J. M. (2019). In situ measurements of lead and other trace elements in abyssal peridotite sulfides. American Mineralogist: Journal of Earth and Planetary Materials, 104(2), 190-206.

Desissa, M., Johnson, N. E., Whaler, K. A., Hautot, S., Fisseha, S., & Dawes, G. J. K. (2013). A mantle magma reservoir beneath an incipient mid-ocean ridge in Afar, Ethiopia. Nature Geoscience, 6(10), 861-865.

Dick, H. J., Fisher, R. L., & Bryan, W. B. (1984). Mineralogic variability of the uppermost mantle along mid-ocean ridges. Earth and Planetary Science Letters, 69(1), 88-106.

Dobosi, G. (1995). Late-Cenozoic alkalic basalt magmatism in northern Hungary and Slovakia: petrology, source compositions and relationship to tectonics. Acta Vulcano., 7, 199-207.

Dobosi, G., Jenner, G. A., Embey-Isztin, A., & Downes, H. (2010). Cryptic metasomatism in clino-and orthopyroxene in the upper mantle beneath the Pannonian region. Geological Society, London, Special Publications, 337(1), 177-194.

Dobosi, G., Kurat, G., Jenner, G. A., & Brandstätter, F. (1999). Cryptic metasomatism in the upper mantle beneath Southeastern Austria: a laser ablation microprobe-ICP-MS study. Mineralogy and Petrology, 67(3-4), 143-161.

Dombrádi, E., Sokoutis, D., Bada, G., Cloetingh, S., & Horváth, F. (2010). Modelling recent deformation of the Pannonian lithosphere: lithospheric folding and tectonic topography. Tectonophysics, 484(1-4), 103-118.

Doucet, L. S., Peslier, A. H., Ionov, D. A., Brandon, A. D., Golovin, A. V., Goncharov, A. G., & Ashchepkov, I. V. (2014). High water contents in the Siberian cratonic mantle linked to metasomatism: An FTIR study of Udachnaya peridotite xenoliths. Geochimica et Cosmochimica Acta, 137, 159-187.

Downes, H. (1997). Shallow continental lithospheric mantle heterogeneity - petrological constraints. In: Fuchs, K. (ed.) Upper Mantle Heterogeneities from Active and Passive Seismology. Springer, pp. 295-308.

Downes, H. (2001). Formation and modification of the shallow sub-continental lithospheric mantle: a review of geochemical evidence from ultramafic xenolith suites and tectonically emplaced ultramafic massifs of western and central Europe. Journal of Petrology, 42(1), 233-250.

Downes, H., Embey-Isztin, A., & Thirlwall, M. F. (1992). Petrology and geochemistry of spinel peridotite xenoliths from the western Pannonian Basin (Hungary): evidence for an association between enrichment and texture in the upper mantle. Contributions to Mineralogy and Petrology, 109(3), 340-354.

Ebinger, C. J., Keir, D., Bastow, I. D., Whaler, K., Hammond, J. O., Ayele, A., Miller, M. S., Tiberi, C. & Hautot, S. (2017). Crustal structure of active deformation zones in Africa: Implications for global crustal processes. Tectonics, 36(12), 3298-3332.

Embey-Isztin, A. (1978). On the petrology of spinel lherzolite nodules in basaltic rocks from Hungary and Auvergne, France. Annales Hitorico-Naturales Musei Nationalis Hungarici, 70, 27-44.

Embey-Isztin, A., Dobosi, G., & Downes, H. (2001). Geochemical characterization of the Pannonian Basin mantle lithosphere and asthenosphere: an overview. Acta Geologica Hungarica, 44(2-3), 259-280.

Embey-Isztin, A., Dobosi, G., Bodinier, J. L., Bosch, D., Jenner, G. A., Pourtales, S., & Bruguier, O. (2014). Origin and significance of poikilitic and mosaic peridotite xenoliths in the western Pannonian Basin: geochemical and petrological evidences. Contributions to Mineralogy and Petrology, 168(3), 1054.

Embey-Isztin, A., Downes, H., James, D. E., Upton, B. G. J., Dobosi, G., Ingram, G.A., Harmon, R.S., & Scharbert, H.G. (1993). The petrogenesis of Pliocene alkaline volcanic rocks from the Pannonian Basin, Eastern Central Europe. Journal of Petrology, 34(2), 317-343.

Embey-Isztin, A., Scharbert, H. G., Dietrich, H., & Poultidis, H. (1989). Petrology and geochemistry of peridotite xenoliths in alkali basalts from the Transdanubian Volcanic Region, West Hungary. Journal of Petrology, 30(1), 79-105.

Falus, G., Szabó, C., & Vaselli, O. (2000). Mantle upwelling within the Pannonian Basin: evidence from xenolith lithology and mineral chemistry. Terra nova, 12(6), 295-302.

Falus, G., Szabó, C., Kovács, I., Zajacz, Z., & Halter, W. (2007). Symplectite in spinel lherzolite xenoliths from the Little Hungarian Plain, Western Hungary: A key for understanding the complex history of the upper mantle of the Pannonian Basin. Lithos, 94(1-4), 230-247.

Falus, G., Tommasi, A., & Soustelle, V. (2011). The effect of dynamic recrystallization on olivine crystal preferred orientations in mantle xenoliths deformed under varied stress conditions. Journal of Structural Geology, 33(11), 1528-1540.

Falus, G., Tommasi, A., Ingrin, J., & Szabó, C. (2008). Deformation and seismic anisotropy of the lithospheric mantle in the southeastern Carpathians inferred from the study of mantle xenoliths. Earth and Planetary Science Letters, 272(1-2), 50-64.

Fellows, S. A., & Canil, D. (2012). Experimental study of the partitioning of Cu during partial melting of Earth's mantle. Earth and Planetary Science Letters, 337, 133-143.

Fodor, L., Csontos, L., Bada, G., Györfi, I., & Benkovics, L. (1999). Tertiary tectonic evolution of the Pannonian Basin system and neighbouring orogens: a new synthesis of palaeostress data. Geological Society, London, Special Publications, 156(1), 295-334.

Fodor, L., Jelen, B., Márton, E., Skaberne, D., Čar, J., & Vrabec, M. (1998). Miocene-Pliocene tectonic evolution of the Slovenian Periadriatic fault: Implications for Alpine-Carpathian extrusion models. Tectonics, 17(5), 690-709.

Frey, F. A., & Prinz, M. (1978). Ultramafic inclusions from San Carlos, Arizona: petrologic and geochemical data bearing on their petrogenesis. Earth and Planetary Science Letters, 38(1), 129-176.

Fullea, J. (2017). On joint modelling of electrical conductivity and other geophysical and petrological observables to infer the structure of the lithosphere and underlying upper mantle. Surveys in Geophysics, 38(5), 963-1004.

Fullea, J., Muller, M. R., & Jones, A. G. (2011). Electrical conductivity of continental lithospheric mantle from integrated geophysical and petrological modeling: Application to the Kaapvaal Craton and Rehoboth Terrane, southern Africa. Journal of Geophysical Research: Solid Earth, 116(B10).

Garuti, G., Gorgoni, C., & Sighinolfi, G. P. (1984). Sulfide mineralogy and chalcophile and siderophile element abundances in the Ivrea-Verbano mantle peridotites (Western Italian Alps). Earth and Planetary Science Letters, 70(1), 69-87.

Gaul, O. F., Griffin, W. L., O'Reilly, S. Y., & Pearson, N. J. (2000). Mapping olivine composition in the lithospheric mantle. Earth and Planetary Science Letters, 182(3-4), 223-235.

Gervasoni, F., Klemme, S., Rohrbach, A., Grützner, T., & Berndt, J. (2017). Experimental constraints on mantle metasomatism caused by silicate and carbonate melts. Lithos, 282, 173-186.

Girardeau, J., & Francheteau, J. (1993). Plagioclase-wehrlites and peridotites on the East Pacific Rise (Hess Deep) and the Mid-Atlantic Ridge (DSDP Site 334): evidence for magma percolation in the oceanic upper mantle. Earth and Planetary Science Letters, 115(1-4), 137-149.

Glover, P. W. J. (1996). Graphite and electrical conductivity in the lower continental crust: a review. Physics and Chemistry of the Earth, 21(4), 279-287.

González-Jiménez, J. M., Villaseca, C., Griffin, W. L., O'Reilly, S. Y., Belousova, E., Ancochea, E., & Pearson, N. J. (2014). Significance of ancient sulfide PGE and Re–Os signatures in the mantle beneath Calatrava, Central Spain. Contributions to Mineralogy and Petrology, 168(2), 1047.

Grad, M., Guterch, A., Keller, G. R., Janik, T., Hegedűs, E., Vozár, J., Ślączka, A., Tiira, T. & Yliniemi, J. (2006). Lithospheric structure beneath trans-Carpathian transect from Precambrian platform to Pannonian basin: CELEBRATION 2000 seismic profile CEL05. Journal of Geophysical Research: Solid Earth, 111(B3).

Griffin, W. L., Spetsius, Z. V., Pearson, N. J., & O'Reilly, S. Y. (2002). In situ Re-Os analysis of sulfide inclusions in kimberlitic olivine: New constraints on depletion events in the Siberian lithospheric mantle. Geochemistry, Geophysics, Geosystems, 3(11), 1-25.

Gu, X., Ingrin, J., Deloule, E., France, L., & Xia, Q. (2018). Metasomatism in the sub-continental lithospheric mantle beneath the south French Massif Central: Constraints from trace elements, Li and H in peridotite minerals. Chemical Geology, 478, 2-17.

Guillong, M., Meier, D. L., Allan, M. M., Heinrich, C. A., & Yardley, B. W. (2008). Appendix A6: SILLS: A MATLAB-based program for the reduction of laser ablation ICP-MS data of homogeneous materials and inclusions. Mineralogical Association of Canada Short Course, 40, 328-333.

Guo, J., Griffin, W. L., & O'Reilly, S. Y. (1999). Geochemistry and origin of sulphide minerals in mantle xenoliths: Qilin, Southeastern China. Journal of Petrology, 40(7), 1125-1149.

Guzmics, T., Zajacz, Z., Kodolányi, J., Halter, W., & Szabó, C. (2008). LA-ICP-MS study of apatite-and K feldspar-hosted primary carbonatite melt inclusions in clinopyroxenite xenoliths from lamprophyres, Hungary: Implications for significance of carbonatite melts in the Earth's mantle. Geochimica et Cosmochimica Acta, 72(7), 1864-1886.

Hao, Y. T., Xia, Q. K., Jia, Z. B., Zhao, Q. C., Li, P., Feng, M., & Liu, S. C. (2016a). Regional heterogeneity in the water content of the Cenozoic lithospheric mantle of Eastern China. Journal of Geophysical Research: Solid Earth, 121(2), 517-537.

Hao, Y. T., Xia, Q. K., Tian, Z. Z., & Liu, J. (2016b). Mantle metasomatism did not modify the initial H2O content in peridotite xenoliths from the Tianchang basalts of eastern China. Lithos, 260, 315-327.

Hao, Y., Xia, Q., Li, Q., Chen, H., & Feng, M. (2014). Partial melting control of water contents in the Cenozoic lithospheric mantle of the Cathaysia block of South China. Chemical Geology, 380, 7-19.

Hao, Y., Xia, Q., Liu, S., Feng, M., & Zhang, Y. (2012). Recognizing juvenile and relict lithospheric mantle beneath the North China Craton: combined analysis of H2O, major and trace elements and Sr–Nd isotope compositions of clinopyroxenes. Lithos, 149, 136-145.

Harangi, S. (2001). Neogene to Quaternary volcanism of the Carpathian–Pannonian Region - a review. Acta Geologica Hungarica, 44(2), 223-258.

Harangi, S., & Lenkey, L. (2007). Genesis of the Neogene to Quaternary volcanism in the Carpathian-Pannonian region: Role of subduction, extension, and mantle plume. Special Papers-Geological Society of America, 418, 67.

Harangi, S., Downes, H., Kósa, L., Szabó, C., Thirlwall, M. F., Mason, P. R. D., & Mattey, D. (2001). Almandine garnet in calc-alkaline volcanic rocks of the Northern Pannonian Basin (Eastern–Central Europe): Geochemistry, petrogenesis and geodynamic implications. Journal of Petrology, 42(10), 1813-1843.

Harangi, S., Jankovics, M. É., Sági, T., Kiss, B., Lukács, R., & Soós, I. (2015). Origin and geodynamic relationships of the Late Miocene to Quaternary alkaline basalt volcanism in the Pannonian basin, eastern–central Europe. International Journal of Earth Sciences, 104(8), 2007-2032.

Harangi, S., Mason, P. R., & Lukács, R. (2005). Correlation and petrogenesis of silicic pyroclastic rocks in the Northern Pannonian Basin, Eastern-Central Europe: In situ trace element data of glass shards and mineral chemical constraints. Journal of Volcanology and Geothermal Research, 143(4), 237-257.

Harangi, S., Wilson, M., & Tonarini, S. (1995). Petrogenesis of Neogene potassic volcanic rocks in the. Acta Vulcanologica, 7(2), 125-134.

Hart, S. R., & Dunn, T. (1993). Experimental cpx/melt partitioning of 24 trace elements. Contributions to Mineralogy and Petrology, 113(1), 1-8.

Harte B (1983) Mantle peridotites and processes: the kimberlite sample. In: Hawkesworth CJ, Norry MJ (eds) Continental basalts and their xenoliths. Shiva, Nantwich, pp. 46-91.

Harvey, J., König, S., & Luguet, A. (2015). The effects of melt depletion and metasomatism on highly siderophile and strongly chalcophile elements: S–Se–Te–Re–PGE systematics of peridotite xenoliths from Kilbourne Hole, New Mexico. Geochimica et Cosmochimica Acta, 166, 210-233.

Haughton, D. R., Roeder, P. L., & Skinner, B. J. (1974). Solubility of sulfur in mafic magmas. Economic Geology, 69(4), 451-467.

Hauri, E. H., Shimizu, N., Dieu, J. J., & Hart, S. R. (1993). Evidence for hotspot-related carbonatite metasomatism in the oceanic upper mantle. Nature, 365(6443), 221.

Helmy, H. M., Ballhaus, C., Wohlgemuth-Ueberwasser, C., Fonseca, R. O., & Laurenz, V. (2010). Partitioning of Se, As, Sb, Te and Bi between monosulfide solid solution and sulfide melt–application to magmatic sulfide deposits. Geochimica et Cosmochimica Acta, 74(21), 6174-6179.

Herzberg, C., & Asimow, P. D. (2008). Petrology of some oceanic island basalts: PRIMELT2. XLS software for primary magma calculation. Geochemistry, Geophysics, Geosystems, 9(9).

Hidas, K., Falus, G., Szabó, C., Szabó, P. J., Kovács, I., & Földes, T. (2007). Geodynamic implications of flattened tabular equigranular textured peridotites from the Bakony-Balaton Highland Volcanic Field (Western Hungary). Journal of Geodynamics, 43(4-5), 484-503.

Hidas, K., Guzmics, T., Szabó, C., Kovács, I., Bodnar, R. J., Zajacz, Z., Nédli, Z., Vaccari, L., & Perucchi, A. (2010). Coexisting silicate melt inclusions and H_2O-bearing, CO_2-rich fluid inclusions in mantle peridotite xenoliths from the Carpathian–Pannonian region (central Hungary). Chemical Geology, 274(1-2), 1-18.

Hinze, E., Will, G., & Cemič, L. (1981). Electrical conductivity measurements on synthetic olivines and on olivine, enstatite and diopside from Dreiser Weiher, Eifel (Germany) under defined thermodynamic activities as a function of temperature and pressure. Physics of the Earth and Planetary Interiors, 25(3), 245-254.

Hirschmann, M. M., Tenner, T., Aubaud, C., & Withers, A. C. (2009). Dehydration melting of nominally anhydrous mantle: The primacy of partitioning. Physics of the Earth and Planetary Interiors, 176(1-2), 54-68.

Holwell, B. D., & McDonald, I. (2010). A review of the behaviour of platinum group elements within natural magmatic sulfide ore systems. Platinum Metals Review, 54(1), 26-36.

Horn, I., & von Blanckenburg, F. (2007). Investigation on elemental and isotopic fractionation during 196 nm femtosecond laser ablation multiple collector inductively coupled plasma mass spectrometry. Spectrochimica Acta Part B: Atomic Spectroscopy, 62(4), 410-422.

Horváth, F. (1993). Towards a mechanical model for the formation of the Pannonian basin. Tectonophysics, 226(1-4), 333-357.

Horváth, F., & Cloetingh, S. A. P. L. (1996). Stress-induced late-stage subsidence anomalies in the Pannonian basin. Tectonophysics, 266(1-4), 287-300.

Horváth, F., Bada, G., Szafián, P., Tari, G., Ádám, A., & Cloetingh, S. (2006). Formation and deformation of the Pannonian Basin: constraints from observational data. Geological Society, London, Memoirs, 32(1), 191-206.

Houseman, G. A., & Gemmer, L. (2007). Intra-orogenic extension driven by gravitational instability: Carpathian-Pannonian orogeny. Geology, 35(12), 1135-1138.

Hovorka, D., & Fejdi, P. (1980). Spinel peridotite xenoliths in the west Carpathian late Cenozoic alkali basalts and their tectonic significance. Bulletin Volcanologique, 43(1), 95.

Huang, F., Zhang, Z., Lundstrom, C. C., & Zhi, X. (2011). Iron and magnesium isotopic compositions of peridotite xenoliths from Eastern China. Geochimica et Cosmochimica Acta, 75(12), 3318-3334.

Huismans, R. S., Podladchikov, Y. Y., & Cloetingh, S. (2001). Dynamic modeling of the transition from passive to active rifting, application to the Pannonian basin. Tectonics, 20(6), 1021-1039.

Hurai, V., Danišík, M., Huraiová, M., Paquette, J.L., & Ádám, A. (2013). Combined U/Pb and (U–Th)/He geochronometry of basalt maars in Western Carpathians: implications for age of intraplate volcanism and origin of zircon metasomatism. Contributions to Mineralogy and Petrology, 166(4), 1235-1251.

Huraiová, M., & Konečný, P. (1994). Pressure-temperature conditions and oxidation state of the upper mantle in southern Slovakia. Acta Geologica Hungarica, 37, 29-39.

Ingrin, J., Latrous, K., Doukhan, J. C., & Doukhan, N. (1989). Water in diopside: an electron microscopy and infrared spectroscopy study. European Journal of Mineralogy, 327-342.

Ionov, D. A., Bodinier, J. L., Mukasa, S. B., & Zanetti, A. (2002). Mechanisms and sources of mantle metasomatism: major and trace element compositions of peridotite xenoliths from Spitsbergen in the context of numerical modelling. Journal of Petrology, 43(12), 2219-2259.

Ionov, D. A., Chanefo, I., & Bodinier, J. L. (2005). Origin of Fe-rich lherzolites and wehrlites from Tok, SE Siberia by reactive melt percolation in refractory mantle peridotites. Contributions to Mineralogy and Petrology, 150(3), 335-353.

Ionov, D. A., Griffin, W. L., & O'Reilly, S. Y. (1997). Volatile-bearing minerals and lithophile trace elements in the upper mantle. Chemical Geology, 141(3-4), 153-184.

Johnson, N. E., Whaler, K. A., Hautot, S., Fisseha, S., Desissa, M., & Dawes, G. J. K. (2016). Magma imaged magnetotellurically beneath an active and an inactive magmatic segment in Afar, Ethiopia. Geological Society, London, Special Publications, 420(1), 105-125.

Jones, A. G., Fullea, J., Evans, R. L., & Muller, M. R. (2012). Water in cratonic lithosphere: Calibrating laboratory-determined models of electrical conductivity of mantle minerals using geophysical and petrological observations. Geochemistry, Geophysics, Geosystems, 13(6).

Jones, A. G., Lezaeta, P., Ferguson, I. J., Chave, A. D., Evans, R. L., Garcia, X., & Spratt, J. (2003). The electrical structure of the Slave craton. Lithos, 71(2-4), 505-527.

Jones, A. P., Smith, J. V., Dawson, J. B., & Hansen, E. C. (1983). Metamorphism, partial melting, and K-metasomatism of garnet-scapolite-kyanite granulite xenoliths from Lashaine, Tanzania. The Journal of Geology, 91(2), 143-165.

Jugo, P. J., Luth, R. W., & Richards, J. P. (2005). An experimental study of the sulfur content in basaltic melts saturated with immiscible sulfide or sulfate liquids at 1300° C and 1.0 GPa. Journal of Petrology, 46(4), 783-798.

Jugovics, L. (1971). Észak-magyarországi-Salgótarján környéki-bazaltterületek (North Hungarian basaltic areas in the vicinty of Salgótarján). Annual report of the Geological Institute of Hungary of 1968, 145-165.

Kang, P., Lamb, W. M., & Drury, M. (2017). Using mineral equilibria to estimate H2O activities in peridotites from the Western Gneiss Region of Norway. American Mineralogist, 102(5), 1021-1036.

Karato, S-I. & Wang, D. (2013). Electrical conductivity of minerals and rocks. In: Karato, S-I. (ed.) Physics and Chemistry of the deep earth. Wiley, Chichester.

Kázmér, M., & Kovács, S. (1985). Permian-Paleogene paleogeography along the eastern part of the Insubric-Periadriatic lineament system: evidence for continental escape of the Bakony-Drauzug unit. Acta Geologica Hungarica, 28(1-2), 71-84.

Keays, R. R. (1995). The role of komatiitic and picritic magmatism and S-saturation in the formation of ore deposits. Lithos, 34(1-3), 1-18.

Kelemen, P. B., Dick, H. J., & Quick, J. E. (1992). Formation of harzburgite by pervasive melt/rock reaction in the upper mantle. Nature, 358(6388), 635.

Kelemen, P.B. (1990). Reaction between ultramafic rock and fractionating basaltic magma I. Phase relations, the origin of calc-alkaline magma series, and the formation of discordant dunite. Journal of Petrology, 31(1), 51-98.

Kelley, S. P., & Wartho, J. A. (2000). Rapid kimberlite ascent and the significance of Ar-Ar ages in xenolith phlogopites. Science, 289(5479), 609-611.

Khan, A., Connolly, J. A. D., & Olsen, N. (2006). Constraining the composition and thermal state of the mantle beneath Europe from inversion of long-period electromagnetic sounding data. Journal of Geophysical Research: Solid Earth, 111(B10).

Kilgore, M. L., Peslier, A. H., Brandon, A. D., & Lamb, W. M. (2018). Water and Oxygen Fugacity in the Lithospheric Mantle Wedge beneath the Northern Canadian Cordillera (Alligator Lake). Geochemistry, Geophysics, Geosystems, 19(10), 3844-3869.

Klébesz, R., Gráczer, Z., Szanyi, G., Liptai, N., Kovács, I., Patkó, L., Pintér, Z., Falus, G., Wesztergom, V., & Szabó, C. (2015). Constraints on the thickness and seismic properties of the lithosphere in an extensional setting (Nógrád-Gömör Volcanic Field, Northern Pannonian Basin). Acta Geodaetica et Geophysica, 50(2), 133-149.

Klébesz, R., Patkó, L., Novák, A., Wesztergom, V. & Szabó, Cs. (2016): Metasomatism and current state of the lithospheric mantle beneath the Nógrád-Gömör Volcanic Field constrained by trace element modelling and magnetotelluric survey. Geophysical Research Abstracts, 18, EGU2016-15597.

Kogarko, L., Kurat, G., & Ntaflos, T. (2001). Carbonate metasomatism of the oceanic mantle beneath Fernando de Noronha Island, Brazil. Contributions to Mineralogy and Petrology, 140(5), 577-587.

Konečný, P., Huraiová, M., & Bielik, M. (1999). P-T-X-fO2 conditions in upper mantle: evidence from lherzolitic xenoliths hosted by plio-pleistocene alkali basalts (Southern-Slovakia). GeoLines, 9, 59-66.

Konečný, P., Konečný, V., Lexa, J., & Huraiová, M. (1995b). Mantle xenoliths in alkali basalts of Southern Slovakia. Acta Vulcanologica, 7, 241-247.

Konečný, V., Lexa, J., Balogh, K., & Konečný, P. (1995a). Alkali basalt volcanism in Southern Slovakia: volcanic forms and time evolution. Acta Vulcanologica, 7, 167-172.

Kovács, I. J., Patkó, L., Liptai, N., Lange, T. P., Taracsák, Z., Cloetingh, S. A. P. L., Török, K., Király, E., Karátson, D., Biró, T., Kiss, J., Pálos, Zs., Aradi, L. E., Falus, Gy., Hidas, K., Berkesi, M., Koptev, A., Novák, A., Wesztergom, V., Fancsik, T. & Szabó, Cs. (2020). The role of water and compression in the genesis of alkaline basalts: Inferences from the Carpathian-Pannonian region. Lithos, 354, 105323.

Kovács, I., & Szabó, C. (2008). Middle Miocene volcanism in the vicinity of the Middle Hungarian zone: evidence for an inherited enriched mantle source. Journal of Geodynamics, 45(1), 1-17.

Kovács, I., Csontos, L., Szabó, C., Bali, E., Falus, G., Benedek, K., & Zajacz, Z. (2007). Paleogene-early Miocene igneous rocks and geodynamics of the Alpine-Carpathian-Pannonian-Dinaric region: an integrated approach. Geological Society of America Special Paper, 418, 93-112.

Kovács, I., Demény, A., Czuppon, G., Lécuyer, C., Fourel, F., Xia, Q. K., Liu, J., Pintér, Zs., Király, E., Török, K., Szabó, Á., Deloule, E., Falus, Gy., Fancsik, T., Zajacz, Z., Kovács S. J. & Udvardi, B. (2016). Water concentrations and hydrogen isotope compositions of alkaline basalt-hosted clinopyroxene megacrysts and amphibole clinopyroxenites: the role of structural hydroxyl groups and molecular water. Contributions to Mineralogy and Petrology, 171(5), 38.

Kovács, I., Falus, G., Stuart, G., Hidas, K., Szabó, C., Flower, M. F. J., hegedűs, E., Posgay, K., & Zilahi-Sebess, L. (2012a). Seismic anisotropy and deformation patterns in upper mantle xenoliths from the central Carpathian–Pannonian region: Asthenospheric flow as a driving force for Cenozoic extension and extrusion? Tectonophysics, 514, 168-179.

Kovács, I., Green, D. H., Rosenthal, A., Hermann, J., O'neill, H. S. C., Hibberson, W. O., & Udvardi, B. (2012b). An experimental study of water in nominally anhydrous minerals in the upper mantle near the water-saturated solidus. Journal of Petrology, 53(10), 2067-2093.

Kovács, I., Hermann, J., O'Neill, H. S. C., Gerald, J. F., Sambridge, M., & Horváth, G. (2008). Quantitative absorbance spectroscopy with unpolarized light: Part II. Experimental evaluation and development of a protocol for quantitative analysis of mineral IR spectra. American Mineralogist, 93(5-6), 765-778.

Kovács, I., Patkó, L., Falus, G., Aradi, L. E., Szanyi, G., Gráczer, Z., & Szabó, C. (2018). Upper mantle xenoliths as sources of geophysical information: the Perşani Mts. area as a case study. Acta Geodaetica et Geophysica, 53(3), 415-438.

Kovács, I., Zajacz, Z., & Szabó, C. (2004). Type-II xenoliths and related metasomatism from the Nógrád-Gömör Volcanic Field, Carpathian-Pannonian region (northern Hungary–southern Slovakia). Tectonophysics, 393(1-4), 139-161.

Kovács, S., Szederkényi, T., Haas, J., Buda, G., Császár, G., & Nagymarosy, A. (2000). in the pre-Neogene basement of the Hungarian part of the Pannonian area. Acta GeologicaHungarica, 43(3), 225-328.

Kullerud G., Yund R. A. and Moh G. (1969). Phase relations in Fe-Ni-S, Cu-Fe-S and Cu-Ni-S systems. Economic Geology, 61, 804.

Kurat, G., Palme, H., Spettel, B., Baddenhausen, H., Hofmeister, H., Palme, C., & Wänke, H. (1980). Geochemistry of ultramafic xenoliths from Kapfenstein, Austria: evidence for a variety of upper mantle processes. Geochimica et Cosmochimica Acta, 44(1), 45-60.

Lange, T. P., Szabó, C., Liptai, N., Patkó, L., Gelencsér, O., Aradi, L. E., & Kovács, I. J. (2019). Rheology study on the earth's mantle: Application of quantitative Fourier transform infrared spectroscopyon upper mantle xenolith from the Perşani Mountains (*in Hungarian*). Földtani Közlöny, 149(3, 4), 233-233.

Lantai, C. (1991). Genetics of garnets from andesites of the Karancs Mountains. Acta Geologica Hungarica, 34(1-2), 133-154.

Le Roux, V., Bodinier, J. L., Tommasi, A., Alard, O., Dautria, J. M., Vauchez, A., & Riches, A. J. V. (2007). The Lherz spinel lherzolite: refertilized rather than pristine mantle. Earth and Planetary Science Letters, 259(3-4), 599-612.

Lee, W. J., & Wyllie, P. J. (1997). Liquid immiscibility between nephelinite and carbonatite from 1.0 to 2.5 GPa compared with mantle melt compositions. Contributions to Mineralogy and Petrology, 127(1-2), 1-16.

Lenkey, L. (1999). Geothermics of the Pannonian Basin and its bearing on the tectonics of basin evolution. Ph.D. thesis, Vrije University, Amsterdam, pp. 215.

Lenoir, X., Garrido, C. J., Bodinier, J. L., & Dautria, J. M. (2000). Contrasting lithospheric mantle domains beneath the Massif Central (France) revealed by geochemistry of peridotite xenoliths. Earth and Planetary Science Letters, 181(3), 359-375.

Lexa, J., Seghedi, I., Németh, K., Szakács, A., Konečný, V., Pécskay, Z., Fülöp, A., & Kovács, M. (2010). Neogene-Quaternary volcanic forms in the Carpathian-Pannonian Region: a review. Central European Journal of Geosciense, 2(3), 207-270.

Li, P., Xia, Q. K., Deloule, E., Chen, H., Gu, X. Y., & Feng, M. (2015). Temporal variation of H2O content in the lithospheric mantle beneath the eastern North China Craton: Implications for the destruction of cratons. Gondwana Research, 28(1), 276-287.

Li, Y., & Audétat, A. (2012). Partitioning of V, Mn, Co, Ni, Cu, Zn, As, Mo, Ag, Sn, Sb, W, Au, Pb, and Bi between sulfide phases and hydrous basanite melt at upper mantle conditions. Earth and Planetary Science Letters, 355, 327-340.

Libowitzky, E., & Rossman, G. R. (1997). An IR absorption calibration for water in minerals. American Mineralogist, 82(11-12), 1111-1115.

Liptai, N. (2018). Geochemical and physical properties and evolution of the lithospheric mantle beneath the Nógrád-Gömör Volcanic Field (Northern Pannonian Basin, Central Europe). Ph.D. Thesis. Macquarie University and Eötvös Loránd University, pp. 176.

Liptai, N., Hidas, K., Tommasi, A., Patkó, L., Kovács, I. J., Griffin, W. L., O'Reilly, S. Y., Pearson, N. J., & Szabó, C. (2019b). Lateral and vertical heterogeneity in the lithospheric mantle at the northern margin of the Pannonian Basin reconstructed from peridotite xenolith microstructures. Journal of Geophysical Research: Solid Earth, 124, 6315-6336.

Liptai, N., Lange, T. P., Patkó, L., Pálos, Zs., Berkesi, M., Aradi, L. E., Szabó, Cs. & Kovács, I.J. (2019a). The effect of 'water' on the rheology of the lithospheric mantle in the Carpathian-Pannonian region. 14th Workshop of the International Lithosphere Program Task Force Sedimentary Basins, 15-19 October, Hévíz (Hungary), Abstracts, 78-79.19

Liptai, N., Lange, T. P., Patkó, L., Pintér, Zs., Berkesi, M., Aradi, L. E., Szabó, Cs. & Kovács, I. J. Effect of 'water' on the rheology of the lithospheric mantle in young extensional basin systems as shown by xenoliths from the Carpathian-Pannonian region. In prep.

Liptai, N., Patkó, L., Kovács, I. J., Hidas, K., Pintér, Z., Jeffries, T., Zajacz Z., O'Reilly, S. Y., Griffin W. L., Pearson N. J., & Szabó, C. (2017). Multiple metasomatism beneath the Nógrád–Gömör Volcanic Field (Northern Pannonian Basin) revealed by upper mantle peridotite xenoliths. Journal of Petrology, 58(6), 1107-1144.

Liu, J., Rudnick, R. L., Walker, R. J., Gao, S., Wu, F., & Piccoli, P. M. (2010). Processes controlling highly siderophile element fractionations in xenolithic peridotites and their influence on Os isotopes. Earth and Planetary Science Letters, 297(1-2), 287-297.

Liu, J., Xia, Q. K., Deloule, E., Ingrin, J., Chen, H., & Feng, M. (2015). Water content and oxygen isotopic composition of alkali basalts from the Taihang Mountains, China: recycled oceanic components in the mantle source. Journal of Petrology, 56(4), 681-702.

Liu, Y., & Brenan, J. (2015). Partitioning of platinum-group elements (PGE) and chalcogens (Se, Te, As, Sb, Bi) between monosulfide-solid solution (MSS), intermediate solid solution (ISS) and sulfide liquid at controlled fO_2–fS_2 conditions. Geochimica et Cosmochimica Acta, 159, 139-161.

Lloyd, A. S., Ferriss, E., Ruprecht, P., Hauri, E. H., Jicha, B. R., & Plank, T. (2016). An assessment of clinopyroxene as a recorder of magmatic water and magma ascent rate. Journal of Petrology, 57(10), 1865-1886.

Lorand, J. P., & Alard, O. (2010). Determination of selenium and tellurium concentrations in Pyrenean peridotites (Ariege, France): new insight into S/Se/Te systematics of the upper in mantle samples. Chemical Geology, 278(1-2), 120-130.

Lorand, J. P., & Luguet, A. (2016). Chalcophile and siderophile elements in mantle rocks: Trace elements controlled by trace minerals. Reviews in Mineralogy and Geochemistry, 81(1), 441-488.

Lorand, J. P., Delpech, G., Grégoire, M., Moine, B., O'Reilly, S. Y., & Cottin, J. Y. (2004). Platinum-group elements and the multistage metasomatic history of Kerguelen lithospheric mantle (South Indian Ocean). Chemical Geology, 208(1-4), 195-215.

Lorand, J. P., Reisberg, L., & Bedini, R. M. (2003). Platinum-group elements and melt percolation processes in Sidamo spinel peridotite xenoliths, Ethiopia, East African Rift. Chemical Geology, 196(1-4), 57-75.

Luffi, P., Seghedi, I., & Ducea, M. (2015). Subcreted oceanic crust melting beneath the Southeastern-Carpathians: evidence from garnet pyroxenite xenoliths from Quaternary basalts of the Perşani Mts. Mineralogia, Special Papers, 43, 63-64.

Luguet, A., & Reisberg, L. (2016). Highly siderophile element and ^{187}Os signatures in non-cratonic basalt-hosted peridotite xenoliths: Unravelling the origin and evolution of the post-Archean lithospheric mantle. Reviews in Mineralogy and Geochemistry, 81(1), 305-367.

Luguet, A., Pearson, D. G., Nowell, G. M., Dreher, S. T., Coggon, J. A., Spetsius, Z. V., & Parman, S. W. (2008). Enriched Pt-Re-Os isotope systematics in plume lavas explained by metasomatic sulfides. Science, 319(5862), 453-456.

Luguet, A., Shirey, S. B., Lorand, J. P., Horan, M. F., & Carlson, R. W. (2007). Residual platinum-group minerals from highly depleted harzburgites of the Lherz massif (France) and their role in HSE fractionation of the mantle. Geochimica et Cosmochimica Acta, 71(12), 3082-3097.

Lukács, R., Harangi, S., Ntaflos, T., & Mason, P. R. (2005). Silicate melt inclusions in the phenocrysts of the Szomolya Ignimbrite, Bükkalja Volcanic Field (Northern Hungary): Implications for magma chamber processes. Chemical Geology, 223(1-3), 46-67.

Magee, C., Stevenson, C. T., Ebmeier, S. K., Keir, D., Hammond, J. O., Gottsmann, J. H., Whaler, K. A., Schofield, N., Jackson, C. A-L., Petronis, M. S., O'Driscoll, B., Morgan, J., Cruden, A., Vollgger, S. A., Dering, G., Micklethwaite, S. & Jackson, M. D. (2018). Magma plumbing systems: a geophysical perspective. Journal of Petrology, 59(6), 1217-1251.

Mareschal, M., Kellett, R. L., Kurtz, R. D., Ludden, J. N., Ji, S., & Bailey, R. C. (1995). Archaean cratonic roots, mantle shear zones and deep electrical anisotropy. Nature, 375(6527), 134-137.

Marshall, E. W., Lassiter, J. C., & Barnes, J. D. (2018). On the (mis) behavior of water in the mantle: Controls on nominally anhydrous mineral water content in mantle peridotites. Earth and Planetary Science Letters, 499, 219-229.

Márton, E. (1987). Palaeomagnetism and tectonics in the Mediterranean region. Journal of Geodynamics, 7(1-2), 33-57.

Márton, E., & Fodor, L. (2003). Tertiary paleomagnetic results and structural analysis from the Transdanubian Range (Hungary): rotational disintegration of the Alcapa unit. Tectonophysics, 363(3-4), 201-224.

Mason, P. R., Downes, H., Thirlwall, M. F., Seghedi, I., Szakács, A., Lowry, D., & Mattey, D. (1996). Crustal assimilation as a major petrogenetic process in the East Carpathian Neogene and Quaternary continental margin arc, Romania. Journal of Petrology, 37(4), 927-959.

Mason, P. R., Seghedi, I., Szákacs, A., & Downes, H. (1998). Magmatic constraints on geodynamic models of subduction in the East Carpathians, Romania. Tectonophysics, 297(1-4), 157-176.

Mavrogenes, J. A., & O'Neill, H. S. C. (1999). The relative effects of pressure, temperature and oxygen fugacity on the solubility of sulfide in mafic magmas. Geochimica et Cosmochimica Acta, 63(7-8), 1173-1180.

McCoy-West, A. J., Fitton, J. G., Pons, M. L., Inglis, E. C., & Williams, H. M. (2018). The Fe and Zn isotope composition of deep mantle source regions: Insights from Baffin Island picrites. Geochimica et Cosmochimica Acta, 238, 542-562.

McDonough, W. F., & Sun, S. S. (1995). The composition of the Earth. Chemical geology, 120(3-4), 223-253.

Mercier, J. C. C. (1977). Natural peridotites: chemical and rheological heterogeneity of the upper mantle. Ph.D. Thesis, State Univ. of New York.

Mercier, J. C., & Nicolas, A. (1975). Textures and fabrics of upper-mantle peridotites as illustrated by xenoliths from basalts. Journal of Petrology, 16(1), 454-487.

Mitchell, A. L., & Grove, T. L. (2016). Experiments on melt–rock reaction in the shallow mantle wedge. Contributions to Mineralogy and Petrology, 171(12), 107.

Montgomery, D.C., Peck, E.A., Vining, G.G. (2012). Introduction to Linear Regression Analysis, vol. 821. John Wiley & Sons, ISBN 978-0-470-54281-1.

Morimoto, N. (1988). Nomenclature of pyroxenes. Mineralogy and Petrology, 39(1), 55-76.

Mungall, J. E., & Su, S. (2005). Interfacial tension between magmatic sulfide and silicate liquids: Constraints on kinetics of sulfide liquation and sulfide migration through silicate rocks. Earth and Planetary Science Letters, 234(1-2), 135-149.

Mutchler, S. R., Fedele, L., & Bodnar, R. J. (2008). Analysis Management System (AMS) for reduction of laser ablation ICPMS data. In Laser-Ablation-ICPMS in the Earth sciences: Current practices and outstanding issues (Vol. 40, pp. 318-327). Mineralogical Association of Canada Quebec.

Navon, O., & Stolper, E. (1987). Geochemical consequences of melt percolation: the upper mantle as a chromatographic column. The Journal of Geology, 95(3), 285-307.

Nédli, Z., Princivalle, F., Dobosi, G., & Embey-Isztin, A. (2009). Crystal chemistry of clinopyroxenes from upper-mantle xenolith series in the Balaton–Bakony volcanic area (Carpathian–Pannonian region, Hungary). European Journal of Mineralogy, 21(2), 433-442.

Neumann, E. R., Wulff-Pedersen, E., Pearson, N. J., & Spencer, E. A. (2002). Mantle xenoliths from Tenerife (Canary Islands): evidence for reactions between mantle peridotites and silicic carbonatite melts inducing Ca metasomatism. Journal of Petrology, 43(5), 825-857.

Nimis, P., & Grütter, H. (2010). Internally consistent geothermometers for garnet peridotites and pyroxenites. Contributions to Mineralogy and Petrology, 159(3), 411-427.

Novák, A., Klébesz, R., Szabó, C., Wesztergom, V., Patkó, L., Liptai, N., Ádam, A., Semenov, V.Y., Lemperger, I., Kis, A., & Gribovszki, K. (2014). Combined geophysical (magnetotellurics) and geochemical results for determination of the lithosphere-asthenosphere boundary (LAB) beneath the Nógrád-Gömör Volcanic Field. 22nd EM Induction Workshop, Weimar, Germany. pp. 4.

Novella, D., Jacobsen, B., Weber, P. K., Tyburczy, J. A., Ryerson, F. J., & Du Frane, W. L. (2017). Hydrogen self-diffusion in single crystal olivine and electrical conductivity of the Earth's mantle. Scientific Reports, 7(1), 5344.

O'Neill, H. S. C. (1981). The transition between spinel lherzolite and garnet lherzolite, and its use as a geobarometer. Contributions to Mineralogy and Petrology, 77(2), 185-194.

O'Neill, H. S. C., & Mavrogenes, J. A. (2002). The sulfide capacity and the sulfur content at sulfide saturation of silicate melts at 1400 C and 1 bar. Journal of Petrology, 43(6), 1049-1087.

O'Reilly, S. Y., & Griffin, W. L. (2013). Mantle metasomatism. In: Harlov and Austrheim (ed.) Metasomatism and the chemical transformation of rock. Springer, Berlin, Heidelberg, pp. 471-533.

O'Reilly, S. Y., Chen, D., Griffin, W. L., & Ryan, C. G. (1997). Minor elements in olivine from spinel lherzolite xenoliths: implications for thermobarometry. Mineralogical Magazine, 61(2), 257-269.

Oeser, M., Weyer, S., Horn, I., & Schuth, S. (2014). High-precision fe and mg isotope ratios of silicate reference glasses determined in situ by femtosecond LA-MC-ICP-MS and by solution nebulisation MC-ICP-MS. Geostandards and Geoanalytical Research, 38(3), 311–328.

Omura, K., Kurita, K., & Kumazawa, M. (1989). Experimental study of pressure dependence of electrical conductivity of olivine at high temperatures. Physics of the earth and planetary interiors, 57(3-4), 291-303.

Patkó, L., Liptai, N., Aradi, L. E., Klébesz, R., Sendula, E., Bodnar, R. J., Kovács, I. J., Hidas, K., Cesare, B., Novák, A., Trásy, B., & Szabó, Cs. (2020). Metasomatism-induced wehrlite formation in the upper mantle beneath the Nógrád-Gömör Volcanic Field (Northern Pannonian Basin): evidence from xenoliths. Geoscience Frontiers, 11, 1-22. (accepted paper)

Patkó, L., Liptai, N., Aradi, L.E., Bodnar, R.J., Sendula, E., Kovács, I.J., Klébesz, R., & Szabó, C. (2018). Deciphering mantle metasomatism using silicate melt inclusions beneath the Nógrád-Gömör Volcanic Field (Northern Pannonian Basin). EGU General Assembly, 8-13 April, Vienna (Austria), Geophysical Research Abstracts, Vol. 20, EGU2018-785.

Patkó, L., Liptai, N., Kovács, I. J., Aradi, L., Xia, Q-K., Ingrin, J., Mihály, J., O'Reilly, S., Griffin, W.L., Wesztergom, V., & Szabó, Cs. (2019) Extremely low structural hydroxyl contents in upper mantle xenoliths from the Nógrád-Gömör Volcanic Field (northern Pannonian Basin): geodynamic implications and the role of post-eruptive re-equilibration. Chemical Geology, 507, 23-41.

Pearce, N. J., Perkins, W. T., Westgate, J. A., Gorton, M. P., Jackson, S. E., Neal, C. R., & Chenery, S. P. (1997). A compilation of new and published major and trace element data for NIST SRM 610 and NIST SRM 612 glass reference materials. Geostandards Newsletter, 21(1), 115-144.

Pearson, D. G., Irvine, G. J., Ionov, D. A., Boyd, F. R., & Dreibus, G. E. (2004). Re–Os isotope systematics and platinum group element fractionation during mantle melt extraction: a study of massif and xenolith peridotite suites. Chemical Geology, 208(1-4), 29-59.

Pécskay, Z., Lexa, J., Szakács, A., Balogh, K., Seghedi, I., Konečný, V., Kovács, M., Márton, E., Kaličiak, M., Széky-Fux, V., Póka, T., Gyarmati, P., Edelstein, O., Rosu, E., & Žec, B. (1995). Space and time distribution of Neogene-Quartenary volcanism in the Carpatho-Pannonian Region. Acta Vulcanologica, 7(2), 15-28.

Pécskay, Z., Lexa, J., Szakács, A., Seghedi, I., Balogh, K., Konečný, V., Zelenka, T., Kovacs, M., Póka, T., Fülöp, A., Márton, E., Panaiotu, C., & Cvetković, V. (2006). Geochronology of Neogene magmatism in the Carpathian arc and intra-Carpathian area. Geologica Carpathica, 57 (6), 511-530.

Peslier, A. H. (2010). A review of water contents of nominally anhydrous natural minerals in the mantles of Earth, Mars and the Moon. Journal of Volcanology and Geothermal Research, 197(1-4), 239-258.

Peslier, A. H., & Bizimis, M. (2015). Water in H awaiian peridotite minerals: A case for a dry metasomatized oceanic mantle lithosphere. Geochemistry, Geophysics, Geosystems, 16(4), 1211-1232.

Peslier, A. H., & Luhr, J. F. (2006). Hydrogen loss from olivines in mantle xenoliths from Simcoe (USA) and Mexico: Mafic alkalic magma ascent rates and water budget of the sub-continental lithosphere. Earth and Planetary Science Letters, 242(3-4), 302-319.

Peslier, A. H., Francis, D., & Ludden, J. (2002a). The lithospheric mantle beneath continental margins: melting and melt–rock reaction in Canadian Cordillera xenoliths. Journal of Petrology, 43(11), 2013-2047.

Peslier, A. H., Luhr, J. F., & Post, J. (2002b). Low water contents in pyroxenes from spinel-peridotites of the oxidized, sub-arc mantle wedge. Earth and Planetary Science Letters, 201(1), 69-86.

Peslier, A. H., Schönbächler, M., Busemann, H., & Karato, S. I. (2017). Water in the Earth's interior: Distribution and origin. Space Science Reviews, 212(1-2), 743-810.

Peters, B. J., Shahar, A., Carlson, R. W., Day, J. M., & Mock, T. D. (2019). A sulfide perspective on iron isotope fractionation during ocean island basalt petrogenesis. Geochimica et Cosmochimica Acta, 245, 59-78.

Pieterek, B. (2018). Layer boundaries attract sulfides throughout the igneous layering of the lower oceanic crust: IODP Hole U1473A, Atlantis Bank, Southwest Indian Ridge. Master thesis, Adam Mickiewicz University in Poznań, pp. 78.

Pintér, Zs, Patkó, L., Djoukam, J. F. T., Kovács, I., Tchouankoue, J. P., Falus, Gy., Konc, Z., Tommasi, A., Barou, F., Mihály, J., Németh, Cs. & Jeffries, T. (2015). Characterization of the sub-continental lithospheric mantle beneath the Cameroon volcanic line inferred from alkaline basalt hosted peridotite xenoliths from Barombi Mbo and Nyos Lakes. Journal of African Earth Sciences, 111, 170–193.

Poe, B. T., Romano, C., Nestola, F., & Smyth, J. R. (2010). Electrical conductivity anisotropy of dry and hydrous olivine at 8 GPa. Physics of the Earth and Planetary Interiors, 181(3-4), 103-111.

Poitrasson, F., Delpech, G., & Grégoire, M. (2013). On the iron isotope heterogeneity of lithospheric mantle xenoliths: implications for mantle metasomatism, the origin of basalts and the iron isotope composition of the Earth. Contributions to Mineralogy and Petrology, 165(6), 1243-1258.

Póka, T., Szakács, A., Seghedi, I., Simonits, A., Zelenka, T., & Nagy, G. (1998). Petrology and geochemistry of the Miocene acidic explosive volcanism of the Bukk Foreland; Pannonian Basin, Hungary. Acta Geologica Hungarica, 41(4), 437-466.

Pouchou, J. L., & Pichoir, F. (1991). Quantitative analysis of homogeneous or stratified microvolumes applying the model "PAP". In Electron probe quantitation (pp. 31-75). Springer, Boston, MA.

Puziewicz, J., Koepke, J., Grégoire, M., Ntaflos, T., & Matusiak-Małek, M. (2011). Lithospheric mantle modification during Cenozoic rifting in Central Europe: evidence from the Księginki nephelinite (SW Poland) xenolith suite. Journal of Petrology, 52(11), 2107-2145.

Raffone, N., Chazot, G., Pin, C., Vannucci, R., & Zanetti, A. (2009). Metasomatism in the lithospheric mantle beneath Middle Atlas (Morocco) and the origin of Fe-and Mg-rich wehrlites. Journal of Petrology, 50(2), 197-249.

Ratschbacher, L., Merle, O., Davy, P., & Cobbold, P. (1991). Lateral extrusion in the Eastern Alps, part 1: boundary conditions and experiments scaled for gravity. Tectonics, 10(2), 245-256.

Reisberg, L., Zhi, X., Lorand, J. P., Wagner, C., Peng, Z., & Zimmermann, C. (2005). Re–Os and S systematics of spinel peridotite xenoliths from east central China: evidence for contrasting effects of melt percolation. Earth and Planetary Science Letters, 239(3-4), 286-308.

Rivalenti, G., Zanetti, A., Mazzucchelli, M., Vannucci, R., & Cingolani, C. A. (2004). Equivocal carbonatite markers in the mantle xenoliths of the Patagonia backarc: the Gobernador Gregores case (Santa Cruz Province, Argentina). Contributions to Mineralogy and Petrology, 147(6), 647-670.

Rocco, I., Lustrino, M., Zanetti, A., Morra, V., & Melluso, L. (2013). Petrology of ultramafic xenoliths in Cenozoic alkaline rocks of northern Madagascar (Nosy Be archipelago). Journal of South American Earth Sciences, 41, 122-139.

Roedder, E. (1984) Volume 12: Fluid inclusions. Mineralogical Society of America.

Royden, L. H., Horvath, F., & Burchfiel, B. C. (1982). Transform faulting, extension, and subduction in the Carpathian Pannonian region. Geological Society of America Bulletin, 93(8), 717-725.

Rudnick, R. L., McDonough, W. F., & Chappell, B. W. (1993). Carbonatite metasomatism in the northern Tanzanian mantle: petrographic and geochemical characteristics. Earth and Planetary Science Letters, 114(4), 463-475.

Sambridge, M., Gerald, J. F., Kovács, I., O'Neill, H. S. C., & Hermann, J. (2008). Quantitative absorbance spectroscopy with unpolarized light: Part I. Physical and mathematical development. American Mineralogist, 93(5-6), 751-764.

Santos, F. A. M., Mateus, A., Almeida, E. P., Pous, J., & Mendes-Victor, L. A. (2002). Are some of the deep crustal conductive features found in SW Iberia caused by graphite? Earth and Planetary Science Letters, 201(2), 353-367.

Saper, L., & Liang, Y. (2014). Formation of plagioclase-bearing peridotite and plagioclase-bearing wehrlite and gabbro suite through reactive crystallization: an experimental study. Contributions to Mineralogy and Petrology, 167(3), 985.

Saunders, J. E., Pearson, N. J., O'Reilly, S. Y., & Griffin, W. L. (2016). Gold in the mantle: the role of pyroxenites. Lithos, 244, 205-217.

Saunders, J. E., Pearson, N. J., O'Reilly, S. Y., & Griffin, W. L. (2015). Sulfide metasomatism and the mobility of gold in the lithospheric mantle. Chemical Geology, 410, 149-161.

Schmädicke, E., & Gose, J. (2017). Water transport by subduction: Clues from garnet of Erzgebirge UHP eclogite. American Mineralogist, 102(5), 975-986.

Schmädicke, E., Gose, J., Witt-Eickschen, G., & Brätz, H. (2013). Olivine from spinel peridotite xenoliths: Hydroxyl incorporation and mineral composition. American Mineralogist, 98(10), 1870-1880.

Schmid, S. M., Bernoulli, D., Fügenschuh, B., Matenco, L., Schefer, S., Schuster, R., Tischler, M., & Ustaszewski, K. (2008). The Alpine-Carpathian-Dinaridic orogenic system: correlation and evolution of tectonic units. Swiss Journal of Geosciences, 101(1), 139-183.

Schoenberg, R., & von Blanckenburg, F. (2006). Modes of planetary-scale Fe isotope fractionation. Earth and Planetary Science Letters, 252(3-4), 342-359.

Schoenberg, R., Marks, M. A., Schuessler, J. A., von Blanckenburg, F., & Markl, G. (2009). Fe isotope systematics of coexisting amphibole and pyroxene in the alkaline igneous rock suite of the Ilímaussaq Complex, South Greenland. Chemical Geology, 258(1-2), 65-77.

Schuessler, J. A., Schoenberg, R., & Sigmarsson, O. (2009). Iron and lithium isotope systematics of the Hekla volcano, Iceland—evidence for Fe isotope fractionation during magma differentiation. Chemical Geology, 258(1-2), 78-91.

Scott, J. M., Hodgkinson, A., Palin, J. M., Waight, T. E., Van der Meer, Q. H. A., & Cooper, A. F. (2014). Ancient melt depletion overprinted by young carbonatitic metasomatism in the New Zealand lithospheric mantle. Contributions to Mineralogy and Petrology, 167(1), 963.

Seghedi, I., & Downes, H. (2011). Geochemistry and tectonic development of Cenozoic magmatism in the Carpathian–Pannonian region. Gondwana Research, 20(4), 655-672.

Seghedi, I., Downes, H., Szakács, A., Mason, P. R., Thirlwall, M. F., Roşu, E., Pécskay, Z., Márton, E., & Panaiotu, C. (2004a). Neogene–Quaternary magmatism and geodynamics in the Carpathian–Pannonian region: a synthesis. Lithos, 72(3-4), 117-146.

Seghedi, I., Downes, H., Vaselli, O., Szakács, A., Balogh, K., & Pécskay, Z. (2004b). Post-collisional Tertiary–Quaternary mafic alkalic magmatism in the Carpathian–Pannonian region: a review. Tectonophysics, 393(1-4), 43-62.

Seifert, K. F., Will, G. & Voigt, R. (1982). Electrical conductivity measurements on synthetic pyroxenes $MgSiO_3$–$FeSiO_3$ at high pressures and temperatures under defined thermodynamic conditions. In: Schreyer, W. (ed) High-pressure researches in geoscience. Schweizerbartsche, Stuttgart, pp 419–432.

Selway, K. (2014). On the causes of electrical conductivity anomalies in tectonically stable lithosphere. Surveys in Geophysics, 35(1), 219-257.

Selway, K., O'Donnell, J. P., & Özaydin, S. (2019). Upper mantle melt distribution from petrologically constrained magnetotellurics. Geochemistry, Geophysics, Geosystems, 20(7), 3328-3346.

Shaw, C. S. (1999). Dissolution of orthopyroxene in basanitic magma between 0.4 and 2 GPa: further implications for the origin of Si-rich alkaline glass inclusions in mantle xenoliths. Contributions to Mineralogy and Petrology, 135(2-3), 114-132.

Shaw, C. S., Eyzaguirre, J., Fryer, B., & Gagnon, J. (2005). Regional variations in the mineralogy of metasomatic assemblages in mantle xenoliths from the West Eifel Volcanic Field, Germany. Journal of Petrology, 46(5), 945-972.

Shaw, C. S., Lebert, B. S., & Woodland, A. B. (2018). Thermodynamic Modelling of Mantle–Melt Interaction Evidenced by Veined Wehrlite Xenoliths from the Rockeskyllerkopf Volcanic Complex, West Eifel Volcanic Field, Germany. Journal of Petrology, 59(1), 59-86.

Sokol, A. G., Kupriyanov, I. N., & Palyanov, Y. N. (2013). Partitioning of H2O between olivine and carbonate–silicate melts at 6.3 GPa and 1400 C: Implications for kimberlite formation. Earth and Planetary Science Letters, 383, 58-67.

Soustelle, V., Tommasi, A., Demouchy, S., & Ionov, D. A. (2010). Deformation and fluid–rock interaction in the supra-subduction mantle: microstructures and water contents in peridotite xenoliths from the Avacha Volcano, Kamchatka. Journal of Petrology, 51(1-2), 363-394.

Stalder, R., & Ludwig, T. (2007). OH incorporation in synthetic diopside. European Journal of Mineralogy, 19(3), 373-380.

Stegena, L., Geczy, B., & Horváth, F. (1975). Late Cenozoic evolution of the Pannonian basin. Tectonophysics, 26(1-2), 71-90.

Streckeisen, A. (1976). To each plutonic rock its proper name. Earth-Science Reviews, 12(1), 1-33.

Suhr, G., Kelemen, P., & Paulick, H. (2008). Microstructures in Hole 1274A peridotites, ODP Leg 209, Mid-Atlantic Ridge: Tracking the fate of melts percolating in peridotite as the lithosphere is intercepted. Geochemistry, Geophysics, Geosystems, 9(3).

Sun, S. S., & McDonough, W. F. (1989). Chemical and isotopic systematics of oceanic basalts: implications for mantle composition and processes. Geological Society, London, Special Publications, 42(1), 313-345.

Szabó, Á. (2013) Effect of metasomatic melt on lithospheric mantle beneath the Eastern Transylvanian Basin *(in Hungarian)*. M.Sc. Thesis, Lithosphere Fluid Research Lab, Department of Petrology and Geochemistry, Eötvös University, Budapest, pp: 67.

Szabó, C., & Bodnar, R. J. (1995). Chemistry and origin of mantle sulfides in spinel peridotite xenoliths from alkaline basaltic lavas, Nógrád-Gömör Volcanic Field, northern Hungary and southern Slovakia. Geochimica et Cosmochimica Acta, 59(19), 3917-3927.

Szabó, C., & Bodnar, R. J. (1996). Changing magma ascent rates in the Nógrád-Gömör volcanic field Northern Hungary/Southern Slovakia: evidence from CO_2-rich fluid inclusions in metasomatized upper mantle xenoliths. Petrology, 4(3), 221-230.

Szabó, C., & Bodnar, R. J. (1998). Fluid-inclusion evidence for an upper-mantle origin for green clinopyroxenes in late Cenozoic basanites from the Nógrád-Gömör Volcanic Field, northern Hungary/southern Slovakia. International Geology Review, 40(9), 765-773.

Szabó, C., & Taylor, L. A. (1994). Mantle petrology and geochemistry beneath the Nógrád-Gömör volcanic field, Carpathian-Pannonian region. International Geology Review, 36(4), 328-358.

Szabó, C., Bodnar, R. J., & Sobolev, A. V. (1996). Metasomatism associated with subduction-related, volatile-rich silicate melt in the upper mantle beneath the Nograd-Gomor volcanic field, northern Hungary/southern Slovakia; evidence from silicate melt inclusions. European Journal of Mineralogy, 8(5), 881-899.

Szabó, C., Falus, G., Zajacz, Z., Kovács, I., & Bali, E. (2004). Composition and evolution of lithosphere beneath the Carpathian–Pannonian Region: a review. Tectonophysics, 393(1-4), 119-137.

Szabó, C., Harangi, S., & Csontos, L. (1992). Review of Neogene and Quaternary volcanism of the Carpathian-Pannonian region. Tectonophysics, 208(1-3), 243-256.

Szabó, C., Harangi, S., & VaseIli, H. (1995). Temperature and oxygen fugacity in peridotite xenoliths from the Carpathian-Pannonian Region. Acta Vulcanologica, 7(2), 231-239.

Szabó, C., Hidas, K., Bali, E., Zajacz, Z., Kovács, I., Yang, K., Guzmics, T., & Török, K. (2009). Melt–wall rock interaction in the mantle shown by silicate melt inclusions in peridotite xenoliths from the central Pannonian Basin (western Hungary). Island Arc, 18(2), 375-400.

Szabó, Cs., Patkó, L., Ciążela, J., Aradi, L. E., Liptai, N., Pieterek, B., Lazarov, M., Holtz, F. & Kovács I. J. (2019). Fe-Cu stable isotope and trace element variations during mantle metasomatism - a study on sulfide blebs from peridotite xenoliths from Nógrád-Gömör Volcanic Field (Northern Pannonian Basin). 29th Goldschmidt Conference, Barcelona, Goldschmidt2019 Abstracts.

Szakács, A., Márton, E., Póka, T., Zelenka, T., Pécskay, Z., & Seghedi, I. (1998). Miocene acidic explosive volcanism in the Bukk Foreland, Hungary: identifying eruptive sequences and searching for source locations. Acta Geologica Hungarica, 41(4), 413-435.

Tašárová, A., Afonso, J. C., Bielik, M., Götze, H. J., & Hók, J. (2009). The lithospheric structure of the Western Carpathian–Pannonian Basin region based on the CELEBRATION 2000 seismic experiment and gravity modelling. Tectonophysics, 475(3-4), 454-469.

Teng, F. Z., Dauphas, N., Helz, R. T., Gao, S., & Huang, S. (2011). Diffusion-driven magnesium and iron isotope fractionation in Hawaiian olivine. Earth and Planetary Science Letters, 308(3-4), 317-324.

Teng, F. Z., Dauphas, N., Huang, S., & Marty, B. (2013). Iron isotopic systematics of oceanic basalts. Geochimica et Cosmochimica Acta, 107, 12-26.

Tian, Z. Z., Liu, J., Xia, Q. K., Ingrin, J., Hao, Y. T., & Christophe, D. (2017). Water concentration profiles in natural mantle orthopyroxenes: A geochronometer for long annealing of xenoliths within magma. Geology, 45(1), 87-90.

Tollan, P., & Hermann, J. (2019). Arc magmas oxidized by water dissociation and hydrogen incorporation in orthopyroxene. Nature geoscience, 12(8), 667-671.

Tommasi, A., Tikoff, B., & Vauchez, A. (1999). Upper mantle tectonics: three-dimensional deformation, olivine crystallographic fabrics and seismic properties. Earth and Planetary Science Letters, 168(1-2), 173-186.

Tóth, A., Dobosi, G., Beard, A., Downes, H., Bali, E., & Szabó, C. (2006). Garnet Pyroxenites from Eastern Transylvanian Basin: an Inte-grated Textural and Geochemical Study. Geolines, 20, 128.

Tursack, E., & Liang, Y. (2012). A comparative study of melt-rock reactions in the mantle: laboratory dissolution experiments and geological field observations. Contributions to Mineralogy and Petrology, 163(5), 861-876.

Van Den Bleeken, G., Müntener, O., & Ulmer, P. (2010). Reaction processes between tholeiitic melt and residual peridotite in the uppermost mantle: An experimental study at 0· 8 GPa. Journal of petrology, 51(1-2), 153-183.

Vaselli, O., Downes, H., Thirlwall, M. F., Vannucci, R., & Coradossi, N. (1996). Spinel-peridotite xenoliths from Kapfenstein (Graz Basin, Eastern Austria): a geochemical and petrological study. Mineralogy and Petrology, 57(1-2), 23-50.

Vaselli, O., Downes, H., Thirlwall, M., Dobosi, G., Coradossi, N., Seghedi, I., Szakács, A., & Vannucci, R. (1995). Ultramafic xenoliths in Plio-Pleistocene alkali basalts from the Eastern Transylvanian Basin: depleted mantle enriched by vein metasomatism. Journal of Petrology, 36(1), 23-53.

Vernières, J., Godard, M., & Bodinier, J. L. (1997). A plate model for the simulation of trace element fractionation during partial melting and magma transport in the Earth's upper mantle. Journal of Geophysical Research: Solid Earth, 102(B11), 24771-24784.

Vozár, J., Jones, A. G., Fullea, J., Agius, M. R., Lebedev, S., Le Pape, F., & Wei, W. (2014). Integrated geophysical-petrological modeling of lithosphere-asthenosphere boundary in central Tibet using electromagnetic and seismic data. Geochemistry, Geophysics, Geosystems, 15(10), 3965-3988.

Wainwright, A. N., Luguet, A., Fonseca, R. O. C., & Pearson, D. G. (2015). Investigating metasomatic effects on the ^{187}Os isotopic signature: a case study on micrometric base metal sulphides in metasomatised peridotite from the Letlhakane kimberlite (Botswana). Lithos, 232, 35-48.

Wang, D., Mookherjee, M., Xu, Y., & Karato, S. I. (2006). The effect of water on the electrical conductivity of olivine. Nature, 443(7114), 977.

Wang, K. L., O'Reilly, S. Y., Griffin, W. L., Pearson, N. J., & Zhang, M. (2009). Sulfides in mantle peridotites from Penghu Islands, Taiwan: melt percolation, PGE fractionation, and the lithospheric evolution of the South China block. Geochimica et Cosmochimica Acta, 73(15), 4531-4557.

Wang, Z., Lazarov, M., Steinmann, L. K., Becker, H., Zou, Z., & Geng, X. (2018). The distribution of lead and thallium in mantle rocks: Insights from the Balmuccia peridotite massif (Italian Alps). American Mineralogist: Journal of Earth and Planetary Materials, 103(8), 1185-1199.

Westner, K. J., Beier, C., Klemd, R., Osbahr, I., & Brooks, N. (2019). In Situ Chalcophile and Siderophile Element Behavior in Sulfides from Moroccan Middle Atlas Spinel Peridotite Xenoliths during Metasomatism and Weathering. Minerals, 9(5), 276.

Weyer, S., & Ionov, D. A. (2007). Partial melting and melt percolation in the mantle: the message from Fe isotopes. Earth and Planetary Science Letters, 259(1-2), 119-133.

Weyer, S., Anbar, A. D., Brey, G. P., Münker, C., Mezger, K., & Woodland, A. B. (2005). Iron isotope fractionation during planetary differentiation. Earth and Planetary Science Letters, 240(2), 251-264.

Williams, H. M., McCammon, C. A., Peslier, A. H., Halliday, A. N., Teutsch, N., Levasseur, S., & Burg, J. P. (2004). Iron isotope fractionation and the oxygen fugacity of the mantle. Science, 304(5677), 1656-1659.

Williams, H. M., Peslier, A. H., McCammon, C., Halliday, A. N., Levasseur, S., Teutsch, N., & Burg, J. P. (2005). Systematic iron isotope variations in mantle rocks and minerals: the effects of partial melting and oxygen fugacity. Earth and Planetary Science Letters, 235(1-2), 435-452.

Williams, H. M., Prytulak, J., Woodhead, J. D., Kelley, K. A., Brounce, M., & Plank, T. (2018). Interplay of crystal fractionation, sulfide saturation and oxygen fugacity on the iron isotope composition of arc lavas: an example from the Marianas. Geochimica et Cosmochimica Acta, 226, 224-243.

Willingshofer, E., Van Wees, J. D., Cloetingh, S. A. P. L., & Neubauer, F. (1999). Thermomechanical consequences of Cretaceous continent-continent collision in the eastern Alps (Austria): Insights from two-dimensional modeling. Tectonics, 18(5), 809-826.

Wilson, M., & Downes, H. (2006). Tertiary-Quaternary intra-plate magmatism in Europe and its relationship to mantle dynamics. Geological Society, London, Memoirs, 32(1), 147-166.

Xia, Q. K., Hao, Y. T., Liu, S. C., Gu, X. Y., & Feng, M. (2013b). Water contents of the Cenozoic lithospheric mantle beneath the western part of the North China Craton: Peridotite xenolith constraints. Gondwana Research, 23(1), 108-118.

Xia, Q. K., Hao, Y., Li, P., Deloule, E., Coltorti, M., Dallai, L., Yang, X. & Feng, M. (2010). Low water content of the Cenozoic lithospheric mantle beneath the eastern part of the North China Craton. Journal of Geophysical Research: Solid Earth, 115(B7).

Xia, Q. K., Liu, J., Kovács, I., Hao, Y. T., Li, P., Yang, X. Z., Chen, H., & Sheng, Y. M. (2019). Water in the upper mantle and deep crust of eastern China: concentration, distribution and implications. National Science Review, 6(1), 125-144.

Xia, Q. K., Liu, J., Liu, S. C., Kovács, I., Feng, M., & Dang, L. (2013a). High water content in Mesozoic primitive basalts of the North China Craton and implications on the destruction of cratonic mantle lithosphere. Earth and Planetary Science Letters, 361, 85-97.

Xiao, Y., Zhang, H. F., Fan, W. M., Ying, J. F., Zhang, J., Zhao, X. M., & Su, B. X. (2010). Evolution of lithospheric mantle beneath the Tan-Lu fault zone, eastern North China Craton: evidence from petrology and geochemistry of peridotite xenoliths. Lithos, 117(1-4), 229-246.

Xu, Y., Mercier, J. C., Lin, C., Shi, L., Menzies, M. A., Ross, J. V., & Harte, B. (1996). K-rich glass-bearing wehrlite xenoliths from Yitong, Northeastern China: petrological and chemical evidence for mantle metasomatism. Contributions to Mineralogy and Petrology, 125(4), 406-420.

Xu, Y., Shankland, T. J., & Duba, A. G. (2000). Pressure effect on electrical conductivity of mantle olivine. Physics of the Earth and Planetary Interiors, 118(1-2), 149-161.

Yang, X. Z., Xia, Q. K., Deloule, E., Dallai, L., Fan, Q. C., & Feng, M. (2008). Water in minerals of the continental lithospheric mantle and overlying lower crust: a comparative study of peridotite and granulite xenoliths from the North China Craton. Chemical Geology, 256(1-2), 33-45.

Yang, X., Keppler, H., McCammon, C., Ni, H., Xia, Q., & Fan, Q. (2011). Effect of water on the electrical conductivity of lower crustal clinopyroxene. Journal of Geophysical Research: Solid Earth, 116(B4).

Yaxley, G. M., Crawford, A. J., & Green, D. H. (1991). Evidence for carbonatite metasomatism in spinel peridotite xenoliths from western Victoria, Australia. Earth and Planetary Science Letters, 107(2), 305-317.

Yaxley, G. M., Green, D. H., & Kamenetsky, V. (1998). Carbonatite metasomatism in the southeastern Australian lithosphere. Journal of Petrology, 39(11-12), 1917-1930.

Yoshino, T., Matsuzaki, T., Shatskiy, A., & Katsura, T. (2009). The effect of water on the electrical conductivity of olivine aggregates and its implications for the electrical structure of the upper mantle. Earth and Planetary Science Letters, 288(1-2), 291-300.

Yoshino, T., Shimojuku, A., Shan, S., Guo, X., Yamazaki, D., Ito, E., Higo, J. & Funakoshi, K. I. (2012). Effect of temperature, pressure and iron content on the electrical conductivity of olivine and its high-pressure polymorphs. Journal of Geophysical Research: Solid Earth, 117(B8).

Yu, Y., Xu, X. S., Griffin, W. L., O'Reilly, S. Y., & Xia, Q. K. (2011). H_2O contents and their modification in the Cenozoic subcontinental lithospheric mantle beneath the Cathaysia block, SE China. Lithos, 126(3-4), 182-197.

Zajacz, Z., & Szabó, C. (2003). Origin of sulfide inclusions in cumulate xenoliths from Nógrád–Gömör Volcanic Field, Pannonian Basin (north Hungary/south Slovakia). Chemical Geology, 194(1-3), 105-117.

Zajacz, Z., Candela, P. A., Piccoli, P. M., Sanchez-Valle, C., & Wälle, M. (2013). Solubility and partitioning behavior of Au, Cu, Ag and reduced S in magmas. Geochimica et Cosmochimica Acta, 112, 288-304.

Zajacz, Z., Kovács, I., Szabó, C., Halter, W., & Pettke, T. (2007). Evolution of mafic alkaline melts crystallized in the uppermost lithospheric mantle: a melt inclusion study of olivine-clinopyroxenite xenoliths, northern Hungary. Journal of Petrology, 48(5), 853-883.

Zanetti, A., Vannucci, R., Oberti, R., & Dobosi, G. (1995). Trace-element composition and crystal-chemistry of mantle amphiboles from the Carpatho-Pannonian Region. Acta Vulcanologica, 7, 265-276.

Zhang, H. F., Nakamura, E., Kobayashi, K., Ying, J. F., & Tang, Y. J. (2010). Recycled crustal melt injection into lithospheric mantle: implication from cumulative composite and pyroxenite xenoliths. International Journal of Earth Sciences, 99(6), 1167-1186.

Zhang, H., Zheng, J., Lu, J., Pan, S., Zhao, Y., Lin, A., & Xiang, L. (2018). Composition and evolution of the lithospheric mantle beneath the interior of the South China Block: insights from trace elements and water contents of peridotite xenoliths. Contributions to Mineralogy and Petrology, 173(7), 53.

Zhang, L., Sun, W. D., Zhang, Z., An, Y., & Liu, F. (2019). Iron isotopic composition of supra-subduction zone ophiolitic peridotite from northern Tibet. Geochimica et Cosmochimica Acta, 258, 274-289.

Zhang, Z., & Hirschmann, M. M. (2016). Experimental constraints on mantle sulfide melting up to 8 GPa. American Mineralogist, 101(1), 181-192.

Zhao, X., Zhang, H., Zhu, X., Tang, S., & Tang, Y. (2010). Iron isotope variations in spinel peridotite xenoliths from North China Craton: implications for mantle metasomatism. Contributions to Mineralogy and Petrology, 160(1), 1-14.

Zhao, X., Zhang, H., Zhu, X., Tang, S., & Yan, B. (2012). Iron isotope evidence for multistage melt–peridotite interactions in the lithospheric mantle of eastern China. Chemical geology, 292, 127-139.

Zhu, X. K., Guo, Y., Williams, R. J. P., O'nions, R. K., Matthews, A., Belshaw, N. S., Canters G. W., de Waal E. C., Weser U., Burgess B. K. & Salvato, B. (2002). Mass fractionation processes of transition metal isotopes. Earth and Planetary Science Letters, 200(1-2), 47-62.

Zinngrebe, E., & Foley, S. F. (1995). Metasomatism in mantle xenoliths from Gees, West Eifel, Germany: evidence for the genesis of calc-alkaline glasses and metasomatic Ca-enrichment. Contributions to Mineralogy and Petrology, 122(1-2), 79-96.

ADATLAP

a doktori értekezés nyilvánosságra hozatalához

I. A doktori értekezés adatai

A szerző neve:Patkó Levente
MTMT-azonosító: 10056849
A doktori értekezés címe és alcíme: Integrated study on the interaction between upper mantle and mafic melt evidenced by wehrlite xenoliths from the Nógrád-Gömör Volcanic Field(Northern Pannonian Basin, Central Europe)
DOI-azonosító[46]: 10.15476/ELTE.2020.022
A doktori iskola neve: Földtudományi Doktori Iskola
A doktori iskolán belüli doktori program neve: Földtan-Geofizika doktori program
A témavezető neve és tudományos fokozata: Dr. Szabó Csaba; egyetemi docens
A témavezető munkahelye: ELTE-TTK, FFI; Kőzettani és Geokémiai Tanszék

II. Nyilatkozatok

1. A doktori értekezés szerzőjeként
a) hozzájárulok, hogy a doktori fokozat megszerzését követően a doktori értekezésem és a tézisek nyilvánosságra kerüljenek az ELTE Digitális Intézményi Tudástárban. Felhatalmazom a Természettudományi kar Dékáni Hivatal Doktori, Habilitációs és Nemzetközi Ügyek Csoportjának ügyintézőjét, hogy az értekezést és a téziseket feltöltse az ELTE Digitális Intézményi Tudástárba, és ennek során kitöltse a feltöltéshez szükséges nyilatkozatokat.
b) kérem, hogy a mellékelt kérelemben részletezett szabadalmi, illetőleg oltalmi bejelentés közzétételéig a doktori értekezést ne bocsássák nyilvánosságra az Egyetemi Könyvtárban és az ELTE Digitális Intézményi Tudástárban;
c) kérem, hogy a nemzetbiztonsági okból minősített adatot tartalmazó doktori értekezést a minősítés (*dátum*)-ig tartó időtartama alatt ne bocsássák nyilvánosságra az Egyetemi Könyvtárban és az ELTE Digitális Intézményi Tudástárban;
d) kérem, hogy a mű kiadására vonatkozó mellékelt kiadó szerződésre tekintettel a doktori értekezést a könyv megjelenéséig ne bocsássák nyilvánosságra az Egyetemi Könyvtárban, és az ELTE Digitális Intézményi Tudástárban csak a könyv bibliográfiai adatait tegyék közzé. Ha a könyv a fokozatszerzést követőn egy évig nem jelenik meg, hozzájárulok, hogy a doktori értekezésem és a tézisek nyilvánosságra kerüljenek az Egyetemi Könyvtárban és az ELTE Digitális Intézményi Tudástárban.
2. A doktori értekezés szerzőjeként kijelentem, hogy
a) az ELTE Digitális Intézményi Tudástárba feltöltendő doktori értekezés és a tézisek saját eredeti, önálló szellemi munkám és legjobb tudomásom szerint nem sértem vele senki szerzői jogait;
b) a doktori értekezés és a tézisek nyomtatott változatai és az elektronikus adathordozón benyújtott tartalmak (szöveg és ábrák) mindenben megegyeznek.
3. A doktori értekezés szerzőjeként hozzájárulok a doktori értekezés és a tézisek szövegének plágiumkereső adatbázisba helyezéséhez és plágiumellenőrző vizsgálatok lefuttatásához.

Kelt: Budapest, 2020.04.27.